Università degli Studi di Trieste
Dottorato di ricerca in fisica – XIII ciclo
anno accademico 2000/01

Semihard parton rescatterings in heavy-ion interactions at collider energies

Alberto Accardi

Ph.D. Thesis

Tutore: prof. Daniele Treleani (università di Trieste)
Coordinatore: prof. Nello Paver (università di Trieste)

To my grandmother nonna Gemma
and my godfather Augusto

Contents

Overview **5**

1 Nucleus-nucleus collisions and the quark-gluon plasma **11**
1.1 Useful variables . . . 11
1.1.1 Light-cone variables . . . 12
1.1.2 Rapidity . . . 13
1.1.3 Pseudorapidity . . . 14
1.2 Nucleon-nucleon collisions . . . 16
1.3 Nucleon-nucleus and nucleus-nucleus collisions . . . 19
1.3.1 Glauber model . . . 20
1.3.2 The wounded nucleon model . . . 24
1.3.3 The nuclear interaction area . . . 26
1.3.4 Self-shadowing . . . 28
1.4 The quark-gluon plasma . . . 30
1.4.1 Baryon stopping and the QGP . . . 30
1.4.2 Bjorken's picture of the QGP . . . 32
1.5 Global observables and signatures of the QGP . . . 35
1.5.1 RHIC: the new energy frontier . . . 37
1.5.2 LHC: the future . . . 41

2 Semihard parton rescatterings **43**
2.1 Minijet cross section in Eikonal approximation . . . 45
2.1.1 Minijets . . . 45
2.1.2 The Eikonal model of minijet production . . . 46
2.1.3 The fate of the minijets . . . 49
2.2 Rescatterings, wounded partons and minijets . . . 49
2.3 Nonperturbative input: multiparton distributions . . . 52
2.4 Perturbative input: semihard rescatterings . . . 54
2.5 Minijet cross section . . . 56
2.5.1 Nucleus-nucleus scattering with no parton rescatterings . . . 58
2.5.2 Hadron-nucleus scattering . . . 59
2.6 Global average quantities . . . 61
2.6.1 Average number of wounded partons . . . 62
2.6.2 Average number of parton-parton collisions and of scatterings per parton . . . 64
2.6.3 Transverse spectrum of wounded partons . . . 65

2.6.4 Average transverse energy 66

3 Initial conditions in heavy-ion collisions 69
3.1 Parton rescatterings: average number and transverse energy of minijets . . 70
3.2 Numerical results and discussion 74
3.3 Conclusions 78

4 Parton saturation 81
4.1 Initial state saturation 82
4.1.1 Semi-classical QCD 83
4.1.2 Perturbative QCD 84
4.1.3 Charged particle multiplicity in high-density QCD 86
4.2 Final state saturation 88
4.2.1 Global criterion 89
4.2.2 Local criterion 91
4.2.3 Centrality and charged particle multiplicity 92
4.3 Saturation in the minijet production 99
4.3.1 Global criterion and initial conditions 99
4.3.2 Local criterion 103
4.3.3 Charged particle multiplicity 104
4.4 Comparing the saturation mechanisms 109
4.5 Conclusions 112

5 Minijet transverse spectrum 113
5.1 Inclusive minijet transverse spectrum 114
5.2 Expansion in the number of scatterings 116
5.2.1 Cancellation of the divergences 116
5.3 Numerical results and discussion 117
5.3.1 Effects of rescatterings 118
5.3.2 Minijet inclusive transverse spectrum 120
5.4 Conclusions 123

Appendix A More on the transverse spectrum 125
A.1 Cancellation of the divergences in the three-scattering term 125
A.2 Symmetrization of the expansion in the number of scatterings . . . 127
A.3 Generalization of the transverse spectrum 130

Bibliography 135

Overview

Heavy-ion physics and the quark-gluon plasma

Quantum Chromo-Dynamics (QCD) is almost universally accepted as the theory describing the strong interactions, and is nowadays a fundamental block of the Standard Model of elementary particle physics. However, most of the applications of QCD have been confined to the regime of very short distances and high energy transfers, where the theory can be linearized and perturbation theory is adequate. Indeed, thanks to the property called asymptotic freedom, the coupling constant in such a regime is small, allowing a systematic theoretical treatment. On the other hand, when one decreases the momentum transfer the coupling constant increases; at the same time the dynamics becomes rapidly nonlinear, so that its study becomes very difficult and has mostly to rely on models or lattice simulations.

Heavy-ion collisions allow physicists to study strong interactions under extreme conditions of the hadronic matter. Indeed, by increasing the atomic number of the colliding systems and by raising the energy of the collision, we get access to a regime where a very high energy density is created in the collision volume, and very dense matter at high temperature and pressure is produced. In this regime the coupling constant may be relatively small while the fields may be still in the nonlinear regime, giving us access to an entirely new set of phenomena, which we may try to describe from first principles. Heavy-ion collisions allow, therefore, to study QCD in a region not accessible to more traditional methods, see Fig. 1.

The possible states of QCD matter may be represented on a two dimensional phase diagram with the temperature T on the y-axis, and with the chemical potential μ_B as-

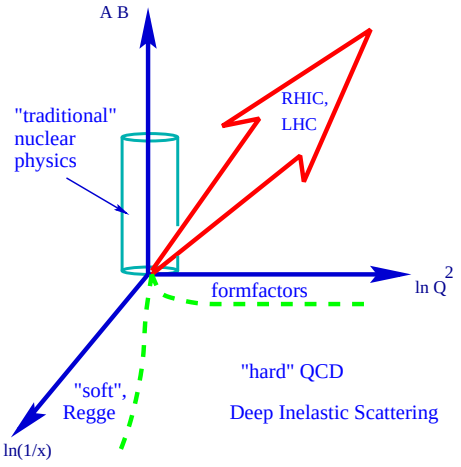

Figure 1: The place of heavy-ion physics in the study of QCD. The vertical axis is the product of the two atomic number of the projectile and the target. On the horizontal axis there are the logarithm of the momentum transfer Q and the "rapidity" $y = \log(1/x)$, where x is the Bjorken's scaling variable. The big arrow shows the region accessible to heavy-ion interactions at collider energies. Figure taken from Ref. [58].

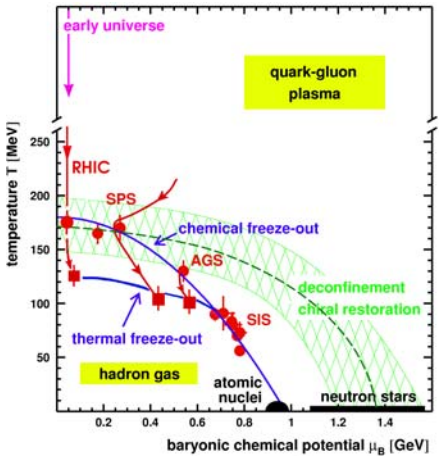

Figure 2: Sketch of the QCD phase diagram. The temperature T and the baryon chemical potential μ_B are represented on the vertical and horizontal axis, respectively. The cross-hatched region shows where the transition to the QGP phase is expected and the present theoretical uncertainty. The lines with the arrows indicate the trajectories of thermalized matter produced in nuclear collisions at different energies. Figure taken from Ref. [48].

sociated with the baryon density ρ_B on the x-axis (the higher μ_B, the higher ρ_B), see Fig. 2. Our knowledge of QCD matter at $\mu_B = 0$ is based on lattice QCD [56], but at $\mu_B \neq 0$ we have to rely on models which interpolate between low-density hadronic matter, described by low-energy effective theories and high-density quark-gluon plasma (QGP), which can be described by perturbative QCD (pQCD), see, e.g., Ref. [83]. These studies predict basically two phases for the strongly interacting matter, which can be created in the laboratory by heavy-ion collisions. At low temperature (i.e., low energy density) or low baryon density the matter is a gas of hadron resonances. Conversely, at high temperature (i.e., high energy densities) or high baryon density the matter may enter in the *quark-gluon plasma phase*. This phase of the matter is characterized by the possibility for the basic QCD degrees of freedom, the quarks and the gluons, to propagate freely over much larger distances than the hadron scales over which they are usually confined. At zero baryon density, lattice simulations of QCD with three light quark flavour predict a critical temperature $T_c = 170$ MeV $\pm$ 10% for the phase transition. This value decreases with increasing baryon density.

Heavy-ion collisions allow to explore the QCD phase diagram. At low energies – $\sqrt{s} \approx 2$ AGeV[1] at the Darmstadt Heavy Ion Synchrotron (SIS) – the nuclei are stopped, compressed and moderately heated; moderately high baryon densities but low energy densities are reached. At higher energies – $\sqrt{s} \approx 4$ AGeV at the Brookhaven AGS accelerator, and $\sqrt{s} \approx 17$ AGeV at the CERN Super Proton Synchrotron (SPS) – the colliding nuclei are no longer completely stopped and the baryon density of the produced system decreases. At collider energies – $\sqrt{s} = 200$ AGeV at the Brookhaven Relativistic Heavy Ion Collider (RHIC), and $\sqrt{s} \approx 6000$ AGeV at the CERN Large Hadron Collider (LHC) – the two nuclei nearly pass through each other, losing a large amount of energy in the process. The produced system has a large energy density and very low baryon content, simulating the conditions of the matter in the very early universe.

One of the problems in identifying experimentally the formation of the QGP is that it is indeed difficult to compute accurately its detailed properties. Progress in this direction is constant and the gap between what we can calculate and what we can measure is diminishing (see the theoretical summary talk [14] of the "Quark Matter 2001" conference

[1] A is the atomic number of the projectile nucleus in fixed target experiments and of the colliding nuclei, assumed equal, in collider experiments

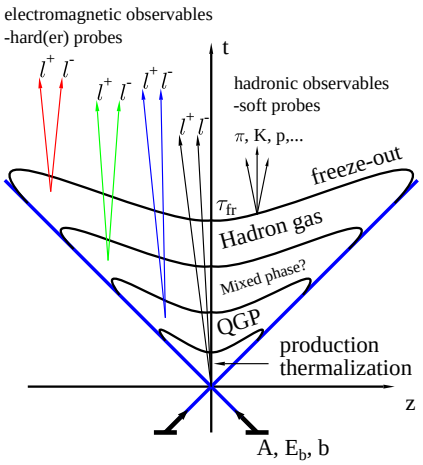

Figure 3: Space-time evolution of the system produced in a nuclear collision and some of the observables which allow to reconstruct its evolution and properties. Figure taken from Ref. [32].

[1]). The second difficulty is that it is not possible to observe directly the QGP and we have to reconstruct its properties from many later stage observables, like multiplicities and transverse momentum spectra of the produced hadrons. The main problem is that hadrons are produced more or less altogether at a late stage of the system evolution, see Fig. 3. An exception are leptonic observables. Indeed, leptons are produced at all the stages of the evolution of the system and interact rather weakly with the system, so that they carry direct information on its evolution. The great challenge of heavy-ion physics is thus to study and combine a large number of observables.

When the two nuclei collide ($t = z = 0$ in Fig. 3) a system of particles is produced. At collider energies these particles are mainly quarks and gluons. The energy density created in the collision is well above the critical energy density. The system then expands, mainly in the beam direction, and the energy density drops down. If the system thermalizes quickly enough for the energy density to remain above the critical one, it will pass through the phase transition and a QGP is formed. It is then of fundamental importance to have a quantitative control over the initial conditions. If this is reached, one can use hydrodynamic or transport models to describe the evolution of the produced system and compute final state observables to be compared with experimental data.

Plan of the thesis

One of the main advantages of heavy-ion interactions at collider energies is that, given the very high incident energy, semihard and hard processes are an important feature at RHIC and will be dominant at LHC. The result of the nuclear interaction is therefore the production of a very large number of partons, also called *minijets* in a very short time $\tau \sim 0.1 - 0.2$ fm after the two nuclei passed through each other. This system of partons, also called *minijet plasma*, will then expand and tend to thermalize, possibly entering in the QGP phase. Thanks to the dominance of semihard and hard processes it is possible to compute in perturbative QCD the gross properties of the interaction, and in particular the initial conditions of the minijet plasma. The application of perturbative QCD to these computations is the object of this thesis. The detailed discussion will be preceded by a general introduction to nucleus-nucleus interactions, the quark-gluon plasma, and the most recent data from RHIC [Chapter 1].

Parton rescatterings

At ultrarelativistic energies the parton density of the colliding nuclei is so high that the probability becomes high for a projectile parton to have more than one parton-parton collision per event. We may distinguish these multiple collisions in two types: (a) *disconnected collisions*, when more than one pair of partons interact in different points in transverse space, and (b) *rescatterings*, when the same parton scatters more than once against the target partons. The conventional perturbative approach takes into account only the first kind of multiple interactions; however, as the energy and the target nuclear mass increase the rescattering probability becomes larger and larger, and gives a non negligible effect both at RHIC and at LHC.

Inclusion of the rescatterings in the interaction dynamics can be performed without introducing new free parameters, and after this a number of observables like the multiplicity and the transverse energy of the produced minijets get a weaker dependence on the cutoff introduced to separate soft and hard interactions [Chapter 2]. This allows to push in a reliable way the perturbative computations to lower values of this cutoff, in a region of transition between a perturbative and a genuinely non perturbative regime.

Parton saturation and initial conditions

In Chapter 3 I show that the initial multiplicity and transverse energy of the minijets show a tendency to saturate at low cutoff values. Based on this, in Chapter 4 I introduce a *saturation criterion* to fix the cutoff to a physically meaningful value. The *saturation cutoff* obtained in this way represents the typical scale of the interaction at which semihard interactions extract from the two nuclei almost all their partons. This allows the complete computation of the semihard contribution to global observables. The soft part of the interaction, i.e., the part which cannot be described in terms of partons and their interactions, may be introduced in a phenomenological way and its contribution is found to be the 15-20% of the total at RHIC and around the 5% at LHC. With these methods I analyzed the RHIC data on charged multiplicities in Au-Au collisions at a nucleon-nucleon center of mass energy of 130 GeV finding a good agreement with experimental data. This allowed me to make prediction on multiplicities at 200 GeV which have been recently verified by the PHOBOS collaboration in the case of central collisions.

In Chapter 4 this saturation model is, moreover, compared with an "initial state" saturation model [60, 61] and a "final state" saturation model [33, 35]. Moreover, I slightly modified the latter by introducing the concept of "nuclear interaction area", i.e. the average area in the transverse plane where interactions among the constituents of the nuclei take place. For some observables I obtained a qualitatively different result with respect to the original model, and a better agreement with experimental data. Predictions are made for some observables at LHC energies, and the possibility to distinguish experimentally which of the three models is more correct is discussed.

Transverse momentum spectrum of minijets

Semihard parton rescatterings also have a large effect on the transverse momentum distribution of the minijets [Chapter 5 and Appendix A]. I studied this observable by an expansion in the number of interactions suffered by a projectile parton in its interac-

tion with the target nucleus. This expansion is valid at high transverse momenta and generalizes the results known in literature, which consider terms up to two scatterings. I developed numerical methods to compute each term of the expansion, and I studied them numerically up to the three-scattering term. Moreover, I show that it is possible to compute numerically the transverse spectrum resummed to all orders in the number of scatterings. In this way it is possible to study it completely up to zero transverse momentum. I applied these methods to the study of the deformation of the transverse spectrum with respect to what one expects from a simple superposition of proton-nucleon collisions (Cronin effect).

The case of proton-nucleus collisions (considered in the numerical computations) is especially interesting since it allows an accurate test of the dynamics proposed. Indeed, this is a situation where one does not expect the formation of the QGP, which could further modify the spectrum. A thorough quantitative understanding of proton-nucleus collisions is then a very important baseline for the detection and the study of the QGP in nucleus-nucleus collisions.

Conclusions

In this thesis I show that at RHIC energies it is very important, and at LHC energies it is essential, to include parton semihard rescatterings in the perturbative computations of the initial conditions of the minijet plasma and of global characteristics of the minijets, like their transverse momentum spectrum.

After introducing the rescatterings, the interaction is unitarized, and a number of observables may be computed much more reliably in perturbative QCD because of the softening of their infrared divergences. The initial conditions for the minijet plasma evolution may be computed by introducing a saturation criterion to fix the infrared cutoff. The resulting model needs no phenomenological parameters, and is rather stable against variations of the few theoretical choices which have to be made, namely, the choice of the k factor which simulates next-to-leading order corrections, and the choice of the parton distribution functions. The model has been tested against the first RHIC data on charged multiplicities and is in good agreement with experimental observations.

Further tests of the model are needed to verify the correctness of the multiple semihard scattering dynamics it describes. In particular, this can be done by studying hadron or minijet transverse momentum spectra in proton-nucleus collisions. This is an intermediate step to relate the dynamics of nucleon-nucleon collisions to the dynamics of heavy-ion collisions, in a setting where the formation of hot and dense matter is not expected. The minijet transverse spectrum has been computed at all orders in the number of semihard parton rescatterings, and shows some interesting features which might be accurately tested experimentally. More work has to be done to use these results in the computation of hadron spectra. It would also be interesting to include inelastic processes, like gluon *bremsstrahlung*, in this multiparton scattering model.

Further applications of the formalism are under investigation, in particular the study of two-particle azimuthal correlations induced by semihard scatterings. These studies might be important since they give a further test of the multi-scattering parton dynamics. Moreover, these semi-hard correlations might be a large source of background for global observables like the elliptic flow.

Chapter 1

Nucleus-nucleus collisions and the quark-gluon plasma

A nucleus is a composite system of many nucleons, so that hadron-nucleon (hA) collisions and nucleus-nucleus (AA) collisions depend on the dynamics of the colliding nucleons[1]. An important question is how nucleon-nucleon collisions add up to give a nuclear collision, e.g., to what extent the latter may be thought as a simple superposition of the former. In particular, the energy dissipated in the collision of two heavy nuclei, with a release into other degrees of freedom, is expected to be rather high, being the result of many nucleon-nucleon collisions. Is the energy density so created high enough to allow the formation of the quark-gluon plasma? What are the experimental signatures of such a state of the matter? A necessary step to answer these questions is to understand what it is to be expected in nuclear collisions from an extrapolation of the known nucleon-nucleon dynamics to hA collisions and finally to AA collisions.

In this chapter, after a brief introduction to the relevant kinematic variables (Sec. 1.1), we will summarize some aspects of nucleon-nucleon collisions (Sec. 1.2) and will discuss the Glauber model of nuclear interactions, in which nucleon-nucleon collisions are added up in a way that summarizes the basic geometrical and dynamical aspects of nuclear collisions (Sec. 1.3). We will then discuss the possibility of the formation of the Quark-Gluon Plasma (QGP) and describe the Bjorken's picture of its space-time evolution(Sec. 1.4). Finally we will discuss the global observables which allow to constrain the initial matter and energy density conditions for the formation of the QGP and some of its experimental signatures (Sec. 1.5). The emphasis will be on recent data from RHIC and on the observables which will be discussed in the following chapters. Many of the discussions of this chapter have been inspired by Refs. [45, 73, 94], to which we refer for an introduction to the subject.

1.1 Useful variables

Consider a collision of two "particles" a and b (they may be hadrons or nuclei) in the center of mass frame, see Fig. 1.1. Here we assume that the colliding particles are energetic

[1]We denote by h a generic hadron, and will use the symbol of a specific hadron when needed, e.g., p for a proton. By the generic name of *nucleons* we will call both protons and neutrons inside a nucleus and other hadrons. The capitol letter A stands both for a generic nucleus and for a given nucleus atomic number.

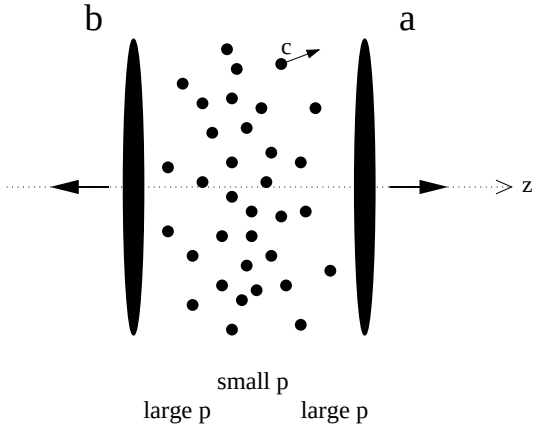

Figure 1.1: A collision of two "particles" a and b in the center of mass frame. The two particles are strongly Lorentz contracted and just passed through one another. In the collision a particle c and a "remnant" X made of other particles are produced (the produced particles are represented by little black disks).

enough to pass through one another and produce hadrons in the middle. This is an experimental fact: at high energies the degrees of freedom which carry the particle quantum numbers lose only a small fraction of their longitudinal momentum in the collision. In many high-energy collisions of this kind it is useful to use kinematic variables with simple transformation properties with respect to boosts along the beam axis. In this section we consider a reaction $a + b \to c + X$ in which a particle c is detected in the final state and discuss some of these variables. We call z *axis* the beam axis, and call *transverse plane* the plane transverse to the beam (the xy-plane). We use natural units, where the speed of light is $c = 1$ and the Minkowsky space metric has signature $(+---)$. For simplicity of notation when referring to a given particle a we will use the same letter to represent also its four momentum. By convention we will consider a to be the *projectile or beam particle* and b to be the *target particle*.

1.1.1 Light-cone variables

Given the four-momentum of a particle, $p = (p_0, \vec{p}_T, p_z)$, two special combinations of its components, called *forward (backward) light-cone momentum*, have simple transformations with respect to longitudinal boosts; we define

$$p^{\pm} = p_0 \pm p_z \ ,$$

so that the four-momentum may be represented by $(p^+, \vec{p}_T, p^-)$. Note that the invariant dot product becomes

$$p \cdot q = p^+ p^- - \vec{p}_T \cdot \vec{q}_T$$

and when the particle is on the mass-shell

$$p^+ p^- = (E^2 - p_z^2) = (p_T^2 + m^2) \equiv m_T^2 \ ; \tag{1.1.1}$$

here m is the rest mass of the particle, $p^2 = m^2$, and the last equality defines the *transverse mass* m_T.

For a high-energy particle moving in the positive z axis direction (a in Fig. 1.1) the forward light-cone momentum is large and the backward light-cone momentum is small; the opposite is true for a particle moving toward the negative z axis direction (b in

Fig. 1.1). Given a longitudinal boost of velocity β in the positive z direction, the forward light-cone momentum in the new frame, p'^+ is related to p^+ by

$$p'^+ = \gamma\,(1-\beta)p^+ \ ,$$

where $\gamma = 1/\sqrt{1-\beta^2}$. Sometimes the particle c may be thought to originate from, say, a. In this case it is useful to introduce the *light-cone variable* x^+ as

$$x^+ = \frac{c^+}{a^+} \ . \tag{1.1.2}$$

This is the boost-invariant generalization of the *Feynman's x*, $x_F = c_z^*/c_{z|max}^*$, defined as the fraction of the actual longitudinal momentum of c in the center of mass frame to its maximum momentum (starred symbols refer to the center of mass frame). Therefore, $x^\pm$ is also called *light-cone momentum fraction*. Similarly we can define $x^- = \frac{c^-}{a^-}$ At high center of mass energy $\sqrt{s}$ we have $x_F \approx x^\pm$ for positive (negative) longitudinal momentum c_z^*. The light-cone momentum fraction is invariant under longitudinal boosts:

$$x'^\pm = x^\pm \ .$$

In some problems (e.g., in deep inelastic scattering or high-energy hadron and nuclear collisions) the beam particle, a, may be considered as a composite system of a constituent particle c and other parts X. In this case c is not a free particle, does not satisfy the mass-shell condition $c^2 = m^2$, and it is in interaction with the remaining constituents X. It is nonetheless useful to describe it by its light-cone momentum fraction x^+ with respect to its parent particle. In this case one usually writes $x^\pm = x$ and calls it *Bjorken's x*.

1.1.2 Rapidity

Another useful variable which transforms simply under longitudinal boosts and gives a relativistic generalization of the velocity of a particle is the *rapidity* variable. The rapidity is defined by

$$y = \frac{1}{2}\ln\left(\frac{p^+}{p^-}\right) = \ln\left(\frac{p^+}{m_T}\right) \ , \tag{1.1.3}$$

where the last equality holds for on-shell particles. The rapidity y may be either positive or negative, and describes a particle moving in the positive or negative z direction, respectively. From Eq. (1.1.3) we have $e^{\pm y} = \sqrt{p^\pm/p^\mp}$, and by using Eq. (1.1.1) it is immediate to see that

$$p_0 = m_T\,\cosh y \tag{1.1.4}$$

$$p_z = m_T\,\sinh y \ . \tag{1.1.5}$$

In the nonrelativistic limit the modulus of the rapidity coincides with the particle velocity v measured in units of the speed of the light:

$$|y| \underset{\beta\to 0}{=} v + O(v^2) \ . \tag{1.1.6}$$

Under a boost of velocity β the particle's rapidity in the new reference frame is

$$y' = y - y_\beta \ , \tag{1.1.7}$$

where

$$y_\beta = \frac{1}{2}\ln\left(\frac{1+\beta}{1-\beta}\right) \ .$$

y_β may be conveniently called the *rapidity of the moving frame* since y_β is the rapidity that a particle at rest in a frame moving at velocity β would have in the old frame. Under a reversal of the z axis, $z \to -z$, it changes sign: $y' = -y$. The simple additive laws (1.1.6) and Eq. (1.1.7) are analogous to the velocity transformation laws in the nonrelativistic limit and justify considering the rapidity as the relativistic generalization of the velocity of a particle.

Consider the collision of a beam particle a against a target particle b, which have $\vec{a}_T = \vec{b}_T = \vec{0}$. From the Eqs. (1.1.3) and (1.1.5) the particle rapidities are:

$$\begin{aligned} y_a &= \ln(a^+/m_{aT}) = \sinh^{-1}(a_z/m_a) \\ y_b &= \ln(b^+/m_{bT}) = \sinh^{-1}(b_z/m_a) \ . \end{aligned}$$

In the case that $m_a = m_b$ the rapidity of the center of mass frame is

$$y_{cm} = \frac{y_a + y_b}{2}$$

and in the center of mass frame the rapidities are

$$\begin{aligned} y_a^* &= (y_a - y_b)/2 \\ y_b^* &= (y_b - y_a)/2 \ . \end{aligned}$$

Therefore, the greater the collision energy the greater the distance in rapidity between the beam and the target particle, $\Delta y = y_a - y_b$. The region about midway the projectile and target rapidity is called *central rapidity region* and is where most of the particles produced in the collisions lie.

While the light-cone variables $x^\pm$ describe a daughter-parent relationship between two particles and is frame independent, the rapidity is a kinematic variable related to a single particle in a given reference system. From the definitions (1.1.3) and (1.1.2) we obtain a relationship between these two variables:

$$\begin{aligned} x^+ &= \frac{m_{cT}}{m_b} e^{y - y_b} \\ x^- &= \frac{m_{cT}}{m_a} e^{y_a - y} \ . \end{aligned}$$

1.1.3 Pseudorapidity

To obtain the rapidity of a particle one needs to measure two independent variables, say, its energy and its longitudinal momentum. However not in all experiments this is possible, while it is rather easy to measure the angle θ between the particle trajectory

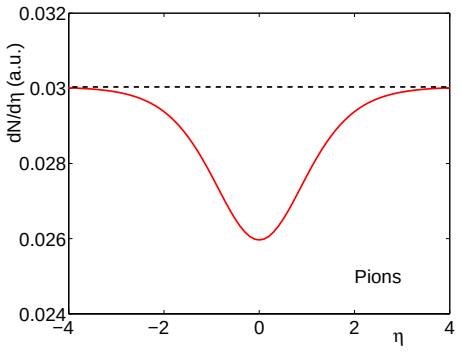

Figure 1.2: Transformation from rapidity to pseudorapidity distributions of pions (viz., dashed and solid line) in the center of mass frame. For illustration purposes it is assumed that the rapidity distribution is flat in the whole rapidity interval, so that the role of the Jacobian in Eq. (1.1.10) is shown. At mid-rapidity the suppression factor is around 0.9. Figure taken from Ref. [63].

and the beam axis. This angle is related to the particle momentum, $\cos\theta = p_z/|\vec{p}|$, where $|\vec{p}| = \sqrt{p_T^2 + p_z^2}$. Then we define the *pseudorapidity* variable as

$$\eta = \frac{1}{2}\ln\left[\tan(\theta/2)\right] = \frac{1}{2}\ln\left(\frac{|\vec{p}| + p_z}{|\vec{p}| - p_z}\right) \ . \tag{1.1.8}$$

Note that this variable requires, to be measured, only a good tracking capability of the detector and is independent on its particle identification capability. From definition (1.1.8) it is easy to see that

$$\begin{aligned} |\vec{p}| &= p_T \cosh\eta \\ pz &= p_T \cosh\eta \ . \end{aligned}$$

Let's study the relation between pseudorapidity and rapidity. From definitions (1.1.8) and (1.1.3) it follows that for massless particles $\eta = y$. This suggests also that at large momentum, $|vecp| \gg m$ the two variables should be approximately the same. Indeed,

$$\eta = \frac{1}{2}\ln\left(\frac{\sqrt{m_T^2\cosh^2 y - m^2} + m_T \sinh y}{\sqrt{m_T^2\cosh^2 y - m^2} - m_T \sinh y}\right) \underset{\substack{m^2/p_T^2\to 0 \\ \text{or } y\to y_{max})}}{\sim} y \ . \tag{1.1.9}$$

Since in some experiments only the pseudorapidity may be measured, it is useful to have the transformation law from pseudorapidity to rapidity distributions. From Eq. (1.1.9) it is straightforward to compute the Jacobian of the transformation from $(\eta, \vec{p}_T)$ to $(y, \vec{p}_T)$, and

$$\frac{dN}{d\eta\, d^2p_T} = \sqrt{1 - \frac{m^2}{m_T^2\,\cosh^2 y}}\,\frac{dN}{dy\, d^2p_T} \ . \tag{1.1.10}$$

We can see that, in general, pseudorapidity distribution are smaller than rapidity distributions. The suppression is larger the smaller p_T, the larger m, and around the peak of the distribution, i.e., around mid-rapidity. At high p_T and large y the two distributions approach one another. In the center of mass frame the suppression factor is maximum at $y \approx \eta \approx 0$ and is roughly $[1 - m^2/\langle m_T^2\rangle]^{1/2}$. As an example, we may take $\langle m_T^2\rangle \approx 300 MeV$ at $\sqrt{s} = 30.6$ GeV for basically all kinds of particles, see Eq. (1.2.2). This gives for pions, the most abundantly produced particles whose mass is $m_\pi = 140$ MeV, a suppression

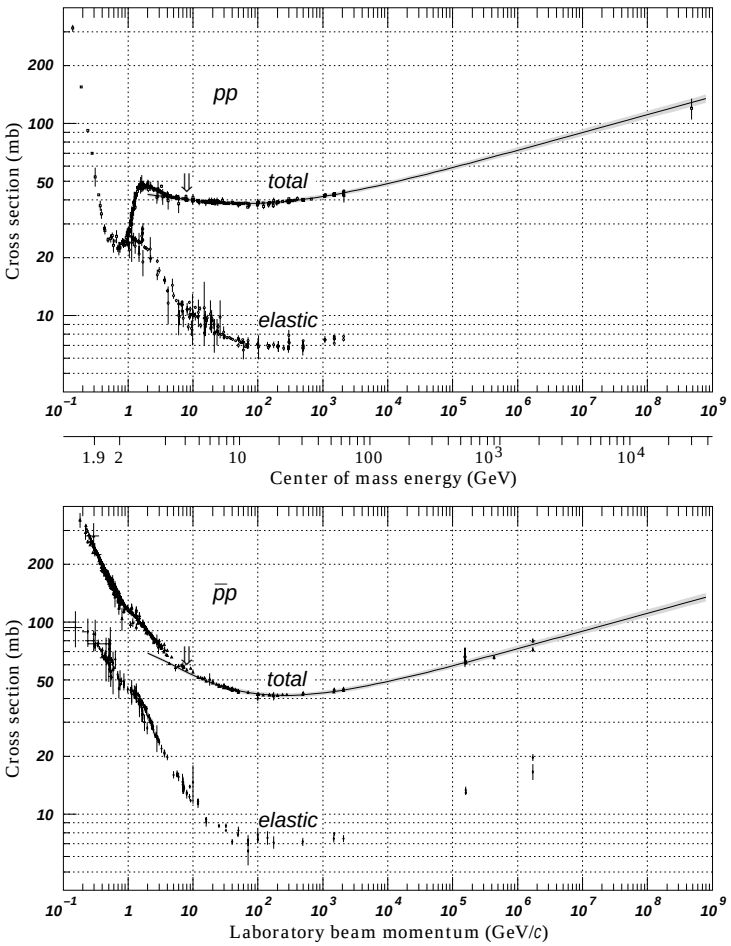

Figure 1.3: Total and elastic cross sections for pp and $p\bar{p}$ collisions as a function of the laboratory beam momentum and total center-of-mass energy. Figure taken from Ref. [121].

factor of ~ 0.9 at central rapidities. This value decreases with increasing η and at large pseudorapidities it is nearly one. Since experimentally particles are distributed uniformly in rapidity we e expect to see a dip around central pseudorapidity, see Fig. 1.2. Conversely, in the laboratory frame the peak of the distribution is located at $\eta \approx y_b/2$ and the maximum suppression factor is roughly $[1 - m^2/(\langle m_T^2 \rangle \cosh^2 y_b)]^{1/2} \approx 1$. Therefore in fixed target experiments the two distribution roughly coincide.

1.2 Nucleon-nucleon collisions

The nucleon nucleon total cross-section in the energy range 3 GeV $< \sqrt{s} <$ 100 GeV is roughly constant and has a value of about 40 mb, see Fig. 1.3. It includes *elastic scattering* processes in which the colliding nucleons do not lose any energy, and *inelastic scattering* processes in which they lose varying amounts of energy and a varying amount of particles are produced. The inelastic nucleon-nucleon cross section $\sigma_{in} = \sigma_{in}(\sqrt{s})$ may be estimated as the difference of the total and elastic $p\bar{p}$ cross-section, see Fig. 1.4. Using

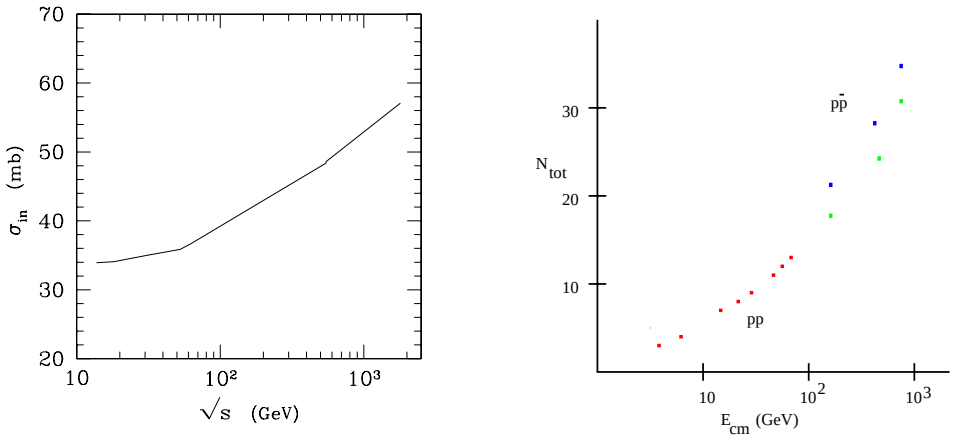

Figure 1.4: *Left:* Inelastic cross section σ_{in} computed as the difference of total and elastic cross section in $p\bar{p}$ scattering. Data are taken from Ref. [121]. *Right:* Total multiplicity of particles produced in pp (leftmost points) and $p\bar{p}$ collisions (six rightmost points) as a function of the center of mass energy. Figure taken from Ref. [73].

data on pp interactions would not change significantly the result. At SPS and RHIC energies, $\sqrt{s} = 17 \ldots 200$, it has a value $\sigma_{in} = 34 \ldots 42$ mb. However, there are no experimental data for $\sqrt{s} > 1.8$ TeV, and at LHC energies we estimate $\sigma_{in} \sim 70$ mb. Among the inelastic processes there are also *diffractive processes*, where one nucleon may be considered as an absorber and a diffractive pattern appears in the very forward or very backward rapidity region due to interference between scattering amplitudes. In these events one nucleon becomes excited and a small number of particles are produced at large rapidities, but the energy loss is small. Since we are interested in mid-rapidity or near-mid-rapidity production processes at ultrarelativistic energies, we will neglect altogether these diffractive processes.

Experimental data reveal that about 90% of the produced particles are pions, and the rest consists of mostly kaons, around 1% of protons and very small fractions of other hadrons. The total number of particles produced in a collision is called the *multiplicity* of the collision. Charged particles are easier to detect since they ionize easily a medium. In this case one speaks of the *charged multiplicity* of the collision. In Fig. 1.4 the multiplicity of produced particles in pp and $p\bar{p}$ collisions is plotted. The last six points correspond to the multiplicity in $p\bar{p}$, the lower three being the same as the upper three but with zero energy multiplicity subtracted. After subtraction all the points fall on the same curve, which means that whatever is the particle production mechanism it may be the same both in pp and in $p\bar{p}$ collisions. The charged multiplicity in nucleon-nucleon collisions increases with $\sqrt{s}$ in an approximately logarithmic way. To have a quantitative feeling, we quote the CDF fit to the pseudorapidity density of charged particles produced at $\eta = 0$ in $p\bar{p}$ collision as a function of the center of mass energy $\sqrt{s}$ [97]:

$$n_{p\bar{p}}(s) = 2.5 - 0.25 \log(s) + 0.023 \log^2(s) \ . \tag{1.2.1}$$

In the center of mass frame particles are always produced in the rapidity range $-\bar{y} < y < \bar{y}$, where $\bar{y} = \ln(p^+_{\rm proj}/m_{\rm proj})$, $p^+_{\rm proj}$ and $m_{\rm proj}$ are, respectively, the forward light-cone momentum and the mass of the projectile, in our case a nucleon. The forward (backward) rapidity region $y \lesssim \bar{y}$ ($y \gtrsim -\bar{y}$) are called the *fragmentation regions* of the right-moving and left-moving particles, respectively. In the respective fragmentation

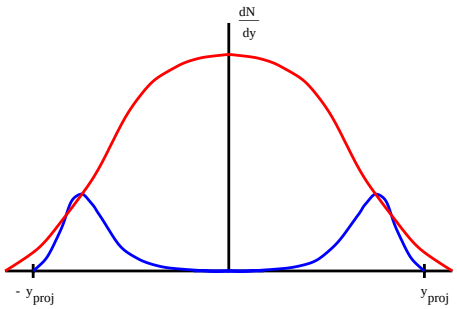

Figure 1.5: Rapidity distribution of particles produced in a nucleon-nucleon collisions. The lower curve is the leading particle distribution and the upper curve the meson distribution. Figure taken from Ref. [73].

regions there is a high probability to find particles that closely resemble the incident particles. They carry a large fraction of $\sqrt{s}$ and are among the fastest particles in those regions. They are called *leading particles* and their rapidity distribution is shown schematically by the lower curve of Fig. 1.5. In the same figure the upper curve shows the typical distribution of produced mesons. At low energies, say $\sqrt{s} = 13.8$ GeV, the pseudorapidity distribution has the form of a bell-shaped curve, while at higher energies a plateau at mid-rapidity appears, see Fig. 1.6. A remarkable feature of these distribution, known as *Feynman scaling*, is that if we plot them as a function of the distance in rapidity from the fragmentation region the distributions are to a good approximation independent of the energy. The exception is the height of the plateau, which is constant at low energies but becomes an increasing function of $\sqrt{s}$ at higher energies.

The average transverse momentum of the produced pions is about 350 MeV and increases for heavier particles and with increasing $\sqrt{s}$. We shall call $dN/d^2p_t \equiv dN/(2\pi p_t dp_t)$ the *transverse momentum distribution*, which is found experimentally to have a roughly exponential shape at low p_t and an inverse power shape at p_t larger than a few GeV, where perturbative computations begin to be valid. We will refer to particles with a transverse momentum smaller than 1 GeV as *soft particles* and to such low p_t region as the *soft region* of transverse momenta. When the $p_t \gtrsim 1$ GeV we will use the names *hard particles* and *hard region*, respectively. Hard particle production is understood in pQCD as due to parton-parton scatterings and successive hadronization of the partons. It turns out that the transverse particle spectrum is nearly independent of the particle species if it is plotted as a function of the transverse mass $m_T = \sqrt{p_T^2 + m^2}$ and that

$$E\frac{dN}{dp_z\, d^2p_t} = \frac{dN}{dy\, d^2p_t} \approx A\frac{e^{-m_T/T}}{(m_T/GeV)^\lambda}\ , \tag{1.2.2}$$

where at $\sqrt{s} = 30.6$ GeV we have $T = 0.290$ GeV, $A = 13.9$ mb/GeV^2 and $\lambda = 1.5$ [41]. Notice that T is an approximately universal parameter for all particle species, see Fig. 1.6. This approximately universal behaviour is known as m_T *scaling*.

The last feature of nucleon-nucleon collision we want to mark out is the *nucleon rapidity loss*. The baryon number must be conserved in any reaction, therefore there must be at least two baryons among the produced particles. Baryons found in the projectile and target fragmentation regions are called *leading baryons*. If we consider the leading baryon related to the colliding nucleons, we can view a nucleon-nucleon collision as a process in which the two energetic nucleon suffer a degradation of their momenta and emerge as leading baryons. It is therefore natural to ask how much momentum they lost, or

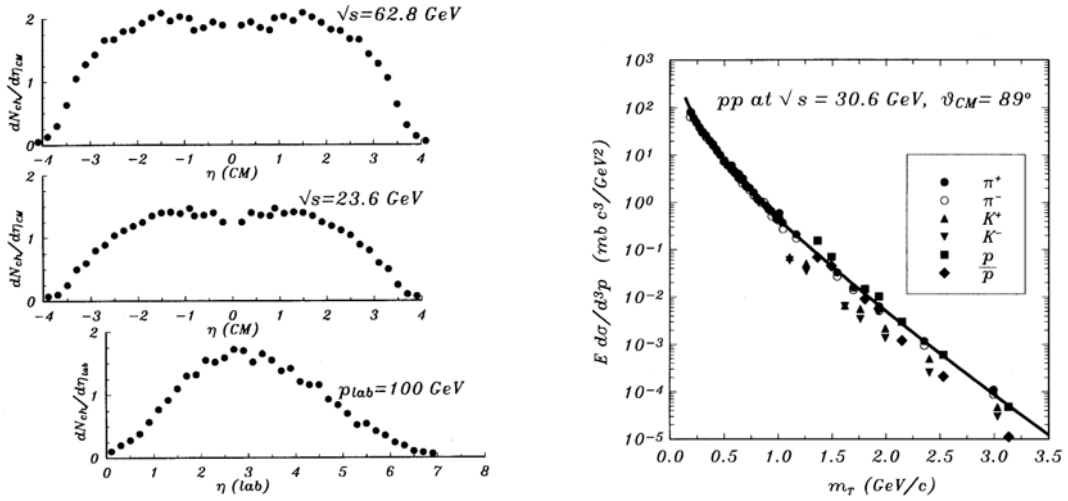

Figure 1.6: *Left:* pseudorapidity distribution of charged particles at various energies from Refs. [120, 131]. Pseudorapidity is measured either in the center of mass frame (η_{CM}) or in the laboratory frame (η_{lab}) and suitably shifted for comparison of the results. *Right:* invariant cross section for the production of different particles in pp reactions at $\sqrt{s} = 30.6$ GeV as a function of the particle transverse mass m_T from Ref. [108]. Both figures taken from Ref. [94].

better how much rapidity they lost, the higher the rapidity loss the higher the degree of inelasticity of the collision. In Fig. 1.7 the inelastic cross section $d\sigma/dx^+$ is shown for pp reactions at $\sqrt{s} = 13.8$ and 18.2 GeV [117]. Except for the diffractive dissociation region $x^+ \sim 1$ it is a nearly constant function of x^+, therefore the average value of the light-cone variable is

$$\langle x^+ \rangle = \frac{1}{2} \ .$$

Consider a leading proton in the projectile fragmentation region. It is found that at both energies its average transverse momentum is $\langle p_T \rangle \approx 0.460$ GeV. The rapidity distribution is

$$\frac{d\sigma}{dy_l} = \frac{d\sigma}{dx^+}\frac{dy_l}{dx} = \frac{d\sigma}{dx}\frac{m_{lT}}{m_p}e^{y_l - y_p} \ ,$$

where m_l is the transverse mass of the leading proton and y_l its rapidity, while m_p and y_p refer to the colliding proton. Since $d\sigma/dx^+$ is almost constant in the fragmentation region, the average rapidity of the leading proton is

$$\langle y \rangle = \frac{\int y_l \frac{d\sigma}{dy_l} dy_l}{\int \frac{d\sigma}{dy_l} dy_l} \approx y_p - 1 \ .$$

Therefore, on the average an incident proton loses one unit of rapidity in a nucleon-nucleon collision.

1.3 Nucleon-nucleus and nucleus-nucleus collisions

In this section we will review the Glauber model of pA and AA collisions, which describes the underlying multiple nucleon-nucleon collision in an elementary but rather precise way,

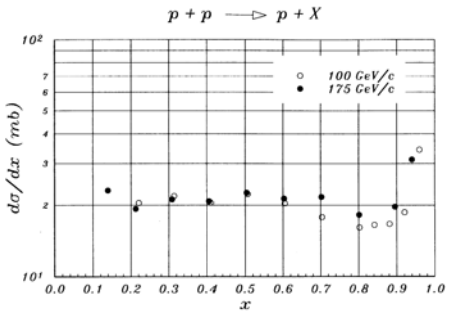

Figure 1.7: The differential cross section $d\sigma/dx^+$ for the reaction $p+p \to p+X$ at different laboratory energies as a function of the proton forward light-cone variable $x \equiv x^+$. Data taken from Ref. [117]. Figure taken from Ref. [94].

and encodes the geometrical features of the nuclear collision. We will then review the wounded nucleon model of particle production. Based on these results, we will introduce a way to compute the *interaction area*, i.e., the area in the plane transverse to the beam where the nucleon-nucleon interactions take place. Finally, we will review the concept of self-shadowing of the hard nucleon nucleon interactions, which allows one to compute the hard part of the inelastic pA or AA cross-section without the need of knowing also the soft part.

1.3.1 Glauber model

Multiple nucleon-nucleon interactions occurring in a AA collision may be described in the Glauber model of nuclear interactions, which provides a quantitative description of the geometrical configuration of the system. It is based on the assumption that the inelastic collision of two nuclei can be described as an incoherent superposition of the collisions of each individual nucleon, and has proved to be useful in estimating global observables like inelastic cross-sections, multiplicities, dispersions and their dependence on nuclear parameters. Although a baryon of one nucleus may become excited in the interaction and may, in principle, have a different cross-section when passing through the other nucleus, we can understand the basic features of the nuclear collision by taking the nucleon-nucleon cross-section to be the same throughout the entire path of a nucleon through the target nucleus. Since our basic assumption is that nucleon-nucleon collisions are incoherent, we may describe the nuclear collision by using probability calculus.

We start by defining the *nucleon spatial density* of a nucleon of atomic number A,

$$\rho_A(r,z) = \frac{dN(r,z)}{d^2r\,dz} \ ,$$

where r is the coordinate in the (two dimensional) plane transverse to the beam, z is the coordinate along the beam and $dN(r,z)$ is the average number of nucleons contained in the volume element $dV = d^2r\,dz$ located at $\vec{r} = (r,z)$. By definition ρ_A is normalized to A:

$$\int d^2r\,dz\,\rho_A(r,z) = A \ . \tag{1.3.1}$$

The probability density of finding a nucleon at a given point $\vec{r}$ is, therefore, $\rho_A(r,z)/A$. A useful quantity is the *nuclear thickness function*

$$\tau_A(r) = \int dz\,\rho_A(r,z) \ ,$$

which represents the nuclear density projected on a plane transverse to the beam, or in other words the thickness of the nucleus at a given point r in the transverse plane. We will discuss later the explicit form of the nuclear densities and thickness functions.

Next, we have to discuss nucleon-nucleon collisions. Given two nucleons situated at an impact parameter b relative to one another, we define $t_{pp}(b)d^2b$ as the probability for having a nucleon-nucleon collision within an area element d^2b. By definition t is normalized to 1:

$$\int d^2b\, t_{pp}(b) = 1 \ . \tag{1.3.2}$$

Given a nucleon at impact parameter b relative to another nucleon, the probability of a nucleon-nucleon inelastic collision is thus $t_{pp}(b)\sigma_{in}$.

The above definitions allow to write allow to write the probability distribution P for the occurrence of nucleon-nucleon collisions when the nuclei have an impact parameter b and the two nucleons sit at (r_A, z_A) and (r_B, z_B), respectively. It is given by the product of *(i)* the probability of finding a nucleon in the A nucleus at (r_A, z_A), *(ii)* the probability of finding a nucleon in the B nucleus at (r_B, z_B) and *(iii)* the probability that the two collide:

$$P(b; r_a, z_A, r_b, z_b) = \frac{1}{A}\rho_A(r_A, z_A) \times \frac{1}{B}\rho_B(r_B, z_B) \times t_{pp}(b - r_A - r_B)\sigma_{in} \ .$$

By integrating over the nucleon coordinates we obtain the total probability, $\frac{1}{AB}T_{AB}(b)\sigma_{in}$, for the occurrence of a nucleon-nucleon collision in a nuclear collision with impact parameter b:

$$\frac{1}{AB}T_{AB}(b)\sigma_{in} = \frac{1}{AB}\int d^2r_A\, dz_A\, d^2r_B\, dz_B\, \rho_A(r_A, z_A)\, \rho_B(r_B, z_B)\, t_{pp}(b - r_A - r_B)\sigma_{in} \ .$$

This equation defines the *overlap function* for the collision of the A nucleus with the B nucleus, which can be expressed in terms of the thickness functions by integration over z_A and z_B:

$$T_{AB}(b) = \int d^2r_A\, d^2r_B\, \tau_A(r_A)\, \tau_B(r_B)\, t_{pp}(b - r_A - r_B) \ . \tag{1.3.3}$$

From Eqs. (1.3.1) and (1.3.2) it is easy to see that the overlap function is normalized to AB:

$$\int d^2b\, T_{AB}(b) = AB \ .$$

We are now in the position to write the basic expression for all the following computations, i.e., the *probability of n inelastic nucleon-nucleon collisions* at nuclear impact parameter b:

$$\boxed{P(n, b) = \binom{AB}{n}\left[\frac{T_{AB}(b)}{AB}\sigma_{in}\right]^n\left[1 - \frac{T_{AB}(b)}{AB}\sigma_{in}\right]^n} \ . \tag{1.3.4}$$

The above expression is obtained by multiplying the probability that n nucleon-nucleon interactions occur by the probability that the remaining $AB - n$ pairs of nucleon do not

interact. By summing over n we obtain the probability that at least one inelastic nucleon-nucleon collision occurs in the nuclear collision, or in other words the transverse plane differential inelastic cross section:

$$\frac{d\sigma_{in}^{AB}}{d^2b} = \sum_{n=1,AB} P(n,b) = 1 - \left[1 - \frac{T_{AB}(b)}{AB}\sigma_{in}\right]^{AB} .$$

By integrating over b we obtain, finally, the *nuclear inelastic cross section*

$$\boxed{\sigma_{in}^{AB} = \int d^2b \left\{1 - \left[1 - \frac{T_{AB}(b)}{AB}\sigma_{in}\right]^{AB}\right\}} . \tag{1.3.5}$$

Starting from Eq. (1.3.4) we may compute the average number of nucleon-nucleon collisions N_{coll} at fixed impact parameter b:

$$\begin{aligned} N_{coll}(b) &= \sum_{n=1,AB} n\, P(n,b) \\ &= \left\{ x\frac{d}{dx} \sum_{n=0,AB} \binom{AB}{n} [x\sigma_{in}]^n \left[1 - \frac{T_{AB}(b)}{AB}\sigma_{in}\right]^n \right\}_{x=T_{AB}(b)/AB} \\ &= \left\{ x\frac{d}{dx} \left[1 - \frac{T_{AB}(b)}{AB}\sigma_{in} + x\sigma_{in}\right]^{AB} \right\}_{x=T_{AB}(b)/AB} , \end{aligned}$$

and finally

$$\boxed{N_{coll}(b) = T_{AB}(b)\,\sigma_{in}} . \tag{1.3.6}$$

A useful approximation of the probability of having n collisions [Eq. (1.3.4)] valid at large AB is

$$P(n,b) \underset{AB\to\infty}{\sim} \frac{[T_{AB}(b)\,\sigma_{in}]^n}{n!} e^{-T_{AB}(b)\,\sigma_{in}} ,$$

which shows that at fixed b nucleon-nucleon collisions follow approximately a Poisson distribution with average number $N_{coll}(b)$.

Thickness functions and analytical examples

The basic probability density for a nucleon-nucleon collision may be well approximated by a Gaussian function with standard deviation $\Delta_{pp} = 0.86$ fm:

$$t_{pp}(r) = \frac{1}{2\pi\Delta_{pp}^2} e^{-r^2/2\Delta_{pp}^2} .$$

Light nuclei may be well approximated by Gaussian thickness functions, as well, with a standard deviation proportional to their radius:

$$\tau_A^{ga}(r) = \frac{A}{2\pi\Delta_A^2} e^{-r^2/2\Delta_A^2} , \tag{1.3.7}$$

where $\Delta_A = \frac{r_0'}{\sqrt{3}} A^{1/3}$ and $r_0' = 1.05$ fm, [94]. In this case the overlap function T_{AB} [Eq. (1.3.3)] is a Gaussian with standard deviation $\Delta^2 = \Delta_A^2 + \Delta_B^2 + \Delta_p^2$:

$$T_{AB}(b) = \frac{A}{2\pi\Delta_A^2} e^{-b^2/2\Delta_A^2} \ ,$$

and the total inelastic cross section may be computed analytically [94]:

$$\sigma_{in}^{AB} = 2\pi\Delta^2 \sum_{n=1,AB} \frac{1-(1-f)^n}{n} \ ,$$

where f is a dimensionless quantity,

$$f = \frac{\sigma_{in}}{2\pi\Delta^2} \ ;$$

when f is small, i.e., when the two nuclei are large enough, the cross section reduces to $\sigma_{in}^{AB} \approx AB\sigma_{in}$.

When one nucleus is much larger than the other we may approximate them with the so-called *hard-sphere* distribution, corresponding to a sphere of given radius R with uniform spatial density $\rho(r,z) = (3A/4\pi R_A^3)\theta(R_A^2 - r^2 - z^2)$; then the *hard-sphere thickness function* is

$$\tau_A^{hs}(r) = \frac{3A}{2\pi R_A^3} \sqrt{R_A^2 - r^2}\ \theta(R_A^2 - r^2) \ , \tag{1.3.8}$$

where the nuclear radius is

$$R_A = r_0 A^{1/3} \quad ; \quad r_0 = 1.12\text{fm} \ .$$

In this case the overlap function T_{AB} may be well approximated by a hard-sphere thickness function, as well, with radius

$$R = R_A + R_B \ ,$$

and the total inelastic cross section may be computed analytically:

$$\sigma_{in}^{AB} = \pi R^2 \left\{ 1 + \frac{2}{F^2} \left[\frac{1-(1-F)^{AB+2}}{AB+2} - \frac{1-(1-F)^{AB+1}}{AB+1} \right] \right\} \underset{F\to 0}{\approx} AB\sigma_{in} \ ,$$

where F is a dimensionless quantity,

$$F = \frac{3\sigma_{in}}{2\pi R^2} \ .$$

Heavy nuclei are better approximated by the *Woods-Saxon* distribution,

$$\rho_A^{WS}(r,z) = \frac{1}{\mathcal{N}} \frac{4\pi R_A^2}{1 + e^{(|\vec{r}| - R_A)/a_0}} \ ,$$

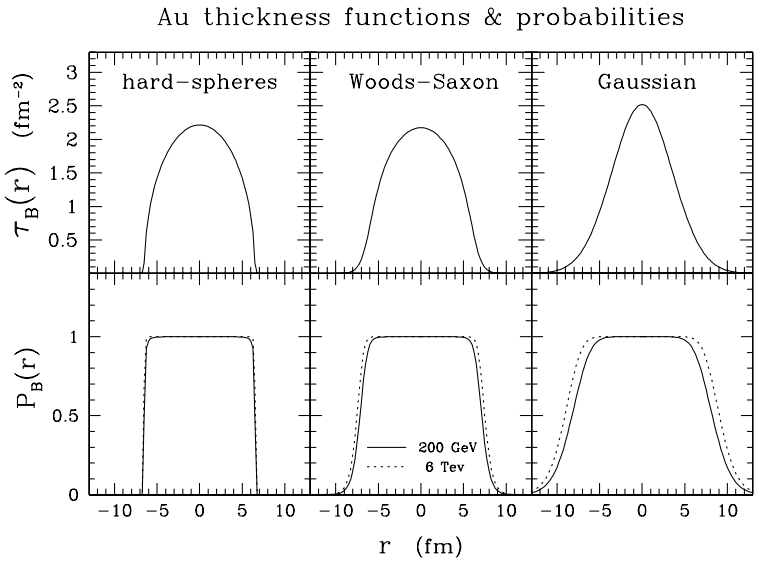

Figure 1.8: Thickness functions τ_B [Eqs. (1.3.7), (1.3.8), (1.3.9)] and probability $\mathcal{P}_B$ of participating in the interaction [Eq. (1.3.15)] as a function of the distance r from the center of the B nucleus.

where $|\vec{r}| = \sqrt{r^2+z^2}$ and $\mathcal{N}$ is such that $\int d^r dz \rho_A^{WS}(r,z) = A$. The nuclear radius is $R_A = r_0 A^{1/3} - 0.86 A^{1/3}$, and $a_0 = 0.523$ controls how fast ρ_A^{WS} goes to zero at the nuclear periphery. In this case the thickness function

$$\tau_A^{WS}(r,z) = \int dz \rho_A^{WS}(r,z) \tag{1.3.9}$$

has no analytic expression and must be computed numerically.

The different thickness functions described above are compared in the upper three panels of Fig. 1.8. We will use in general the Woods-Saxon thickness function (1.3.9), and since we are interested in ultrarelativistic energies we will approximate $t_{pp}(r) \approx \delta^{(2)}(r)$.

A special case is represented by pA interactions. In the formalism for multiple semihard interactions which we will describe in Chapter 2 we cannot approximate also τ_p with a delta function, as it is usually done, because we need to exponentiate it. Then we might exchange the role of τ_p and t_{pp}, so that $\tau_p \approx \frac{1}{2\pi\Delta_{pp}^2} e^{-r^2/2\Delta_{pp}^2}$, and take $t_{pp}(r) \approx \delta^{(2)}(r)$ as above. A different choice, used in Chapter 5, is to consider also the proton a hard-sphere and use the thickness function in Eq. (1.3.8).

1.3.2 The wounded nucleon model

We want to discuss multiplicity distributions of particles produced in heavy-ion collisions in the framework of the Glauber model probabilistic picture of the interaction. Our discussion will follow closely Ref. [11].

In hadron-nucleus collisions a fundamental role is played by the number ν of collisions suffered by the incident hadron. Indeed, the average particle multiplicities in a high-energy hA collision follow approximately the formula

$$\bar{n}_A = \frac{1}{2}(N_{coll}+1)\bar{n}_h \ , \tag{1.3.10}$$

where $\bar{n}_A$ is the average multiplicity in a collision of a hadron with a nucleus of atomic number A, $\bar{n}_h$ is the average multiplicity in a hadron-hadron collision and $N_{coll} \equiv \bar{\nu}$ is

the average number of hadron-nucleon collisions (see Eq. (1.3.6)). This formula may be rewritten in an equivalent way by introducing the number w of *wounded nucleons*, i.e., of nucleons that underwent at least one inelastic scattering. Note that we call "nucleon" also the incident hadron. It is immediately clear that for a hA collision $w = \nu + 1$. Then if we define $N_{part} \equiv \bar{w}$ to be the *average number of participants*, i.e. the average number of wounded nucleons, the following relation holds:

$$N_{part} = N_{coll} + 1 \ .$$

The formula (1.3.10) may then be rewritten as

$$\bar{n}_A = \frac{1}{2}(N_{coll} + 1)\bar{n}_h = N_{part} \times \frac{1}{2}\bar{n}_h \ ,$$

which suggests that the contribution of the incident hadron to the final particle multiplicity is the same as that of each hit nucleon and is equal *on average* to $\frac{1}{2}\bar{n}_h$. It seems that there is no difference in the produced multiplicity if a nucleon is hit once or several times, which justifies the relevance of w as a good variable to describe the process.

The generalization to AA collisions is not unique because in this case there is no unique relation between ν and w, and a choice between the two has to be made. The *wounded nucleon model* is the assumption that the relevant variable to describe particle multiplicity distributions is w, the number of wounded nucleons, rather than ν, the number of nucleon-nucleon collisions. This is equivalent to assume that inelastic collisions of a projectile nucleon after the first one are effective in wounding the hit nucleon, but do not contribute to particle production. This assumption has been proved to be phenomenologically correct up to SPS energies ($\sqrt{s} = 17$ GeV), but begins to break down at RHIC energies ($\sqrt{s} =$ 130...200 GeV) due to hard scattering processes (see, e.g., Ref. [124]). While the "hard" multiplicities naturally scale as N_{coll}, there is also a "soft" contribution proportional to N_{coll} whose importance rises with the collision energy [21]. The wounded nucleon model implies that in the collisions of a nucleus of atomic number A with a nucleus of atomic number B the multiplicity scales as

$$\bar{n}_{AB} = N_{part}^{AB} \times \frac{1}{2}\bar{n}_H \ ,$$

where by definition the number of participants in the AB collision is given by the sum of the number of participants of the A and of the B nucleus:

$$N_{part}^{AB} = N_{part}^{A} + N_{part}^{B} \ .$$

Our next task is then to compute N_{part}^{A}. From our assumption of incoherence of the nucleon-nucleon interactions we can write in analogy with Eq. (1.3.4) the probability that a nucleon from the A nucleus sitting at a given transverse coordinate r undergo at least one inelastic interaction when scattering on the B nucleus:

$$P_{wound}(b) = \sum_{n=1,B} \binom{B}{n} \left[\frac{T_{hB}(b)}{B}\sigma_{in}\right]^n \left[1 - \frac{T_{hB}(b)}{B}\sigma_{in}\right]^{B-n} = 1 - \left[1 - \frac{T_{hB}(b)}{B}\sigma_{in}\right]^B \ ,$$

where $T_{hB}(b) = T_{AB}(b)|_{A=1}$ is the overlap function for a hadron-nucleus collision. By approximating the basic thickness function by a delta function, we obtain

$$T_{hB}(b) = \tau_B(b) \ . \tag{1.3.11}$$

The number of participants is then obtained by multiplying the average number of A nucleons at r (i.e., $\tau_A(b-r)$) by the above probability and by integrating over r:

$$\boxed{\begin{array}{rcl} N^A_{part}(b) & = & \displaystyle\int d^2r\, \tau_A(b-r) \left\{ 1 - \left[1 - \frac{\tau_B(b)}{B}\sigma_{in} \right]^B \right\} \\ & \underset{B\to\infty}{\sim} & \displaystyle\int d^2r\, \tau_A(b-r) \left\{ 1 - e^{-\tau_B(b)\sigma_{in}} \right\} \end{array}} \ . \tag{1.3.12}$$

The number of participants from the B nucleus is obtained by interchanging A and B in the formula above. This formula is very important because it gives a way to obtain the impact parameter of the nuclear collision event-by-event by measuring the number of participants. This is obtained experimentally by measuring the number N_{spec} of *spectators*, i.e., the nucleon that did not have an inelastic collision and continue to flow along the beam axis. Their energy E_{spec} may be measured by a *zero degree calorimeter* (ZDC) and is proportional to their number:

$$E_{spec}(b) = \epsilon\, N_{spec}(b) = \epsilon \left(A + B - N_{part}(b) \right) \ ,$$

where ϵ is the energy per initial state nucleon (e.g., in the center of mass frame $\epsilon = \sqrt{s_{AB}}/(A+B)$, where $\sqrt{s_{AB}}$ is the center of mass energy of the two nuclei).

1.3.3 The nuclear interaction area

When considering nucleus-nucleus collisions an interesting quantity, which will be extensively used in Chapter 4, is the value of the nuclear *interaction area* $\mathcal{A}_T(b)$, where b is the nuclear impact parameter. The interaction area is defined as the average value of the area in the transverse plane where nucleon-nucleon collisions took place. Heuristically, if we imagine the nuclei to be hard-spheres with a given radius, we may assume that the interaction area is simply given by the geometric overlap area $\mathcal{A}_T^{geom}$ of two discs of radius equal to the nuclear radius. When the two nuclei are equal the geometric overlap area may be computed analytically:

$$\mathcal{A}_T^{geom}(b) = 2 \left[R_A^2 \arccos\left(\frac{b}{2R_A} \right) - \frac{b}{2}\sqrt{R_A^2 - \frac{b^2}{4}} \right] \ . \tag{1.3.13}$$

However this is true only for hard-sphere nuclei and in the very high energy limit, where the probability for an incident nucleon to scatter on the target nucleus is one if its impact parameter is smaller than the nuclear radius and zero otherwise. For realistic nuclei we should relate the definition of the transverse area to the dynamics of the nuclear collision. To do this we start from the Glauber model formula for the wounded A-nucleons, namely, the nucleons from the A nucleus which had an interaction with the B nucleus:

$$N^A_{part}(b) = \int d^2r\, \tau_A(b-r)\, \mathcal{P}_B(r) \ , \tag{1.3.14}$$

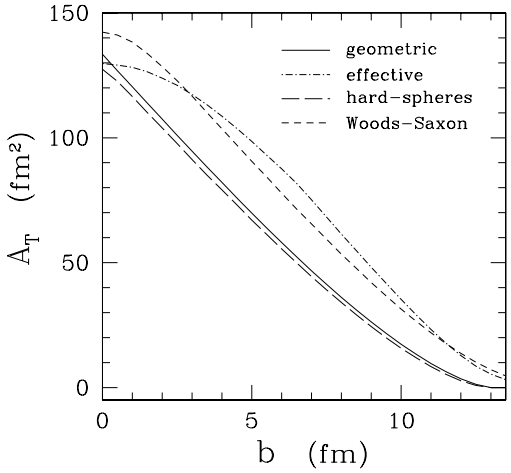

Figure 1.9: The nuclear interaction area as a function of the nuclear impact parameter in a Au-Au collision at $\sqrt{s}$)130 GeV per nucleon pair. Shown are the geometric estimate [Eq. (1.3.13)], the Glauber model inspired formula [Eq. (1.3.16)] with hard-sphere and Woods-Saxon thickness functions, and the effective estimate [Eq. (1.3.16)].

where

$$\mathcal{P}_B(r) = 1 - \left[1 - \frac{\sigma_{in}}{B}\tau_B(r)\right]^B \underset{B\to\infty}{\sim} 1 - e^{-\sigma_{in}\tau_B(r)} \ . \tag{1.3.15}$$

is the probability that a nucleon at a given transverse coordinate r relative to the center of the B nucleus has at least one inelastic interaction with the target nucleus. In Fig. 1.8 we plotted the three thickness functions discussed previously in the upper panels and the corresponding interaction probability (1.3.15) in the lower panels. Loosely speaking, $\mathcal{P}_B(r)$ may be thought as the profile of the B nucleus as "seen" by the projectile nucleons. When using the hard-sphere thickness function the B nucleus has well-defined and sharp edges, while with Woods-Saxon and Gaussian thickness functions the borders are less and less sharp. These considerations suggest to define the *average* interaction area, by multiplying each area element in the transverse plane by the probability that at least one nucleon from A and one from B interacted inside it:

$$\boxed{\mathcal{A}_T(b) = \int d^2s P_A(b-s)P_B(s) = \int d^2s \left(1 - e^{-\sigma_{in}\tau_A(b-s)}\right)\left(1 - e^{-\sigma_{in}\tau_B(s)}\right)} \ . \tag{1.3.16}$$

The transverse area in Au-Au collisions at $\sqrt{s} = 200$ GeV per nucleon pair is plotted in Fig. 1.9 and compared to the geometrical area (1.3.13). As anticipated, when using hard-sphere functions at such ultra-relativistic energies $\mathcal{A}_T(b) \approx \mathcal{A}_T^{geom}(b)$. This Glauber model inspired computation of the transverse area has the advantage of being parameter-free and to be uniquely defined by the choice of the thickness function.

A different way of computing the transverse area in the case that $A = B$, used for example in [92], is to compute the number of participants at impact parameter b. Then, one may take as interaction area at impact parameter b, the overlap area of two nuclei of atomic number $A_{eff} = N^{part}/2$ undergoing a central collision. In other words, the overlap area is the transverse area of a nucleus of radius A_{eff}:

$$\mathcal{A}_{eff}^T(b) = \pi R_{A_{eff}}^2 \ . \tag{1.3.17}$$

We call $\mathcal{A}_{eff}^T$ the *effective interaction area*. However, this computation gives a transverse area which is much less steep than the geometric and Glauber-type ones and in all cases

overestimates the transverse area at large impact parameter, see Fig. 1.9. The difference in the slope has big consequences, e.g., when computing global observables like the charged particle multiplicity per participant pair, see Sec. 4.2.

1.3.4 Self-shadowing

Let's consider the inelastic hadron-nucleus cross section $(\sigma_{in})_A$, whose expression may be expanded, in the Glauber approach, as a binomial probability distribution of inelastic nucleon-nucleon collisions (see Eqs. (1.3.5) and (1.3.11)):

$$\begin{aligned}(\sigma_{in})_A &= \int d^2b \Big[1 - \Big(1 - \sigma_{in}\frac{\tau_A(b)}{A}\Big)^A\Big] \\ &= \int d^2b \sum_{n=1}^{A} \binom{A}{n} \Big(\sigma_{in}\frac{\tau_A(b)}{A}\Big)^n \Big(1 - \sigma_{in}\frac{\tau_A(b)}{A}\Big)^{A-n} \end{aligned} \tag{1.3.18}$$

In Eq. (1.3.18) $\tau_A(b)$ is the nuclear thickness function, which depends on the impact parameter b and is normalized to one, A is the atomic mass number and σ_{in} is the inelastic hadron-nucleon cross section. One may classify all events according to a given selection criterion, which we call $\mathcal{C}$, while we call $\mathcal{N}$ the events that are not of kind $\mathcal{C}$ [15]. We assume that in a hadron-nucleon collision all events of kind $\mathcal{C}$ contribute to $\sigma_{\mathcal{C}}$, all other events contribute to $\sigma_{\mathcal{N}}$, so that the inelastic hadron-nucleon cross section may be written as

$$\sigma_{in} = \sigma_{\mathcal{C}} + \sigma_{\mathcal{N}} \ .$$

One may then ask for the expression for the cross section $(\sigma_{\mathcal{C}})_A$ to produce events of kind $\mathcal{C}$ in a collision of a hadron against a nuclear target. Then, to obtain $(\sigma_{\mathcal{C}})_A$, one may express $(\sigma_{in})^n$ in Eq. (1.3.18) as a binomial sum of "elementary" events of kind $\mathcal{C}$ and of kind $\mathcal{N}$:

$$\sigma_{in}^n = \big(\sigma_{\mathcal{C}} + \sigma_{\mathcal{N}}\big)^n = \sum_{k=0}^{n} \binom{n}{k} \sigma_{\mathcal{C}}^k \sigma_{\mathcal{N}}^{n-k} \ . \tag{1.3.19}$$

An interesting case to consider is when the events of kind $\mathcal{C}$ are such that any superposition of elementary events of kind $\mathcal{C}$, both with events of kind $\mathcal{C}$ and of kind $\mathcal{N}$, always gives an event of kind $\mathcal{C}$. In this case, all the terms of the sum in Eq. (1.3.19), with the only exception of the term with $k = 0$, contribute to $(\sigma_{\mathcal{C}})_A$, which is therefore given by:

$$(\sigma_{\mathcal{C}})_A = \int d^2b \sum_{n=1}^{A} \binom{A}{n} \Big[\sum_{k=1}^{n} \binom{n}{k} \sigma_{\mathcal{C}}^k \sigma_{\mathcal{N}}^{n-k}\Big] \Big(\frac{\tau_A(b)}{A}\Big)^n \Big(1 - \sigma_{in}\frac{\tau_A(b)}{A}\Big)^{A-n} \ .$$

By using the relation

$$\sum_{k=1}^{n} \binom{n}{k} \sigma_{\mathcal{C}}^k \sigma_{\mathcal{N}}^{n-k} = \sigma_{in}^n - \sigma_{\mathcal{N}}^n \ ,$$

one obtains:

$$
\begin{aligned}
(\sigma_{\mathcal{C}})_A &= \int d^2b \sum_{n=1}^{A} \binom{A}{n} \Big[\Big(\sigma_{in}\frac{\tau_A(b)}{A}\Big)^n - \Big(\sigma_{\mathcal{N}}\frac{\tau_A(b)}{A}\Big)^n \Big] \Big[1-\sigma_{in}\frac{\tau_A(b)}{A}\Big]^{A-n} \\
&= \int d^2b \Big[\Big(\sigma_{in}\frac{\tau_A(b)}{A} + 1 - \sigma_{in}\frac{\tau_A(b)}{A}\Big)^A - \Big(\sigma_{\mathcal{N}}\frac{\tau_A(b)}{A} + 1 - \sigma_{in}\frac{\tau_A(b)}{A}\Big)^A \Big] \\
&= \int d^2b \Big[1 - \Big(1 - \sigma_{\mathcal{C}}\frac{\tau_A(b)}{A}\Big)^A \Big] \\
&= \int d^2b \sum_{n=1}^{A} \binom{A}{n} \Big[\sigma_{\mathcal{C}}\frac{\tau_A(b)}{A}\Big]^n \Big[1-\sigma_{\mathcal{C}}\frac{\tau_A(b)}{A}\Big]^{A-n} . \qquad (1.3.20)
\end{aligned}
$$

Note that, in spite of the fact that we included superpositions of elementary events of kind $\mathcal{C}$ with events both of kind $\mathcal{C}$ and of kind $\mathcal{N}$, the nuclear cross section $(\sigma_{\mathcal{C}})_A$ is obtained by summing all possible multiple hadron-nucleon interactions of kind $\mathcal{C}$ alone with a binomial probability distribution, precisely as $(\sigma_{in})_A$ is obtained by a binomial distribution of hadron-nucleon inelastic interactions. This relation states the self shadowing property of the events of kind $\mathcal{C}$: all unitarity corrections, namely the term $\big[1-\sigma_{\mathcal{C}}\tau_A(b)/A\big]^A$ in the third line of Eq. (1.3.20), are expressed by means of the cross section $\sigma_{\mathcal{C}}$ only. However, this does not mean that $(\sigma_{\mathcal{C}})_A$ doesn't contain events of kind $\mathcal{N}$, but rather that they are irrelevant to obtain $(\sigma_{\mathcal{C}})_A$. The property that an event of kind $\mathcal{C}$ remains of kind $\mathcal{C}$ even after any number of events of kind $\mathcal{N}$ translates into the disappearance of $\sigma_{\mathcal{N}}$ in the nuclear cross section $(\sigma_{\mathcal{C}})_A$.

Given the discussion above, the only part of the nuclear interaction that still misses is the cross section for elementary events of kind $\mathcal{N}$ alone. It can be obtained by considering the following difference

$$
\begin{aligned}
\frac{d(\sigma_{in})_A}{d^2b} - \frac{d(\sigma_{\mathcal{C}})_A}{d^2b} &= \Big[1-\sigma_{\mathcal{C}}\frac{\tau_A(b)}{A}\Big]^A - \Big[1-(\sigma_{\mathcal{C}}+\sigma_{\mathcal{N}})\frac{\tau_A(b)}{A}\Big]^A \\
&= \Big[1-\sigma_{\mathcal{C}}\frac{\tau_A(b)}{A}\Big]^A \times \left\{ 1 - \left[1 - \frac{\sigma_{\mathcal{N}}\tau_A(b)/A}{1-\sigma_{\mathcal{C}}\tau_A(b)/A} \right]^A \right\} \qquad (1.3.21) \\
&= \Big[1-\sigma_{\mathcal{C}}\frac{\tau_A(b)}{A}\Big]^A \times \sum_{k=1}^{A} \binom{A}{k} \left(\frac{\sigma_{\mathcal{N}}\tau_A(b)/A}{1-\sigma_{\mathcal{C}}\tau_A(b)/A} \right)^k \left(1 - \frac{\sigma_{\mathcal{N}}\tau_A(b)/A}{1-\sigma_{\mathcal{C}}\tau_A(b)/Axs} \right)^{A-k} ,
\end{aligned}
$$

which is therefore bounded by $\big[1-\sigma_{\mathcal{C}}\tau_A(b)/A\big]^A$ (second line of 1.3.21), namely by the probability of not having any interaction of kind $\mathcal{C}$ at a given impact parameter b. The ratio $[\sigma_{\mathcal{N}}\tau_A(b)/A]/[1-\sigma_{\mathcal{C}}\tau_A(b)/A]$ is in fact a quantity smaller than one, since $\sigma_{in}\tau_A(b)/A$, which is equal to $\sigma_{\mathcal{C}}+\sigma_{\mathcal{N}})\tau_A(b)/A$, is a probability. It may be understood as the probability of an hadron-nucleon interaction at a given impact parameter, under the condition that no event of kind $\mathcal{C}$ takes place. Hence the last line of Eq. (1.3.21) shows that after removing all events of kind $\mathcal{C}$ the interaction is expressed by a binomial distribution of events of kind $\mathcal{N}$.

Finally, we observe that if we compute the average number of hadron-nucleon collisions

of kind $\mathcal{C}$, $\langle n\rangle(\sigma_{\mathcal{C}})_A$, rather than the cross section $(\sigma_{\mathcal{C}})_A$, the result is:

$$\begin{aligned}\langle n\rangle(\sigma_{\mathcal{C}})_A &= \int d^2b \sum_{n=1}^{A} n\binom{A}{n}\big(\sigma_{\mathcal{C}}\frac{\tau_A(b)}{A}\big)^n\big(1-\sigma_{\mathcal{C}}\frac{\tau_A(b)}{A}\big)^{A-n}\\ &= \int d^2b \frac{d}{d\gamma}\sum_{n=1}^{A}\binom{A}{n}\big(\sigma_{\mathcal{C}}\frac{\tau_A(b)}{A}\gamma\big)^n\big(1-\sigma_{\mathcal{C}}\frac{\tau_A(b)}{A}\big)^{A-n}\Big|_{\gamma=1}\\ &= A\sigma_{\mathcal{C}}\end{aligned}$$

Note that the average number of interactions of kind $\mathcal{C}$ is expressed by the single-scattering term, without any unitarity correction.

1.4 The quark-gluon plasma

In AA collisions a nucleon suffers many nucleon-nucleon collisions, losing about one unit of rapidity in each collision, and consequently losing a great amount of energy. If the number of collisions it undergoes is large enough, its final rapidity may be close to zero (in the center of mass frame) so that the nucleon might be "stopped" by the target nucleus. Moreover, the loss of the incident nucleons energy is accompanied by an abundant particle production, mostly pions, in the vicinity of the center of mass of the colliding nuclei. In Sec. 1.3.1 we showed that the number of collisions increases with the thickness of the target nucleus. Therefore the larger the atomic number of the colliding nuclei, the larger the energy lost by each nucleus and the higher the multiplicity of produced particles. Then, in a heavy-ion collision at high energy there is the possibility to create a sufficiently high baryon and energy density region to cause a transition of the produced system to the QGP phase.

1.4.1 Baryon stopping and the QGP

Much of the evidence for the occurrence of multiple nucleon-nucleon collision comes from experiments. They suggests that after an incident nucleon suffers a collision, the baryon-like object that emerges in the fragmentation region – we called it the leading baryon in Sec. 1.2 – will continue to collide with other nucleons from the target nucleus, each time loosing some fraction of its energy. This may be inferred, e.g., from the data shown in Fig. 1.10a on $p + A \to p' + X$ reaction in the projectile fragmentation region at a laboratory momentum of 100 GeV, corresponding to $\sqrt{s} = 13.8$ GeV. In the figure the inelastic cross section $d\sigma/(dx^+d^2p_t)$ at $p_t = 0.3$ GeV is shown as a function of x^+. While the cross section for pp collisions is nearly flat, it becomes a decreasing function of x^+ in pA collisions, the steeper the higher the atomic number A of the nuclear target. As a consequence the average value $\langle x^+\rangle$ of the light-cone variable is shifted from $\langle x^+\rangle = 1/2$ in pp collisions toward smaller and smaller values as A increases. This means that the total average energy (and rapidity) loss of the incident proton is larger in pA collisions than in pp collisions, suggesting the occurrence of more than one nucleon-nucleon collision. The degree of slowing down of the incident proton is also called *baryon stopping power*.

Indirect evidence for baryon stopping in heavy-ion collisions also comes, e.g., from data on collisions of ^{16}O on various nuclear targets shown in Fig. 1.10 (left panel). In

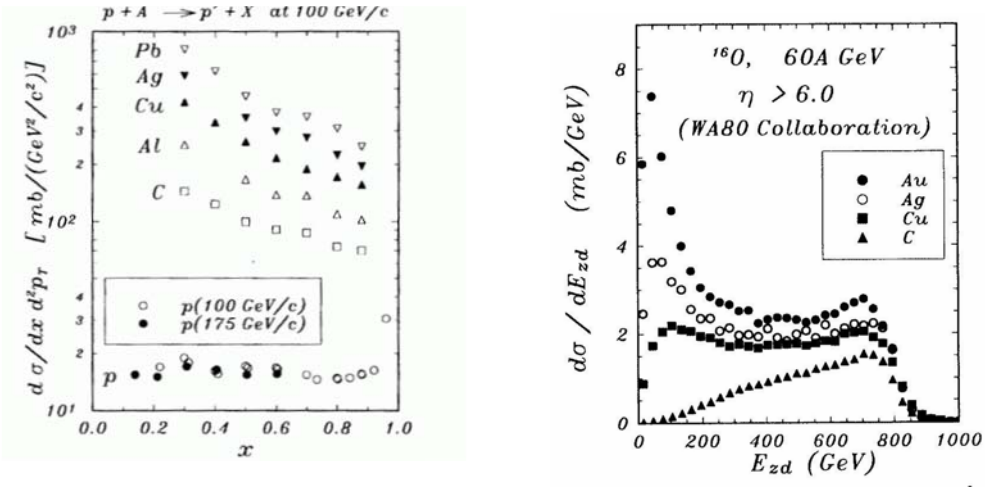

Figure 1.10: *Left:* The differential cross section $d\sigma/(dx^+ d^2p_T)$ for the reaction $p + A \to p' + X$ at different laboratory energies and for different targets as a function of the proton forward light-cone variable $x \equiv x^+$. Data taken from Refs. [117] and [115]. *Left:* The differential cross section $d\sigma/dE_{ZDC}$ as a function of the energy deposited in the zero-degree calorimeter for the collision of a ^{16}O nucleus on various targets at a laboratory energy of 60 AGeV. Data from Ref. [130]. Both figures taken from Ref. [94].

these measurements one collects all the particles emitted within 0.3 degrees from the beam axis ($\eta > 6$) and measures their *zero-degree energy* E_{ZDC} in a so-called *zero-degree calorimeter* (ZDC). E_{ZDC} represents therefore the energy of the particles that emerge in the very forward direction after the collision. If the stopping of incident nucleons is not effective, the probability that they will be deflected from the beam direction is small. As a consequence the probability for the projectile nucleus to loose a large fraction of its energy is small, so that E_{ZDC} will be on average large. Conversely, if the target is thick enough we expect a higher probability to have more than one nucleon-nucleon collisions for each incident nucleon (see Sec. 1.3.1), and we expect a higher energy loss and a lower average E_{ZDC}. The discussed effect is evident in Fig. 1.10 (right panel). The cross section for O-C collisions is peaked around $E_{ZDC} = 750$ GeV and decreases with decreasing zero-degree energy. At higher atomic numbers of the target a plateau at $E_{ZDC} = 200 - 800$ GeV develops, and a second peak at a very small energy appears. In summary the average zero-degree energy decreases with increasing target atomic mass, pointing to an increasing stopping power of the target.

The degree of baryon stopping reveals whether the produced energy or baryon densities are high enough for the QGP to be formed. As we saw in Sec. 1.2, a nucleon loses on average about one unit of rapidity in a nucleon-nucleon collision. When a nucleon collides on a nuclear target, its average rapidity loss may be estimated [94] to be $1 + (n-1)/3 < \Delta y < n$, where n is the number of collisions suffered by the incident nucleon. The upper bound corresponds to assuming the leading baryons emerging after the first collision to behave exactly as the father nucleon, while the lower bound correspond to assuming a diminished baryon stopping of the leading baryons relative to the original nucleon. For example a nucleon hitting a Au nucleus at a distance $r = 0$ from its center undergoes on average $n \approx 6$ collisions. If we average over the nucleon-nucleus impact parameter r we have $n \approx 4$. Then the average rapidity loss is about $2 \lesssim \Delta y \lesssim 4$.

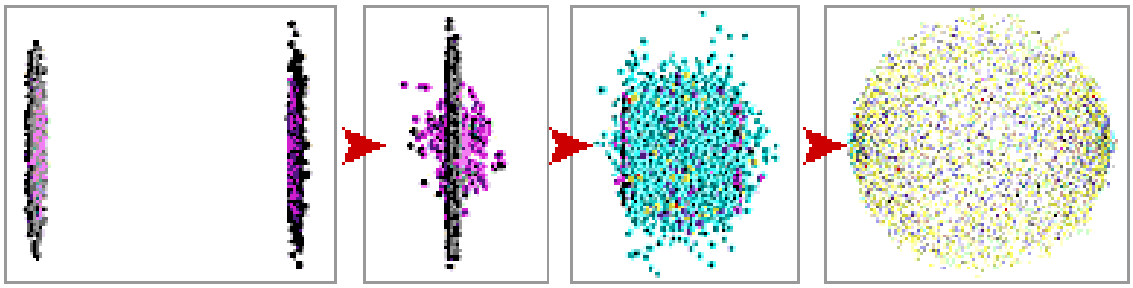

Figure 1.11: A computer simulation of a Au-Au collision at $\sqrt{s} = 200$AGeV. In the first image the two nuclei, which are traveling from the left and right sides of the picture toward the center, approach one another. They appear flat, instead of spherical, due to Lorentz contraction. their height is approximately 14 fm and their width approximately 1 fm. In the second image, the two ions collide, smashing into one another and then passing through one another (third and fourth image). Some of the energy is converted into hadrons. (Figure taken from RHIC home page, at `http://www.bnl.gov/rhic/heavy_ion.htm`).

In a heavy-ion collision at a center of mass energy of a few GeV per nucleon the separation between the beam rapidity and the target rapidity is about 3-4 units. Since this is of the same order of the average rapidity loss, in these collisions the incoming nucleons are very likely to be stopped in the center of mass frame. Moreover the Lorentz contraction pile up the nucleons in a narrow spatial region before the collisions. As a consequence the baryon density created in the collision mat be very high [16], and the matter created in the collision may enter the QGP phase. We call this few GeV energy region the *baryon-rich QGP* region. In nuclear collision at $\sqrt{s} \gtrsim 100$ GeV the difference between the beam and target rapidities is similar or greater than 10 units, which is large enough for the central rapidity region to be low in net baryon content, still having a high energy density. We call the energy region $\sqrt{s} \gtrsim 100$ the *baryon-free QGP* region or *pure QGP* region. This is the region we are interested in and which will be studied in this thesis.

1.4.2 Bjorken's picture of the QGP

Consider for simplicity an equal nuclei collision at ultrarelativistic energy, see Fig. 1.11. The nuclei are strongly Lorentz contracted in the beam direction, and at these energies we may neglect their longitudinal thickness and take the longitudinal coordinates of the nucleons belonging to the same nucleus to be approximately equal. The projectile nucleus A and the target nucleus B approach one another from $z = +\infty$ and $-\infty$, respectively. They travel nearly at the speed of light and meet at $z = 0$. The evolution of the system of particles produced in the collisions may be followed on the space-time diagram of Fig. 1.12. The trajectories of the two nuclei are represented by thick lines, and the hyperboles represent equal proper time surfaces, where the proper time is defined as $\tau = \sqrt{t + 2 - z^2}$.

- *Formation stage.* During the collision the nucleons experience many collisions each and lose a large fraction of their energy. A large amount of energy is then deposited in a small region around $z = 0$ in a short time τ_F after the beginning of the collisions, at which we set the proper time to zero. The matter created in this region has a very high energy density but a rather small net baryon content. The matter and

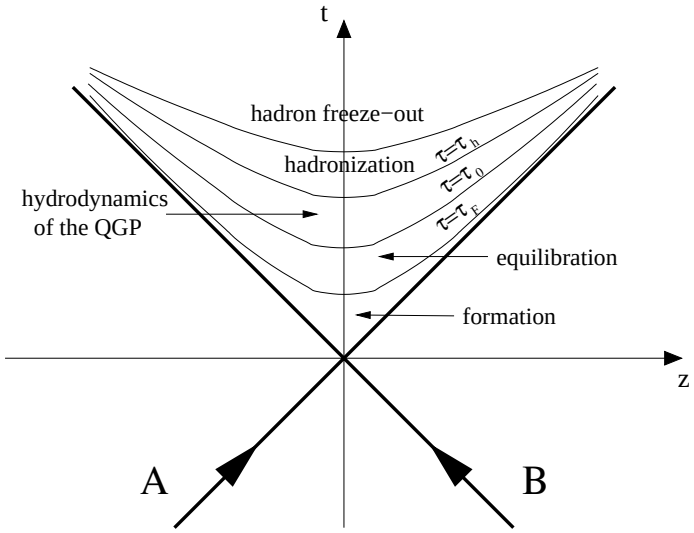

Figure 1.12: Space-time picture of the evolution of the minijet plasma.

energy density produced in this stage are commonly called *initial conditions*. It is yet an unresolved question under what form the quanta produced in these first instants appear, whether quarks and gluons, or hadrons, or "strings", or in other nonperturbative forms. It is commonly believed that at RHIC and LHC energies a large fraction of the matter is created under the form of quarks and gluons, and that perturbative QCD may be used to describe it. This dense system of partons is also called *minijet plasma*.

- *Equilibration stage*. At $\tau = \tau_F$ the minijet plasma is likely not to be in thermal equilibrium, but interactions between partons may drive it to thermal equilibrium at a proper time τ_0 called *equilibration time* (see, e.g., [10]). From perturbative computations of the initial conditions it appears that the minijet plasma could be locally equilibrated already after the formation stage [33].

- *Hydrodynamic stage*. The energy density of the minijet plasma at the equilibration time may be high enough for a transition of the system to the QGP phase. Due also to the very high quark and gluon density of the system, further evolution of the QGP may be described by hydrodynamic laws. The plasma expands and cools down.

- *Hadronization stage*. As the QGP expands the temperature drops down and hadronization of the plasma takes place at a proper time τ_h, called *hadronization time*.

- *Freeze-out stage*. The formed hadrons continues to interact with each other. As the system further expands the average distance between the hadrons becomes smaller than their mean free path: the hadrons stop interacting and "freeze out". They continue to stream freely and are finally detected by the experimental apparatus.

This space-time scenario of the formation and evolution of the QGP was proposed by Bjorken in Ref. [12], where a simplified 1+1 dimensional hydrodynamic model for the evolution of the plasma was studied. The initial conditions are not directly observable,

but may be traced back from the observed particle distribution. In particular, to estimate the initial energy density ϵ_0 we need to find out the amount of energy deposited in the collision region and the relevant volume V. The volume may be estimated as the product of the interaction area $\mathcal{A}_T$ (see the discussion in Sec. 1.3.1) and the formation time τ_F, which gives an estimate of the maximum distance traveled by the produced particles. It is possible to reconstruct their initial spatial distribution by relating their space-time coordinates to their rapidity variable, and using the information provided by their observed rapidity distribution dN/dy. The resulting estimate is [12, 94]

$$\epsilon_F = \frac{\langle m_T \rangle}{\mathcal{A}_T \tau_0} \left. \frac{dN}{dy} \right|_{y=0} ,$$

where $\langle m_T \rangle$ is the average transverse mass of the produced particles. Various estimates give for the formation time a value of $0.4 \text{ fm} \lesssim \tau_F \lesssim 1.2 \text{ fm}$. The recently measured value of dN/dy in central collision at $\sqrt{s} = 200$ GeV per nucleon [113] is $dN/dy = 975 \pm 52$ (here we assumed that the total multiplicity is nearly 3/2 of the charged multiplicity actually measured). Estimating the interaction area as the geometrical transverse area of a Au nucleus, $\mathcal{A}_T \approx \pi R_A^2 = 133 \text{ fm}^2$, and using $\langle m_T \rangle \approx 0.38$ GeV we obtain

$$2 \text{ GeV} \lesssim \epsilon_F \lesssim 7 \text{ GeV} .$$

Assuming that the initially produced system of particles is made predominantly by gluons, and treating them as an ideal relativistic boson gas [33], we may convert ϵ_F to the initial minijet plasma temperature $T_F \approx 30\epsilon_F/(16\pi^2)$. The resulting value of the initial temperature is

$$0.8 \text{ GeV} \lesssim T_F \lesssim 1.1 \text{ GeV} ,$$

which is well above the critical temperature $T_c \approx 0.150$ GeV for the QGP phase transition at nearly zero baryon density. However, during the thermalization stage the system expands quickly, hence thermalization will be reached at a temperature $T_0 < T_F$. Depending on the duration of the thermalization stage the system may reach the equilibrium with an energy density which is still above the critical temperature or not. Therefore a quantitative precise understanding of the formation and of the thermalization stage is of vital importance.

When the system has reached thermal equilibrium, and possibly entered the QGP phase, we may describe its successive evolution by hydrodynamics and ask how the energy density and other thermodynamic variables evolve with time. Since particle production is characterized by a plateau in the pseudorapidity distribution dN/dy at central rapidities, we may assume the QGP to be invariant under longitudinal Lorentz boosts. This allows to idealize the QGP as a continuum with longitudinal translational invariance, so that the energy density and all other variables are invariant, as well. Moreover, the longitudinal expansion proceeds much more rapidly than the transverse expansion. It is therefore useful to study the hydrodynamic evolution in a two-dimensional space time with coordinates (t, z). The assumed Lorentz invariance implies that all the quantities which describe the system depend only on the proper time $\tau = \sqrt{t^2 - z^2}$. We can choose as independent thermodynamic variables the energy density ϵ and the pressure p. Bjorken showed that

under these assumptions ϵ and p satisfy the following differential equation:

$$\frac{d\epsilon}{d\tau} + \frac{\epsilon + p}{\tau} = 0 \ . \tag{1.4.1}$$

If we assume that the QGP is an ideal relativistic gas of quarks and gluons the temperature T is related to the pressure by $p \propto T^4$ and the following equation of state holds:

$$p = \frac{\epsilon}{3} \ .$$

With this equation of state Eq. (1.4.1) may be solved, obtaining the proper time evolution of the system:

$$\begin{aligned} \frac{\epsilon(\tau)}{\epsilon_0} &= \left(\frac{\tau}{\tau_0}\right)^{4/3} \\ \frac{p(\tau)}{p_0} &= \left(\frac{\tau}{\tau_0}\right)^{4/3} \\ \frac{T(\tau)}{T_0} &= \left(\frac{\tau}{\tau_0}\right)^{1/3} \ . \end{aligned}$$

As we can see the pressure and the energy density drop rather quickly, while the temperature decreases in time more slowly. Given an initial temperature T_0 above the critical temperature, the system will remain in the QGP phase up to a proper time τ_h given by

$$\tau_h = \left(\frac{T_0}{T_c}\right)^3 \tau_0 \ , \tag{1.4.2}$$

after which the transition to hadronic matter will take place. From our previous estimates, and taking τ_0 to be about 1 fm (slightly larger than τ_F) and T_0 about 0.5 fm (slightly smaller than T_F), we obtain $\tau_h \approx 35$ fm. Note that the estimate (1.4.2) for the hadronization time is very sensitive to little changes in T_0 or T_F. In conclusion, given the several assumptions made, we may state that the system is likely to remain in the QGP phase for a rather long time, of the order of the tens of fm.

1.5 Global observables and signatures of the QGP

> "At a special seminar on 10 February 2000, spokespersons from the experiments on CERN's Heavy Ion program presented compelling evidence for the existence of a new state of matter in which quarks, instead of being bound up into more complex particles such as protons and neutrons, are liberated to roam freely. [...] The data from any one experiment is not enough to give the full picture but the combined results from all experiments agree and fit. Whereas all attempts to explain them using established particle interactions have failed, many of the observations are consistent with the predicted signatures of a quark-gluon plasma".
>
> From 10^{th} February 2000 CERN press release

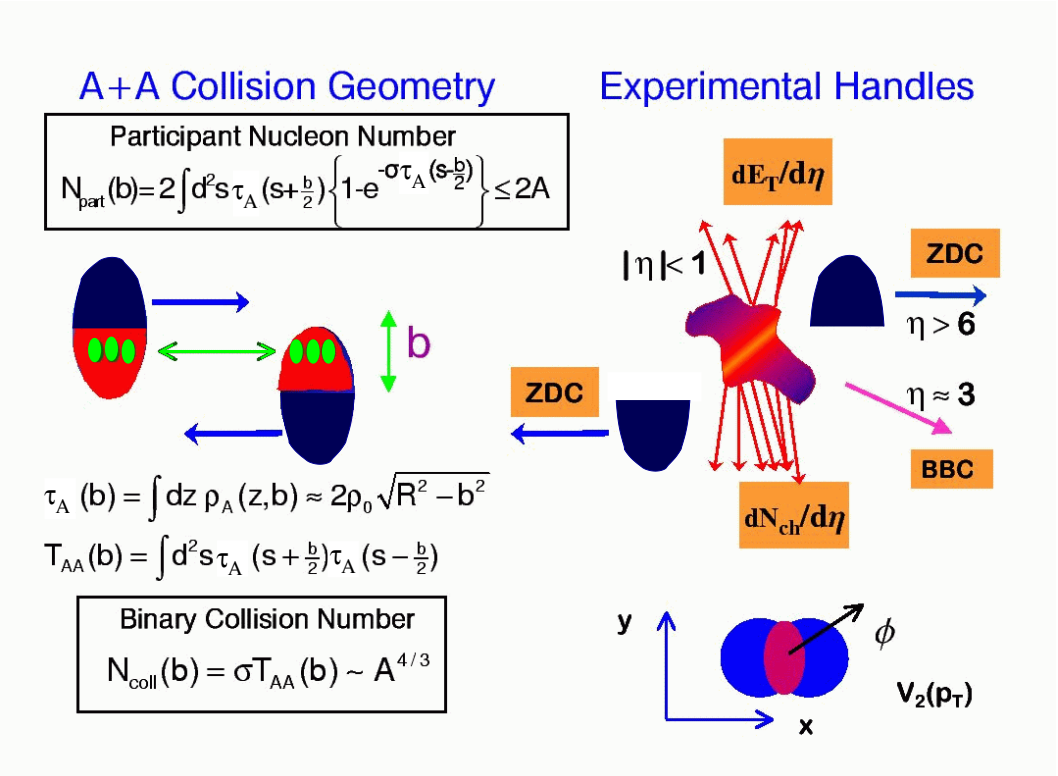

Figure 1.13: Ilustration of the basic geometrical features and of some of the global observables of a heavy-ion collision. Figure taken from Ref. [45].

The real challenge in QGP physics is to find, study and combine many different observables that carry information on a state of the matter which is short-lived and not at all directly observable. We may classify these observables into two large groups, which in part overlap one another: *(i)* the *global observables*, which help in determining the geometry of the collision, the initial conditions and some general feature of the produced system such as its shape and spatial evolution, and *(ii)* the *signatures of the QGP*, i.e., observables which have a different behaviour whether the plasma is formed or not. All these observable must be then globally analyzed to understand what happened during the collision. As U. Heinz and M. Jacob say in Ref. [46]:

> "A common assessment of the collected data leads us to conclude that we now have compelling evidence that a new state of matter has indeed been created, at energy densities which had never been reached over appreciable volumes in laboratory experiments before and which exceed by more than a factor 20 that of normal nuclear matter. The new state of matter found in heavy ion collisions at the SPS features many of the characteristics of the theoretically predicted quark-gluon plasma."

The goal of this section is to provide a quick overview especially of the first kind of observables. Moreover we will concentrate on the results of the first RHIC run at $\sqrt{s} = 130$ A GeV and on the first results at $\sqrt{s} = 200$ A GeV. For a review of results at CERN SPS at $\sqrt{s} = 17$ AGeV and a discussion about the "compelling evidence" of the QGP formation see Refs. [46, 47]. For reviews on RHIC observables, see Ref. [14, 45, 48, 78]. General overviews on various aspects of the physics of ultrarelativistic heavy-ion collisions, including LHC physics, may be found in Refs. [8, 32]. See also the book by Wong [94], and the proceedings of the "Quark Matter 2001" conference [1].

The basic experimental features of heavy-ion collisions and some of the observables

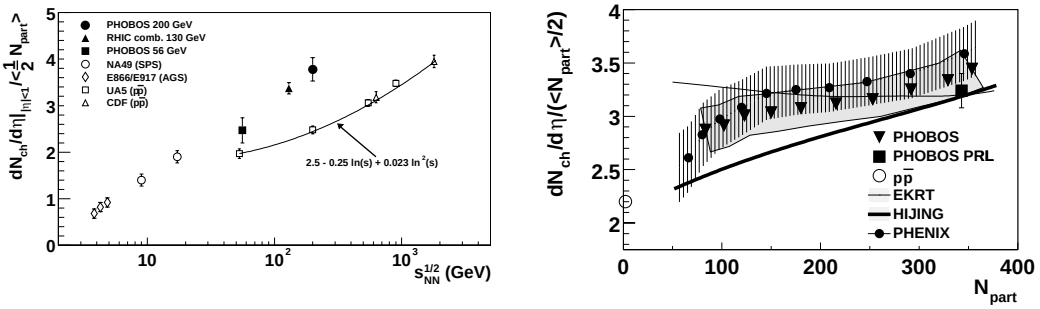

Figure 1.14: *Left:* Measured pseudorapidity density of charged particles produced in Au-Au collisions as a function of the center of mass energy. The three black points are RHIC results from Refs. [110, 113]. The charged multiplicity has been normalized to the number of participant pairs, which allows a comparison with data from pp collisions at CERN SPS. *Right:* Normalized pseudorapidity density at $\eta = 0$ as a function of the number of participants (data from PHOBOS [111] and PHENIX [99]; see also the data from BRAHMS [116] not shown in figure. Predictions based on HIJING model and on the EKRT model are shown.

that allow to constrain the geometry and the dynamics of the collisions are summarized in Fig. 1.13. The two nuclei come from the left and from the right toward one another at an impact parameter b. After the collision the nucleons which were not inside the interaction area proceed almost undisturbed along their direction of motion and their energy is measured by the zero-degree calorimeters (ZDC) placed along the beam at a certain distance from the interaction region. The ZDC measures the energy of hadrons with $\eta > 6$, corresponding to a cone of angular opening of 0.3 degrees with vertex in the interaction region and axis along the beam. Since the energy of each nucleon is known with good accuracy [it is simply $\sqrt{s}/(2A)$ in an equal nuclei collision] the number of spectator nucleons, and as a consequence the number N_{part} of participants nucleons, may be derived. N_{part} may be related to the impact parameter b both by theoretical computations, like Eq. (1.3.12), and by using Monte Carlo simulations (for a comparison of the two methods see Ref. [111]). A complementary information on the impact parameter comes from the minimum bias charged multiplicity distribution measured by the *beam-beam* counters, which collect particles with $\eta \approx 3$. Indeed it is found experimentally that this observable is a monotonic function of the impact parameter. Many detectors are dedicated to measurements in the central rapidity region. As explained in Sec. 1.4 this region is of special interest, and it is a region where it is possible to achieve a good particle identification and the most accurate measurements. Specially interesting global observables in this rapidity region are the charged particle multiplicity and transverse energy.

1.5.1 RHIC: the new energy frontier

The Relativistic Heavy Ion Collider (RHIC), located at the Brookhaven National Laboratories (BNL), is the first collider specifically designed to study heavy ion collisions and the possible formation and characteristics of the QGP. It has currently four approved experiments, BRAHMS, PHENIX, PHOBOS, and STAR, and two empty halls. The first Au-Au collision took place in June 2000, and many results have been presented for collisions at $\sqrt{s} = 56$ AGeV and $\sqrt{s} = 130$ AGeV (see, e.g., Ref. [128, 132]). On 18 July 2001 the first Au-Au collision at the full energy of $\sqrt{s} = 200$ AGeV occurred, and the first data

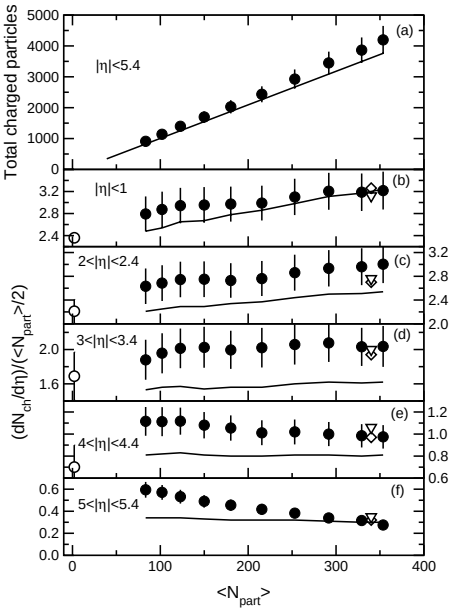

Figure 1.15: Normalized charged multiplicity dependence on centrality in different pseudorapidity intervals. The upper panel shows the total charged multiplicity corresponding to an interval $|\eta| < 5.4$. Points are PHOBOS data at $\sqrt{s} = 130$ GeV and solid lines are computations by HIJING. Open diamonds and triangles refer to predictions of the AMPT [95] and LUCIFER [53] models for the 6% most central collisions. Open circles represent values from pp and $p\bar{p}$ collisions. Figure taken from Ref. [112]

have been presented in [113]. This is the highest collision energy ever reached in heavy ion collisions.

Initial conditions

In Fig. 1.14 (right panel) the charged multiplicity pseudorapidity density at $\eta = 0$, normalized to the number of participant nucleon pairs, is plotted as a function of the collision energy both for Au-Au and pp collisions. As it is clearly visible, produced particle multiplicity is 50% larger in nuclear collisions than in pp collisions. This shows that some extra mechanism is at work in AA collisions. Many models describe correctly the RHIC points, among them the HIJING model [87] and the EKRT model [35], which include parton-parton hard scatterings in the dynamics of the collision in different ways . To distinguish between them it is useful to study the centrality dependence of the normalized charged multiplicity, as proposed in [92]. RHIC results on the centrality dependence of $dN^{ch}/d\eta$ are shown in the right panel of Fig. 1.14. The observed increase of the normalized multiplicity with energy relative to pp collisions and its increase with the number of participants supports the prediction of a copious minijet production at RHIC. We will discuss these observables and some of the theoretical models at length in Chapter 4. Moreover, the

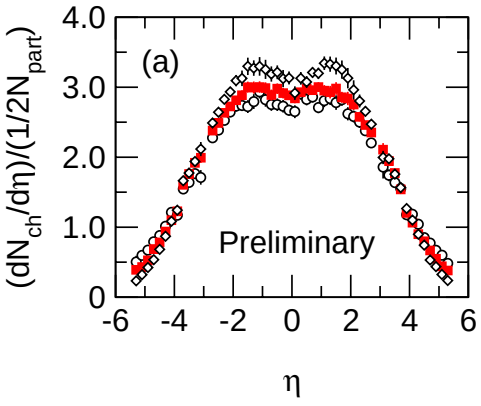

Figure 1.16: Measured pseudorapidity density of charged multiplicity normalized to the number of participant pairs at $N_{part} = 102$ (circles), 216 (squares), and 354 (diamonds). Figure taken from Ref. [128].

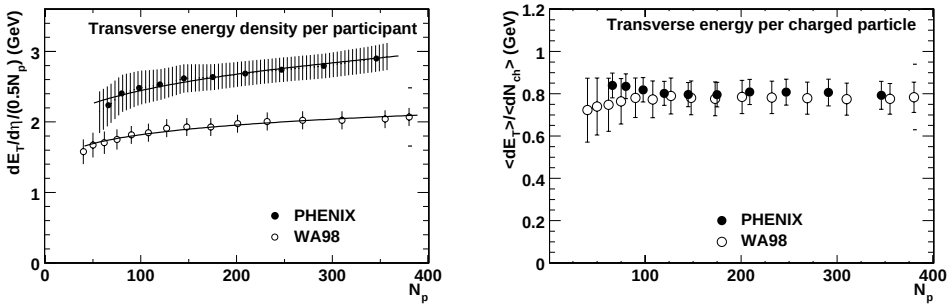

Figure 1.17: *Left:* Charged particle transverse energy density $dE_T/d\eta|_{\eta=0}$ normalized to the number of participant pairs as a function of N_{part} at $\sqrt{s}$ = 130 AGeV (PHENIX [100]) and $\sqrt{s} = 17$ AGeV (WA98 [106]). The solid lines represent the best fits to N^{α}_{part}. *Right:* Transverse energy per charged particle as a function of the number of participants. Both figures taken from Ref. [124].

slope of $dN^{ch}/d\eta$ as a function of N_{part} depends on the rapidity at which one makes the measurement, as shown in Fig. 1.15. A complementary observable is the pseudorapidity dependence of the charged multiplicity, see Fig. 1.16

Another important observable is the average transverse energy per charged particle, since it gives a measure of the internal pressure in the hot and dense system created by the collision. The PHENIX data are shown in Fig. 1.17, and it is compared to data from the CERN WA98 experiment. While the normalized charged particle transverse energy has increased relative to *pp* collisions and to *AA* collisions at SPS energy, the transverse energy per particle $E_T/Nch \approx 0.8$ is almost independent on centrality and on $\sqrt{s}$. Expectations from HIJING and transport models would be an increase with energy. The plasma seems not to do enough thermodynamic work: it is "as lazy as at SPS" [45].

Jet quenching and Cronin effect

One of the predicted observable effects of the formation of a hot and dense medium is the suppression of jet transverse momentum spectrum and of the high-p_T hadrons resulting from their hadronization. This suppression, also called *jet quenching* is due to energy loss of the minijets in the medium caused by gluon *bremsstrahlung* radiation [9, 93]. The

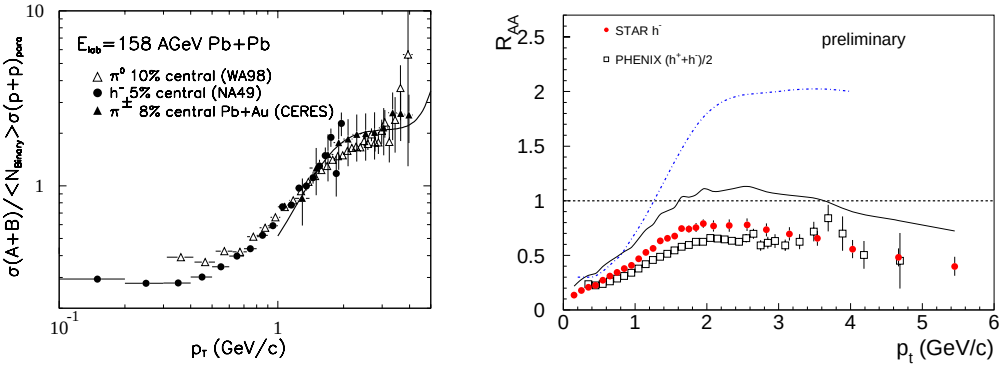

Figure 1.18: *Left:* the nuclear modification factor $R_{AA} = \sigma_{AA}/(N_{coll}\sigma_{pp})$ for hadrons produced in Pb-Pb collisions at $\sqrt{s}$ = 17 GeV. Data from Refs. [104, 105, 109]. The solid line is a pQCD computation from Ref. [86]. *Right:* the nuclear modification factor for hadrons in Au-Au collisions at $\sqrt{s} = 130$ GeV. Figure taken from [78].

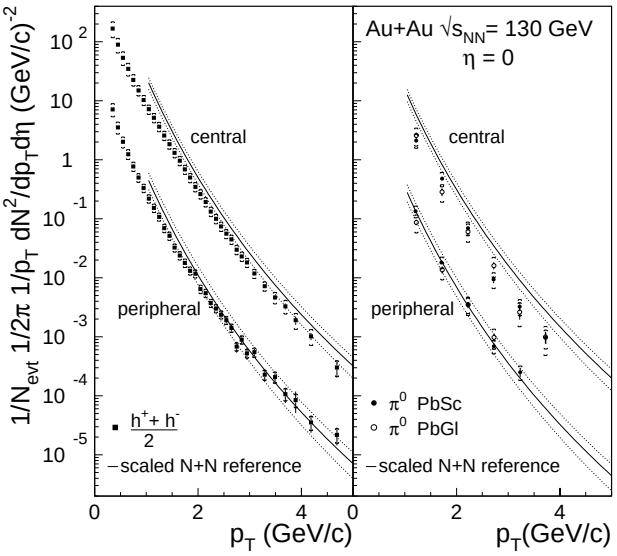

Figure 1.19: Normalized charged particles and neutral pions p_T spectrum in 0%-10% most central events (upper curves) and 60%-80% most cenral events (lower curves) in Au-Au collisions at $\sqrt{s} = 130$ GeV from PHENIX. Error bars indicate statistical errors. The data are compared to a parameterization of the yield in nucleon-nucleon collision from data on pp and $p\bar{p}$ collisions at $\sqrt{s} = 23 - 1800$ GeV. Figure taken from [101].

quenching factor should also be sensitive to the type of dense matter formed, whether it is a QGP or just a hadronic system. In AA collisions, on the other hand, there exists also a competing mechanism, the *Cronin effect* that enhances the p_T spectra relative to a simple extrapolation from pp data. The Cronin effect is due to multiple elastic collisions of partons in their way through the target nucleus, which induces at low p_T or low $\sqrt{s}$ a random-walk in the transverse momentum. As a consequence the average transverse momentum squared is enhanced: $\langle p_T^2 \rangle = \langle p_T^2 \rangle_{pp} + \delta\, A^{1/3}\, \delta p_T^2$, where $\langle p_T^2 \rangle_{pp}$ is the average transverse momentum squared in pp collisions. At SPS the Cronin enhancement is clearly observed and consistent with pQCD [86], and no quenching has been observed, see Fig. 1.18 (left panel). Conversely, both PHENIX and STAR reported a suppression factor of two or more for hadrons at $p_T > 2$ GeV [101, 102], see Fig. 1.18 (right panel). Moreover, the suppression is observed in central collisions, but not in peripheral collisions see Fig. 1.19. These observations may be explained by jet quenching [45, 69]. All these observations are a good hint that something new happens in AA collisions at $\sqrt{s} = 130$ GeV, possibly the formation of a dense matter system. To assess such a hypothesis we need also to understand better what happens in pA collisions at the same nucleon-nucleon center of mas energy, to really extract from the data any signal of new physics. This topic will be studied in the framework of pQCD in Chapter 5.

Other observables

There are many other interesting observables which can give a lot of information on the evolution of the system created in the collisions. Here we simply list a couple of them, and we refer to the reviews cited at the beginning of this section for a more complete discussion.

- *Elliptic flow.* In non central collisions the overlap area in the transverse plane is anisotrpic, see the lower right picture in Fig. 1.13. If the system thermalizes quickly, pressure is generated inside, and the transverse space anisotropy translates in anisotropic pressure gradients. This generates a stronger collective flow in the shorter direction than in the longer direction (viz., horizontally and vertically in

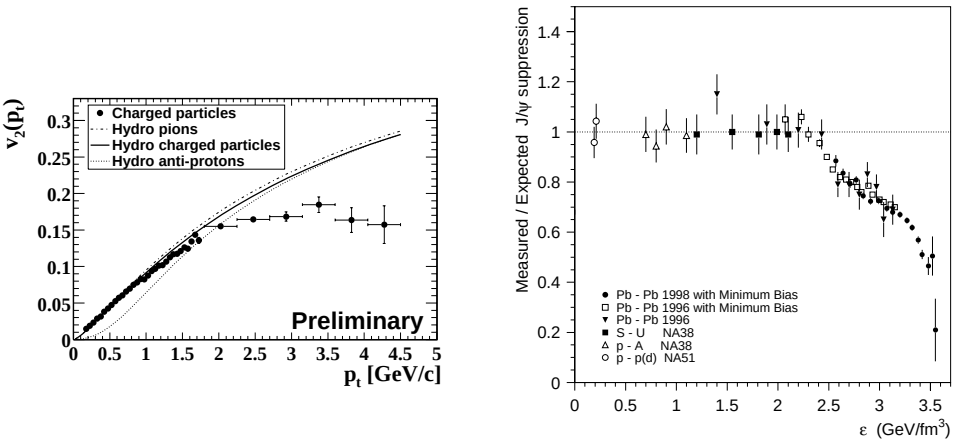

Figure 1.20: *Left:* Saturation of elliptic flow as measured by STAR [129]. Curves are extrapolation from the hydrodynamic computations of Ref. [64] to high p_T. *Right:* Anomalous J/ψ suppression as a function of the initial energy density from CERN NA50 experiment [98].

Fig. 1.13. As a consequence also the p_T distribution of produced particles will reflect this anisotropy. Conversely, if there is no thermalization no pressure gradients form up and the hadron p_T spectra will be isotropic. This effect is commonly characterized by the so-called *elliptic flow coefficient* $v_2 = \langle \cos(2\phi) \rangle$, where ϕ is the azimuthal angle between the observed hadron and the *reaction plane* defined by the beam axis and the shorter direction. At RHIC the elliptic flow is well described, for particles with $p_T \lesssim 2$ GeV, by hydrodynamic models and increases is an increasing function of p_T, while at higher momenta it tends to saturate, see Fig. 1.20.

- *J/ψ anomalous suppression.* The J/ψ particle is a bound state of a c and a $\bar{c}$ quark. In a deconfined medium the gluon density is so high that it can Debye-screen the colour interaction between the c and $\bar{c}$ quarks, either melting a bound pair or preventing the formation of a bound state. The result should be the suppression of the production of the J/ψ or other charmonium states (χ_c, ψ') with respect to pp and pA interactions. Note that in the latter case a "normal" J/ψ suppression has been already observed. Any deviation from the normal suppression, called therefore *anomalous suppression*, is usually thought to be a signal of the formation of the QGP, though alternative explanations exist. Anomalous suppression has been observed by CERN NA50 experiment at $\sqrt{s} = 17$ GeV, see Fig. 1.20.

1.5.2 LHC: the future

The CERN Large Hadron Collider (LHC) is the highest energy hadronic collider which will be built in the near future. It will produce pp collisions at $\sqrt{s} = 14$ TeV and Pb-Pb collisions at $\sqrt{s} = 6$ TeV. There is currently an increasing interest in the theorist and experimenters community also for a pA collisions program, which has not yet been scheduled. Heavy-ion physics will be studied by A Large Ion Collider Experiment (ALICE), which is a detector entirely dedicated to heavy ion collision (see, e.g., [123]), and by the Compact Muon Solenoid (CMS), a detector oriented to pp physics, with some capability to study heavy ion collisions [122]. The first Pb-Pb collisions at LHC are scheduled for year 2007.

The gains in increasing the center of mass energy of AA collisions are that the system will be initially bigger, denser and hotter, it forms faster, its lifetime grows and it develops collectively for a longer time. Also, hard probes are produced more abundantly and perturbative QCD becomes applicable to explain a larger and larger fraction of the events. In particular, the computation of the initial conditions might be reliably calculated in pQCD.

As SPS may have produced for the first time a QGP in the laboratory, RHIC is expected to study accurately the phase transition from normal matter to deconfined matter, since it may produce energy densities which are close to the critical one. Finally, LHC will study the QGP phase well above the critical point.

Chapter 2

Semihard parton rescatterings

In this chapter we will discuss the main ideas and tools which lead to the introduction of semihard many-parton interactions in the dynamics of nuclear collisions at very high energies. In the next chapters we will apply them to the study of the initial minijet-plasma conditions, whose control is of the greatest importance for the detection and study of the quark-gluon plasma.

Given the rapid growth of the hard cross section in hadronic and nuclear collisions [27, 40, 107], the typical inelastic event will be dominated by the perturbative regime at very high energies so that, at the LHC, one may expect to be able to derive global features of the inelastic interaction by perturbative methods. Such a capability, unavoidably limited to a restricted number of physical observables, implies however a few non trivial improvements in the understanding of the mechanisms operating in the interaction process. To be estimated in a sensible way, different physical quantities may in fact need a different degree of understanding of the interaction dynamics, since many details of the process may be of little relevance for some observables, while they may be essential for other quantities. Identifying and evaluating such physical observables represents a non trivial improvement in our capability of using perturbative QCD to describe physical processes.

An obvious problem will appear when trying to elaborate along these lines. A perturbative calculation does not introduce any scale in the dynamics, so that in this case the kinematic variables are the quantities which give the dimensionality to the related physical observables. On the other hand the dimensional factor which characterizes the global features of the typical inelastic event is, rather, the hadron or nuclear scale. When the perturbative regime dominates a physical observable which represents global features of the inelastic interaction, the hadron or nuclear scale should therefore appear also in the corresponding perturbative calculation, presumably introduced through the nonperturbative input. The structure functions, namely the nonperturbative input of basically all perturbative calculations, are on the other hand dimensionless quantities. This implies that the structure functions, in their present form, will no longer be an adequate nonperturbative input when trying to accomplish the program outlined above.

A related aspect is the complexity of the interacting states. The canonical perturbative QCD approach considers only perturbative processes initiated by a pair of partons. The approach is appropriate in the case of very dilute interacting systems, while it becomes obviously inadequate in a regime with very large parton densities, which we call *black disk regime* or *black disk limit*. In the case of a partonic interaction in the black disk regime,

the initial configuration is in fact isotropic in transverse space, differently from the final state produced by an interaction initiated by two partons (namely, at the leading order in α_S, two jets back-to-back in p_t), where a direction in the transverse plane is singled out. A natural way to recover the black disk symmetry in the final state, is to include in the interaction perturbative processes initiated by more than two partons (namely, semihard parton rescatterings), whose relevant property is to produce many large-p_t jets also at the lowest order in α_S. Multiple partonic interactions may be divided in two classes:

1. *disconnected collisions*: different parton pairs interact at different points in the plane transverse to the beam – each parton interacts at most once;
2. *parton rescatterings*: a given parton may experience more than one scattering against the target partons – we neglect rescatterings on the same parton.

Note that the term "disconnected collisions" refers in general to different groups of partons interacting with other partons of the same group but not with partons from another group, see Fig. 2.1. However, when used in opposition to the term "rescatterings" it has the special meaning that the different groups are made of a pair of partons each.

To deal with processes initiated by more than two partons one needs to introduce, as a nonperturbative input, the many-body structure functions, which contain independent informations on the hadron (or nuclear) structure with respect to the one-body structure functions needed to deal with processes initiated by two partons. A basic difference is that the n-body structure functions are dimensional quantities, in such a way that when n is larger than one the many-parton initiated processes introduce nonperturbative scale factors in the dynamics of the interaction in a natural way, allowing one to deal with the problem of dimensionality previously mentioned. By introducing interactions initiated by many partons one may therefore gain the capability of describing, by means of perturbative QCD, at least a few general properties of the typical interaction at very high energy. To pursue such a program one should then *i*) evaluate in perturbative QCD processes involving many partons in the initial state, *ii*) face the problem of the unknown non perturbative input and develop a strategy in that respect, and *iii*) study the infrared problem by finding observable quantities which are infrared stable. This last step represents the final achievement of the whole program.

An explicit approach to semihard interactions in heavy ion collisions at collider energies on the lines previously described, has been pursued with the help of a few simplifying hypotheses in [17–20], and various physical quantities have been evaluated in [3–6]. In this approach one faces the problem of unitarity corrections to the computation of various global observables of a hadron-nucleus or nucleus-nucleus collision by using the self-shadowing property of the hard component of the interaction, which was discussed in Sec. 1.3.4. There we treated the case of a Glauber type computation of the hadron-nucleus cross section, in which the interaction is viewed as a suitable superposition of nucleon-nucleon interactions. However, the goal is to represent the semihard hadron-nucleus cross section in a way analogous to (1.3.20), but considering as elementary objects the partons instead of the nucleons. Indeed, the hard component of the interaction satisfies the requirements of self-shadowing if one assumes that a parton which has undergone interactions with large momentum exchange may be recognized in principle in the final state. Obviously the unavoidable restriction of all considerations done by perturbative means is that they are limited to partonic final states, whose properties will hopefully survive hadronization.

In Sec. 2.1 we briefly recall the canonical approach to semihard interactions in heavy-ion collisions, which takes into account only the disconnected collisions. In the rest of the chapter we discuss how to introduce also the parton rescatterings in the dynamics of the process. The relevance of this kind of multiple scattering is discussed in Sec. 2.2, where the key-concept of *wounded parton* is introduced. To represent the interaction between hadrons and nuclei in terms of multiple semihard partonic interactions we need to write the cross section for a given nonperturbative input, namely for a definite partonic configuration of the two interacting objects. In Sec. 2.3 we introduce a functional formalism to deal with these multiparton distributions. Then, as a perturbative input, we need the probability of having at least one semihard interactions between the two configurations of partons. In Sec. 2.4 we discuss the simplest case of rescattering, namely a three-parton interaction, and generalize the result to an arbitrary number of rescattering. In Sec. 2.5 we combine the perturbative and the nonperturbative inputs to obtain the hA and AA cross sections. Finally, in Sec. 2.6 we compute a number of observables whose phenomenological relevance will be studied in the following chapters.

2.1 Minijet cross section in Eikonal approximation

2.1.1 Minijets

In hadronic and nuclear interactions at high energies an increasing fraction of the cross section is made of events which present on or more clusters of hadrons in the final state [103, 107, 114]. These clusters are characterized by a large total transverse energy E_T, defined as the sum of the transverse energies of all the particles in the cluster. The particles in a cluster are interpreted as the result of the hadronization of a parton which had a hard scattering.Therefore they stream along the parton's direction of motion and. Large transverse energy clusters are typically observed experimentally by selecting groups of particles contained in a pseudorapidity and azimuthal angle region of size $\Delta R = \sqrt{\Delta\eta^2 + \Delta\phi^2} \approx 0.7$ around the most energetic particle of the group, and by requiring their total transverse energy, E_T, to be larger than a given value, E_T^{jet}. When E_T^{jet} is large, $E_T^{jet} \gtrsim 10$ GeV, the clusters are called *jets*. For smaller transverse energies, $E_T^{jet} \gtrsim 4$ GeV the term *minijet* is preferred because of the small transverse energy and number of particles of the cluster. At still lower values of E_T^{jet} one reaches a regime where it becomes difficult to interpret the data in terms of clusters and jets. This is due to several reasons:

1. soft events with high multiplicity and E_T fluctuations may occasionally produce a large-E_T cluster not related to a hard-scattered parton;
2. an increasing relative contribution to E_T from gluon radiation as the momentum transfer in the hard scattering decreases;
3. multiple parton-parton interactions.

Minijets with $E_T^{jet} \gtrsim 5GeV$ have been observed in hadron-hadron collision at $\sqrt{s} = 27 - 900$ GeV [107, 118, 125], and with $E_T^{jet} \gtrsim 3GeV$ at [118, 125]. Even if at very low E_T^{jet} minijets can no more be distinguished from the background we can still study the production of partons in the *semihard region* $\Lambda_{QCD} \ll p_0 \lesssim 4$ GeV, where p_0 is the minimum transverse momentum of the parton. Note that the lower bound of the semihard region cannot be defined in a precise way, but is rather a matter of definition, since

the subdivision into hard and soft interaction is a theoretical artifice [127]. Partons in the semihard region are still expected to hadronize giving small jets of particles along their direction of motion. These particles, therefore, have strong correlations both in the azimuthal angle and in rapidity, while particles from the background are produced in an isotropically way in the phase space. Therefore, one could study minijets in the semihard region by measuring two-particle correlations between hadrons in the final state, see e.g. [88]. The simplest observable of this kind is the distribution of charged particle pairs with respect to their relative azimuthal angle. The most probable result of a semihard parton-parton scattering is the production in the final state of two jets of particles superposed on an isotropic background. If no rescattering or gluon radiation occurs, the two jets are back-to-back in the plane transverse to the beam. Hence, the expected signature of the minijets is the presence of two peaks in the particle pair angular distribution, one at 180 degrees from the other, the width of the peak being a measure of the angular width of the minijets. Rescatterings or hard gluon radiation may be revealed as a broadening of the width of the peaks. Some preliminary results on such an observables in Pb-Pb collisions at $\sqrt{s} = 17$ GeV have been reported in Ref. [126].

2.1.2 The Eikonal model of minijet production

In nuclear collisions minijets are not thought of as actually observable physical entities. Indeed the very large hadron multiplicities produced in a typical collision do not allow jet reconstruction unless for large transverse jet energies. Rather, they are thought to give the initial conditions for the evolution of the produced system of particles, whose properties may be observed in the final state [13, 43, 55]. The description of the semihard component of a nucleus-nucleus interaction, adopted by the majority of the papers on the subject, follows the approach of Refs. [27, 55]: the semihard component of the inelastic cross section in a collision of two nuclei with atomic mass numbers A and B, also called *minijet cross section*, is written as:

$$\begin{aligned} \sigma_{mj}^{AA} &= \int d^2b \left(1 - \mathrm{e}^{-\sigma_H T_{AB}(b)}\right) \\ &= \sum_{n=1}^{\infty} \int d^2b \, \frac{(\sigma_H T_{AB}(b))^n}{n!} \, \mathrm{e}^{-\sigma_H T_{AB}(b)} \ , \end{aligned} \tag{2.1.1}$$

where

$$\begin{aligned} \sigma_H &= \int_{xx's>4p_0^2} dx dx' \sum_{ff'} G_A^f(x) \sigma^{ff'}(xx') G_B^{f'}(x') \\ T_{AB}(b) &= \int d^2r \, \tau_A(r) \tau_B(r-b) \ . \end{aligned} \tag{2.1.2}$$

Here $\tau_A(r-b)$ and $\tau_B(b)$ are the thickness functions of the two interacting nuclei, normalized to A and B, respectively, and depending on the transverse coordinates of the interacting partons, $r-b$ and r, where b is the impact parameter of the nuclear collision, see Fig. 2.1. σ_H is the single scattering jet cross section in pp collisions, expressed as a convolution of the nucleon parton distributions $G_A^f(x)$, $G_B^{f'}(x')$ and of the partonic cross section $\sigma^{ff'} = \int d^2p_t d\sigma^{ff'}/d_t^p$. The indices f and f' label the different kinds of interacting

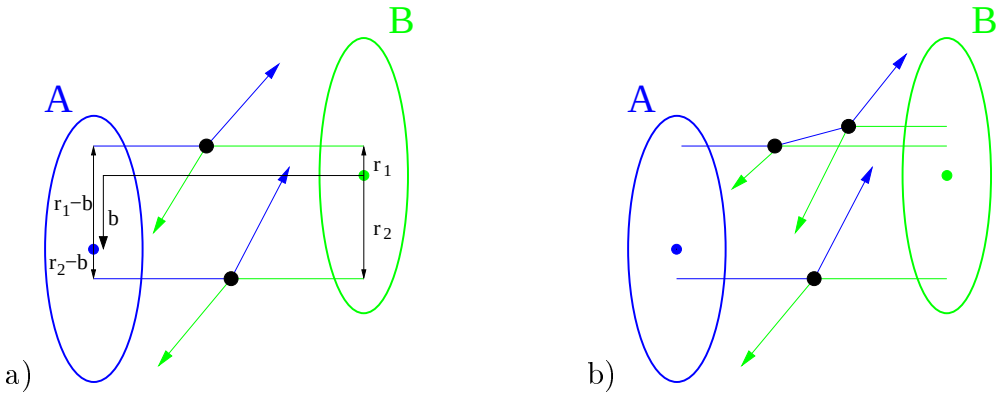

Figure 2.1: a) An example of parton disconnected collisions in a collision with nuclear impact parameter b. The origin of the transverse coordinates, r_i, is the center of the B nucleus. b) An example of parton rescatterings: the upper A nucleus parton has two scatterings against two different B nucleus partons. The lower A nucleus parton has a single scattering, not connected with the upper three-parton scattering (note that they may be nevertheless connected by the multiparton distributions of the two nuclei.

partons and the momentum fractions x, x' are defined with respect to the single nucleon momentum. At the lowest order in pQCD and in the high-energy limit the gluon-gluon cross section is

$$\sigma^{gg}(xx') = \frac{9}{2}\pi\alpha_s^2\frac{1}{p_0^2}\left(1-\frac{4p_0^2}{xx's}\right)\theta(xx's-4p_0^2)\theta(1-x)\theta(1-x') \ , \tag{2.1.3}$$

and we may account for different flavours by using effective parton distribution functions $G^{eff} = G^g + 4/9\sum_q G^q$, so that $\sigma_H = \int dxdx' G^{eff}(x)\sigma^{gg}(xx')G^{eff}(x')$. Note that in the expression of the gluon-gluon cross section we included all kinematic limits and an infrared cutoff p_0 on the transverse momentum to prevent integration over the singularity of the pQCD differential cross section. Both the parton distribution functions and the strong coupling constant, α_s, depend on a scale Q, which will be understood in the following. The minijet cross section is a smooth function of p_0 for small values of the cut-off: its limiting value of is indeed the geometrical limit $\sigma_{mj}^{AA} \approx \pi(R_A+R_B)^2$, R_A and R_B being the two nuclear radii. The corrections to the naive minijet cross section $\sigma_{mj}^{AA} = T_{AB}\sigma_H$ introduced by the Eikonal model have therefore led to its unitarization.

In the Eikonal model of nucleus-nucleus interactions Eq. (2.1.1) is the hard component of the nucleus-nucleus inelastic cross section, σ_{inel}^{AA}, which is obtained by writing the inelastic nucleon-nucleon cross section as a sum of a soft and a hard part, $\sigma_{inel}^{pp} = \sigma_S + \sigma_H$. Then the nuclear inelastic cross section may be as well decomposed into a soft and a hard part, $\sigma_{inel}^{AA} = \sigma_{inel}^{AA} + \sigma_{mj}^{AA}$, where

$$\sigma_{soft}^{AA} \ = \ \int d^2b\left(1-\ e^{-\sigma_S T_{AB}(b)}\right)\ e^{-\sigma_S T_{AB}(b)} \ . \tag{2.1.4}$$

The factors $\exp[-\sigma_S T_{AB}(b)]$ and $\exp[-\sigma_H T_{AB}(b)]$ are interpreted, respectively, as the probability of no soft interactions and of no semihard interactions at fixed impact parameter b. Then the minijet cross section (2.1.1) represents the contribution to the total inelastic cross section of all events with at least one semihard partonic interaction, and

the soft cross section (2.1.4) the contribution of all events with no semihard interactions and at least one semihard partonic interaction. Note that as the semihard partonic cross section σ_H grows, the probability of a hard interaction increases and the soft nuclear cross section decreases, and the minijet cross section tends to saturate σ_{inel}^{AA}. Therefore we expect that at high energies and large atomic numbers minijet production will be the dominant component of an heavy-ion collision. Note also that, as long as we are concerned with the semihard part of the nuclear cross section we do not have to make any commitment on the soft pp cross section, which in general has to be modeled in a phenomenological way.

The physical picture corresponding to Eq.(2.1.1) is that of a distribution of multiple independent two-parton collisions localized in different points in transverse space and with the average number depending on the nuclear impact parameter, see Fig. 2.1a. The average number of parton-parton interactions at fixed b is

$$\langle N_{coll}(b)\rangle = \sigma_H T_{AB}(b) \ .$$

Hence, if σ_H is at the lowest order in α_S the average multiplicity of partons, i.e., of minijets, produced in a given nuclear collision, i.e., at fixed b, is just twice the average number of collisions:

$$\langle N^{mj}(b)\rangle = 2\langle N_{coll}(b)\rangle = 2\,\sigma_H T_{AB}(b) \ . \tag{2.1.5}$$

The inclusive cross section for producing minijets in a nuclear collision is therefore given by $\sigma_{incl}^{mj} = 2\int d^2b\langle N(b)\rangle$. This shows that the description of the process given by Eq.(2.1.1) is consistent with the AGK cancellation [2] (all unitarity corrections cancel in the inclusive). The cancellation property obviously holds for all averages, that are therefore equal to the result obtained by means of the single scattering expression, so that the transverse energy produced by minijets is given by

$$\langle E_t(b)\rangle = 2\,T_{AB}(b)\int_{p_t\geq p_0} p_t\frac{d\sigma_H}{d^2p_t}\,d^2p_t \ . \tag{2.1.6}$$

While the semihard cross section σ_{mj}^{AA} is a smooth function of the cutoff, $\langle N(b)\rangle$ and $\langle E_t(b)\rangle$ are singular at small p_0 and their behaviour may be roughly estimated on dimensional grounds to be $\langle N(b)\rangle \simeq 1/p_0^2$ and $\langle E_t(b)\rangle \simeq 1/p_0$. The singular behavior at low p_0 can be used to set the limits of validity of the picture. Indeed, for the picture of the interaction to be valid one should take a relatively large value of the cut-off p_0; in this way the whole semihard interaction takes place in a relatively dilute system and the overall number of interactions will be relatively small. To deal with a regime where the number of parton interactions and the density of the interacting partons are large, the main modification adopted by the majority of papers is to include shadowing corrections in the nuclear parton distributions [28, 29]. In this way one obtains a substantial reduction of the number of projectile and target partons at low x and the picture can be extended to sizably lower values of the cutoff p_0. Even so, when p_0 is further reduced, one reaches the condition of a highly dense interacting system where the whole picture ceases to be valid, which sets the lower limit for a sensible choice of the cutoff p_0 [33, 43, 55]. The overall features of the Eikonal picture of semihard interactions are that the minimum p_0 at which the picture is still valid is different when varying the atomic mass number of the interacting nuclei and their energy, and that the distribution in the number of hard

collisions at a fixed value of the impact parameter b is a Poissonian in the whole semihard regime so that all average quantities are computed, as above, with the single scattering expression.

- Discuss the average number of minijet pairs, if correlations will be discussed in the thesis

2.1.3 The fate of the minijets

In heavy-ion interactions the number of minijets may become very large. Indeed, by using hard-sphere thickness functions we have for a central AA collision $T_{AA}(0) = \frac{9}{8\pi r_0^2} A^{4/3}$, where $r_0 = 1.12$ fm is the proton radius. Since the perturbative minijet cross section is proportional to the inverse square of the regulator p_0, we get

$$\langle N^{mj}(0) \rangle \propto \mathcal{N}(\sqrt{s}) \frac{A^{4/3}}{r_0^2 p_0^2} \ ,$$

where r_0 is the proton radius. $\mathcal{N}$ is the number of partons participating in the interaction, which is an increasing function of $\sqrt{s}$, due to the small-x increase of the parton distribution functions. For the same reasons, also σ_H is growing with $\sqrt{s}$, which means that the minijet cross section is saturating the nuclear inelastic cross section, as explained above. Therefore, minijets will play an important role in high-energy heavy-ion collisions, their multiplicity growing with A and $\sqrt(s)$. What happens of them, after their production? Minijets at RHIC and LHC energies are mainly made of gluons. Therefore we can model them as a gluon gas, which is produced in a very short time after the two nuclei collided. The formation time may be estimated by uncertainty principle to be $\tau_F \approx 1/p_0 = 2(1)$ fm at RHIC (LHC). In a gluon gas at a temperature $T \approx 200 MeV$ the parton mean free path is [49]

$$\lambda_{free} \approx \frac{p_0}{2T^2} \frac{1}{\ln(6p_0/T)}.$$

For $p_0 = 1..2$ GeV, we get λ_{free} of the order of some hundredth of a fm. Therefore, minijets are likely to rescatter many times and thus thermalize, possibly entering in the QGP phase.

2.2 Rescatterings, wounded partons and minijets

The clean physical interpretation of the approach described in the last section, which incorporates the geometrical features of the nuclear process, unitarity, the factorization of the hard component of the interaction and the AGK cancellation rules, justifies its the great success. Still there are a few delicate points which deserve further investigation and where the description of the process might be improved, first of all how to deal with the black disk regime and if it is possible to do that in pQCD. Indeed, at very high energies the target parton densities experienced by projectile partons are so high that the probability for them to have more than one semihard scattering may become non negligible. At such regimes the perturbative computation obtained by eikonalization of the minijet cross

section may become inadequate since it takes into account only disconnected two-parton semihard interactions.

When rescatterings are taken into account there is no more a simple relation between the average number of parton-parton collisions and the average number of minijets. If only disconnected collisions are taken into account the minijet multiplicity is simply twice the number of collisions, see Fig. 2.1a. On the other hand if rescatterings are included, we have only $\langle N^{mj}(b)\rangle \leq 2\langle N_{coll}(b)\rangle$. As an example in Fig. 2.1b we have 3 parton-parton semihard scatterings but only 5 minijets because the upper A nucleus parton had 1 rescattering before leaving the nucleus. It is then clear that the minijet counting requires a detailed knowledge of the actual multiple scatterings in a given process, which becomes rapidly very complicated when the incoming parton flux and the target parton density increase. To simplify the task we define a *wounded parton* as a parton that had *at least* one semihard scattering against the target partons. It is then clear that the number of minijets coincides with the number of wounded partons and that the (transverse) energy produced by semihard interactions is the (transverse) energy of the wounded partons. As it will become clear in the remaining of the chapter this definition and some suitable simplifying hypotheses will make treatable the problem of the inclusion of parton rescatterings in the interaction dynamics and of the computation of global observables, like the minijet cross section and the average minijet multiplicity and (transverse) energy.

To have a quantitative feeling for the relevance of rescatterings we need to evaluate the average number of semihard collisions *per incoming parton*, $\langle N^{scatt}\rangle$, which can be obtained by studying the average number of produced minijets, Eq. (2.1.5). For later convenience we define the *nuclear distribution functions*, Γ_A, of a nucleus of atomic number A as the product of the nuclear thickness function, τ_A, and the parton distribution function, G:

$$\Gamma_A(x,r) = \tau_A(r)G(x) \ . \tag{2.2.1}$$

With this notation we rewrite the average number of minijets in the Eikonal approximation, Eq. (2.1.5), as follows:

$$\begin{aligned}\langle N_{mj}(b)\rangle &= 2\int d^2r\, dx\, dx'\, \Gamma_A(x,r-b)\,\sigma(xx')\,\Gamma_B(x',r) \qquad (2.2.2)\\ &= \int d^2r\, dx\, \Gamma_A(x,r-b)\,\langle n_B^{scatt}(x,r)\rangle + \int d^2r\, dx'\, \Gamma_B(x',r)\,\langle n_A^{scatt}(x',r-b)\rangle \ ,\end{aligned}$$

where

$$\langle n_B^{scatt}(x,r)\rangle = \int dx'\,\sigma(xx')\,\Gamma_B(x',r) \ , \tag{2.2.3}$$

and analogously for $\langle n_A^{scatt}\rangle$. Eq. (2.2.2) may, therefore, be interpreted as the average number, Γ_A, of incoming partons from the A nucleus multiplied by the average number, $\langle n_B^{scatt}\rangle$, of collisions against the partons of nucleus B (plus the analogous term with A and B interchanged). We point out that although Eq. (2.2.3) has been derived in the Eikonal approximation it is valid also when rescatterings are introduced in the collision dynamics, see Sec. 2.6.2.

In Fig. 2.2 we plot $\langle n_B\rangle$, the average number of scatterings suffered by a gluon in a collision against a gold nucleus, as a function of the projectile parton fractional momentum

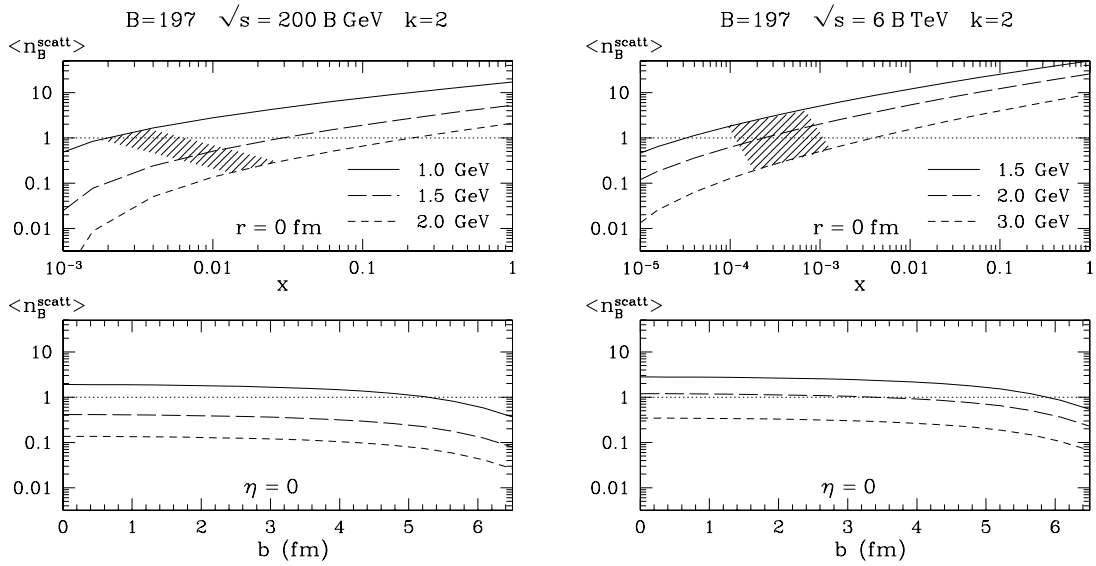

Figure 2.2: Average number $\langle n_B^{scatt} \rangle$ of semihard scatterings suffered by a gluon scattering on a gold nucleus at $\sqrt{s} = 200$ GeV per nucleon pair (*leftmost panels*) and $\sqrt{s} = 6$ TeV per nucleon pair (*rightmost panels*). The scale is $Q = p_0$, the k factor is $k = 2$. Woods-Saxon thickness functions have been used. *Top panels:* $\langle n_B \rangle$ is plotted as a function of the projectile parton fractional momentum x in the case of a central parton-nucleus collision. The three curves refer to different cutoff values (see legend) and the shaded area corresponds to the central pseudorapidity region $|\eta| \leq 1$, where $\eta = \log(x\sqrt{(}s)/p_0)$. The dotted line marks the transition value of 1 scattering per parton. *Bottom panels:* $\langle n_B \rangle$ is plotted as a function of the impact parameter for a parton emerging with pseudorapidity $\eta = 0$.

x and of its impact parameter, r, on the target nucleus. At RHIC energy and at a cut-off $p_0 = 1$ GeV a gluon in the central rapidity region experiences on average 1 to 2 scatterings over the whole target transverse area except the very peripheral regions. At LHC and $p_0 = 2$ GeV the average number of scatterings raises to 2-3. At higher cut-off values the number of scatterings decreases. As a result, semihard rescatterings should be negligible down to $p_0 \simeq 2$ GeV at RHIC and down to $p_0 \simeq 3$ GeV at LHC, where their effects begin to show up. At $p_0 \approx 1(2)$ GeV they may have a large effect and should not be neglected. These conclusions will be confirmed by the numerical computations discussed in Chapter 3.

Note that we chose different cutoff values as a reference value to discuss the regime where parton rescatterings become important at RHIC and LHC. The reason is that, as discussed in the introduction, the saturation scale, Q_s, at which nonperturbative effects due to high parton densities are expected to show up is a function of the collision energy. As we would like to push perturbative computations as far as possible, in this discussion we took the estimated values $Q_s \approx 1(2)$ GeV at RHIC (LHC) as the approximate limits for p_0 in the two cases. A detailed discussion of saturation in perturbative and semi-classical QCD can be found in Chapter 4.

The dependence on $\sqrt{s}$ of the average number of scatterings per incoming parton is shown in Fig. 2.3 for $r = 0$ and different pseudorapidities $\eta \approx \log(x\sqrt{s}/p_0$. We can see that semihard rescatterings in nuclear collisions are negligible in the backward pseudorapidity region at all energies. At central and forward rapidities they should affect global

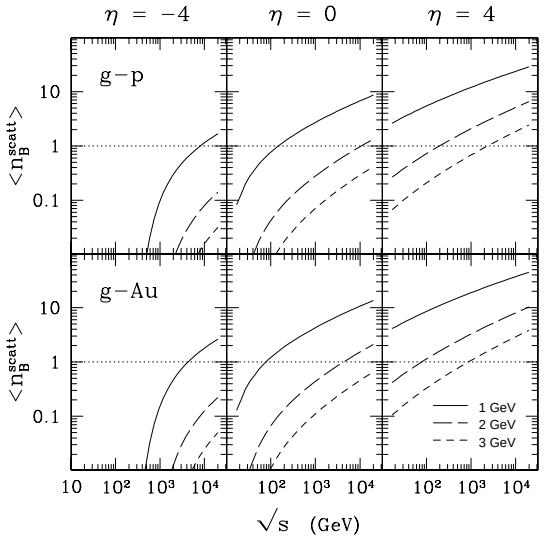

Figure 2.3: Average number $\langle n_B \rangle$ of semihard scatterings suffered by a gluon scattering on a proton (*upper three panels*) and on a gold nucleus (*lower three panels*) at impact parameter $r = 0$. The result for backward, central and forward gluon rapidities are shown (we used the approximate relation $\eta = \log(x\sqrt{s}/p_0)$). The solid, long-dashed and short-dashed lines refer to a cut-off value of $p_0 = 1, 2, 3$ GeV, respectively. For the proton we used Gaussian thickness function and for the gold nucleus the Woods-Saxon one.

observables at $\sqrt{s} \gtrsim 100$ GeV, i.e. from RHIC energies on. Effects of rescatterings on more exclusive observables like the two-jet angular correlations in hA collisions have been reported in Refs. [118] and [125].

The cases of a hadron and a nuclear target should be compared with care. Indeed, in hadronic collisions it is at best very difficult to control the centrality of the event. Therefore the values average number of scatterings shown in Fig. 2.3 for a gluon-proton collision are the peak values that can be reached when the gluon hits centrally the proton. Actual observable depend rather on the average of $\langle n_p^{scatt}(b) \rangle$ over the transverse plane, which results in a lowering of the values plotted in the figure by a factor two, approximately. Moreover, in pp collisions the saturation scale is very low, $Q_s \gtrsim \Lambda_{QCD}$, hence there is no more a natural scale where to stop perturbative computations and the choice of a reference value for p_0 becomes a matter of definition of what is hard and what is soft [127], and will depend also on the actual choice of the observable. Indeed, minijets may be identified in the final state as clusters of particles flowing along the direction of motion of a parton whose hadronization originated them. Unambiguous identification of a cluster as a minijet instead of a background fluctuation is possible down to cluster transverse energies $E_T \gtrsim 5$ GeV, corresponding to $p_0 \gtrsim 3 - 4$ GeV [107]. Therefore, we expect that rescatterings could play a role in minijet physics in hadronic collisions only at forward rapidities and energy higher than some TeV. For observables like many particle correlations, or hadron transverse spectra, the reference value is $p_0 = 1GeV$ and rescattering may play an important role already at $\sqrt{s} \gtrsim 300$ GeV, say at Tevatron energies.

2.3 Nonperturbative input: multiparton distributions

In this section we discuss the nonperturbative input to the computation of multiple partonic interactions, namely the multiparton distributions. To approach the problem in the most general form we use the functional formalism introduced in [19]. At a given resolution, provided by the regulator p_0, one may find the nuclear (or hadronic) system in various partonic configurations. We call $P^{(n)}(u_1 \dots u_n)$ the probability of a configuration with n partons (the *exclusive n-parton distribution*) where $u_i \equiv (b_i, x_i)$ represents the

transverse coordinate of the ith parton, b_i, and its longitudinal fractional momentum, x_i. The distributions are symmetric in the variables u_i, and can be obtained from a generating functional defined with the help of auxiliary functions $J(u)$ as follows:

$$\mathcal{Z}[J] = \sum_n \frac{1}{n!} \int J(u_1) \dots J(u_n) P^{(n)}(u_1, \dots, u_n) du_1 \dots du_n \ .$$

In the above formula all infrared divergences are regularized by the cutoff p_0, which is implicit in all equations. Probability conservation yields the normalization condition

$$\mathcal{Z}[1] = 1 \ . \tag{2.3.1}$$

Then, the exclusive n-parton distributions can be obtained by differentiating the generating functional $\mathcal{Z}$ with respect to the auxiliary functions:

$$P^{(n)}(u_1, \dots, u_n) = \frac{\delta}{\delta J(u_1)} \dots \frac{\delta}{\delta J(u_n)} \mathcal{Z}[J] \ |_{J=0} \ .$$

A useful representation of $\mathcal{Z}$ may be found by introducing its logarithm, $\mathcal{F}$, with normalization $\mathcal{F}[1] = 0$, so that

$$\mathcal{Z}[J] = \ e^{\mathcal{F}[J]} \ , \tag{2.3.2}$$

and by studying the *inclusive n-parton distribution*, $D^{(n)}$. They can be obtained as functional derivatives of $\mathcal{Z}$ or of $\mathcal{F}$. Indeed

$$\begin{aligned} D^{(1)}(u) &\equiv \Gamma(u) \equiv P^{(1)}(u) + \int P^{(2)}(u, u') du' + \frac{1}{2} \int P^{(3)}(u, u', u'') du' du'' + \dots \\ &= \frac{\delta \mathcal{Z}}{\delta J(u)} \bigg|_{J=1} = \frac{\delta \mathcal{F}}{\delta J(u)} \bigg|_{J=1} \ , \end{aligned} \tag{2.3.3}$$

$$\begin{aligned} D^{(2)}(u_1, u_2) &\equiv P^{(2)}(u_1, u_2) + \int P^{(3)}(u_1, u_2, u') du' + \frac{1}{2} \int P^{(4)}(u_1, u_2, u', u'') du' du'' + \dots \\ &= \frac{\delta^2 \mathcal{Z}}{\delta J(u_1) \delta J(u_2)} \bigg|_{J=1} = \frac{\delta^2 \mathcal{F}}{\delta J(u_1) \delta J(u_2)} \bigg|_{J=1} + \frac{\delta \mathcal{F}}{\delta J(u_1)} \frac{\delta \mathcal{F}}{\delta J(u_2)} \bigg|_{J=1} \ , \end{aligned} \tag{2.3.4}$$

and so on for higher multiparton distributions. We use $\Gamma(u) \equiv D^{(1)}(u)$ for consistency with the notation used in [3–6, 17, 18]. These relations show that the correlated part, $C^{(n)}$, of the inclusive n-parton distribution (also called *n-parton correlation*) is simply given by differentiation of the generating functional $\mathcal{F}$:

$$C^{(n)}(u_1, \dots, u_n) = \frac{\delta}{\delta J(u_1)} \dots \frac{\delta}{\delta J(u_n)} \mathcal{F}[J] \ |_{J=1} \ ,$$

so that the expansion of $\mathcal{F}$ near $J = 1$ reads:

$$\mathcal{F}[J] = \int \Gamma(u)[J(u) - 1] du \tag{2.3.5}$$

$$+ \sum_{n=2}^{\infty} \frac{1}{n!} \int C^{(n)}(u_1 \dots u_n) \big[J(u_1) - 1\big] \dots \big[J(u_n) - 1\big] du_1 \dots du_n \ . \tag{2.3.6}$$

In this way we have obtained a convenient representation of the generating functional $\mathcal{Z} = \exp[\mathcal{F}]$ in terms of the single parton distribution, Γ, and of the multiparton correlations, $C^{(n)}$.

In the simplest case where we neglect all the correlations between the partons, namely $C^{(n\geq 2)} = 0$, the generating functional is given by

$$\mathcal{Z}[J] = e^{\int \Gamma(u)[J(u)-1]du} . \tag{2.3.7}$$

and the the many-parton distribution is Poissonian:

$$P^{(n)}(u_1, \ldots, u_n) = D^{(n)}(u_1, \ldots, u_n) = \frac{1}{n!}\Gamma(u_1)\ldots\Gamma(u_n)e^{-\int du\Gamma(u)} . \tag{2.3.8}$$

It is then easy to see that the multiparton inclusive distributions are factorized in terms of the single-parton ones:

$$D^{(n)}(u_1, \ldots, u_2) = \Gamma(u_1)\cdots\Gamma(u_n) .$$

The deviations from a Poissonian distribution may have two different origins:

1. the many-parton distributions are still factorized in terms of the single-parton distribution, Γ, but are not Poissonian, namely the exclusive and inclusive n-parton distributions have different coefficients. In this case $C^{(n)}$ is factorized, as well;
2. genuine two- and many-body correlations, in which case $C^{(n)}$ does not factorize.

For more details, we refer to [19].

2.4 Perturbative input: semihard rescatterings

A very general approach to nuclear interactions at high-energy is through the reggeon diagram technique, which describes the interaction at high energy where as an exchange of many pomerons, including both independent exchanges between different nucleons and multi-pomeron interactions, which represent the collision of a given projectile nucleon with several different target nucleons in a given interaction process. Each partonic collision corresponds to a fluctuation with a large transverse momentum inside the structure of an exchanged pomeron. While the simplest case is that with a single partonic loop with large p_t, whose discontinuity corresponds to a $2 \to 2$ partonic collision, one might imagine more complicated fluctuations, with several connected parton lines, all with large p_t, in the structure of a multi-pomeron interaction. The simplest case of this kind is illustrated in Fig.2.4, where the Pomerons are represented by parton ladders. Discontinuities of such fluctuations originate configurations, where the compensation of transverse momenta in the final state involves several large p_t partons, while the whole large p_t configuration is generated by partons belonging to different chains, representing Pomerons attached to different nucleon lines. In the picture of the semihard interaction just recalled those configurations contribute to the shadowing corrections of the nuclear parton distributions. Their discontinuities, on the contrary, are not included in the semihard interaction dynamics. On the other hand, when approaching the black disk limit, the initial and final partonic states become locally isotropic in transverse space, so that both initial and final

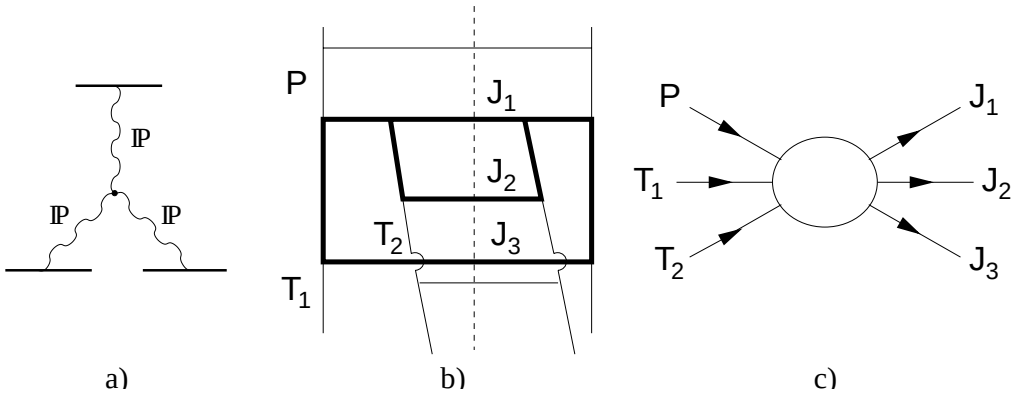

Figure 2.4: a) A triple pomeron interaction between 3 nucleons. b) Parton ladders with the topology of Fig.2.4a). The thick lines are fluctuations with high p_t and the dashed line is a possible cut. c) Partonic view of the cut of Fig.2.4b): P is a projectile parton interacting with two target partons T_i and the final state is given by the three large-p_t jets J_i.

state configurations need to be built up with lots of partons. A proper discussion of semihard dynamics in the black disk limit requires therefore taking into account fluctuations with many large p_t parton lines, which are to be included not only in the virtual corrections but also in the production process. Hence one needs to consider partonic interactions where several partons, with low virtuality and p_t and sizable longitudinal components (so that, in the nucleus-nucleus c.m. frame, each one may be ascribed to a definite nucleus) interact producing large p_t jets.

The simplest multiparton interaction of the kind described above was discussed in Ref.[20] (see also [84]), where the forward amplitude of the process and all the cuts were derived in the case of a point-like projectile against two point-like targets, in the limit of an infinite number of colors and for $t/s \to 0$. The result is that the leading contributions to the various cut of the $3 \to 3$ forward amplitude are all proportional one to another and the proportionality factors are exactly the AGK weights [2]. Even more, the leading contribution comes from a configuration where the intermediate parton between two successive collisions is on shell. A consequence of this analysis is that in the limit considered we may express the three-body cross section as a product of two two-body cross sections. Therefore we can interpret the process in terms of two successive scatterings of the projectile parton against two different target partons, as depicted in Fig. 2.5.

The results obtained in the simple case of a three-parton scattering may indicate a convenient approximation of the many-parton interaction probability. One can in fact argue that the many-parton interaction process may be approximated by a product of two-parton interactions, so that one can call the process *reinteraction* or *rescattering*. The whole interaction is therefore expressed in terms of two-body interaction probabilities,

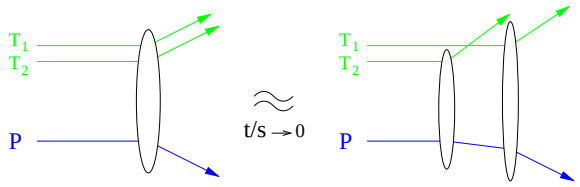

Figure 2.5: Three parton interaction as two successive scatterings of a projectile parton, P, on two target partons, T_i.

precisely as the interaction between two nuclei is expressed in terms of nucleon-nucleon collisions. Hence, given a configuration with n partons of the projectile and l partons of the target, we introduce the probability, $\mathcal{P}_{n,l}$, of having at least one partonic collision, in a way analogous to the expression of the inelastic nucleus-nucleus cross section [11]:

$$\boxed{\mathcal{P}_{n,l} = \left[1 - \prod_{i=1,n} \prod_{k=1,l} (1 - \hat{\sigma}_{ik})\right]}, \tag{2.4.1}$$

where $\hat{\sigma}_{ik}$ is the probability of interaction of a given pair of partons i and k. Since the distance over which the hard interactions are localized is much smaller than the soft interaction scale, one may approximate $\hat{\sigma}(x_i x_k; b_i - b_k) \approx \sigma(x_i x_k)\delta^{(2)}(b_i - b_k)$, where x_i and x_k are the momentum fractions of the colliding partons, b_i and b_k their transverse coordinates and $\sigma(x_i x_k)$ is the partonic semihard cross section, whose infrared divergence is cured by introducing a regulator p_0. For example, p_0 may be the lower cutoff on the momentum exchange in each partonic collision, see Eq. (2.1.3), or a small mass introduced in the transverse propagator to prevent the divergence of the cross section at zero momentum exchange. The expression of $\mathcal{P}_{n,l}$ is the analogue of Eq. (1.3.20) and represents the explicit implementation of self-shadowing for the interaction of two partonic configurations, see Ref. [84]. Note that because of self-shadowing all unitarity corrections to the semihard cross section will be therefore expressed by means of the semihard partonic cross section only, so that we don't need to make any commitment on the soft component when only the semihard part of the interaction is of interest. Self-shadowing allows moreover to control also the soft component of the interaction by perturbative means, since that contribution is limited to a fraction of the cross section proportional to the probability of not having any hard interaction at all [see Eq. 1.3.21)].

2.5 Minijet cross section

In this section we want to compute the semihard inelastic cross section for the interaction of two colliding nuclei with atomic numbers A and B[1] at fixed impact parameter b. The minijet inelastic cross section $d\sigma_{mj}^{AB}/d^2b$ is obtained by folding the interaction probability,

[1] In the case of a hadron-nucleon collision, we will denote the hadron with the subscript h in general, p for the proton and so on.

Eq. (2.4.1), with the multiparton exclusive distributions of the two colliding nuclei:

$$\begin{aligned}\frac{d\sigma^{AB}_{mj}}{d^2b} &= \int \sum_{\substack{n=1,\infty\\ l=1,\infty}} P_A^{(n)} \times P_B^{(l)} \times \mathcal{P}_{n,l} \\ &= \int \sum_{\substack{n=1,\infty\\ l=1,\infty}} \frac{1}{n!}\frac{\delta}{\delta J(u_1-b)}\cdots\frac{\delta}{\delta J(u_n-b)}\mathcal{Z}_A[J]\ |_{J=0} \\ &\quad\times \frac{1}{l!}\frac{\delta}{\delta J'(u'_1)}\cdots\frac{\delta}{\delta J'(u'_l)}\mathcal{Z}_B[J']\ |_{J'=0} \\ &\quad\times \Big\{1-\prod_{\substack{i=1,n\\ k=1,l}}[1-\hat\sigma(u_i,u'_l)]\Big\}\prod_{i=1,n} du_i \prod_{k=1,l} du'_k\ , \end{aligned} \tag{2.5.1}$$

where b is the impact parameter of the collisions. We used the shorthand $u=(x,r)$ and $u-b=(x,r-b)$ to represent the parton fractional momentum, x, and the transverse coordinate, r and $r-b$, respectively. In other words, the semihard cross section is constructed by summing over all possible projectile and target parton configurations, and for each given configuration by summing over all possible multiparton interactions. The latter is obtained by considering the probability $\mathcal{P}_{n,l}$, Eq. (2.4.1), that at least one pair of partons, one from A and the other from B, have a semihard scattering. The expansion of $\mathcal{P}_{n,l}$ gives all possible multiparton interactions. The $\frac{1}{n!}$ and $\frac{1}{l!}$ are due to the indistiguishability of the partons (remember that we are considering only the gluons). All the consideration here can be generalized to include also the quarks [17].

To simplify the notation we introduce the following operators:

$$\delta_i = \int du_i \frac{\delta}{\delta J(u_i-b)}\ \ ;\ \ \delta'_k = \int du'_k \frac{\delta}{\delta J'(u'_k)}\ .$$

Note that these operators commute with each other. We also write the two-parton interaction probability as $\hat\sigma_{ik}=\hat\sigma(u_i,u'_k)$, and will *not* understand the summation over repeated indices. As an example,

$$\begin{aligned}\delta_i\delta'_k\hat\sigma_{ik} &= \int du_i du'_k \frac{\delta}{\delta J(u_i-b)}\frac{\delta}{\delta J'(u'_k)}\hat\sigma(u_i,u'_k) \\ &= \int du_j du'_k\, \Gamma_A(u_i)\hat\sigma(u_i,u'_k)\Gamma_B(u'_k)\ +\ \text{correlation terms.}\end{aligned}$$

Moreover, a generic index will be indicated with a star symbol, e.g., $\delta'_\star\sigma_{i\star} = \int du'_\star\,[\delta/\delta J'(u'_\star)]\sigma(u_i,u'_\star)$. When in a product of many items one is missing we will bar it: for example,

$$\delta_1\cdots\not{\delta}_k\cdots\delta_n$$

is the product of the operator δ_i, with i ranging from 1 to n, *except* δ_k. When there is no need to mark out any particular parton index we will omit them, e.g.

$$\sum_{n=0,\infty}\frac{1}{n}\delta_1\cdots\delta_n \equiv \sum_{n=0,\infty}\frac{1}{n}\delta^n \equiv e^\delta\ ,$$

When the δ operators or the scattering probability $\hat{\sigma}$ have no indices, they are understood to refer to the variables u and u' as in the following example:

$$\delta\, e^{-\delta'\hat{\sigma}} = \int du \frac{\delta}{\delta J(u-b)} e^{-\int du' \frac{\delta}{\delta J'(u')}\hat{\sigma}(u,u')} \ .$$

Given two functions $f = f(u)$ and $g = g(u)$, the following identity holds:

$$e^{\delta f}\mathcal{Z}[J+g] = \mathcal{Z}[J+g+f] \ . \tag{2.5.2}$$

In other words, the exponential of the operator δ acts on the generating functional $\mathcal{Z}$ by shifting its argument by the amount f.

With this notation we can rewrite Eq. (2.5.1) as follows:

$$\boxed{\frac{d\sigma_{mj}^{AB}}{d^2b} = \sum_{\substack{n=1,\infty\\ l=1,\infty}} \frac{1}{n!}\delta_1\cdots\delta_n \ \frac{1}{l!}\delta'_1\cdots\delta'_l \left\{1 - \prod_{\substack{i=1,n\\ k=1,l}}\left[1-\hat{\sigma}_{ik}\right]\right\} \mathcal{Z}_A[J]\mathcal{Z}_B[J'] \ _{|J=J'=0}} \tag{2.5.3}$$

This equation is the starting point for the computation of many observables. In this section we will examine the AA and the hA cross sections. The first one may be computed explicitly under the assumption that the partons do not suffer any rescatterings and by taking some definite assumption on their correlations. In the case of no correlations we shall recover the result obtained in the Eikonal approximation, Eq. (2.1.1). In the case of hA interactions we shall be able to relax the approximations. The computations are done with some detail to get acquainted with the formalism.

2.5.1 Nucleus-nucleus scattering with no parton rescatterings

In nucleus-nucleus interactions at high energy the largest contributions to the cross section comes from semihard disconnected collisions. Therefore we may neglect completely parton rescatterings, in which case the probability of no semihard interaction probability may be written as

$$\mathcal{P}_{n,l} = 1 - \prod_{\substack{i=1,n\\ k=1,l}}\left[1-\hat{\sigma}_{ik}\right] \simeq \sum_{\substack{i=1,n\\ k=1,l}}\hat{\sigma}_{ik} - \frac{1}{2!}\sum_{\substack{i=1,n\\ k=1,l}}\sum_{\substack{p=1,n\\ q=1,l\\ p\neq i;\ q\neq k}}\hat{\sigma}_{ik}\hat{\sigma}_{pq} + \ldots \tag{2.5.4}$$

When substituting it in (2.5.3) we may do explicitly the sum over n and m. Indeed, by exploiting the fact that the δ and δ' operators commute with one another we get:

$$\begin{aligned}\frac{d\sigma_{mj}^{AB}}{d^2b} = &\sum_{\substack{n=1,\infty\\ l=1,\infty}}\sum_{\substack{i=1,n\\ k=1,l}} \frac{1}{n!}\delta_1\cdots\not{\delta}_i\cdots\delta_n \ \frac{1}{l!}\delta'_1\cdots\not{\delta}'_k\cdots\delta'_l \ \left(\delta_i\delta'_k\hat{\sigma}_{ik}\right)\mathcal{Z}_A[J]\mathcal{Z}_B[J'] \ _{|J=J'=0}\\ &- \frac{1}{2!}\sum_{\substack{n=2,\infty\\ l=2,\infty}}\sum_{\substack{i=1,n\\ k=1,l}}\sum_{\substack{p=1,n\\ q=1,l\\ k\neq i;\ j\neq l}} \frac{1}{n!}\delta_1\cdots\not{\delta}_i\cdots\not{\delta}_p\cdots\delta_n \ \frac{1}{l!}\delta'_1\cdots\not{\delta}'_k\cdots\not{\delta}'_q\cdots\delta'_l\\ &\qquad\qquad \times\left(\delta_i\delta'_k\hat{\sigma}_{ik}\right)\left(\delta_p\delta'_q\hat{\sigma}_{pq}\right)\mathcal{Z}_A[J]\mathcal{Z}_B[J'] \ _{|J=J'=0} + \ldots\end{aligned}$$

Next, we observe that $\delta_i\hat{\sigma}_{ij}\delta'_j = \delta_k\hat{\sigma}_{kl}\delta'_l \equiv \delta\delta'\hat{\sigma}$, so that

$$\frac{d\sigma^{AB}_{mj}}{d^2b} = (\delta\delta'\hat{\sigma}) \sum_{\substack{n=1,\infty \\ l=1,\infty}} nl \frac{1}{n!}\delta_1 \cdots \not{\delta}_i \cdots \delta_n \; \frac{1}{l!}\delta'_1 \cdots \not{\delta}'_k \cdots \delta'_l \; \mathcal{Z}_A[J]\mathcal{Z}_B[J'] \; |_{J=J'=0}$$
$$- \frac{1}{2!}(\delta\delta'\hat{\sigma})^2 \sum_{\substack{n=2,\infty \\ m=2,\infty}} n(n-1)l(l-1)\frac{1}{n!}\delta_1 \cdots \not{\delta}_i \cdots \not{\delta}_p \cdots \delta_n$$
$$\times \frac{1}{l!}\delta'_1 \cdots \not{\delta}'_k \cdots \not{\delta}'_q \cdots \delta'_l \; \mathcal{Z}_A[J]\mathcal{Z}_B[J'] \; |_{J=J'=0} + \ldots \tag{2.5.5}$$

If we redefine the summation indices n and m, we obtain :

$$\frac{d\sigma^{AB}_{mj}}{d^2b} = \left[(\delta\delta'\hat{\sigma}) - \frac{1}{2!}(\delta\delta'\hat{\sigma})^2 + \ldots\right] \sum_{n=0,\infty} \frac{1}{n!}\delta_1 \cdots \delta_n \mathcal{Z}_A[J] \sum_{l=0,\infty} \frac{1}{l!}\delta'_1 \cdots \delta'_l \mathcal{Z}_B[J'] \; |_{J=J'=0}$$
$$= \left[1 - e^{-\delta\hat{\sigma}\delta'}\right] \; e^{\delta} \; \mathcal{Z}_A[J] \; e^{\delta'} \mathcal{Z}_B[J'] \; |_{J=J'=0} \; . \tag{2.5.6}$$

Finally, by using the identity (2.5.2) we get the general expression for the semihard nucleus-nucleus cross section when parton rescatterings are neglected:

$$\boxed{\frac{d\sigma^{AB}_{mj}}{d^2b} = \left[1 - e^{-\delta\delta'\hat{\sigma}\delta'}\right] \mathcal{Z}_A[J+1]\mathcal{Z}_B[J'+1] \; |_{J=J'=0}} \; . \tag{2.5.7}$$

This expression is too complicated to be worked out explicitly due to the multiparton correlations present in $\mathcal{Z}_A[J+1]$ and $\mathcal{Z}_B[J'+1]$. If we further assume the partons in both nuclei to be uncorrelated, we can use Eq. (2.3.7) in (2.5.7) and get the semihard cross section in the Eikonal approximation discussed in Sec. 2.1:

$$\frac{d\sigma^{AB}_{mj}}{d^2b} = 1 - e^{-\int dudu' \Gamma_A(u)\hat{\sigma}(u,u')\Gamma_B(u')} \; ,$$

where we used the normalization condition (2.3.1). For a discussion of the case of two-parton correlations we refer to Ref. [19].

2.5.2 Hadron-nucleus scattering

In the case of hadron-nucleus interactions[2] one may neglect the rescatterings of the partons of the target nucleus. Indeed, even at very high center of mass energies the average number of scattering suffered by the nuclear partons scattering on the hadron is smaller than than one except in the very forward rapidity region, see Sec. 2.2. With this assumption the number of collisions be equal to the number of wounded target partons and the interaction

[2]By convention, we consider the hadron to be the projectile and the nucleus to be the target.

probability may be simplified as follows:

$$\begin{aligned}\mathcal{P}_{n,l} &= \Big\{1-\prod_{\substack{i=1,n\\k=1,l}}[1-\hat{\sigma}_{ik}]\Big\}\\ &\simeq \sum_{i=1,n}\sum_{k=1,l}\hat{\sigma}_{ik}-\frac{1}{2!}\sum_{i,p=1,n}\sum_{\substack{k,q=1,l\\k\neq q}}\hat{\sigma}_{ik}\hat{\sigma}_{pq}+\frac{1}{3!}\sum_{i,p,r=1,n}\sum_{\substack{k,q,s=1,m\\k\neq q\neq s}}\hat{\sigma}_{ik}\hat{\sigma}_{pq}\hat{\sigma}_{rs}+\dots\end{aligned} \tag{2.5.8}$$

where by $k\neq q\neq s$ we actually mean that all three indices must be different. After inserting Eq. (2.5.8) with the differentiation operators in Eq. (2.5.3) we can perform the sums over the target indices, and after redefining them as when going from Eq. (2.5.5) to Eq. (2.5.6) one obtains

$$\begin{aligned}\frac{d\sigma^{hA}_{mj}}{d^2b} &= \sum_{n=1,\infty}\frac{1}{n!}\delta_1\cdots\delta_n\sum_{l=0,\infty}\frac{1}{l!}\delta_1\cdots\delta_l\Bigg(\sum_{i=1,n}(\delta'_\star\hat{\sigma}_{i\star})-\frac{1}{2!}\sum_{i,p=1,n}(\delta'_\star\hat{\sigma}_{i\star})(\delta'_\star\hat{\sigma}_{p\star})\\ &\quad+\frac{1}{3!}\sum_{i,p,r=1,n}(\delta'_\star\hat{\sigma}_{i\star})(\delta'_\star\hat{\sigma}_{p\star})(\delta'_\star\hat{\sigma}_{r\star})+\dots\Bigg)\mathcal{Z}_h[J]\mathcal{Z}_A[J']\;{}_{|J=J'=0}\\ &\equiv \mathcal{A}\mathcal{Z}_A[J]\mathcal{Z}_B[J']\;{}_{|J=J'=0}\;.\end{aligned} \tag{2.5.9}$$

The last equality defines the operator $\mathcal{A}$. Given a number n of projectile partons and a number q of collisions, we have the following identity:

$$\sum_{i_1,i_2,\dots,i_q=1,n}(\delta'_\star\hat{\sigma}_{i_1\star})(\delta'_\star\hat{\sigma}_{i_2\star})\cdots(\delta'_\star\hat{\sigma}_{i_q\star})=\big[(\delta'_\star\hat{\sigma}_{i_1\star})+(\delta'_\star\hat{\sigma}_{i_2\star})+\cdots+(\delta'_\star\hat{\sigma}_{i_q\star})\big]^n\;.$$

Therefore the operator $\mathcal{A}$ in Eq. (2.5.9) becomes:

$$\begin{aligned}\mathcal{A} &= \sum_{n=1,\infty}\frac{1}{n!}\delta^n\sum_{q\geq1}\frac{(-1)^{q-1}}{q!}\Big[\sum_{i=1}^n\delta'_\star\hat{\sigma}_{i\star}\Big]^q=\sum_{n=1,\infty}\frac{1}{n!}\delta^n\Big[1-\exp\Big(-\sum_{i=1}^n\delta'_\star\cdot\hat{\sigma}_{i\star}\Big)\Big]\\ &=\Big[\sum_{n=1,\infty}\frac{1}{n!}\delta^n-\sum_{n=1,\infty}\frac{1}{n!}\Big(\delta e^{-\delta'\hat{\sigma}}\Big)^n\Big]e^{\delta'}=\Big\{1-\exp\Big[\delta\cdot(e^{-\delta'\hat{\sigma}}-1)\Big]\Big\}e^{\delta+\delta'}\end{aligned}$$

Finally, by inserting $\mathcal{A}$ in Eq. (2.5.9) and by using the identity (2.5.2) we obtain the general expression of the hadron-nucleus semihard cross section:

$$\boxed{\frac{d\sigma^{hA}_{mj}}{d^2b}=\Big\{1-\exp\Big[\delta\cdot(e^{-\delta'\hat{\sigma}}-1)\Big]\Big\}\mathcal{Z}_h[J+1]\mathcal{Z}_A[J'+1]\;{}_{|J=J'=0}}\;. \tag{2.5.10}$$

This result includes all possible parton correlations of both the projectile and the target: the only assumption made is that target partons do not suffer any semihard rescattering. A meaningful approximation (see Ref.[19]) is to consider the nuclear partons uncorrelated, namely $C_A^{(n\geq2)}=0$. Then, by using Eq. (2.3.7) the cross section reduces to:

$$\begin{aligned}\frac{d\sigma^{hA}_{mj}}{d^2b} &= \sum_{n=1,\infty}\frac{\delta^n}{n!}\sum_{l=0,n}(-1)^{n-l}\binom{l}{n}\mathcal{Z}_A[1-l\hat{\sigma}]\mathcal{Z}_h[J+1]\;{}_{|J=0}=\\ &=1-\mathcal{Z}_h\Big[e^{-\int\hat{\sigma}(\cdot,u')\Gamma_A(u')du'}\Big]\;.\end{aligned} \tag{2.5.11}$$

If we neglect also the correlations between the partons of the projectile, we get a further simplification:

$$\frac{d\sigma_{mj}^{hA}}{d^2b} = 1 - \exp\left\{ - \int du \Gamma_h(u-b) \left[1 - e^{-\int \hat{\sigma}(u,u')\Gamma_A(u')du'} \right] \right\} . \tag{2.5.12}$$

Both in Eq. (2.5.11) and in Eq. (2.5.12) the cross section is a function of

$$\overline{N}_h(u,b) = \Gamma_h(u-b) \left[1 - e^{-\int \hat{\sigma}(u,u')\Gamma_A(u')du'} \right] \tag{2.5.13}$$

$$\equiv \Gamma_h(u-b)\mathcal{P}_A(u) , \tag{2.5.14}$$

which represents the number of projectile partons that have interacted with the target, i.e., the projectile wounded partons. As we discussed in Sec. 2.2 we identify them with the minijets even if they did not yet hadronize. The square parentheses is interpreted as the probability that a projectile parton with given $u = (x, b)$ has at least one semihard interaction with the target, hence the cross section is obtained by summing all events with at least one semihard interaction. Note that in the limit of large cutoff p_0 the interaction probability $\hat{\sigma}$, which is proportional to the gluon-gluon perturbative cross section, become very small and so does the probability of having more than one scattering. As a consequence the cross section recovers the Eikonal result, Eq. (2.5.7), obtained in Sec. 2.5.1.

Of course, the projectile parton correlations appear explicitly in the total hadron-nucleus cross section. In the simplest case of two-parton correlations one would obtain:

$$\frac{d\sigma_{mj}^{hA}}{d^2b} = 1 - \exp\left\{ - \int du \overline{N}_h(u-b) + \frac{1}{2!} \int du du' \mathcal{P}_A(u) C_h^{(2)}(u-b, u'-b) \mathcal{P}_A(u') \right\} . \tag{2.5.15}$$

The effect of correlations on $d\sigma_{mj}^{hA}/d^2b$ is however small, both when unitarity corrections are small (i.e., when the semihard parton-parton cross section is small, so that $\mathcal{P}_A$ and $\overline{N}_h$ are both of order σ_{mj}^{hA}) and when they are large (i.e., when σ_{mj}^{hA} is large, $\mathcal{P}_A \sim 1$ and $\overline{N}_h$ is large). If, on the other hand, one is looking for correlations, the simplest quantity which depends linearly on $C_h^{(2)}$ is the double-jet inclusive cross section [23].

2.6 Global average quantities

The semihard cross section, Eq. (2.5.3), though difficult to calculate itself, is the starting point for the analytical computation of a number of average quantities, whose physical relevance will be studied in detail in the next chapters. In this section we will compute global observables like the average number of wounded partons and their transverse energy. We will also study the corresponding differential observables, like the transverse momentum distribution of wounded partons and the double differential distribution of pairs of wounded partons. The phenomenological applications will be discussed in the next chapters.

Given l "target" partons in the B nucleus, the probability, $\widehat{\mathcal{P}}_{i,l}$ that the ith "projectile parton" from the A nucleus has at least one semihard interaction with them is obtained

analogously to Eq. (2.4.1):

$$\widehat{\mathcal{P}}_{i,l} = \Big[1 - \prod_{k=1,l}(1-\hat{\sigma}_{kl})\Big] \ . \tag{2.6.1}$$

Then, we can write the *average number of A nucleus wounded partons* at fixed impact parameter by looking at two given parton configuration of the projectile and target nucleus, summing over each projectile nucleus multiplied by the probability $\widehat{\mathcal{P}}$ that it becomes wounded and finally summing over all the possible partonic configurations:

$$\boxed{\overline{N}_A(b) \ = \ \sum_{n=1,\infty}\frac{1}{n!}\sum_{i=1,n}\delta_1\cdots\delta_i\cdots\delta_n\sum_{l=1,\infty}\frac{1}{l!}\delta'_1\cdots\delta'_l\widehat{\mathcal{P}}_{i,l}\ \mathcal{Z}_A[J]\mathcal{Z}_B[J']\ _{|J=J'=0}} \tag{2.6.2}$$

This is the starting point for the computation of the average quantities we discuss in the next subsections.

2.6.1 Average number of wounded partons

Since the δ operators commute, we can perform the sum over s explicitly and rewrite this equation as follows:

$$\begin{aligned}
\overline{N}_A(b) \ &= \ \sum_{n=1,\infty} n\frac{1}{n!}\delta_2\cdots\delta_n \\
&\quad\times\delta_1\Big[\sum_{l=1,\infty}\frac{1}{l!}\delta'^l_\star - \sum_{l=1,\infty}\frac{1}{l!}\big[\delta'_\star\big(1-\hat{\sigma}_{\star\star}\big)\big]^l\Big]\mathcal{Z}_A[J]\mathcal{Z}_B[J']\ _{|J=J'=0} \\
&= \delta_\star e^{\,\delta}\Big[e^{\,\delta'_\star} - e^{\,\delta'_\star(1-\hat{\sigma}_{\star\star})}\Big]\mathcal{Z}_A[J]\mathcal{Z}_B[J']\ _{|J=J'=0} \\
&= \delta e^{\,\delta}\mathcal{Z}_A[J]\ _{|J=0}\times\Big[1-e^{\,-\delta'\hat{\sigma}_{11}}\Big]e^{\,\delta'}\mathcal{Z}_B[J']\ _{|J'=0} \ .
\end{aligned}$$

Finally we get the average number of A nucleus wounded partons:

$$\boxed{\overline{N}_A(b) = \ \delta\mathcal{Z}_A[J+1]\ _{|J=0}\times\Big[1-\mathcal{Z}[1-\hat{\sigma}]\Big] \ .} \tag{2.6.3}$$

The result is obtained under the only assumption that all the target partons are uncorrelated. Therefore, $\int db\, N_A(b)$ represents the integrated inclusive cross section to detect all scattered projectile partons, and takes into account the correlations of the projectile partons at all orders. From the explicit form for the generating functional $\mathcal{Z}$, Eqs. (2.3.2) and (2.3.6), and by the definition of the single-parton exclusive distribution function $\Gamma(u)$, Eq. (2.3.3), we have

$$\delta_1 e^{\,\delta}\mathcal{Z}_A[J]\ _{|J=0} = \delta_1\mathcal{Z}_A[J+1]\ _{|J=0} = \int du\Gamma_A(u-b) \ , \tag{2.6.4}$$

where the last term has to be read as an integral operator acting on the second term in Eq. (2.6.2). Note that multiparton correlations have dropped out of Eq. (2.6.4). It is then easy to obtain an explicit expression for the wounded partons:

$$\overline{N}_A(b) = \int du\Gamma_A(u-b)e^{-\int du'\sigma(u,u')\Gamma_B(u')+\frac{1}{2!}\int du'_1du'_2\sigma(u,u'_1)C^{(2)}_B(u'_1,u'_2)\sigma(u,u'_2)+\ldots} \ . \tag{2.6.5}$$

We can interpret the average number of A nucleus wounded partons, Eq. (2.6.5), as the integral over u of the average number of partons in the A nucleus, Γ_A, times the probability, $\widehat{\mathcal{P}}_{1B}$, that it a parton with coordinate u has at least one semihard scattering against the target nucleus:

$$\overline{N}_A(b) = \int du \Gamma_A(u-b) \widehat{\mathcal{P}}_{1B}(u) \ , \tag{2.6.6}$$

where

$$\widehat{\mathcal{P}}_{1B}(u) = 1 - \mathcal{Z}_B[J'+1-\hat{\sigma}] \ _{|J'=0} \tag{2.6.7}$$

It is interesting to interpret Eq. (2.6.7) in terms of multiple scattering probabilities. By using the identity

$$1 = \mathcal{Z}_B[J'+1] \ _{|J'=0} = e^{\,\delta'} \mathcal{Z}[J'] \ _{|J'=0} = \sum_{m=1,\infty} \frac{1}{m!} \delta'^m \mathcal{Z}[J'] \ _{|J'=0} \ ,$$

we can expand $\mathcal{Z}_B[J'+1-\hat{\sigma}]$ around $J'=0$, obtaining

$$\begin{aligned} \widehat{\mathcal{P}}_{1B}(u_1) &= \sum_{l=1,\infty} \frac{1}{l!} \delta'^l \left[1-(1-\hat{\sigma})^l\right] \mathcal{Z}[J'] \ _{|J'=0} \\ &= \sum_{l=1,\infty} \frac{1}{l!} \delta'^l \sum_{\nu=1,l} \binom{\nu}{l} \hat{\sigma}^\nu (1-\hat{\sigma})^{l-\nu} \mathcal{Z}[J'] \ _{|J'=0} \\ &= \sum_{\nu=1,\infty} \frac{1}{\nu!} \left[\delta'\hat{\sigma}\right]^\nu \times \sum_{l=\nu,\infty} \frac{1}{l!} \left[\delta'(1-\hat{\sigma})\right]^{l-\nu} \mathcal{Z}[J'] \ _{|J'=0} \ . \end{aligned} \tag{2.6.8}$$

In the above equation we used the fact that all the partons are of the same flavour to group together all the pairs that had a scattering and all those that did not. The technique to deal with an arbitrary number of flavours is discussed in Appendix 1 of Ref. [17]. The second line of Eq. (2.6.8) shows the expansion of the scattering probability $\widehat{\mathcal{P}}_{1B}$ in the number, ν, of semihard scatterings suffered by the projectile parton scattering on the B nucleus. Note also that probability conservation is explicitly taken into account for each given number $m \geq \nu$ of partons in the target. Indeed in the first term in the last line of Eq. (2.6.8) is the probability of having ν scatterings against ν target partons and the second one is the probability of no scattering against the remaining $l-\nu$ partons of the target. Loosely speaking, we will refer to this probability conservation as the unitarization of the average number of wounded partons, though it is actually a weaker result. Finally, we perform the sum over l explicitly and find the general expression for the probability of at least one semihard scattering, expanded in the number of scatterings, ν:

$$\boxed{\widehat{\mathcal{P}}_{1B}(u_1) = \sum_{\nu=1,\infty} \frac{1}{\nu!} \left[\delta'\hat{\sigma}\right]^\nu e^{-\delta'\hat{\sigma}} \ \mathcal{Z}[J'+1] \ _{|J'=0}} \tag{2.6.9}$$

The term $e^{-\delta'\hat{\sigma}}$, which we will call *absorption term*, represents therefore the probability that the projectile parton does not have any rescattering after the νth one, with no

restrictions on the total number of target partons. The above expression for the scattering probability $\widehat{\mathcal{P}}_{1B}$ could have been derived directly by expanding the exponential in the square brackets in the identity $1-\mathcal{Z}[1-\hat{\sigma}] = \left[1-e^{-\delta'_1\hat{\sigma}_{11}}\right]\mathcal{Z}_B[J'+1]\,|_{J'=0}$. However, in the former derivation the role of the absorption term in implementing probability conservation is fully explicit. An equivalent proof of Eq. (2.6.2) may be obtained by working out directly from Eq. (2.5.3) the average number of projectile partons which have undergone hard interactions [17, 19].

2.6.2 Average number of parton-parton collisions and of scatterings per parton

The average number of semihard parton-parton collisions is equal to the number of scatterings suffered by the wounded partons of one of the two colliding systems, the A nucleus in the following. Indeed, all the A nucleus wounded partons had at least one semihard scattering, and all semihard parton-parton scatterings involve one A nucleus parton, which therefore becomes wounded. Then, to count the average number of collisions we have to use Eq. (2.6.9) in Eq. (2.6.2) to obtain the expansion of the latter in the number of semihard scatterings, Eq. (2.6.9):

$$\begin{aligned}\overline{N}_A(b) &= \sum_{n=1,\infty}\frac{1}{n!}\sum_{s=1,n}\delta_1\cdots\delta_s\cdots\delta_n\times\sum_{\nu=1,\infty}\frac{1}{\nu!}\left[\delta'_\star\hat{\sigma}_{s\star}\right]^\nu e^{-\delta'_\star\hat{\sigma}_{s\star}}\;\mathcal{Z}_A[J]\mathcal{Z}_B[J'+1]\,|_{J=J'=0}\\ &= \delta\mathcal{Z}_A[J+1]\,|_{J=0}\;\times\sum_{\nu=1,\infty}\frac{1}{\nu!}\left[\delta'\hat{\sigma}\right]^\nu e^{-\delta'\hat{\sigma}}\;\mathcal{Z}_B[J'+1]\,|_{J'=0}\end{aligned}\tag{2.6.10}$$

To obtain the average umber of collisions we have to compute the average $\langle\nu\rangle$ by using the above probability measure:

$$\begin{aligned}\langle N_{coll}\rangle(b) &= \delta\mathcal{Z}_A[J+1]\,|_{J=0}\;\times\sum_{\nu=1,\infty}\nu\frac{1}{\nu!}\left[\delta'\hat{\sigma}\right]^\nu e^{-\delta'\hat{\sigma}}\;\mathcal{Z}_B[J'+1]\,|_{J'=0}\\ &= \delta\mathcal{Z}_A[J+1]\,|_{J=0}\times\hat{\sigma}\times\delta'\mathcal{Z}_B[J'+1]\,|_{J'=0}\end{aligned}$$

Finally, by using the identity (2.6.4) we get the general expression of the average number of parton-parton collisions:

$$\boxed{\langle N_{coll}\rangle(b) = \int dudu'\Gamma_A(u-b)\hat{\sigma}(u,u')\Gamma_B(u)}\,.\tag{2.6.11}$$

To obtain this result we did not have to make any restrictive assumption, hence Eq. (2.6.11) includes any possible multiparton correlations. The same result can be obtained by working with Eq. (2.5.3) instead of Eq. (2.6.2) [82]. Note that Eq. (2.6.11) expression multiplied by two coincides with the formula for the average number of minijets in the Eikonal approximation, Eq. (2.1.5). This is a correct statement when the transverse area occupied by the target partons is small, namely, when the parton-parton cross section is small (i.e., at large values of the cutoff) or at small and negative rapidities, where the flux of target partons is small. Indeed in these cases the incoming partons suffer at most one semihard scattering, and two minijets are produced in each collision: $\overline{N}_{mj}\approx 2\langle N_{coll}\rangle$. However, we

want to stress that when multiple parton scatterings are taken into account the correct interpretation of Eq. (2.6.11) is the average number of parton-parton collisions.

Finally, we compute the average number of semihard scatterings per A nucleus parton at fixed u. It can be obtained by dropping the integration over u in Eq. (2.6.11) and by dividing the result by the number of incoming A nucleus partons, $\Gamma_A(u-b)$:

$$\boxed{\langle N_{scatt}\rangle(b) \;=\; \int du' \hat{\sigma}(u,u')\Gamma_B(u)} \,. \tag{2.6.12}$$

We could have obtained this result also by working directly with the scattering probability $\widehat{\mathcal{P}}_{1B}$, Eq. (2.6.9). In Fig. 2.2 and 2.3 we plotted $\langle N_{scatt}\rangle$ as a function of the fractional momentum x, of the centrality of the collision and of the center of mass energy. In the case of a parton scattering against a nucleus the probability of having some rescatterings against a nucleus is sizeable both at RHIC and LHC.

2.6.3 Transverse spectrum of wounded partons

The average number of wounded partons is not the only observable which is modified by the introduction of semihard rescatterings in the dynamics. Indeed, also the transverse momentum distribution of minijets is affected in a non-trivial way [18]. The average number of wounded partons from the A nucleus is obtained by integrating the average number of incoming A partons multiplied by the probability of having at least one semihard scattering, see Eq. (2.6.6). To compute their transverse spectrum we have therefore to multiply the average number of incoming partons by the differential probability $d\widehat{\mathcal{P}}_{1B}/d^2p_t$ of having at least one semihard scattering and emerging from the target nucleus with a given transverse momentum p_t:

$$\overline{N}_A(b) = \int du \Gamma_A(u-b) \frac{d\widehat{\mathcal{P}}_{1B}}{d_t^p}(u) \,.$$

The differential probability may be obtained by introducing a constraint in the transverse momentum integrals that give the scattering probabilities, $\hat{\sigma}$, in the expansion of $\widehat{\mathcal{P}}_{1B}$ in the number of scatterings, Eq. (2.6.9):

$$\frac{d\widehat{\mathcal{P}}_{1B}}{d^2p_t}(u_1) \;=\; \int \sum_{\nu=1,\infty} \frac{1}{\nu!}\, \delta_1' \frac{d\hat{\sigma}_{11}}{d^2k_1} \cdots \delta_\nu' \frac{d\hat{\sigma}_{1\nu}}{d^2k_\nu} e^{-\delta_*'\hat{\sigma}_{1*}} \mathcal{Z}[J'+1] \;|_{J'=0} \tag{2.6.13}$$

$$\times\; \delta^{(2)}(\mathbf{k}_1 + \cdots + \mathbf{k}_\nu - \mathbf{p_t})\, d^2k_1 \ldots d^2k_\nu \; dx_1' \ldots dx_\nu' \,. \tag{2.6.14}$$

A convenient way to perform explicitly the sum over ν is to introduce the Fourier transform of the parton-parton scattering probability:

$$\tilde{\hat{\sigma}}(v) = \int d^2k e^{i\mathbf{k}\cdot\mathbf{v}} \frac{d\hat{\sigma}}{d^2k} \,.$$

and of the differential scattering probability:

$$\tilde{\widehat{\mathcal{P}}}_{1B}(v;u) \;=\; \int \frac{d^2p_t}{} e^{i\mathbf{p_t}\cdot\boldsymbol{v}} \frac{d\widehat{\mathcal{P}}_{1B}}{d^2p_t}(u) \,.$$

Note that $\hat{\tilde{\sigma}}(0) = \hat{\sigma}$and that due to the azimuthal symmetry of $d\sigma/d^2k$, its Fourier transform depends only on the modulus, v, of $\boldsymbol{v}$. Since all the convolutions in Eq. (2.6.14) turn into products after the Fourier transform we get:

$$\tilde{\widehat{\mathcal{P}}}_{1B}(v;u) \;=\; \sum_{\nu=1}^{\infty} \frac{1}{\nu!} \left[\delta' \hat{\tilde{\sigma}}(v)\right]^{\nu} \; e^{-\delta'\left(\hat{\tilde{\sigma}}(v)-\hat{\sigma}\right)} \mathcal{Z}_B[J'+1] \;_{|J'=0}$$

Finally we get the *Fourier transformed differential scattering probability*

$$\boxed{\tilde{\widehat{\mathcal{P}}}_{1B}(v;u) \;=\; \left[e^{\delta'\left(\hat{\tilde{\sigma}}(v)-\hat{\sigma}\right)} - e^{-\delta'\hat{\sigma}}\right] \mathcal{Z}_B[J'+1] \;_{|J'=0}} \,. \tag{2.6.15}$$

Then, the *transverse spectrum of the A nucleus wounded partons* is obtained by performing the Fourier transform back to p_t space and by folding the scattering probability with the average number of incoming projectile parton:

$$\boxed{\frac{d\widehat{\mathcal{P}}_{1B}}{d^2p_t}(u_1) \;=\; \int du\, \Gamma_A(u-b) \int \frac{d^2v}{(2\pi)^2}\, e^{-i\mathbf{p_t}\cdot\boldsymbol{v}} \tilde{\widehat{\mathcal{P}}}_{1B}(v;u)} \,. \tag{2.6.16}$$

Note that since $\hat{\tilde{\sigma}}(v)$ depends only on the modulus of v, the transverse spectrum depends only on the modulus of transverse momentum p_t. As a final remark, Eq. (2.6.16) is correct also when we integrate over a given interval of u in the hypotheses that the interval limits do not depend on p_t. The way of dealing with a p_t-dependent interval on the u integration is briefly discussed in Appendix A.3.

2.6.4 Average transverse energy

If we neglect the parton masses, the transverse energy carried by the A nucleus wounded partons is obtained by integrating the average number of incoming partons, $\Gamma_A(u)$, multiplied by the *average transverse momentum of a wounded parton*, $\langle p_t\rangle_B(u)$, where

$$\langle p_t\rangle_B(u) = \int d^2p_t |p_t| \frac{d\widehat{\mathcal{P}}_{1B}}{d^2p_t}(u) = \int d^2p_t |p_t| \int \frac{d^2v}{(2\pi)^2}\, e^{-i\mathbf{p_t}\cdot\boldsymbol{v}} \tilde{\widehat{\mathcal{P}}}_{1B}(v;u)$$

The way to proceed would be to exchange the two integrations, but to do this we need to introduce a *regularized average transverse momentum* depending on a positive parameter λ: $\langle p_t\rangle_{B|\lambda}(u) = \langle e^{-\lambda p_t} p_t\rangle_B(u)$, so that $\langle p_t\rangle_{B|\lambda}(u) \underrightarrow{\lambda\to 0} \langle p_t\rangle_B(u)$. Let's exchange the integrals in the regularized average transverse momentum and exploiting the azimuthal symmetry of the integrand with respect to both u and p_t:

$$\langle p_t\rangle_{B|\lambda} = \int_0^{\infty} dv\, v \int_0^{i} nfty dp_t p_t^2 J_0(p_t v) \tilde{\widehat{\mathcal{P}}}_{1B}(v) \;,$$

where J_0 is the Bessel function of order 0, and we omitted the dependence on the variable u for ease of notation. Since

$$\int_0^{\infty} dp_t p_t^2 J_0(p_t v) = \frac{1}{v}\frac{d}{dv}\left(\frac{v^2}{(v^2+\lambda^2)^{3/2}}\right)$$

we obtain

$$\langle p_t \rangle_{B|\lambda} = \int_0^\infty dv \, \frac{d}{dv} \left(\frac{v^2}{(v^2+\lambda^2)^{3/2}} \right) \widetilde{\widetilde{\mathcal{P}}}_{1B}(v) = \int_0^\infty dv \, \left(-\frac{v^2}{(v^2+\lambda^2)^{3/2}} \right) \frac{d}{dv} \widetilde{\widetilde{\mathcal{P}}}_{1B}(v) \; . \tag{2.6.17}$$

By Eq. (2.6.15) we have that

$$\frac{d}{dv} \widetilde{\widetilde{\mathcal{P}}}_{1B}(v) = \delta' \hat{\tilde{\sigma}}'(v) e^{\delta' \left(\hat{\tilde{\sigma}}(v) - \hat{\sigma} \right)} \mathcal{Z}_B[J'+1] \, \Big|_{J'=0} \; , \tag{2.6.18}$$

where

$$\hat{\tilde{\sigma}}'(v) = \frac{d}{dv} \hat{\tilde{\sigma}}(v) = -2\pi \int_0^\infty k^2 J_1(kv) \frac{d\hat{\sigma}}{d^2k} \, dk \; . \tag{2.6.19}$$

Note that $\hat{\tilde{\sigma}}'(v)$ is proportional to v because of the argument of the J_1 Bessel function. Therefore the integrand in Eq. (2.6.18) is an integrable function of v also in the limit $\lambda \to 0$. This would have not been the case if we did not introduce the regulator $\exp(-\lambda p_t$. Finally, after taking the limit $\lambda \to 0$ in Eq. (2.6.17) we obtain the average transverse momentum of a wounded parton:

$$\boxed{\langle p_t \rangle_B(u) = \int_0^\infty dv \, \left(-\frac{\delta' \hat{\tilde{\sigma}}'(v)}{v} \right) e^{\delta' \left(\hat{\tilde{\sigma}}(v) - \hat{\sigma} \right)} \mathcal{Z}_B[J'+1] \, \Big|_{J'=0}} \; , \tag{2.6.20}$$

and the *wounded parton average transverse energy*:

$$\boxed{\overline{E}_T(b) = \int du \, \Gamma_A(u-b) \, \langle p_t \rangle_B(u)} \; .$$

The same *caveat* about the integration limits on u discussed at the end of the last subsection is valid.

Chapter 3

Initial conditions in heavy-ion collisions

Semihard physics is one of the most important issues in the interaction of heavy ions at ultra-relativistic energies. Given the total energy involved and the large number of participants, the component of the inelastic interaction which can be described within a perturbative approach is in fact rather substantial at RHIC and might dominate at LHC [54, 89]. The result is the production of a large number of minijets in the typical inelastic event.

The usual perturbative approach takes into account only partonic *disconnected collisions*, namely independent parton-parton scatterings in different points in the plane transverse to the beam. As discussed in Sec. 2.2, at very high energies the partonic densities of the two interacting nuclei may become so large that also *rescatterings* of the same parton on different target partons may become non negligible. An attempt to introduce such more elaborate semihard dynamics, including explicitly semihard parton rescatterings in the interaction, was discussed in Chapter 2. Both the average number of minijets and the average transverse energy are modified by semihard rescatterings, and an interesting feature is that both quantities develop a less singular dependence on the cutoff, in such a way that the choice of p_0 becomes less critical when semihard parton rescatterings are taken into account. The average number of minijets and the transverse energy produced in heavy ion collisions have been recently discussed in several papers, with the purpose to determine the initial conditions for the further evolution and thermalization of the system (see e.g. [28, 31, 79]). We think that it might be interesting to have an indication of the effects of rescatterings on these quantities at LHC and RHIC, and we'll discuss this topic in the present chapter. In the next section, we will recall how to include rescatterings in the picture of the interaction and we will make an heuristic derivation of the average number of minijets and of their transverse energy. Then, we'll give some quantitative indication on the effect and comment the qualitative features induced by the more structured interaction dynamics.

3.1 Parton rescatterings: average number and transverse energy of minijets

The average number of minijets and their average transverse energy have been discussed in Sec. 2.6 in a very general framework, which includes parton correlations in the nuclei at all orders. As an illustration we will repeat those computations here in a more heuristic way. Moreover, we will neglect parton correlations to allow a more transparent interpretation of the results.

After neglecting parton correlations we are left, for each nucleus, with a Poisson multiparton distribution [Eq. (2.3.8)], which corresponds to the case where the information on the initial state is minimal, since the whole distribution is expressed in terms of its own average value only. The hard part is written in terms of two-body collisions by introducing the probability of having at least one interaction between the two configuration (Sec. 2.4). The process is therefore represented as the sum of all possible interactions between all configurations with a definite number of partons of the two nuclei, see Sec. 2.5. Referring to Eq. (2.5.3), the semihard component of the inelastic nucleus-nucleus cross section may, therefore, be written as

$$\begin{aligned}\sigma_H \;=\; & \int \sum_{n=1}^{\infty} \frac{1}{n!}\,\Gamma_A(x_1, b-r_1)\ldots\Gamma_A(x_n, b-r_n)\; e^{-\int dx d^2r\,\Gamma_A(x,b-r)}\,. \\ & \cdot \sum_{l=1}^{\infty} \frac{1}{l!}\,\Gamma_B(x'_1, r'_1)\ldots\Gamma_B(x'_l, r'_l)\; e^{-\int dx' d^2r' \Gamma_B(x',r')}\,. \\ & \cdot \left[1 - \prod_{i=1}^{n}\prod_{k=1}^{l}(1-\hat{\sigma}_{ik})\right] dx_1 d^2r_1 \ldots dx_n d^2r_n dx'_1 d^2r'_1 \ldots dx'_l d^2r'_l\;,\end{aligned} \tag{3.1.1}$$

where

$$\Gamma_A(x,b) = \tau_A(b) G(x)\;.$$

To keep the notation as simple as possible, the indices labeling the different kinds of partons have been suppressed and the dependence on the cutoff p_0 is implicit. The two Poissonian distributions, with average numbers $\Gamma_A(x, b-r)$ and $\Gamma_B(x', b')$, represent the multiparton distributions of the two interacting nuclei. The probability to have at least one partonic interaction, given a configuration with n and l partons in the two nuclei, is represented by the square parenthesis in Eq. (3.1.1) and is constructed by means of the probability $\hat{\sigma}_{ik}$ of interaction of a given pair of partons i and k, see Sec. 2.4. The interaction probability is a function of the cutoff p_0, so that only the interactions with momentum exchange larger than p_0 are taken into account in (3.1.1). The majority of interactions takes place with a momentum exchange close to the cutoff value, hence we evaluate the parton distributions at the scale of the cutoff. Since the distance over which the hard interactions are localized is much smaller than the typical nuclear radius, the probability of interaction can be approximated by

$$\hat{\sigma}(x_i x_k, b_i - b_k) = \sigma(x_i x_k; Q^2)\,\delta^{(2)}(b_i - b_k)\;,$$

where σ is the pQCD gluon-gluon cross section at leading order in the high energy limit:

$$\sigma(xx';Q^2) = k\,\frac{9}{2}\pi\alpha_s^2(Q^2)\frac{1}{p_0^2}\left(1-\frac{4p_0^2}{xx's}\right)\theta(xx's-4p_0^2)\theta(1-x)\theta(1-x')\ . \qquad (3.1.2)$$

In the above expression we included all the kinematic limits and p_0 is the cut-off that discriminates between soft and semihard interactions. We also included explicitly the k factor, k, to take into account higher order corrections. Both the cross section and the parton distributions depend on a scale Q, which we take proportional to the cutoff, and will understand in the following. The most important features of Eq. (3.1.1) are that all possible interactions between the two partonic configurations are included, and that probability conservation is explicitly taken into account by the term in square parentheses. The Eikonal cross section discusses in Sec. 2.1, which corresponds to the inclusion of disconnected collisions only, may be obtained by neglecting all rescatterings in Eq. (3.1.1), in such a way that each parton is allowed to interact at most once (Sec. 2.5.1):

$$\begin{aligned}\sigma_{mj}^{AA} &= \int d^2b\left(1-e^{-\int d^2r dx dx'\,\Gamma_A(x,b-r)\sigma(xx')\Gamma_B(x',r)}\right)\\ &= \sum_{n=1}^{\infty}\int d^2b\,\frac{\left(\int d^2r dx dx'\,\Gamma_A(x,b-r)\sigma(xx')\Gamma_B(x',r)\right)^n}{n!}\\ &\qquad\qquad \times e^{-\int d^r dx dx'\,\Gamma_A(x,b-r)\sigma(xx')\Gamma_B(x',r)}\ .\end{aligned} \qquad (3.1.3)$$

If, on the contrary, we keep rescatterings into account we cannot write a closed expression for σ_H. However, it is possible to obtain simple expressions from Eq. (3.1.1) for many relevant quantities, as shown in Sec. 2.6.

If we work out from Eq. (3.1.1) the average number of parton collisions $\langle N(b)\rangle$ we obtains, as in the traditional approach, the single scattering expression $\langle N(b)\rangle = \sigma_J T_{AB}(b)$, see Sec. 2.6.2. So, the overall average number of parton collisions satisfies the AGK cancellation and is not affected by any unitarity correction; however it is not a simple quantity to observe. A more directly observable quantity, or at least one which can be more directly related to observable quantities, is the average number of produced minijets. An important effect of including rescatterings is that the number of produced minijets is no more proportional to the number of collisions, because now each projectile parton is allowed to interact more than once with the target. As a consequence, while unitarity corrections do not change the average number of collisions, they affect the average number of minijets produced in the nuclear collision.

The correction term can be derived in a straightforward way from Eq. (3.1.1) (Sec. 2.6.1), but we may use also a more heuristic argument. One may in fact obtain the usual semihard cross section, Eq. (3.1.4), by starting from the single scattering cross section to produce large-p_t jets. In the perturbative QCD-parton model this cross section is written as:

$$\sigma_J = \int_{xx's>4p_0} d^2b\,d^2r\,dx\,dx'\,\Gamma_A(x,b-r)\,\sigma(xx')\,\Gamma_B(x',r) = \int d^2b\,\langle N(b)\rangle\ . \qquad (3.1.4)$$

The expression needs however to be unitarized also when the cutoff p_0 has a rather large value, since σ_J is proportional to the large factor $A\times B$. The Eikonal minijet cross

section (3.1.4) is obtained by performing the s-channel unitarization of σ_J. It may also be obtained by noticing that in Eq. (3.1.4) $\langle N(b)\rangle$ is dimensionless and may be understood as the average number of parton interactions at a given impact parameter b. The s-channel unitarized cross section σ_H is the result of replacing this average number with the interaction probability, which, if the distribution in the number of interactions is a Poissonian, is just $1-\exp(-\langle N(b)\rangle)$. Hence the unitarized cross section σ_H represents the contribution to the total cross section of all events with at least one couple of partons interacting with a transverse momentum exchange above p_0, as it is clear from the second line of Eq. (3.1.4). On the other hand σ_J, that includes also the multiplicity of the interactions, represents rather the integrated inclusive cross section (apart from the factor representing the average multiplicity of jets produced in a single collision).
When the cutoff is moved toward low values and rescatterings need to be taken into account, the average number of jets produced is no more proportional to the average number of collisions. In this case one may proceed by applying to $\langle N(b)\rangle$ an argument analogous to that previously used to unitarize σ_J. By looking at Eq. (3.1.4) one can identify

$$\langle n_B(x,b)\rangle \equiv \int_{xx's>4p_0^2} dx'\,\Gamma_B(x',b)\,\sigma(xx') \tag{3.1.5}$$

as the average number of collisions of each interacting A-parton at fixed x and b. Then one can write the average number of produced minijets at fixed impact parameter as

$$2\langle N(b)\rangle = \int_{xs>4p_0^2} d^2r dx \Gamma_A(x,b-r)\,\langle n_B(x,b)\rangle + \int_{x's>4p_0^2} d^2b dx' \Gamma_B(x',r)\,\langle n_A(x',b-r)\rangle\ ,$$

that represents the average number of incoming partons from the nucleus A multiplied by the average number of collisions against the partons of nucleus B, plus the analogous term with A and B interchanged. Then, if one replaces in Eq. (3.1.6) the average number of scatterings of each parton with its interaction probability, viz. $1-\exp(\langle n_B(x,r)\rangle)$ and $1-\exp(\langle n_A(x,b-r)\rangle)$, one obtains the average number of "wounded partons" of the two nuclei, which can be identified with the average number of minijets $N_A^{mj}(x,r)$ and $N_B^{mj}(x',b-r)$, as discussed in Sec. 2.6.1. These ones are the partons of the two nuclei that had at least one hard interaction. The expression for the average number of wounded partons of nucleus A (with transverse coordinate r and momentum fraction x, in an event with nuclear impact parameter b) is therefore

$$N_A^{mj}(x,r,b) = \Gamma_A(x,b-r)\Big[1-\ \mathrm{e}^{-\langle n_B(x,r)\rangle}\Big]\ . \tag{3.1.7}$$

Every wounded parton obtained in this way produces a minijet in the final state and the transverse energy produced by semihard interactions is the transverse energy carried by the wounded partons. As a consequence both the average number of minijets and their average transverse energy are quantities affected by the presence of rescatterings and the corresponding correction term is more and more important when the average number of scatterings $\langle n_B\rangle$ becomes larger and larger, namely at low values of the cutoff p_0 and (or) for large atomic mass numbers. The overall number of produced minijets, i.e. the sum of the wounded partons of nucleus A with those of nucleus B, obviously coincides with

the usual result $2\langle N(b)\rangle$, when the average number of rescatterings is small. When the number of rescatterings is large the two quantities are however different and, while the average number of collisions $\langle N(b)\rangle$ may be divergent in the saturation limit, the average number of wounded partons is on the contrary well defined. In fact one obtains that the square parenthesis in Eq. (3.1.7) has 1 as a limiting value and, in this limit, the average number of wounded partons is just the sum of the average number of partons of the two interacting nuclei.

To have a quantitative feeling for the regime of interest at RHIC and LHC energies we may look at Fig. 2.2, where we plotted $\langle n_B\rangle$, the average number of scatterings per parton from the A-nucleus, as a function of the projectile parton fractional momentum x and impact parameter b. As one can see, at a cut-off $p_0 = 2$ GeV a parton in the central region experiences on average 1 to 3 scatterings over the whole target transverse area except the very peripheral regions. As discussed above, at higher cut-off values the number of scatterings decreases. As a result, semihard rescatterings should be negligible down to $p_0 \simeq 3$ GeV where their effects begin to show up, and already at $p_0 = 2$ GeV they should have a large effect and should not be neglected. At RHIC energies rescatterings begin to play a role at $p_0 \lesssim 2$ GeV and should have large effects at $p_0 \lesssim 1$ GeV, at the edge of the applicability of perturbative computations. These conclusions will be confirmed by the numerical computations discussed in section 3.2.

The average number of minijets is not the only quantity modified by this more elaborate interaction dynamics, which in fact has a non-trivial effect also on the transverse energy carried by the minijets [18]. The wounded partons of nucleus A at a given x and b and in a nuclear interaction with impact parameter b, Eq. (3.1.7) are obtained by multiplying the average number of partons of A (with given x and b) by the corresponding interaction probability, which is a Poisson probability distribution in the number of scatterings, with average $\langle n_B(x,b)\rangle = \int dx' \Gamma_B(x',b)\sigma(xx')$:

$$N_A^{mj}(x,r,b) = \Gamma_A(x,b-r)\sum_{\nu=1}^{\infty}\frac{\langle n_B(x,r)\rangle}{\nu!}\,\mathrm{e}^{-\langle n_B(x,r)\rangle}\ . \tag{3.1.8}$$

We may therefore obtain the differential distribution in the transverse momentum p_t of the wounded A partons by introducing a constraint in the transverse momentum integrals which give the total cross sections in the above expression:

$$\begin{aligned}\frac{dN_A^{mj}}{d^2p_t}(x,r,b) \ &= \\ &= \ \Gamma_A(x,r-b)\sum_{\nu=1}^{\infty}\frac{1}{\nu!}\int \Gamma_B(x_1',r)\ldots\Gamma_B(x_\nu',r)\,\mathrm{e}^{-\int dx'\Gamma_B(x',r)\sigma(xx')}\ \cdot \\ &\quad \cdot\frac{d\sigma}{d^2k_1}\ldots\frac{d\sigma}{d^2k_\nu}\,\delta^{(2)}(\mathbf{k}_1+\cdots+\mathbf{k}_\nu-\mathbf{p_t})\,d^2k_1\ldots d^2k_\nu\,dx_1'\ldots dx_\nu'\ .\end{aligned} \tag{3.1.9}$$

The limits of integration on x_i' and x' are respectively $xx_i's \geq 4k_i^2$ and $xx's \geq 4p_0^2$, and all the distribution functions are evaluated for simplicity at a fixed scale. To obtain the corresponding average transverse energy $\langle p_t(x,r,b)\rangle_A$ one has to integrate Eq. (3.1.9) with an additional factor p_t. This computation has been carried out on general grounds in Sec. 2.6.4. When considering Poissonian multiparton nuclear distributions the result,

Eq. (2.6.20), reads:

$$\frac{dE_T}{dx}(b) = \int d^2r \int_0^\infty dv\, \Gamma_A(x, b-r) \left(\int dx' \frac{-\tilde{\sigma}'(v; xx')}{v} \Gamma_B(x', r) \right) \times e^{\int dx' \Gamma_B(x', r)[\tilde{\sigma}(v; xx') - \tilde{\sigma}(0; xx')]} , \tag{3.1.10}$$

where

$$\tilde{\sigma}(v; xx') = \int d^2k e^{ik\cdot\mathbf{v}} \frac{d\sigma}{d^2p_t}(xx') \quad ; \quad \tilde{\sigma}(0; xx') = \sigma(xx') \tag{3.1.11}$$

is the Fourier transform of the differential parton-parton cross section $d\sigma(xx')/d^2k = 9/2\,\alpha_s^2\; 1/k^4\,\theta(k^2 - p_0^2)\theta(xx's - 4k^2)\theta(1-x)\theta(1-x')$, and

$$\tilde{\sigma}'(v; xx') = -2\pi \int_0^\infty k^2 J_1(kv) \frac{d\sigma}{d^2k}(xx')\, dk , \tag{3.1.12}$$

which is proportional to v because of the argument of the J_1 Bessel function. The average transverse energy in an event with a given impact parameter b is the result of integrating Eq. (3.1.10) on b and x and of summing the two contributions of the wounded partons of the nuclei A and B. Note that the expression in Eq. (3.1.10) is much less dependent on the choice of the cutoff p_0 than the usual average energy evaluated with the single scattering expression for the perturbative QCD parton model: the Rutherford singularity of the parton-parton cross section is in fact smoothed in Eq. (3.1.12) by the Bessel function $J_1(ku)$, in such a way that the dependence on the cutoff p_0 is only logarithmic. The same logarithmic dependence on the cutoff is present in the argument of the exponential

$$\tilde{\sigma}(u) - \tilde{\sigma}(0) = 2\pi \int \Big[J_0(ku) - 1 \Big] \frac{d\sigma}{d^2k}\, k\, dk \tag{3.1.13}$$

as a consequence of the behavior of $\big[J_0(ku) - 1\big]$ for $k \to 0$.

In summary, the effect of rescatterings on the average number of the produced minijets is to reduce the number obtained by means of the single scattering expression, not differently, qualitatively, from the result of including shadowing corrections in the nuclear parton distribution. On the other hand the overall distribution in the number of minijets produced is modified. In the traditional approach there is a strong correlation in the distribution of the number of minijets, since each minijet has a recoiling companion; when the average number of rescatterings increases this correlation gets weaker and weaker, so that in the high density limit no correlation is left and the minijet distribution tends to a Poissonian [17]. A further important difference is that, since W_A and W_B are well defined in this limit, after including rescatterings the average number of minijets becomes much less dependent on the choice of the cutoff at low p_0. Moreover, we may obtain without further approximations a closed analytical form also for the minijet average transverse energy, whose dependence on p_0 for small values of the cutoff is smoothened by the rescatterings.

3.2 Numerical results and discussion

Many papers have been recently devoted to the production of minijets in heavy ion collisions [28, 33, 54, 79, 92] (see also the introduction to Chapter 4). A rather general feature

of the perturbative approaches is that, because of the singular behavior of the elementary parton interaction at low momentum transfer, many relevant quantities depend rather strongly (typically like an inverse power) on the value of the cutoff which distinguishes soft and hard parton interactions (see Ref. [26] for an approach where this problem is absent). This feature is unpleasant since although one might find physical arguments to determine a meaningful value of the cutoff [30, 33, 43, 79], it is rather difficult to fix it in a very precise way. We have therefore tried, in this chapter, to face this issue by studying the effect of a more elaborate interaction dynamics on the average number of minijets produced in a nuclear collision and on the corresponding average transverse energy. While in the traditional picture of the semihard processes each parton is allowed to interact with large momentum transfer only once, we have included semihard parton rescatterings in the dynamics of the interaction. Semihard rescatterings, that are negligible when the threshold between hard and soft processes is high, become more and more important when the threshold is lowered and the target approaches the black disk limit. Naively one would expect that the inclusion of rescatterings in the picture of the interaction might worsen the divergent behavior at low transverse momenta; on the contrary a more careful analysis, that takes probability conservation consistently into account, shows that the result is just the opposite. Following Refs. [17] and [18] we have in fact represented the semihard nuclear cross section with Eq. (3.1.1), where all possible multiparton collisions, including rescatterings, are taken into account and the conservation of probability is explicitly implemented. The average number of minijets and the corresponding transverse energy, at fixed x, b and impact parameter b, are then expressed in a closed analytical form by (3.1.7) and (3.1.10), whose behavior with the cutoff is much less singular in comparison with the analogous averages obtained without taking rescatterings into account. The reason of this smoother behavior is that rescatterings introduce (through Γ_A and Γ_B) a new dimensional quantity in (3.1.7) and (3.1.10), the nuclear radius, which gives the dimensionality to the two average quantities at small p_0. When rescatterings are neglected the dimensionality at small p_0 is provided by the cutoff itself, and the result is that the two quantities behave as an inverse power of the cutoff for $p_0 \to 0$.

Apart from the approximation of writing all connected multiparton processes as products of $2 \to 2$ partonic collisions, our approach states on the assumption of neglecting production processes at the partonic level (namely $2 \to 3$ etc. parton processes) and of using forward kinematics in the nucleon-nucleon c.m. frame. To have a feeling on the validity of such approximations at LHC energy, we have evaluated the average energy of a partonic interaction in the parton-parton center of mass frame, and the average value of momentum fraction x of a projectile parton:

$$\begin{aligned} \langle E_{c.m.} \rangle \sigma_J &= \int dx dx' \sqrt{xx's} \sum_{ff'} G_A^f(x) \sigma^{ff'}(xx') G_B^{f'}(x') \\ \langle x \rangle \sigma_J &= \int dx dx' x \sum_{ff'} G_A^f(x) \sigma^{ff'}(xx') G_B^{f'}(x') \end{aligned} \tag{3.2.1}$$

When the whole rapidity range is considered typical values are $\langle E_{c.m.} \rangle \approx 25$ GeV, $\langle x \rangle \approx 3 \times 10^{-2}$ (corresponding to a momentum of ≈ 45 GeV, if the nucleon-nucleon c.m. energy is 6TeV) with $p_0 = 2$ GeV. The average $\langle x \rangle$ becomes substantially smaller when averaging in a narrow window in the central rapidity region. The relatively low value of $\langle E_{c.m.} \rangle$,

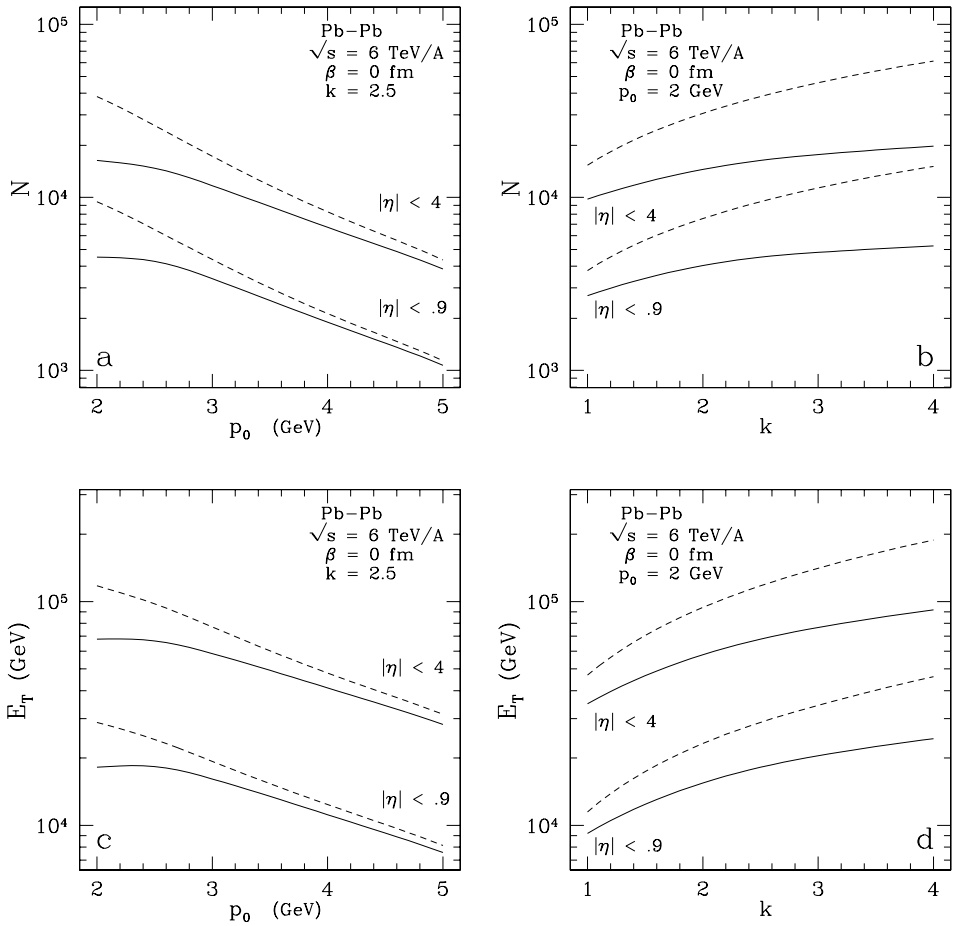

Figure 3.1: Average number N of minijets, a) b), and average transverse energy E_T, c) d), in a Pb-Pb central collision in two different rapidity windows, $|y| < 4$ and $|y| < .9$, as a function of the cutoff, a) and c), and of the k factor, b) and d). The dashed curves are computed without including rescatterings, the continuous curves after including rescatterings.

as compared with the cutoff, indicates that the inclusion of $2 \to 3$, or of higher order partonic processes, should not spoil the whole approach, that could therefore represent a reasonable lowest order approximation. The relatively large value of the momentum boost to go from the nucleon-nucleon c.m. frame to the partonic c.m. frame shows, on the other hand, that forward kinematics is reasonable in the former frame of reference.

The effect of semihard parton rescatterings on the average number of minijets and on the average transverse energy produced in a central Pb-Pb collision at LHC energies is summarized in Fig.3.1. We plotted the average number of minijets and their transverse energy in the case of a very central rapidity window, $|y| < .9$, corresponding to the ALICE detector, and in a larger rapidity interval, $|y| < 4$, that will be covered by the CMS detector. Figure 3.1a) shows, in the two cases, the dependence of the average number of produced minijets on the choice of the cutoff p_0. The dashed curves are the results obtained by the single scattering expression, Eq. (3.1.4), while the continuous curves are the result of the inclusion of semihard parton rescatterings, Eq. (3.1.7) plus

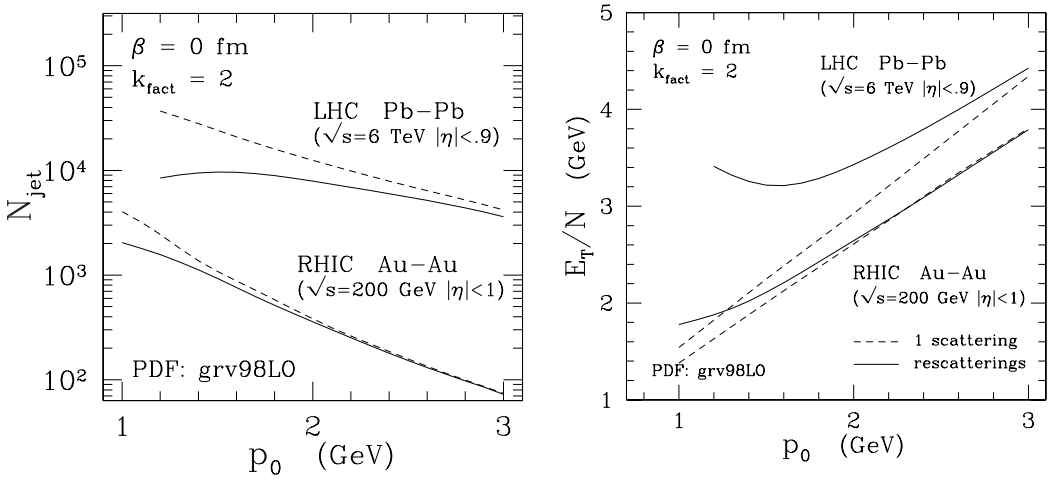

Figure 3.2: *Left:* average number of minijets at RHIC and LHC energies. *Right:* transverse energy per minijet.

the analogous term for the B partons. These expressions have been computed with the GRV98LO distribution functions [135] with no shadowing corrections included, and by representing the elementary partonic interaction at the lowest order in QCD; to account for higher order corrections the result of the elementary interaction has been multiplied by a factor $k = 2.5$. Both the k factor and the scale $Q = p_0/2$ where chosen in order to reproduce the value of the $p\bar{p}$ mini-jet cross section at $\sqrt{s} = 900$ GeV [107][1]. The sensitivity to the value of the k factor is shown in Fig. 3.1*b*), where the curves have the same meaning as in Fig. 3.1*a*), and the cutoff has been fixed to the value $p_0 = 2$ GeV. Analogous curves for the average transverse energy carried by the produced minijets are shown in Fig. 3.1*c*) and 3.1*d*). The average transverse energy without rescatterings has been computed by using Eq. (2.1.6) (dashed curves) and with rescatterings (continuous curves) by using Eq. (3.1.10), after integrating on b and on x (inside the corresponding rapidity windows) and adding the analogous contribution of the B partons.

The inclusion of rescatterings in the interaction dynamics results in a large reduction of the minijet multiplicity and transverse energy at low cutoff compared to the predictions of the Eikonal approach, which neglects rescatterings. At low cutoff both quantities show a plateau at $p_0 \lesssim 2$ GeV and a greatly reduced dependence on the k factor. The effects of rescatterings at RHIC and LHC energies are compared in the left panel of Fig. 3.2, where we plotted the minijet multiplicity as a function of the cutoff note the different choice of Q and k. The same qualitative behaviour is found at the different energies, the plateau at a slightly smaller cutoff, $p_0 \lesssim 1$ GeV, at RHIC. In the right panel of Fig. 3.2 we plotted the *transverse energy per minijet* $\varepsilon_T = E_T/N$. The usual perturbative expectations, based on the Eikonal model results, Eqs. (2.1.5) and (2.1.6), would predict $\varepsilon_T \propto p_0$. Conversely, rescatterings cause ε_T to stabilize at low cutoff around $\varepsilon_T = 3$ GeV at LHC and $\varepsilon_T = 2$ GeV at RHIC. This effect takes place in the same cutoff range where the plateau in the minijet multiplicity develops.

[1] An alternative choice is $Q = p_0$ and $k = 2$. This one is to be preferred at RHIC energies, where the typical p_0 may be estimated to be around 1 GeV

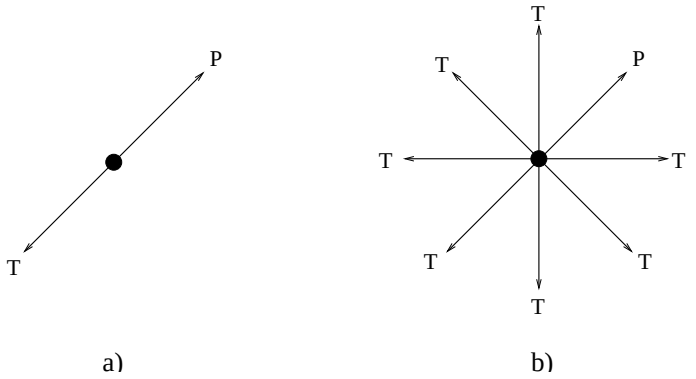

Figure 3.3: Production of minijets in the transverse momentum plane. a) The projectile parton (P) is allowed to interact only once with a target parton (T), so that the two produced minijets are back-to-back. b) The projectile can scatter against more than one target and minijets are produced with a star-shape.

3.3 Conclusions

In this chapter we have discussed the production of minijets in heavy ion collisions at the LHC, by including explicitly semihard parton rescatterings in the dynamics of the interaction. The regime of interest is, in fact, the regime where the nuclear target reaches the black disk limit for a projectile parton interacting with momentum exchange above the cutoff p_0 (which defines the lower limit in p_t for minijet production). In the mechanism of production of minijets usually considered (a projectile parton interacts with only a single target parton) the elementary interaction generates a state with a preferred direction in transverse space (the direction of the two minijets) which is not consistent with local symmetry in the transverse directions implied by the black disk limit. The star-like shape in transverse space of the state produced by the multiple interactions of a projectile with different target partons (scattered projectile + recoils) recovers, on the other hand, the symmetry property of the interaction in the black disk limit, see Fig.3.3.

The basic element in our estimate is to recognize that the usual expression that gives the average number $\langle N(b)\rangle$ of parton collisions at a fixed value of the nuclear impact parameter, Eq. (3.1.4), is obtained by convoluting the average number of partons of the projectile with the average number $\langle n_B(x,b)\rangle$ of interactions of each projectile parton with the target nucleus, Eq. (3.1.5). Note that the evaluation of $\langle n_B(x,b)\rangle$ and its dependence on the momentum fraction is, in this way, determined in a unique way by the parton distributions. Our results are therefore parameter free. Given the expression for the semihard cross section, Eq. (3.1.1), the average number of produced minijets $W(x,r,b)$, Eq. (3.1.7), and the corresponding average transverse energy $\langle p_t(x,r,b)\rangle$, Eq. (3.1.10), are computed without further approximations, so that our result for N and E_T, plotted in the figures, are exact consequences of the nuclear cross section (3.1.1). An approximation that is done when writing the nuclear cross section (3.1.1), is to evaluate the parton distributions at the scale of the cutoff, so that in Eq. (3.1.9) the only dependence on the transverse momenta is in the elementary partonic cross sections, which basically corresponds to neglecting the logarithmic dependence of the distributions in comparison with the inverse power dependence of the cross section. However, our formalism can be extended to take into account a general scale dependence.

The main features of the numerical evaluation are that semihard rescatterings have a sizable effect on the average number of minijets and on the transverse energy produced in heavy ion collisions at the LHC, so that they affect also global characteristics of the

typical inelastic event. The induced correction increases with the value of the k factor, which represents higher orders in the elementary parton collision, and with the size of the rapidity window, since rescatterings are more frequent for partons with a larger momentum fraction. By looking at the dependence on the cutoff, both the average number of minijets and the corresponding average transverse energy are more regular at low p_0, showing a tendency to saturate below $p_0 \simeq 3$ GeV at LHC and below $p_0 \simeq 2$ GeV at RHIC. In this way rescatterings make the choice of the cutoff less critical and suggests a way to fix it to a physically meaningful value, as we will discuss in Chapter 4.

Chapter 4

Parton saturation

In heavy-ion collisions the partonic degrees of freedom of the two interacting nuclei become more and more important as the center of mass energy of the collision increases. At some point the main particle production mechanism in the initial stage becomes the liberation from the nuclear wave functions of a great number of partons, also called *minijet plasma*. At ultra-relativistic energies the partonic density of the two nuclei is so high that perturbative methods on one hand [13, 33, 35, 36, 38, 43, 55, 77, 92] and semi-classical nonperturbative methods on the other [60, 61, 73, 74, 76] become applicable to the computation of the initial conditions of the minijet plasma. It's successive evolution will possibly lead to thermalization of the system and to the transition to the quark-gluon plasma phase, whose formation and characteristics depend crucially on such initial conditions. Though the latter are not directly accessible experimentally, they can be related to final state observables, like the charged particle multiplicity and transverse energy, allowing a test of the proposed theoretical models.

We can divide in general the models in five classes: *(i)* "two-component models" [60, 92], in which particle production is assumed to be decomposable into the sum of a soft and a hard part according to some cutoff p_0; *(ii)* "saturation models" [13, 33, 35, 36, 38, 60, 61], which exploit the high parton densities involved in the process; *(iii)* "Monte Carlo models" [51, 53], in which the whole nuclear collision is simulated at the computer; *iv)* various kinds of "string models" [24]; *v)* "hydrodynamic models" [62]. To distinguish between them, it has been proposed in [92] to study the centrality dependence of the charged particle multiplicity, since this allows to disentangle to some degree the dynamical and the geometrical effects. The study of this observable should be moreover supplemented by a combined study of the energy and rapidity dependence of the charged multiplicity. A review of the results of the above models on the charged multiplicity and of experimental results may be found in [37, 45].

In Sec. 4.1-4.2 we provide a brief introduction to saturation models. In Sec. 4.3 we propose a new one based on the introduction of rescatterings in the collision dynamics and on the results on initial conditions obtained in Chapter 3. In Sec. 4.4 we compare the results of the various models and in Sec. 4.5 we draw our conclusions.

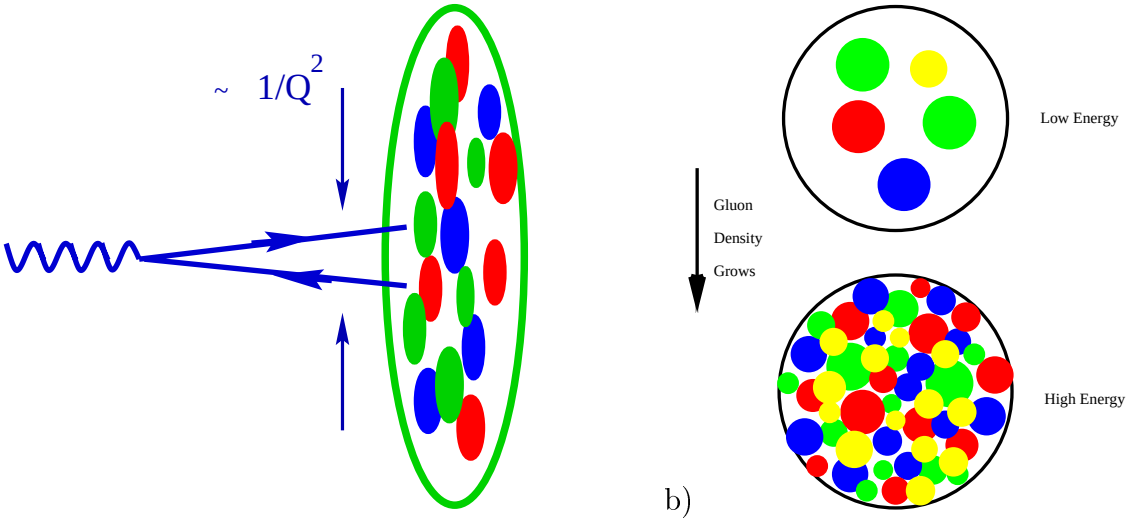

Figure 4.1: *a)* A hard probe interacting with a nuclear target resolves the transverse area proportional to $1/Q^2$ and in the target rest frame a longitudinal distance proportional to $1/mx$. b) Transverse view of the target. As the energy of the collision increases, the typical x probed by the interaction decreases as $x \sim 2Q/\sqrt{s}$, hence the parton density increases. Figures taken from Refs. [61, 73]

4.1 Initial state saturation

The idea of initial state parton saturation [13, 43, 77] states that in some regimes the partons in the initial state hadron or nuclear wave function become so numerous that they begin to interact with each other and a further growth of their density is unlikely.

Consider an external probe interacting with a target nucleus of atomic number A [58]. For definiteness we can think of a virtual photon in a deep inelastic scattering on a nucleus (see Fig. 4.1a), or to a projectile parton in a proton-nucleus scattering. When the probe interacts with nuclear partons of a given Bjorken x, in the target rest frame the interaction develops, by uncertainty principle, over longitudinal distances $z \sim 1/(Mx)$, where M is the mass of a nucleon. At small x values z becomes comparable to the nuclear size and the probe cannot distinguish between nucleons on the front side of the nucleus and those on the back side. Therefore it interacts coherently with all the partons located in a transverse area $\sim 1/Q^2$, where Q is the momentum transfer squared. At this point an increase in the parton density does not affect the interaction of the probe since the coherence means that the probe sees all the partons as one. In the infinite momentum frame, where the partons are well defined physical objects, the picture changes. The typical x at a probe rapidity $y = 0$ is $x \approx 2Q/\sqrt{s}$; since the parton distributions increase for decreasing x, the target looks denser to the probe as the energy of the collision increases or as the scale of the interaction decreases, see Fig. 4.1b.

Let's estimate the highest parton density at which the probe can resolve the partons individually. The probe interacts with a cross section $\sigma \propto \alpha_s(Q^2)/Q^2$ [43], which determines its transverse area. The parton density in the transverse plane is given by

$$\rho_A = \frac{dN_A}{dyd^2r} \approx \frac{xG_A(x,Q^2)}{\pi R_A^2} \propto A^{1/3} \ ,$$

where $R_A \approx (1.12fm)A^{1/3}$ is the nuclear radius, $G_A(x,Q^2) = \int d^2r\, \Gamma_A(x,r,Q^2) = AG(x,Q^2)$, and Γ_A is the nuclear parton distribution function defined in Eq. (2.2.1). Therefore, depending on the momentum transfer, the atomic number and the value of Bjorken x, we may have two regimes:

- $\sigma\rho_A \ll 1$: this is the "dilute" regime of incoherent interactions where pQCD methods apply;
- $\sigma\rho_A \gg 1$: in this regime the probe sees a high parton density. The usual pQCD description in terms of "leading twist", but also the expansion in higher twists, becomes inadequate. Non linear QCD effects become important.

The border between the two regimes is given by $\sigma\rho_A \approx 1$. This condition determines the critical value of the momentum transfer at which the partons in the target begin to look dense to the probe. We call this momentum transfer the *saturation scale*:

$$Q_s^2 \approx \alpha_s(Q_s^2)\frac{xG_A(x,Q_s^2)}{\pi R_A^2} \propto A^{1/3} \ . \tag{4.1.1}$$

At the saturation scale the number of gluons is therefore

$$N_A^{sat} = xG_A(x,Q_s^2) \approx \frac{\pi}{\alpha_s(Q_s^2)}Q_s^2R_A^2 \propto A \ .$$

Note that the saturation scale increases with energy (because of the small-x increase of the parton distribution function G) and the atomic number of the target. Moreover, the number of gluons is proportional to the inverse of α_s. Various estimates give $Q_s \approx 1-2$ GeV at RHIC energies and a slightly higher value at LHC. Hence in heavy-ion collision we may reach a saturation regime characterized by weak coupling and high parton densities. We may thus treat this regime in terms of parton saturation with suitably generalized perturbative methods or in terms of colour fields in semi-classical QCD, as we will discuss in the following.

The partons in the initial state wave functions are then freed in a high energy collision mainly by parton-parton scatterings in the small-x and small Q region. Therefore, if these values are inside the saturation region, the saturated multiplicity N_s determines the multiplicity of produced gluons.

4.1.1 Semi-classical QCD

Equation (4.1.1) may be obtained heuristically in a way that justifies the use of semi-classical QCD in the high-density regime [58]. The first step is to take the QCD Lagrangian density $\mathcal{L} = -1/4G^a_{\mu\nu}G^a_{\mu\nu} + \sum_f \bar{q}^a_f\left(i\not{D} - m_f\right)q^a_f$. Then we rescale the vector fields and the field strength as follows: $\tilde{A}^a_\mu = gA^a_\mu$, and $\tilde{G}^a_{\mu\nu} = gG^a_{\mu\nu} = \partial_\mu\tilde{A}^a_\nu - \partial_\nu\tilde{A}^a_\mu + f^{abc}\tilde{A}^b_\mu\tilde{A}^c_\nu$. In terms of the new field, the only dependence of the action on g is in the pure Yang-Mills term,

$$S \propto \int \frac{1}{g}\tilde{G}^a_{\mu\nu}\tilde{G}^a_{\mu\nu} \ . \tag{4.1.2}$$

Now, we consider a classical configuration of gluon fields, which we think to be associated to a nucleus having a high-energy interaction. Then, by definition, $\tilde{G}^a_{\mu\nu}$ is independent

of g and the action is large, $S \gg \hbar$. The number of quanta (i.e. of gluons) in such a configuration is given by

$$N_g \approx \frac{S}{\hbar} \propto \frac{1}{\alpha_s}\rho_4 V_4 \ , \tag{4.1.3}$$

where ρ_4 is the average action density and V_4 the space-time volume in which the quanta are contained. Non-linear effects will come into play when the field is such that $\partial_\mu \tilde{A}_\mu \approx \tilde{A}_\mu \tilde{A}_\mu$. Solving this equality in momentum space and using it in Eq. (4.1.2) we get:

$$Q_s^2 \approx \tilde{A}^2 \approx (\tilde{G})^2 = \sqrt{\rho_4} \ . \tag{4.1.4}$$

Next, we need an estimate of the space-time volume occupied by the gluons. Their transverse area they occupy is πR_A^2. By uncertainty principle, gluons interacting at a scale Q_s are extended in the longitudinal and proper time directions by $\approx 1/Q_s$. Then, the space-time volume occupied by the gluons which are participating in the interaction is $V_4 \approx \pi R_A^2/Q_s^2$. Thus, by combining Eqs. (4.1.3) and (4.1.4) we get

$$Q_s^4 \approx \rho_4 \approx \alpha_s \frac{N_g}{V_4} \approx \alpha_s^2 n_g Q_s^2 \ ,$$

where $n_g = \frac{N_g}{\pi R_A^2}$ is the gluon density in the transverse plane. If we identify $N_g = xG_A(x, Q_s^2)$ the above equation coincides with the saturation condition Eq. (4.1.1).

The above heuristic derivation says that the physics of the high-density regime may be potentially understood in terms of classical gluon fields. This observation is at the core of the semi-classical McLerran-Venugopalan model [73, 74]. By the more sophisticated methods described in those papers it is possible to derive also the proportionality factor [76] (see [75] for a shorter discussion):

$$Q_s^2 = \frac{8\pi N_c}{N_c^2 - 1}\alpha_s(Q_s^2) n_g(x, r; Q_s) \ , \tag{4.1.5}$$

where $n_g(x, r; Q_s) = \Gamma_A(x, r; Q_s)$ is the transverse plane density of gluons at a given x and r is the transverse coordinate. Note that in general $Q_s = Q_s(x, r)$.

4.1.2 Perturbative QCD

Given the relatively high value for the saturation scale ($Q_s^2 \approx 1$ GeV at RHIC and $Q_s^2 \gtrsim 2$ GeV at LHC), we expect that the high parton density regime may be described also by perturbative methods. A hard scattering with momentum transfer Q probes the nucleus at a distance of order Q^{-1}. At very small scales a nucleus is made predominantly of gluons. As one goes to still smaller scales the gluon density increases because a gluon may be actually made of two gluons of a smaller size. This process is described in pQCD in terms of *parton splitting* processes and leads to the Dokshitzer-Gribov-Lipatov-Altarelli-Parisi (DGLAP) equation for the evolution in x of the parton distribution functions [25]. As the gluon density increases we may expect that also the opposite process, *parton recombination*, will take place. Parton recombination is a process in which two gluons combine to form a single one, which lowers the gluon multiplicity. Its rate is proportional

to the parton density, indeed the higher the density the larger the probability for two partons to be close enough in phase space to fuse. Hence, we expect that when lowering the scale an equilibrium between splitting and recombination will be reached, after which the parton density stops increasing. We call *saturation scale* the scale at which this equilibrium is reached.

In pQCD the interplay of parton splitting and recombination is described by a higher twist modification of the DGLAP equation [77]:

$$Q^2\frac{\partial}{\partial Q^2}x\Gamma_A(x,r;Q^2) = \bar{\alpha}_s\int_x^1\frac{dx'}{x'}\,x'\Gamma_A(x',b;Q^2) - \bar{\alpha}_s\frac{\pi^3}{2Q^2}\int_x^1\frac{dx'}{x'}\,x'^2D_A^{(2)}(x',r;x',r;Q^2) \tag{4.1.6}$$

where $\bar{\alpha}_s = \alpha_s(Q^2)N_c/\pi$ and N_c is the number of colours. Here, we consider only gluons, as they dominate parton production in ultra-relativistic collisions. The first term on the right hand side is the gluon splitting term, which is proportional to $\Gamma_A(x,r;p_t^2)$, the one-gluon inclusive distribution at a given fractional momentum x, transverse coordinate r and scale $Q^2 = p_t^2$. The gluon recombination term comes with an opposite sign and is proportional to the inclusive distribution of two gluons, $D_A^{(2)}$, computed at the same x, b and Q^2 for both gluons. If we neglect parton correlations inside the nucleus we have

$$x^2D_A^{(2)}(x,r;x,r;Q^2) = \left[x\Gamma_A(x,r;Q^2)\right]^2 \ , \tag{4.1.7}$$

as discussed in Sec. 2.3. Following Ref. [13], we expect that gluon recombination will become comparable to gluon splitting when gluons begin to overlap in the transverse plane, i.e. when the scale is such that $x\Gamma_A(x,Q^2) \sim const`times Q^2R^2$. In other words the saturation scale is determined by:

$$Q^2\frac{\partial}{\partial Q^2}x\Gamma_A(x,r;Q^2) = x\Gamma_A(x,r;Q^2) \ . \tag{4.1.8}$$

At lower scales the gluon density stops increasing and at higher values it becomes too small for gluon recombination. Therefore we define the saturation scale Q_s as the largest Q that satisfies Eq. (4.1.8). Note that $Q_s = Q_s(x,r)$ depends on x. Since the gluon distribution increases at small x, the saturation scale is slowly increasing function of the fractional momentum. Eq. (4.1.8) is difficult to be used in (4.1.6), therefore we will use a weaker saturation condition:

$$x\frac{\partial}{\partial x}Q^2\frac{\partial}{\partial Q^2}x\Gamma_A(x,r;Q^2) = 0 \ . \tag{4.1.9}$$

This equation follows from Eq. (4.1.8) if we assume that in the saturation region $Q^2 \leq Q_s^2$ the gluon distribution is independent of x. This is a reasonable assumption. Indeed, starting at a given x and at a scale $Q \lesssim Q_s(x)$ (at fixed r), if we decrease x the saturation scale increases and we remain in the saturation region. Conversely, by increasing x of a small amount the saturation scale decreases a little bit, and if the variation of the fractional momentum is not too high we still remain in the saturation region. Therefore, in both cases the gluon distribution stays approximately constant. By combining Eqs. (4.1.6) and Eq. (4.1.7) with the saturation condition Eq. (4.1.9) we get:

$$0 = \bar{\alpha}_s x\Gamma(x,r;Q^2) - \bar{\alpha}_s\,\frac{\pi^3}{2Q^2}\left[x\Gamma_A(x',r;Q^2)\right]^2 \ .$$

Solving for Q^2 we finally get the saturation scale:

$$Q_s^2 = \frac{\pi N_c}{2}\alpha_s(Q_s^2)\Gamma_A(x,r;Q_s^2) \ . \tag{4.1.10}$$

We can see that the saturation scale obtained in pQCD, Eq. (4.1.10), and with semi-classical methods, Eq. (4.1.5), differ only by some group theoretical factors, which however differ only by factors of order one.

4.1.3 Charged particle multiplicity in high-density QCD

Let us discuss an application of the picture of parton saturation in the initial state to the computation of charged particle distributions [60, 61]. First, we observe that the saturation scale depends on the centrality of the collision. Indeed, Q_s depends on n_g, the density in the transverse plane of the gluons which participate in the collision. In a central collision all the gluons of the nucleus participate, but in a peripheral collision only those which are inside the overlap area of the two colliding nuclei. In a first approximation we may take n_g to be proportional to the density of nucleons which participate in the collision, and if we consider for simplicity a scattering of two equal nuclei we get

$$n_g(x,r,b;Q_s^2) = xG(x,Q_s^2) \times \frac{\rho_{part}(r,b)}{2}\text{‘},$$

where $\rho_{part}(b)$ is the density of participant nucleons, and b is the impact parameter. In the Glauber model we may express the density of participants in an equal nuclei scattering as follows (see Sec. 1.3.1):

$$\frac{\rho_{part}(b)}{2} = \int d^2r\, \tau_A(b-r)\left[1 - e^{-\sigma_{in}(\sqrt{s})\tau_A(r)}\right] \ .$$

Here $\tau_A(r)$ is the nuclear thickness function at a transverse coordinate r and $\sigma_{in}(\sqrt{s})$ the pp inelastic cross section computed at the nucleon-nucleon center of mass energy $\sqrt{s}$ of the nuclear collision. The saturation scale is given by Eq. (4.1.5):

$$Q_s^2 = \frac{8\pi N_c}{N_c^2-1}\alpha_s(Q_s^2)n_g(x_s,r,b;Q_s) \ , \tag{4.1.11}$$

where we evaluated the gluon distribution at the typical Bjorken x of the collision, $x_s = 2Q_s/\sqrt{s}$. The saturation scale may thus be determined by solving iteratively Eq. (4.1.11). For a central collision of two gold nuclei it is found to be $Q_s = 2$ GeV, where $x_sG(x_s,Q_s^2) \simeq 2$ at $x_s \simeq 0.02$ with $\alpha_s(Q_s) \simeq 0.6$.

To compute the number of produced gluons we use a formula derived in Ref. [75, 76] for the number of produced gluons at the saturation scale:

$$\frac{dN_g}{d^2r d\eta} = c\,\frac{N_c^2-1}{4\pi N_c}\frac{1}{\alpha_s(Q_s^2)}\,Q_s^2 \ , \tag{4.1.12}$$

where c is called *parton liberation coefficient*, and accounts for the transformation of virtual partons into on-shell partons caused by the interaction. It is expected to be of

	$\sqrt{s} = 130$ GeV		$\sqrt{s} = 200$ GeV		$\sqrt{s} = 6$ TeV	
b (fm)	N_{part}	Q_s^2	N_{part}	Q_s^2	N_{part}	Q_s^2
0	378	2.05	380	2.33	387	6.47
1	372	2.04	374	2.32	382	6.44
2	354	2.02	356	2.30	368	6.38
3	325	1.98	327	2.25	343	6.25
4	290	1.92	292	2.18	310	6.06
5	251	1.84	253	2.09	271	5.81
6	210	1.74	212	1.98	230	5.49
7	169	1.61	171	1.83	188	5.08
8	130	1.46	132	1.66	148	4.61
9	94.3	1.26	95.7	1.43	110	3.98
10	62.7	1.04	64.0	1.18	76.1	3.28
11	37.5	0.77	38.7	0.88	47.7	2.43

Table 4.1: The number of participants computed in the Glauber model and the saturation scale Q_s at RHIC and LHC energies. At 130 GeV Q_s is determined by solving Eq. (4.1.11) iteratively and is taken from Ref. [60], while at different energies we used the scaling relation (4.1.14).

order one. Putting together Eqs. (4.1.11) and (4.1.12) and integrating over the transverse coordinates r, we get

$$\frac{dN_g}{d\eta} = c\, N_{part}(b)\, x_s G(x_s, Q_s^2) \ .$$

If we assume local parton-hadron duality [85], we may take the charged particle density to be proportional to the density of produced gluons: $dN^{ch}/d\eta = 2/3\, dN_g/d\eta$. With suitable hypotheses on the behaviour of the parton distribution function it is possible to write an analytical formula for charged particle multiplicity valid at all energies [61]. For central pseudorapidities, which is the case we will discuss in this chapter, we have:

$$\frac{1}{N_{part}/2}\ |_{\eta=0} \frac{dN^{ch}}{d\eta} = \bar{c}\, \left(\frac{s}{s_0}\right)^{\frac{\lambda}{2}} \ln\left(\frac{Q_s^2(b,s)}{\Lambda_{QCD}^2}\right) \ , \tag{4.1.13}$$

where $\bar{c}$ is a constant which has to be extracted from the experimental data at some reference energy $\sqrt{s_0}$, as we discuss below. The logarithm in Eq. (4.1.13) is due to the following *ansatz* for the gluon distribution at $Q^2 \sim 1$, which is based on the DGLAP evolution equation [25]:

$$xG(x;Q^2) \propto \log\left(\frac{Q^2}{\Lambda_{QCD}^2}\right) \ .$$

However, at very low Q^2 perturbative computations of parton distribution functions acquire theoretical errors of nearly 100% and this ansatz may be questionable [45]. The saturation scale at energies different from the reference one may be computed from the scaling relation [42]

$$Q_s^2(b,s) = Q_s^2(b,s_0)\left(\frac{s}{s_0}\right)^{\frac{\lambda}{2}} \ . \tag{4.1.14}$$

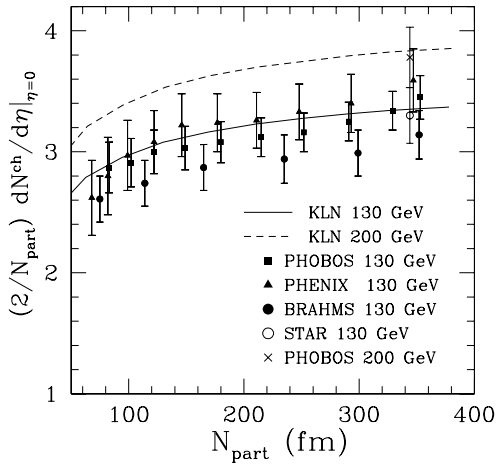

Figure 4.2: Centrality dependence of the charged multiplicity density per participant pair at zero pseudorapidity. The curves show the prediction of the high-density QCD computation by Kharzeev-Levin-Nardi [60, 61] described in the text. Data are taken from [99, 102, 112, 113, 116].

The exponent λ describes the small-x rise of the gluon distribution function and may be determined in deep-inelastic scattering experiments. The HERA data are fitted with $\lambda \approx 0.25 - 0.3$, and $\lambda = 0.25$ is used in Eq. (4.1.13) by the authors of Ref. [61]. In that paper the approach is extended also to arbitrary pseudorapidity.

To determine $\bar{c}$ we use the RHIC data on the charged multiplicity at $\sqrt{s}_0 = 130$ GeV. The combined value [113] of the charged particle density per participant pair from the four RHIC experiments [99, 102, 111–113, 116] is $(2/N_{part})dN^{ch}/d\eta|_{\eta=0} = 3.37 \pm 0.12$. By using $Q_s^2 = 2.05$ GeV^2 at $b = 0$ from Table 4.1 and $\Lambda_{QCD} = 200$ MeV we get[1]

$$\bar{c} = 0.856 \pm 0.060$$

corresponding to a parton liberation coefficient

$$c = 1.28 \pm 0.09 \ .$$

This value compares well with a lattice computation [67] which gives $0.75 < c < 1.20$, and an analytical computation which gives $c = 2 \ln 2 \simeq 1.39$ [66].

In Fig. 4.2 we show the centrality dependence of the charged multiplicity density per participant pair at zero pseudorapidity. The curves are obtained by inserting in Eq. (4.1.13) the computed values of N_{part} at $\sqrt{s} = 130$ and 200 GeV and of Q_s at $\sqrt{s_0} = 130$ GeV from Table 4.1. We can see that data are very well described by the high-density QCD prediction. We also checked that using $\lambda = 0.3$ instead of $\lambda = 0.25$ practically does not change the results. The multiplicity at LHC energy shows a slight increase in the slope, which doesn't depend on λ, but its absolute normalization depends strongly on that parameter (see Fig. 4.13).

4.2 Final state saturation

In heavy-ion collisions at ultrarelativistic energies the average number of minijets produced with $p_T > p_0$ in a given rapidity window, Δy, may be obtained, in a first approxi-

[1] to account for the various approximations introduced, the quoted error on $\bar{c}$ is the double of what one would get from Eq. (4.1.13).

mation, by the Eikonal model discussed in Sec. 2.1:

$$N^{mj}(b, p_0, \Delta y) = 2\, T_{AA}(b)\, \sigma_H(p_0, \Delta y)$$

where $T_{AA}(b) = \int d^2r\, \tau_A(r-b)\tau_A(r)$ is the nuclear overlap function; σ_H is the cross section for minijet production in a rapidity window Δy in proton-proton collisions and is computed with an infrared cutoff p_0. The approach is well suited for large values of p_0, where the nuclei are dilute and the minijet multiplicity is low. However, since roughly $N^{mj} \propto T_{AA}(b)/p_0^2$, when lowering the cutoff p_0 the number of produced partons (mainly gluons) increases rapidly. If sufficiently many partons are produced inside Δy, they begin to overpopulate the available transverse area, which is of the order of the geometrical nuclear overlap area. In this highly dense system of partons final-state fusion processes among them may become important [43]. These processes may therefore lead to a screening of additional parton production, and below some *saturation cutoff* p_{sat} no further growth in the multiplicity is expected. This discussion may be formulated quantitatively in two ways: *(i)* by a *global saturation criterion* (the "EKRT model"), which depends only on the impact parameter of the collision, and *(ii)* by a *local saturation criterion* (the "ℓEKRT model"), which deals with the transverse plane density of produced minijets. We will discuss them in turn in the next two subsections and then we will apply them to the computation of charged particle densities.

4.2.1 Global criterion

Let us assign to the produced partons a transverse area a_T which by uncertainty principle may be taken inversely proportional to their typical momentum transfer: $a_T \sim \pi/p_0^2$. Then the average transverse area occupied by the minijets will be $\mathcal{A}_T^{mj}(b) \sim N^{mj}(b)\, a_T$. At some scale p_{sat} the minijet transverse area becomes comparable to the nuclear overlap area $\mathcal{A}_T(b)$ then the minijets start overlapping transversely. Therefore, we may expect saturation in their production to set in when $\mathcal{A}_T^{mj}(b) \gtrsim \mathcal{A}_T(b)$, i.e., when

$$N^{mj}(b; p_0, \Delta y) = T_{AA}(b) 2\sigma(p_0) = \gamma\, \frac{p_0^2}{\pi}\, \mathcal{A}_T(b)\ . \tag{4.2.1}$$

The factor γ is included to account for the fact that saturation of the transverse area is only an approximate criterion. γ may be also a function of α_s, as in initial state saturation and we expect it to be of order one. Since it may be rescaled inside the k factor by $k \to k' = k/\gamma$, in the following we will set $\gamma = 1$ for simplicity. The cutoff p_0 which solves Eq. (4.2.1) defines the *global saturation cutoff* p_{sat}. The *globally saturated minijet multiplicity* is then obtained by computing N^{mj} at such cutoff:

$$N_{sat}^{mj}(b, \Delta y) = N^{mj}(b; p_{sat}, \Delta y) = p_{sat}^2 \mathcal{A}_T/\pi\ .$$

This computation is depicted in Fig. 4.3 for central Pb-Pb collisions and $\Delta y = [-0.5, 0.5]$.

In this section we are interested in the minijet rapidity density at $y = 0$. Since the rapidity distribution of minijets is nearly flat in the central rapidity region we will always use $\Delta y = [-0.5, 0.5]$ without writing it explicitly, and we may take $dN^{mj}/d\eta|_{y=0} \approx N^{mj}(\Delta y)$. The saturation cutoff and the saturated minijet multiplicity computed by using the global saturation criterion for central collisions may be expressed in terms of

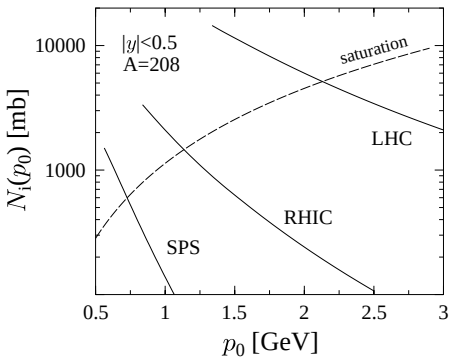

Figure 4.3: Graphical solution of the final state saturation condition (4.2.1) for central Pb-Pb collisions. The l.h.s. is represented by the solid lines, which show the minijet multiplicities in a rapidity window $-0.5 < y < 0.5$ at $\sqrt{s} = 17, 200, 5500\,\mathrm{GeV}$ as a function of the cutoff. The r.h.s. is represented by the solid the dashed line. The intercept of the solid and dashed lines gives the saturation cutoff at a given c.m. energy on the x axis, and the saturated minijet multiplicity on the y axis. Figure taken from [33].

scaling functions of the form $a\,A^c\,\sqrt{s}^{\,d}$. In central collisions, with shadowing included by the EKS98 parameterization [133], the saturation cutoff and the saturated minijet multiplicity are [33, 36]:

$$\begin{aligned} p_{sat} &= 0.208 A^{0.128} \sqrt{s}^{0.191} \\ N_{sat}^{mj} &= 1.383 A^{0.922} \sqrt{s}^{0.383} \quad . \end{aligned} \tag{4.2.2}$$

When shadowing is not included the result is [38]

$$\begin{aligned} p_{sat} &= 0.193 A^{0.137} \sqrt{s}^{0.204} \\ N_{sat}^{mj} &= 1.20 A^{0.941} \sqrt{s}^{0.408} \quad . \end{aligned} \tag{4.2.3}$$

The above numerical results have been obtained by using Woods-Saxon thickness functions and GRV94 [134] distribution functions. Note that in this computations there are no free parameters except the k factor, which however has been fixed to $k = 2$ according to Ref. [34].

The origin of the scaling exponents in Eqs. (4.2.2) and (4.2.3) may be understood by using some approximation on the parton distribution functions such that we can perform the computations analytically [35]. In that paper quarks are neglected and the computations are carried out for gluons only, since they are the main responsible of the scaling exponents. Quarks contribute partially to the absolute normalizations, which are not dealt with in detail. Moreover, shadowing is not included in the computations. The gluon distribution function may be approximated in the relevant range by a power law:

$$x G(x, Q^2) \approx C_0 \left(\frac{Q}{x} \right)^{\delta} \quad ,$$

where $C_0 = 0.32$ and $\delta = 0.5$ fit the behaviour of the GRV94LO parton distribution function [134]. In particular the exponent δ describes the small-x rise of the gluon distribution in the proton (with CTEQ5 parton distributions $C_0 = 0.29$ and $\delta = 0.47$). Shadowing is not included in the computations. Then, it is possible to show that They show that the proton-proton cross section at leading order may be approximated by

$$\sigma(p_0) = c\,\frac{k}{p_0^{2+2\xi}} \left[x_0 G(x_0, p_0^2) \right]^2 = c\,\frac{K}{p_0^{2+2\xi}} \left[C_0 \left(\frac{\sqrt{s}}{2} \right)^{\delta} \right]^2 \quad ,$$

where c is a complicated constant which we are not interested in, $x_0 = 2p_0/\sqrt{s}$, and $\xi = 0.444$ describes the effects of the running coupling constant in the relevant kinematic range. Next, if we use a hard-sphere nuclear geometry the transverse area is simply $\mathcal{A}_T(b=0) = \pi R_A^2$ and the overlap function is $T_{AA}(b=0) = A^2/\pi R_A^2$ (in central collisions using hard-sphere or Woods-Saxon distributions does not change too much the result). Using these values in the saturation criterion (4.2.1) the following scaling law is obtained for the case in which shadowing is not included [35]:

$$\begin{aligned} p_{sat} &\approx 0.163\, k^{\frac{1}{4+2\xi}} A^{\frac{1}{6+3\xi}} \sqrt{s}^{\frac{\delta}{2+\xi}} \\ N_{sat}^{mj} &\approx 0.850\, k^{\frac{1}{2+\xi}} A^{\frac{6+2\xi}{6+3\xi}} \sqrt{s}^{\frac{2\delta}{2+\xi}} \ . \end{aligned} \tag{4.2.4}$$

Note that the dependence on the k factor is rather weak: $N_{sat}^{mj} \propto k^{0.41}$ instead of $\propto k$, as expected from pQCD without saturation. Substituting $k = 2$ and the values of δ and ξ defined above we get:

$$\begin{aligned} p_{sat} &\approx 0.187\, A^{0.136} \sqrt{s}^{0.204} \\ N_{sat}^{mj} &\approx 1.130\, A^{0.939} \sqrt{s}^{0.409} \ , \end{aligned} \tag{4.2.5}$$

which compares very well with the numerical result (4.2.3).

4.2.2 Local criterion

The saturation criterion (4.2.1) requires that at the saturation scale the produced quanta, which have a transverse area $\sim \pi/p_{sat}^2$ fill completely the nuclear overlap area. This criterion does not distinguish, however, between quanta produced by a parton colliding centrally on the target, for which there is a high probability of scattering, or peripherally, in which case the probability is lower. Therefore, the transverse density of produced partons may vary a lot in the transverse plane, and saturation may be reached at different scales in different transverse positions. The global saturation criterion (4.2.1) is easy to generalize to a local one which depends on the transverse coordinate r as well as on the impact parameter b [35]. Eq. (4.2.1) may, indeed, be rewritten as follows:

$$\int d^2r\, \frac{dN^{mj}}{d^2r}(p_0, b, r) = 2\, \sigma(p_0) \int d^2r\, \tau_A(b-r)\tau_A(r) = \frac{p_0^2}{\pi} \int_{r^2<R_A^2} d^2r \ .$$

By dropping the integrations over the transverse coordinate r we obtain the local saturation criterion:

$$\frac{dN^{mj}}{d^2r}(p_0, b, r) = 2\, \tau_A(b-r)\tau_A(r)\, \sigma(p_0) \approx \frac{p_0^2}{\pi} \ . \tag{4.2.6}$$

Solving this equation for p_0 we obtain the *local saturation cutoff* $p_{sat} = p_{sat}(b, r)$. Then by integrating over r Eq. (4.2.6) computed at the saturation cutoff we obtain the *locally saturated minijet multiplicity*: $N_{sat}^{mj}(b) = \int d^2r\, p_{sat}^2(b, r)/\pi$. An important problem arises, i.e., how to deal with values of r located in the periphery of one or the other nucleus. Indeed, at such values of r the nuclear density of at least one of the two nuclei is very low. To obtain saturation we need, therefore, a very small value of $p_{sat}(b, r)$, which could

become comparable to Λ_{QCD}, thereby barring the use of the perturbative approach. One way out is to stop requiring final state saturation in a suitably defined peripheral region. In [35] the peripheral region is defined as the region in the transverse plane such that $p_{sat}(b,r) < p_{lim} = 0.5$ GeV, and it is checked that changing the limit to 0.7 GeV makes only a 4% contribution to the minijet multiplicity at $b = 0$. We call *interaction area* the region in the transverse plane such that $p_{sat}(b,r) \leq p_{lim}$ GeV. Obviously, the relative importance of one or another choice for p_{lim} increases for more peripheral interactions, since the interaction area decreases. Hence, at large enough b we expect this approach to be no longer valid. The locally saturated minijet multiplicity is finally defined by integrating the minijet density over the interaction area[2]. The techniques described in the last section may be used to derive an analytical formula for the local criterion [35]. The result without shadowing corrections is:

$$\begin{aligned} p^2_{sat}(b,r) &\propto \sqrt{s}^{0.409} \left[\tau_A(b-r)\tau_A(r)\right]^{0.204} \\ N^{mj}_{sat}(b) &= \frac{1}{\pi}\int d^2r\, p^2_{sat}(b,r)\,\theta\left(p^2_{sat}(b,r) - p^2_{lim}\right) , \end{aligned} \tag{4.2.7}$$

where integration over the transverse area is limited to the interaction area defined by the theta function. Note that $\tau_A(b-r)\tau_A(r)$ is first exponentiated and then integrated over the transverse plane. In the global saturation criterion the order of the two operations is opposite. This causes the locally saturated multiplicity to be slightly smaller than the global one and determines a different b dependence in the two cases.

4.2.3 Centrality and charged particle multiplicity

The multiplicity of partons produced at $p_T \geq p_0$ is assumed to saturate below $p_0 = p_{sat}$ due to final state parton-parton fusion processes, where p_{sat} may be estimated by the final state saturation criteria discussed above. Although in parton-parton fusions the transverse energy is not screened due to energy conservation, we may argue that also the transverse energy produced in the collision may be estimated as the energy of the saturated minijets. Indeed, as we have seen, the saturation scale at RHIC and LHC is small, $p_{sat} \sim 1-2$ GeV. Therefore, partons produced at $p_T < p_{sat}$, though numerous, carry little transverse energy and we may use $p_0 = p_{sat}$ in the perturbative computation of the transverse minijet energy as a reasonable lower bound on the effective transverse energy produced in the collision. Transverse energy saturation may also be understood perturbatively by the generation of a small transverse mass for low-p_t parton moving in a medium made of higher-p_t partons due to colour screening effects [30]. However, the relation between the two approaches has yet to be studied in detail.

For these reasons in the final state saturation model charged particle multiplicity and transverse energy are assumed to be entirely computable from pQCD supplemented by final state saturation [33]. To convert the number of initially produced minijets to final state charged particles we assume local parton-hadron duality [85], according to which we may roughly expect 2 charged particles every 3 minijets. Using hydrodynamics

[2]To obtain smooth minijet densities in the transverse plane, which is required to use these computation as the initial state in hydrodynamics, the cutoff in the periphery is set equal to its limiting value of 0.5 GeV and no cut on r is used [62].

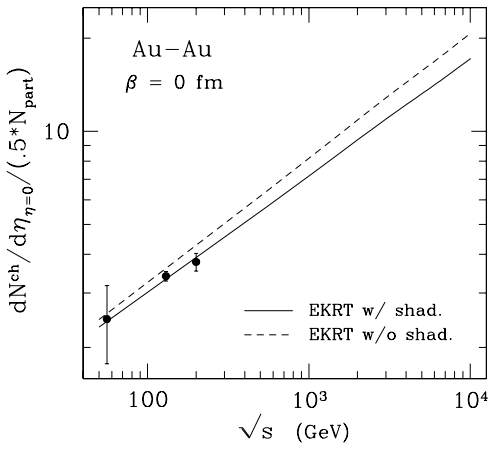

Figure 4.4: Charged particle multiplicity per participant pair in a central Au-Au collision as a function of the center of mass energy of the collision. Shown are the EKRT saturation model predictions with nuclear shadowing (solid line) and without (dashed line).

to describe the evolution of the minijet plasma, it is found that when including also resonance decays in the hadronization process the factor 2/3 is effectively reduced to 0.6 [36]. Moreover, charged multiplicities are divided by the number of participant nucleon pairs to mark out any deviation from the simple expectation of the wounded nucleon model $dN^{ch}/dy \propto N_{part}$. Finally, experiments quote their results in terms of pseudorapidity instead of rapidity. In the central rapidity region the Jacobian of the transformation from y to η may be approximated by a factor 0.9. The observable which we are interested in is, therefore, the *charged particle multiplicity per participant pair*:

$$\frac{2}{N_{part}(b)}\frac{dN^{ch}}{dy}\Big|_{y=0} = 0.54 * \frac{2}{N_{part}(b)}\frac{dN^{mj}_{sat}}{dy}\Big|_{y=0} .$$

In Fig. 4.4 we compare the results of the final state saturation picture with RHIC data for central Au-Au collisions at $\sqrt{s} = 56, 130, 200$ GeV, and extrapolate the computation up to LHC energies. A very good agreement with the data is obtained without the help of any adjustable parameter (the k factor was chosen to be $k = 2$ according to Ref. [34]). Using the local saturation criterion should not change too much the results, since the dependence on $\sqrt{s}$ is the same than with the global criterion, and the absolute normalization turns out numerically to be quite the same at $b = 0$ (see Ref. [35]).

Global saturation and centrality

To extend the results of Eq. (4.2.2) to arbitrary centrality, Gyulassy and Wang have proposed in Ref. [92] to approximate the two nuclei at non-zero impact parameter by two nuclei colliding centrally but with a b-dependent atomic number $A^{eff}(b) = N_{part}(b)/2$, proportional to the average number of nucleons from each nucleus which participate in the collision. The "EKRT(GW)" model is then obtained by using $A^{eff}(b)$ instead of A in Eq. (4.2.2). The result is a charged multiplicity per participant pair which decreases as a function of N_{part} and is almost ruled out by the data at $\sqrt{s} = 130$ GeV (see Fig. 4.7).

This approximation, however, suffers from two drawbacks. First, as noted in Ref. [80], a nucleus with atomic number $A^{eff}(b)$ has an *effective* transverse area

$$\mathcal{A}_T^{eff}(b) \approx \pi R^2_{A^{eff}(b)} = \pi r_0^2 \left(A^{eff}\right)^{2/3} , \qquad (4.2.8)$$

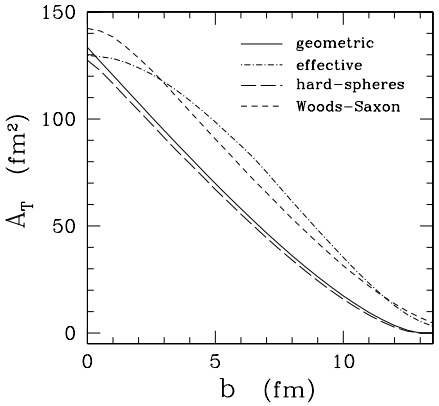

Figure 4.5: The various estimates of the interaction area: the effective area (4.2.8), the geometric area (4.2.9) and the Glauber-type area (4.2.10) with hard-sphere and Woods-Saxon nuclear thickness functions.

where $r_0 = 1.12$ fm is the proton radius. By the approximation introduced above, $\mathcal{A}_T^{eff}(b)$ represents also the overlap area of the two original nuclei at a given b. On the other hand, if we assume a hard-sphere thickness function, the overlap area may be approximated by the geometrical overlap in transverse space of two spheres of radius R_A:

$$\mathcal{A}_T(b) \approx \mathcal{A}_T^{geom}(b) = 2\left[R_A^2 \arccos\left(\frac{b}{2R_A}\right) - \frac{b}{2}\sqrt{R_A^2 - \frac{b^2}{4}}\right] . \tag{4.2.9}$$

In general, as we argued in Sec. 1.3.1, the transverse area may be obtained by the following Glauber model inspired formula:

$$\mathcal{A}_T(b) = \int d^2r \left[1 - e^{-\sigma_{in}\tau_A(b-r)}\right]\left[1 - e^{-\sigma_{in}\tau_A(r)}\right] , \tag{4.2.10}$$

where σ_{in} is the inelastic pp cross section. In this formula the area is defined by weighting the area element d^2r by the probability that at least one nucleon from each nucleus has an interaction at that transverse coordinate. As we can see from Fig. 4.5, the effective area overestimates the overlap area over all the impact parameter range, except in central and very peripheral collisions. When using Woods-Saxon thickness functions in Eq. (4.2.10) we get a slightly larger area in central collisions which however decreases faster than $\mathcal{A}_T^{eff}$ as a function of b. Therefore, by using $\mathcal{A}_T^{eff}$ at $b \neq 0$ in the saturation criterion (4.2.1) we are asking the minijets to saturate a bigger area than the actual overlap area, resulting in a higher multiplicity. Therefore, we expect that a better treatment of the overlap area in the saturation criterion should increase the slope of the minijet multiplicity. As shown in Ref. [80] this is indeed the case.

The second problem is that the A dependence in Eqs. (4.2.2)-(4.2.3) comes from two different sources: the transverse area on the right-hand side of (4.2.1) and the nuclear thickness functions in T_{AA} on the left-hand side. Therefore one should replace A with $A^{eff}(b)$ only on the right-hand side.

To treat correctly T_{AA} and the transverse area we make use of the analytical approximations described in Sec. 4.2.1. Instead of fixing $b = 0$ as done in Sec. 4.2.1 and using the values of the transverse area and of the overlap function at $b = 0$ in the saturation criterion (4.2.1), we keep $\mathcal{A}_T(b)$ and $T_{AA}(b)$ generic in Eq. (4.2.1) and repeat the computation

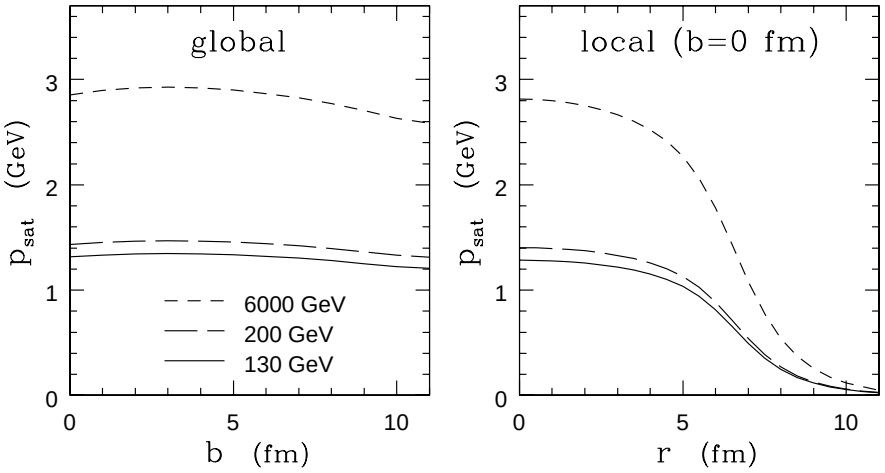

Figure 4.6: *Left:* Global saturation cutoff with no shadowing corrections as a function of the impact parameter. Eq. (4.2.12) is used with the Glauber type transverse area (4.2.10) computed with Woods-Saxon thickness functions. *Right:* Unshadowed local saturation cutoff in central collisions as a function of the transverse coordinate r [see Eq. (4.2.7)].

that led to Eq. (4.2.4). The result is:

$$\begin{aligned} p_{sat} &\approx 0.285\, k^{\frac{1}{4+2\xi}} \left[\frac{T_{AA}(b)}{\mathcal{A}_T(b)}\right]^{\frac{1}{4+2\xi}} \sqrt{s}^{\frac{\delta}{2+\xi}} \\ N_{sat}^{mj} &\approx 0.663\, k^{\frac{1}{2+\xi}} \left[T_{AA}(b)\right]^{\frac{1}{2+\xi}} \left[\mathcal{A}_T(b)\right]^{\frac{1+\xi}{2+\xi}} \sqrt{s}^{\frac{2\delta}{2+\xi}} \ . \end{aligned} \tag{4.2.11}$$

By substituting the numerical values of the parameters as before, we obtain:

$$\begin{aligned} p_{sat} &\approx 0.328 \left[\frac{T_{AA}(b)}{\mathcal{A}_T(b)}\right]^{0.205} \sqrt{s}^{0.205} \\ N_{sat}^{mj} &\approx 0.880 \left[T_{AA}(b)\right]^{0.409} \left[\mathcal{A}_T(b)\right]^{0.591} \sqrt{s}^{0.409} \ , \end{aligned} \tag{4.2.12}$$

where the area is measured in fm^2 and the overlap function in fm^{-2}. Note that by construction these formulae reproduce the result of Eq. (4.2.4) at $b = 0$ and with an hard-sphere nuclear geometry. As anticipated, we can see that the overlap function T_{AA} and the transverse area $\mathcal{A}_T$ play different roles in the saturated minijet multiplicity.

For a better comparison with data and a better extrapolation to LHC energies, we would like to have an approximate analytical parameterization of the effect of shadowing corrections. We make a simplified treatment and assume that the shadowing corrections to the minijet multiplicity amount to a multiplicative factor $S_A(b, \sqrt{s})$:

$$N_{sat}^{mj}{}_{|shad} = S_A(b, \sqrt{s}) \times N_{sat}^{mj} \ . \tag{4.2.13}$$

The EKS98 parameterization of shadowing corrections [133] depends on the atomic number A, but does not depend on the transverse coordinate s at which a parton is hitting the target nucleus[3]. Therefore in absence of other effects (in our case at fixed cutoff) the

[3]For a discussion of the dependence of shadowing on b and s see, e.g., Ref. [28, 50].

shadowing factor should not depend on b. On the other hand, shadowing depends on the typical fractional momenta probed in the interaction. At the saturation scale this is given by $x_{sat} = x_{sat}(b) \sim p_{sat}(b)/\sqrt{s}$ for central rapidity minijet production, and depends on the impact parameter. For typical values of x_{sat} ($\sim 10^{-2}$ at RHIC and $\sim 5 \times 10^{-4}$ at LHC) shadowing increases as x_{sat} decreases. We expect, therefore, S_A to be a decreasing function of b. However, the global saturation cutoff, Eq. (4.2.5), is only a slowly decreasing function of the impact parameter (see Fig. 4.6, left panel). Hence we may approximate the shadowing factor S_A with an impact parameter independent function. Since we are interested in pointing out the role of a correct treatment of the interaction area more than in exact numerical results, this approximation should be not bad, especially at RHIC, where nuclear shadowing is small and is not increasing fast when x_{sat} decreases. We may thus assume the shadowing factor to be of the form: $S_A(b, \sqrt{s}) = S_A(\sqrt{s}) = c\, A^d \sqrt{s}^{\,f}$. Then, by comparing the numerical result of Eq. (4.2.2) with Eq. (4.2.3) multiplied by the shadowing factor (4.2.13) we get

$$S_A(\sqrt{s}) = 1.152\, A^{-0.019}\, \sqrt{s}^{\,-0.025} \ . \tag{4.2.14}$$

We can see that shadowing decreases the saturated minijet multiplicity in central Au-Au collisions by approximately 3% at RHIC and 10% at LHC. Our final result for the globally saturated minijet multiplicity including shadowing is:

$$N_{sat}^{mj} \ \approx \ 1.014\, A^{-0.019}\, \left[T_{AA}(b)\right]^{0.409}\, \left[\mathcal{A}_T(b)\right]^{0.591}\, \sqrt{s}^{\,0.383} \ . \tag{4.2.15}$$

We call "EKRT+ model" this modification of the EKRT computation of globally saturated minijet multiplicity when the Glauber-type transverse area $\mathcal{A}_T$ is used with Woods-Saxon thickness functions, and "EKRT(GW)+ model" when the effective transverse area $\mathcal{A}_T^{eff}$ is used.

Local saturation and centrality

The charged particle multiplicity per participant pair obtained by using the local saturation criterion ("ℓEKRT" model) is shown in Fig. 4.7 by a dotted curve. The result is a nearly flat function of the number of participants and seems disfavoured by the data. We stress that to compute the saturated minijet multiplicity in Eq. (4.2.7) the integration over the transverse coordinate r is limited to the *interaction area*, i.e., the region in the transverse plane such that $p_{sat} \geq p_{lim}$. We think that this method to determine the interaction area is too arbitrary. Indeed, by by taking a small p_{lim} we select a large area, while choosing a large one we select a small area. Since the chosen value $p_{lim} = 0.5$ GeV is rather small this may lead to an overestimate of the interaction area. By the saturation criterion this would lead in turn to an overestimate of the saturated minijet multiplicity. In other words, choosing a limit p_{lim} is like choosing by a radius for the two nuclei: if we choose a too large radius we need to fill with minijets a too large area and we obtain a too large value of N_{sat}^{mj}. In central collisions we expect small effects when changing p_{lim} within reasonable values like 0.5 GeV $< p_{lim} <$ 1 GeV. However, for peripheral collisions the difference may be rather large. We verified this by computing the saturated minijet multiplicity, Eq. (4.2.7), with $p_{lim} = 0.7 GeV$. When dividing it by the number of participant nucleons the result is an increasing curve as a function of the number of participants. Conversely when using $p_{lim} = 0.5$ GeV the result is a nearly flat curve.

A way to reduce this arbitrariness is to relate the definition of the interaction area to the underlying dynamics of the event. As discussed in Sec. 1.3.1 this can be done by making reference to the Glauber model of nuclear collisions. The probability that a projectile nucleon at a given transverse distance r from the center of the target nucleus has an interaction is given by $\mathcal{P}_A(r) = 1 - \exp[-\sigma_{in}\tau_A(r)]$, where σ_{in} is the inelastic pp cross section. In an AA collision the probability of having a nucleon-nucleon scattering at a given r is

$$P_{AA}(b,r) = \mathcal{P}_A(b-r)\mathcal{P}_A(r) \ . \tag{4.2.16}$$

Then, we may expect that the average number of produced minijets at a given r is proportional to the probability (4.2.16) and we may define the saturated minijet multiplicity as follows:

$$N_{sat}^{mj}(b) \ = \frac{1}{\pi}\int d^2r\, p_{sat}^2(b,r)\, P_{AA}(b,r) \ . \tag{4.2.17}$$

We may include shadowing corrections by noting that as $N_{sat}^{mj} \sim p_{sat}^2$ we may simply multiply the saturation cutoff itself by a shadowing factor S_A:

$$p_{sat\ |shad}^2(b,r) = S_A(b,r,\sqrt{s})\, p_{sat}^2(b,r) \ .$$

However, finding a reasonable parameterization for S_A is not as simple as in the case of the global saturation criterion. Indeed, the local saturation cutoff is not a slowly changing function of the transverse coordinate r, see Fig. 4.6 (right panel). Therefore, by using a shadowing factor independent of the transverse coordinate (and of the impact parameter) we would largely underestimate the shadowing corrections in the periphery of both nuclei. This means that we would overestimate $p_{sat}(b,r)$ at large r, which in turn implies largely overestimating $N_{sat}^{mj}(b)$ at large b. With such a b-independent shadowing factor and Eq. (4.2.7), we may reproduce at RHIC energies the numerical results of Ref. [35] by using a slightly larger limit $p_{lim})0.53GeV$ instead of 0.5 GeV. With the same p_{lim} at LHC energy we find a good agreement for $N_{part} \gtrsim 200$ and an overestimate in more peripheral collisions which worsen as N_{part} decreases. On the other hand, by using Eq. (4.2.17) we give the peripheral regions in the transverse plane a small weight and N_{sat}^{mj} is found to be less sensitive on small changes of p_{sat} than when using the cutoff as in Eq. (4.2.7). Since we are interested more in the qualitative changes that a more accurate treatment of the interaction can introduce than in quantitatively accurate results, we think that it is nonetheless worth using the b- and r-independent parameterization of the shadowing factor in Eq. (4.2.14). Then our final expression for the local saturation cutoff and of the saturated minijet multiplicity are:

$$\begin{aligned} p_{sat\ |shad}^2(b,r) \ &= \ 0.346\, A^{-0.019}\sqrt{s}^{\,0.383}\ \left[\tau_A(b-r)\tau_A(r)\right]^{0.409} \\ N_{sat\ |shad}^{mj}(b) \ &= \frac{1}{\pi}\int d^2r\, p_{sat\ |shad}^2(b,r)\, P_{AA}(b,r) \ , \end{aligned} \tag{4.2.18}$$

where the coefficient has been obtained by normalizing the shadowed local saturation cutoff to the numerical result in Fig. 1 of Ref. [35]. We call "ℓEKRT+" model this modified computation of the locally saturated minijet multiplicity, and will use Woods-Saxon nuclear thickness functions in the computation of P_{AA}.

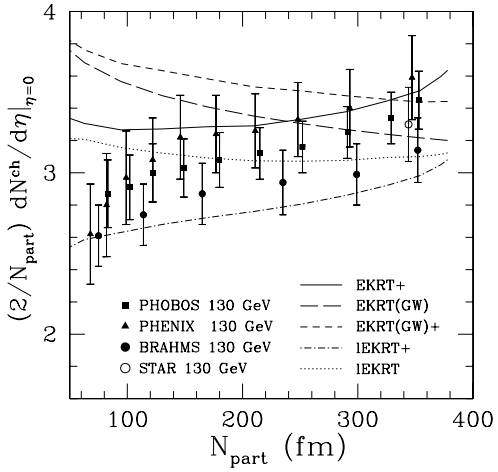

Figure 4.7: Comparison of the variants of the EKRT models discussed in the text. The dotted line represents the ℓEKRT numerical results of Refs. [35, 39]. The other lines are computed as described in the text. Experimental data taken from [99, 102, 111, 116].

Discussion

The centrality dependence of the charged particle multiplicity per participant pair computed in the different variants of the EKRT final state saturation model are presented in Fig. 4.7, for Au-Au collisions at $\sqrt{s} = 130$ GeV.

The global EKRT model in the Gyulassy-Wang approximation gives, as we have discussed, a decreasing function of the number of participants (long-dashed curve). The same approximation supplemented by the correct treatment of T_{AA} at $b \neq 0$ in the saturation criterion gives only a marginal effect, as demonstrated by the short-dashed curve, which was obtained by using the effective area $\mathcal{A}_T^{eff}(b)$ in Eq. (4.2.15). We note, however, that the slope is less negative than in the EKRT(GW) model. A qualitatively different behaviour is obtained in the EKRT+ model, which is defined by the use of the Glauber-type transverse area $\mathcal{A}_T(b)$ (4.2.15) and use of the Woods-Saxon nuclear thickness function (solid line). Indeed, we obtain an increasing charged multiplicity per participant pair, whose slope compares well with experimental data, except in the most peripheral collisions where our naïve treatment of shadowing becomes inadequate[4] As anticipated, the overestimate of the transverse area introduced by the Gyulassy-Wang approximation has a strong effect, both quantitatively and qualitatively.

The local ℓEKRT model result (dotted line) is a nearly flat charged multiplicity per participant pair, which seems disfavoured by experimental data. On the other hand, the ℓEKRT+ model (dot-dashed line), which improves the ℓEKRT model with a treatment of the interaction area inspired by the Glauber model, gives a slightly increasing function of the number of participants, with a slope comparable to the EKRT+ result.

Note that in the EKRT model (in the various formulations discussed) there is some dependence on the k factor (which, however, may be computed at next-to-leading order [34]), and on the factor γ in front of the r.h.s of the saturation condition (4.2.1): $N_{sat}^{mj} \propto k^{0.41}\gamma^{-0.41}$. Moreover, other dynamical effects like intrinsic k_t may increase the multiplicity [80]. These two effects introduce in the computations some theoretical uncertainties, which, however, are difficult to estimate.

In conclusion, both the local and global final state saturation models may account reasonably well for the experimental data at $\sqrt{s} = 130$ GeV when supplemented by a more refined treatment of the interaction area. Its correct definition is a very important issue

[4] By using the hard-sphere thickness function we obtain an even steeper curve.

since global observables are very sensitive to its actual value and qualitatively different behaviours of their centrality dependence may be found for different estimates of this area. The predictions of the local and global models at higher energies will be studied in Sec. 4.4.

4.3 Saturation in the minijet production

At very high energies the target parton densities experienced by projectile partons are so high that the probability for them to have more than one semihard scattering may become non negligible already at RHIC. At such regimes the usual perturbative computation [55], obtained by eikonalization of the minijet cross section, may become inadequate. Indeed, it takes into account only disconnected two-parton interactions located at different points in transverse space but neglects the rescatterings. In Chapter 2 we described how it is possible to include semihard parton rescatterings in the interaction mechanism with the help of a few simplifying hypotheses. In Chapter 3 we showed that they lead to sizeable effects on initial conditions already at RHIC energies. Based on these results, in this section we propose a new saturation mechanism for semihard minijet production and use it in a two-component model to compute charged particle multiplicities at RHIC and at LHC [4, 6].

4.3.1 Global criterion and initial conditions

When rescatterings are included in the interaction of two nuclei of atomic numbers A and B, the average number of A nucleus minijets at fixed impact parameter b is given by [17]:

$$N_A^{mj}(b) = \int d^2r dx \Gamma_A(x, b-r; Q^2) \left[1 - e^{-k \int dx' \sigma_H(xx'; Q^2) \Gamma_B(x', r; Q^2)}\right] , \qquad (4.3.1)$$

and the average minijet initial multiplicity is obtained by summing the analogous contribution from the B nucleus, $N^{mj} = N_A^{mj} + N_B^{mj}$ (see Sec. 2.6.1). For simplicity we omit the flavour indices and consider only gluon-gluon interactions in our formulae, the inclusion of quarks being straightforward. In the numerical computations both the gluons and the quarks have been included. In Eq. (4.3.1), $\Gamma_A = \tau_A(r) G(x)$ is the nuclear parton distribution function $\tau_A(r)$ of the A nucleus is its nuclear thickness function, normalized to A, evaluated at a transverse coordinate r relative to the center of the nucleus and $G(x)$ is the parton distribution function of a proton at a given fractional momentum x. σ_H is the pQCD gluon-gluon cross section at leading order in the high energy limit,

$$\sigma_H(xx'; Q^2) = \frac{9}{2} \pi \alpha_s^2(Q^2) \frac{1}{p_0^2} \left(1 - \frac{4p_0^2}{xx's}\right) \theta(xx's - 4p_0^2) \theta(1-x) \theta(1-x') ,$$

where we included all the kinematic limits and p_0 is the cut-off that discriminates between soft and semihard interactions. We also included explicitly the k factor, k, to take into account higher order corrections. Both the cross section and the parton distributions depend on a scale $Q = p_0$, which we take equal to the cutoff, and will understand in the following. In the numerical computations we will set $k = 2$ and will use Woods-Saxon thickness function and GRV98LO parton distribution functions [135].

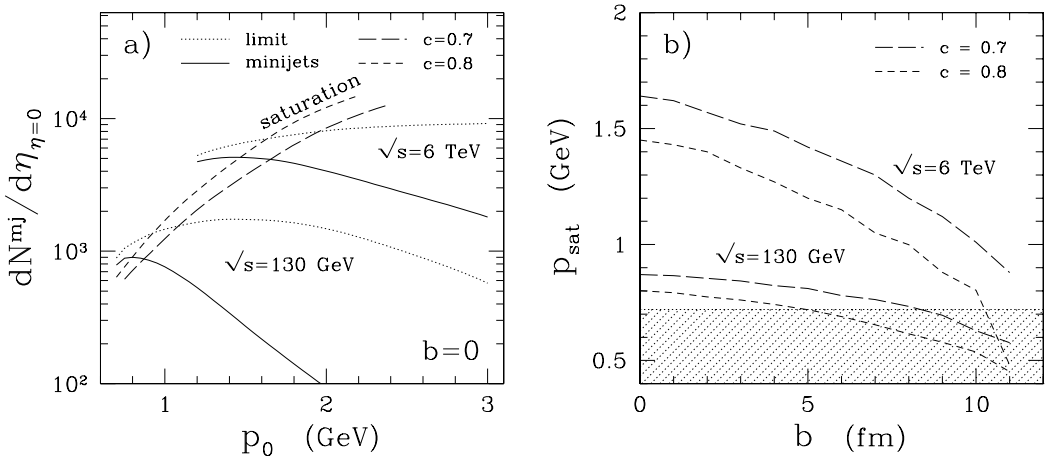

Figure 4.8: *a*) The minijet multiplicity N^{mj} (solid line), and its limiting value N^{mj}_{lim} (dotted line) in a central Au-Au collision as a function of the cutoff p_0 at RHIC and LHC energies. The dashed lines are the saturated minijet multiplicities, N^{mj}_{sat}, with a saturation parameter $c = 0.7$ (long dashes) and $c = 0.8$ (short dashes). The intercept of the dashed lines with the dotted lines determines the saturation cutoff. *b*) The saturation cutoff as a function of the impact parameter at RHIC and LHC energies. The shaded area is the region where we estimate that the saturation criteria ceases to be valid.

Eq. (4.3.1) may be interpreted as the integral of the average density of projectile partons (at a given x and r) times the probability of having at least one semihard scattering against the target. The exponent in Eq. (4.3.1) may be interpreted as the opacity of the target nucleus, being proportional to the total transverse area occupied by its partons at the resolution scale p_0. Two interesting limiting cases may be studied. At high values of p_0 the target has a small opacity and is seen by the incoming partons as a rather dilute system. As a consequence $N^{mj} \approx 2 \int d^2r dx dx' \Gamma_A(x, b-r) \sigma_H(xx') \Gamma_B(x')$, and we recover the usual perturbative result [55]. On the other hand, at low values of p_0 the target opacity increases: the target is becoming black to the projectile partons. As a consequence, the probability of scattering at least once becomes so high that nearly every projectile parton scatters and the minijet multiplicity reaches a limiting value instead of diverging as it happens in the Eikonal computation.

In the regime where the target is almost black the semihard interactions are extracting from the projectile nucleus wave function all its partons, and even if we use a lower cutoff no more partons are there to be extracted. for this reason the minijet multiplicity tends to saturate [3] (see also Fig. 4.8a). We call *saturation cutoff* the value of p_0 at which this happens, and will denote it as p_{sat}. Of course the validity of this picture is limited to the kinematic regions where the saturation cutoff is in the perturbative range, $p_{sat} \gg \Lambda_{QCD}$. To give a quantitative definition of the saturation cutoff we start by considering a central collision of two equal nuclei. We define the *upper bound* for the minijet multiplicity as

$$N^{mj}_{Alim}(b=0) = \lim_{k\to\infty} N^{mj}_A = \int_{4p_0^2/s \le x \le 1} d^2r dx \Gamma_A(x,r) \ . \tag{4.3.2}$$

Taking a very large k factor corresponds, indeed, to the limit in which the target becomes completely black and the semihard interactions are effective in extracting all the partons

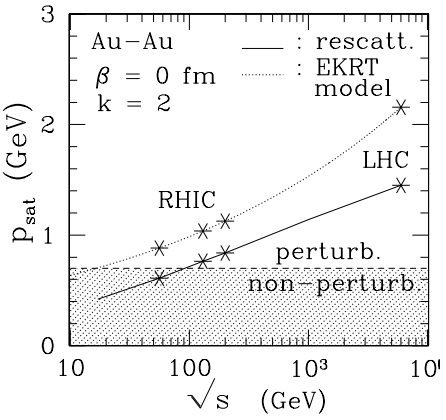

Figure 4.9: The dependence of the saturation cutoff on the center of mass energy in the EKRT model, Eq. (4.2.2), and in the production saturation model, Eq. (4.3.3). The shaded area corresponds to the region where we estimate the production saturation criterion is not applicable.

from the projectile nucleus. The limiting procedure is needed in order to keep track of the kinematic limits. As it is easy to see, $N^{mj} \underset{p_0 \to 0}{\sim} N^{mj}_{lim}$, therefore we can define the saturation cutoff as the value of p_0 such that the minijet multiplicity becomes a substantial fraction of its limiting value:

$$N^{mj}(p_0 = p_{sat}) = c\, N^{mj}_{lim}(p_0 = p_{sat}) \ , \tag{4.3.3}$$

where the *saturation parameter* c is a positive number smaller than one. Note that $p_{sat} = p_{sat}(\sqrt{s}, c)$ is a function also of the energy of the collision. From our discussion it is obvious that c must be close to one to let p_{sat} lie in the region where N^{mj} is saturating. However, to stay in the perturbative regime we cannot choose it too close to one since $p_{sat} \to 0$ as $c \to 1$. Finally, we define the *saturated minijet multiplicity* as the average multiplicity evaluated at the saturation cutoff:

$$N^{mj}_{sat} = N^{mj}_{sat}(\sqrt{s}, c) = N^{mj}(p_0 = p_{sat}) \ . \tag{4.3.4}$$

In our approach this number represents also the multiplicity of partons produced in the early stage of the heavy ion collision.

In Fig. 4.8a we show the minijet multiplicity and its limiting value as a function of the cutoff p_0 at RHIC and LHC energies. The rapidity density at $\eta = 0$ is computed by integrating Eqs. (4.3.1) and (4.3.2) over a pseudorapidity interval $|\eta| \leq 1$, where we approximated $\eta \approx \log(x\sqrt{s}/p_0)$, and by dividing the result by a factor two. The dashed lines represent the saturated initial conditions computed with $c = 0.7$ and $c = 0.8$. We can see that at a given energy N^{mj}_{sat}, which is obtained as the intercept of the solid and dashed lines, is nearly independent of the saturation parameter as long as the latter is close enough to one. Indeed, both at RHIC and LHC energy we obtain approximately a 3% increase in the saturated multiplicity going from $c = 0.7$ and $c = 0.8$. Therefore, whereas c is an arbitrary parameter its actual choice doesn't affect strongly the determination of the initial conditions. The dependence of p_{sat} on $\sqrt{s}$ is shown in Fig. 4.9, where we can see that for central collisions the saturation criterion is applicable from RHIC energies on.

Unless we use nuclear thickness functions with sharp edges, like the hard-sphere distributions, by applying blindly the saturation criteria to non central collisions we would obtain an impact parameter independent bound on the minijet multiplicity. Indeed we would have $N^{mj}_{lim}(b) = \int d^2r dx \Gamma_A(x, b - r) = \int d^2r dx \Gamma_A(x, r)$. In this way, by requiring saturation as in Eq. (4.3.3) we would be asking the semihard interactions to extract all the partons from the projectile nucleus even in a very peripheral region, which is clearly

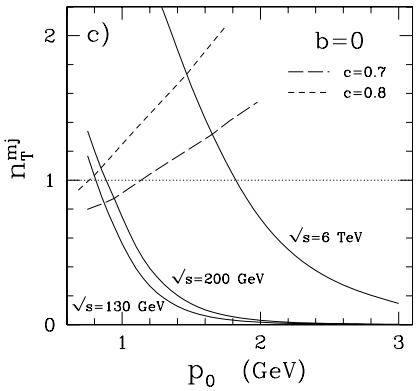

Figure 4.10: The minijet average occupation number density in the transverse area (solid lines): $n_T^{mj} = A_T^{mj}/A_T^{Au}$, where $A_T^{mj} = N^{mj}(p_0) \times \pi/p_0^2$ and $A_T^{Au} = \pi R_{A=197}^2$ is the geometrical transverse area of a gold nucleus (use of the Glauber-type area (4.2.10) with Woods-Saxon thickness functions would result in lower occupation number density). The dashed lines show the average occupation number of the saturated minijets as a function of the saturation momentum. When $n_T^{mj} \gtrsim 1$ the minijets begin to overlap transversely.

unphysical. A simple way to implement the collision geometry in the saturation criterion is to cut by hand the thickness functions outside a given radius R_c of the order of the nuclear radius. However, the minijet multiplicity as a function of the centrality of the collision turns out to depend too strongly on the choice of R_c except at very high centrality or very high energies [4].

To find a less arbitrary way of implementing the collision geometry we look at the Glauber model computation of the average number of nucleons which participate in the collision (see Sec. 1.3.1):

$$N_{part}(b) = \int d^2r\, \tau_A(b-r)\mathcal{P}_B(r) + A \leftrightarrow B \ , \tag{4.3.5}$$

where $\mathcal{P}_B(r) = 1 - [1 - \sigma_{in}(s)\tau_B(r)/B]^B$ and σ_{in} is the inelastic pp cross section, which we take from [121]. At $\sqrt{s} = 130, 200, 6000$ GeV we have $\sigma_{in} = 39, 42, 75$ mbarn, respectively. $\mathcal{P}_B$ is the probability that a projectile nucleus at a given transverse coordinate r has at least one inelastic interaction with the target nucleons. Then, we may require the saturation only for the fraction of projectile partons that belong to a participant nucleon, and define an *effective nuclear distribution function*

$$\overline{\Gamma}_{AB}(x,b,r) = \Gamma_A(x,b-r)\mathcal{P}_B(r) \ .$$

Correspondingly, we have an effective minijet multiplicity, $\overline{N}_A^{mj}(b) = \int d^2r dx \overline{\Gamma}_{AB}(x,b,r) \times \big[1 - \exp\big(-\int dx' \sigma_H(xx')\Gamma_b(x')\big)\big]$, and an effective upper limit $\overline{N}_{Alim}^{mj}(b) = \int d^2r dx\, \overline{\Gamma}_{AB}(x,b,r)$, which is no more b-independent. Then, the saturation criterion generalized to arbitrary impact parameter becomes:

$$\overline{N}_A^{mj}(p_0 = p_{sat}) = c\, \overline{N}_{Alim}^{mj}(p_0 = p_{sat}) \ . \tag{4.3.6}$$

Finally, having determined p_{sat} in this way we use it in Eq. (4.3.4) to compute the average initial parton multiplicity.

In Fig. 4.8b we show the saturation cutoff as a function of the impact parameter at RHIC and LHC energies for different saturation parameters c. The horizontal line show the limit of approximately 0.7 GeV whose intersection with $p_{sat}(b)$ sets the limit of validity of the present approach, as will be discussed in the next section.

In the proposed mechanism saturation is reached when there are no more partons that semihard interactions can extract from the nuclear wave functions. In this sense

this mechanism is a saturation of the minijet production and is intermediate between initial and final state saturation. In initial state saturation the parton density inside the incoming nuclei saturate due to a compensation between parton splitting and parton fusion processes in the DGLAP evolution, which induces a corresponding saturation in the minijet multiplicity (see Sec. 4.1.2). On the contrary, in the final state mechanism (see Sec. 4.2) the saturation is assumed to be caused by the high density of produced minijets, which screens softer parton production due to parton fusion processes in the final state. In particular these final state interactions are assumed to set in when the transverse area occupied by the minijets becomes comparable to the nuclear overlap area. Both processes may, therefore, complement our saturation mechanism since the former modify the input parton distribution functions and the latter deals with a later stage process. However, as we can see in Fig. 4.10, at $\sqrt{s} = 130$ GeV and $\sqrt{s} = 200$ GeV the saturated minijets fill the transverse area only partially. Therefore final state saturation effects should not alter significantly our computations at RHIC energy, but may play some role at LHC.

Note that the saturated initial conditions, are practically determined by the choice of the parton distribution functions and are nearly independent of the remaining free parameters, namely the saturation parameter c and the k factor. Changing c or the k factor should affect the value of the saturation cutoff – namely, the larger the k factor (or the smaller c) the larger p_{sat} – but should not affect strongly the multiplicity. Indeed, the multiplicity as a function of the cutoff presents a plateau for $p_0 \sim p_{sat}$, so that small changes in p_sat result in even smaller changes in the multiplicity. Similar considerations may be done when introducing additional dynamical effects like an intrinsic k_t for the initial partons, which can be done in a straightforward way within our model. The effect of intrinsic k_t should be a slight increase in the saturation cutoff, due to an increased target flux, and an increase in the incoming flux, which induces a smaller increase in the charged multiplicity than when rescatterings are neglected.

4.3.2 Local criterion

The saturation criterion is easy to generalize to a local one. Indeed, we can write Eq. (4.3.6) as follows:

$$\int d^2r \int_{\Delta\eta} dx\, \overline{\Gamma}_{AB}(x,b,r) \left[1 - e^{-k \int dx' \sigma_H(xx') \Gamma_b(x')}\right] = c \lim_{k\to\infty} \int d^2r \int_{\Delta\eta} dx\, \overline{\Gamma}_{AB}(x,b,r) \left[1 - e^{-k \int dx' \sigma_H(xx') \Gamma_b(x')}\right] .$$

Note that $\overline{\Gamma}_{AB}(x,b,r) = G(x)\tau_A(b-r)\mathcal{P}_B(r)$. Then by dropping the integrations over r we get the local version of the saturation criterion:

$$\int_{\Delta\eta} dx\, G(x) \left[1 - e^{-k \int dx' \sigma_H(xx') \Gamma_b(x')}\right] \; |_{p_0=p_{sat}} = c \int_{\Delta\eta} dx\, G(x) \; |_{p_0=p_{sat}} . \qquad (4.3.7)$$

Note that every information on the geometry of the projectile has dropped out, and only the parton distribution of a single nucleon has remained, so that saturation is practically determined by the target nucleus. For this reason there is no more need to take into account the collision geometry and we could perform explicitly the limit for $k\to\infty$. A

further localization of the criterion in the pseudorapidity variable would make any information on the projectile disappear. The meaning of (4.3.7) is as before: at a given transverse coordinate r saturation is reached when the target nucleus extracts on average nearly all the incoming partons. The local saturation cutoff obtained by solving (4.3.7) is b-independent, and we stress that it depends only on the nuclear target: $p_{sat} = p_{sat}(r, B)$. The *locally saturated minijet multiplicity density* in the transverse plane is then obtained by computing the minijet transverse density at a point r with the local saturation cutoff.

The next step is to integrate the locally saturated minijet multiplicity density over the transverse plane. However, the same problem encountered in the local final state saturation model arises. Indeed, at sufficiently large r the saturation cutoff becomes comparable to Λ_{QCD} and we have to find a way to determine which is the transverse area where it is sensible to ask for local saturation. As we discussed in the last subsection, we have to avoid any arbitrary definition and make reference to the actual collision. The most intuitive way of doing that, given the discussion about the global criterion, is to make use of the effective nuclear distribution function for the projectile nucleus. The *locally saturated multiplicity* is therefore defined as

$$N_{sat}^{mj} = N^{mj}(p_0 = p_{sat}) = \int d^2r \int_{\Delta\eta} dx \left\{ \overline{\Gamma}_{AB}(x, b, r) \left[1 - e^{-k \int dx' \sigma_H(xx') \Gamma_b(x')} \right] \right\} \Big|_{p_0 = p_{sat}} .$$

However, a deeper investigation of this problem is needed and is in progress.

Using the local criterion instead of the global one in the computation of the initial conditions should not affect too much the results. Indeed in the global criterion first we integrate over the transverse plane, then we ask for saturation in the gluon production. In other words, we ask that the collision produce in the whole transverse plane, say, 80% of the number of gluons in the initial wave function. When using the local criterion, we first ask for saturation and then integrate over the transverse plane. Since the chosen percentage is a fixed parameter, it comes out of the integration and we are left with the 80% of the gluons present in the nuclear wavefunctions. Therefore, the local criterion determines the exact distribution in the transverse plane of the saturated minijets but doesn't alter the total minijet multiplicity.

In summary, the local criterion should be preferred to the global whenever detailed information about initial conditions in the transverse plane are needed, e.g. for hydrodynamic computations of the evolution of the minijet plasma [62]. Conversely, when only the total minijet multiplicity is needed the two saturation mechanism should be equivalent. Numerical computations with the local saturation criterion are in progress.

4.3.3 Charged particle multiplicity

In this section we want to apply the global saturation criterion for the semihard parton production to the computation of the observable charged particle multiplicity.

Thanks to the self-shadowing property of the semihard interactions (see Sec. 1.3.4) even if in Eq. (4.3.1) only the semihard cross section σ_H appears, we are actually taking into account all the partons that had *at least* one semihard scattering, while their other scatterings may be semihard or soft with no restrictions. A heuristic way of seeing this is to assume that the parton-parton cross section may be divided in a semihard and a soft part (which we don't specify any better, see Ref. [71]) separated by the cutoff p_0:

$\sigma = \sigma_S + \sigma_H$. The probability that a part has at least one soft or hard scattering may therefore be expressed as:

$$\begin{aligned}
\overline{\mathcal{P}}_B(x,r) &= \left[1 - e^{-k\int dx'(\sigma_S(xx')+\sigma_H(xx'))\Gamma_B(x',r)}\right] \\
&= \sum_{n=1,\infty} \frac{1}{n!}\left[\int dx'\Big(\sigma_S(xx') + \sigma_H(xx')\Big)\Gamma_B(x',r)\right]^n e^{-k\int dx'(\sigma_S(xx')+\sigma_H(xx'))\Gamma_B(x',r)} \\
&= \sum_{n=1,\infty} \frac{1}{n!} \sum_{n_H=1,\infty} \binom{n}{n_H} (\sigma_S(xx')\Gamma_B(x',r))^{n-n_H} (\sigma_H(xx')\Gamma_B(x',r))^{n_H} \\
&\qquad \times e^{-k\int dx'(\sigma_S(xx')+\sigma_H(xx'))\Gamma_B(x',r)} \,.
\end{aligned}$$

In the second line we expanded $\mathcal{P}_B$ as a Poisson distribution in the number n of interactions undergone by the parton. In the third line we separated them, at each given n, into n_H semihard interactions and $n_S = n - n_H$ soft interactions. A minijet is defined as a parton which had at least one semihard interactions, without specifying if the remaining ones are semihard or soft. Then it is interesting to separate in the above sums the terms with only soft scatterings, whose sum defines the *soft scattering probability* $\mathcal{P}_B^S$, and those with at least one semihard interaction, whose sum defines the *semi-hard scattering probability* $\mathcal{P}_B^H$. In the latter we may further collect the terms with a fixed number n_H of semihard interactions disregarding the number of additional soft scatterings:

$$\begin{aligned}
\overline{\mathcal{P}}_B(x,r) &= \sum_{n_S=1,\infty} \frac{1}{n_S!}\left[\int dx'\sigma_S(xx')\Gamma_B(x',r)\right]^{n_S} e^{-k\int dx'(\sigma_S(xx')+\sigma_H(xx'))\Gamma_B(x',r)} \\
&\quad + \sum_{n_H=1,\infty} \frac{1}{n_H!}\left[\int dx'\sigma_H(xx')\Gamma_B(x',r)\right]^{n_H} \sum_{n_S=0,\infty} \frac{1}{n_S!}\left[\int dx'\sigma_S(xx')\Gamma_B(x',r)\right]^{n_S} \\
&\qquad e^{-k\int dx'(\sigma_S(xx')+\sigma_H(xx'))\Gamma_B(x',r)} \,. \qquad (4.3.8)
\end{aligned}$$

The sum over n_S and n_H may be performed explicitly, giving the desired result:

$$\overline{\mathcal{P}}_B(x,r) = \overline{\mathcal{P}}_B^S(x,r) + \overline{\mathcal{P}}_B^H(x,r) \,,$$

where

$$\begin{aligned}
\overline{\mathcal{P}}_B^S(x,r) &= \left[1 - e^{-k\int dx'\sigma_S(xx')\Gamma_B(x',r)}\right] e^{-k\int dx'\sigma_h(xx')\Gamma_B(x',r)} \\
\overline{\mathcal{P}}_B^H(x,r) &= \left[1 - e^{-k\int dx'\sigma_H(xx')\Gamma_B(x',r)}\right] .
\end{aligned}$$

Note that in $\overline{\mathcal{P}}^H$, namely, the probability of having at least one semihard interaction, no soft cross section appear in spite of the fact that we included additional soft scatterings explicitly. This is due to the fact that the sum over n_S in the second term of the last line of Eq. (4.3.8) canceled against the soft part of the absorption exponential, namely, $\exp[-\int \sigma_S\Gamma_B]$. Note also that as the *semihard opacity* of the projectile $\int \sigma_H\Gamma_B$ increases, the probability $\mathcal{P}_B^S$ of having only soft scatterings tends to zero, being proportional to the probability of having no semihard scattering, $\exp[-\int \sigma_H\Gamma_B]$. In summary, the probability of having at least one semihard scattering is independent of soft interactions and dominates the scattering probability at small cutoff or high energies.

Given the above discussion, by applying the saturation criterion to compute minijet multiplicity, we are missing only the purely soft part of the initial production mechanism. This leads us to adopt a two-component model in which the charged particle multiplicity is written as the sum of a soft and a semihard part: $dN^{ch}/d\eta(b) = dN^{ch}_{soft}/d\eta(b) + dN^{ch}_{s.h.}/d\eta(b)$. The soft part is assumed to scale with the number of participants, Eq. (4.3.5), so that [60]

$$\frac{dN^{ch}_{soft}}{d\eta}(b) = x n_{p\bar{p}}(s) \frac{N_{part}(b)}{2} \ . \tag{4.3.9}$$

Here $n_{p\bar{p}}(s)$ the pseudorapidity density of charged particles produced at $\eta = 0$ in $p\bar{p}$ collision at a given c.m. energy $\sqrt{s}$. We use the fit [97] $n_{p\bar{p}}(s) = 2.5 - 0.25\log(s) + 0.023\log^2(s)$. The coefficient $x = x(s)$ is a parameter that allows to adjust the relative weight of soft and semihard interactions and will be determined from the experimental data. Further, we assume the semihard part to be completely computable from the saturation criterion for minijet production described in the last section. To convert the minijet multiplicity to charged particle multiplicity, we further assume isentropic expansion of the initially produced minijet plasma and parton-hadron duality, so that

$$\frac{dN^{ch}_{s.h.}}{d\eta}(b) = 0.9 \times \frac{2}{3} \times \frac{dN^{mj}_{sat}}{d\eta}(b) \ , \tag{4.3.10}$$

where the factor 0.9 is due to the different number of degrees of freedom of the system in the minijet-plasma phase and in the hadronic phase [33]. To mark out the contribution of the hard part it is customary to divide the charged multiplicity by the number of participant pairs, so that the observables we are interested in are:

$$\frac{1}{N_{part}(b)/2}\frac{dN^{ch}}{d\eta}(b) = x\, n_{pp}(s) + \frac{1}{N_{part}(b)/2}\frac{dN^{ch}_{s.h.}}{d\eta}(b) \tag{4.3.11}$$

and the fraction of semihard interactions $F_{s.h.} = \frac{dN^{ch}_{s.h.}}{d\eta}/\frac{dN^{ch}}{d\eta}$. Note that any deviation from a flat curve as a function of N_{part} or b is due entirely to semihard interactions. Therefore a positive slope may be interpreted as due to minijet production. There are, however, models that predict also a scaling of the soft part with the number of collisions [21], therefore the last sentence should be considered with care.

To make a comparison with experimental data we have first to relate the observables appearing in Eq. (4.3.11), which are functions of the impact parameter, to the experimental ones, which are obtained as averages over centrality classes of events [99, 110, 111]. Following [59, 60], to which we refer for the details, we do this by studying the minimum bias multiplicity distribution of charged particles and by dividing the events in suitable subsets over which the average is performed. The next step is to extract the parameter x in Eq. (4.3.9) by comparing the computation for the 3% most central events and the PHOBOS data at $\sqrt{s} = 130$ GeV from Ref. [111]. This value is then used to make predictions at higher energy.

In Fig. 4.11 we show both the results for the semihard part before the averaging over the centrality classes, and the results obtained after the averaging and the inclusion of the soft part. For each curve the result obtained by setting $c = 0.7$ and $c = 0.8$ in Eq. (4.3.6) is shown.

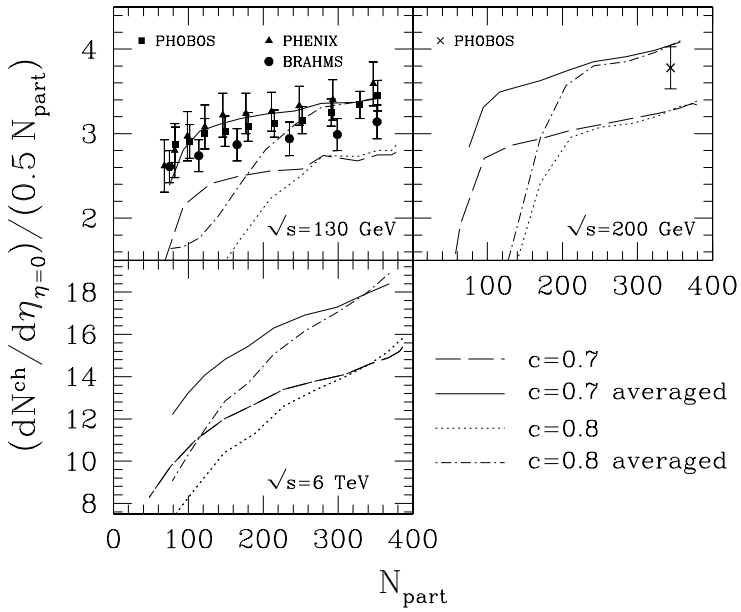

Figure 4.11: Charged particle multiplicity per participant pair, Eq. (4.3.11), as a function of the number of participants at different center of mass energies and saturation parameter $c = 0.7$ and $c = 0.8$. In each panel the lower pair of curves (dashed and dotted lines) represent the semihard contribution. The upper pair of curves (solid and dot-dashed lines) are obtained by averaging the semihard contribution and by adding the soft part. At $\sqrt{s} = 130$ GeV the parameter x is extracted from the 3% most central PHOBOS events at $\sqrt{s} = 130$ GeV [111]. At higher energies the upper curves may be considered an upper bound, while the lower ones give a lower bound, see text. Data taken from [99, 111, 113, 116].

At $\sqrt{s} = 130$ GeV we find $x = 0.445$ and $x = 0.453$, for a saturation parameter $c = 0.7$ and $c = 0.8$, respectively. These values of x correspond to a fraction of semihard interactions $F_{s.h.} = 0.805$ and $F_{s.h.} = 0.817$, respectively, and show a good stability with respect to c. The relatively large value of $F_{s.h.}$ with respect to the common expectation of nearly a half and to the value of 0.37 extracted from PHOBOS data in Ref. [60] is due to the fact that we considered as belonging to the non-soft part of the observable also a *semi*-hard region 0.7 GeV $\lesssim p_0 \lesssim$ 2 GeV. Note that we can push our perturbative computations to such low values of the cutoff because inclusion of parton rescatterings results in a rather small sensitivity of global observables on p_0 in that region [3, 4].

The two curves start with a moderate slope at high centrality and at some point they decrease very fast. This happens when the corresponding saturation cutoff becomes smaller than 0.7 GeV, approximately. The reason for this behaviour is that the distribution functions are fitted just down to a scale $Q \approx 0.9$ GeV and they are numerically extrapolated at lower scales. Below 0.7 GeV the extrapolation gives an unnaturally fast decrease of the parton densities, which results in the rapid fall of the minijet production. Then, we define the region of validity of our computations as the one such that $p_{sat} \gtrsim 0.7$ GeV, or in other words the one to the right of the knee in the charged multiplicity.

The value of p_{sat} at fixed centrality decreases when the saturation parameter c increases (see Fig. 4.8), therefore the curve with $c = 0.8$ is reliable for a smaller range of centrality

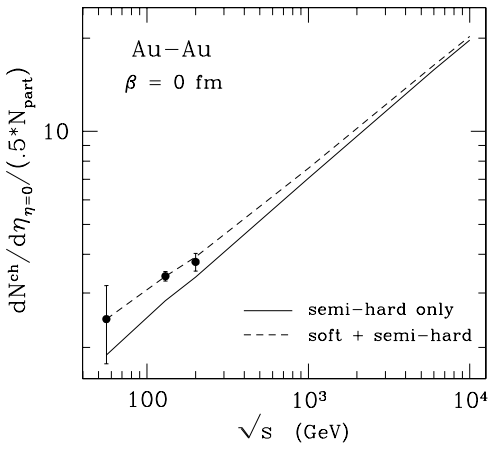

Figure 4.12: Charged particle multiplicity per participant pair in a central Au-Au collision as a function of the center of mass energy of the collision. The solid curve shows the semihard multiplicity obtained by applying the saturation criterion [see Eq. (4.3.10)]. The dashed line is the total multiplicity, which is obtained with a simple parameterization of the relative contribution of the soft part, [see Eqs. (4.3.13) and (4.3.14)].

than the curve with $c = 0.7$. They agree, however, in the common region of validity (showing a slight tendency to increase their slope when increasing c), and after the experimental averaging and the fit to the most central data point, both describe well the experimental data.

The fraction of semihard to soft interactions is expected to grow with the energy of the collision, and we can use the value of $F_{s.h.}$ determined at $\sqrt{s} = 130$ GeV to obtain an approximate upper bound for the charged multiplicities: for $\sqrt{s} \geq 130$

$$x n_{p\bar{p}}(s) \leq \frac{1 - F_{s.h.}|_{b=0,\sqrt{s}=130\ \mathrm{GeV}}}{F_{s.h.}|_{b=0,\sqrt{s}=130\ \mathrm{GeV}}} \frac{dN^{ch}_{s.h.}/d\eta}{N_{part}/2}(b=0,s)\ . \tag{4.3.12}$$

At $\sqrt{s} = 200GeV$ the curves for the two values of c agree over a wider range of neutralities. This is to be expected since the saturation cutoff at fixed centrality grows with the center of mass energy, and goes below the critical value of 0.7 GeV at smaller centrality. Note also that the slope of the curves has increased. The upper and lower bounds shown in Fig. 4.8 are actually predictions of the production saturation model [4, 6], later on verified by PHOBOS [113].

At LHC energy, $\sqrt{s} = 6$ TeV, the particle production is generally believed to be almost completely semihard. Therefore we expect that the data will be close to the averaged semihard multiplicity without any normalization (which is very similar to the lower curve plotted in Fig. 4.11). Though the saturation criterion is applicable over all the centrality range considered (see Fig. 4.8b) the slope of the curves is rather sensitive to the saturation parameter, resulting in a larger theoretical uncertainty. We expect that a better treatment of the scale Q and of the pseudorapidity, which are taken to depend simply on the cutoff p_0, could solve at least partially this problem. However, the average slope has increased confirming the trend observed at lower energies.

The dependence of the charged multiplicity on the energy of the collision is shown in Fig. 4.12. The solid line represents the semihard contribution to the charged multiplicity, Eq. (4.3.10). The relative semihard contribution is expected to increase with energy. Hence, we may parametrize in naïve way the fraction $F_{s.h.}$ of the semihard to total charged multiplicity as follows:

$$F_{s.h.}(\sqrt{s}) = 1 - a\frac{1}{(\sqrt{s})^b} \underset{\sqrt{s}\to\infty}{\longrightarrow} 1\ , \tag{4.3.13}$$

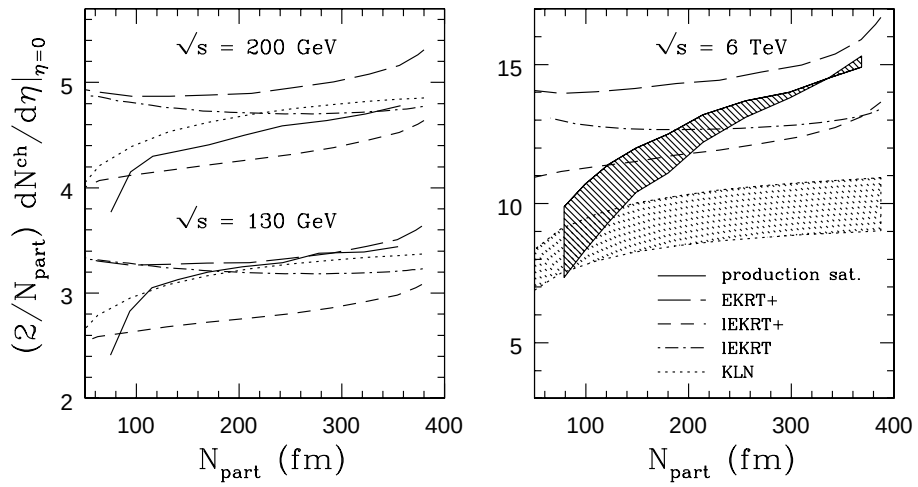

Figure 4.13: Impact parameter dependence of charged multiplicity per participant pair in the three saturation models at $\sqrt{s} = 130, 200$ GeV (*left*) and $\sqrt{s} = 6$ TeV (*right*). Curves at 200 GeV have been shifted upwards by to units to improve clarity. The shaded area indicates actual theoretical uncertainties (EKRT model uncertainties are difficult to evaluate and are not included in the figure). Note that the production saturation result has been averaged over centrality bins, see Sec. 4.3.3.

where a and b are positive coefficients. This parameterization is only meant to give a rough idea of the behaviour of the soft part as the energy increases. The total charged multiplicity is obtained from the semihard part as follows:

$$\frac{dN^{ch}}{d\eta}(\sqrt{s}) = \frac{1}{F_{s.h.}(\sqrt{s})}\frac{dN^{ch}_{s.h.}}{d\eta}(\sqrt{s}) \ . \tag{4.3.14}$$

By fitting Eq. (4.3.14) to the PHOBOS data at $\sqrt{s} = 56, 200$ GeV and to the combined value of the four RHIC experiments [113], we get $a = 0.565$ and $b = 0.415$. With these values, at LHC energies the semihard contribution is nearly the 96 percent of the total.

4.4 Comparing the saturation mechanisms

The main difference in the saturation mechanism described in this chapter is the predicted centrality dependence of the charged multiplicity per participant pair, see Fig. 4.13. We summarize the main features of the results of the various models.

- Initial state saturation *à la* Kharzeev-Levin-Nardi (KLN) gives an increasing curve, whose slope changes slowly with energy.
- Local final state saturation (ℓEKRT) predicts a nearly flat curve at all energies.
- Local final state saturation with improved treatment of the interaction area (ℓEKRT+) gives a slightly increasing curve, whose slope increases smoothly with energy.
- Global final state state saturation with improved treatment of the interaction area (EKRT+) predicts a curve which increases with N_{part}, with a slope comparable to the ℓEKRT+ model. A better treatment of shadowing corrections should correct the tendency of the slope to become negative in most peripheral collisions.

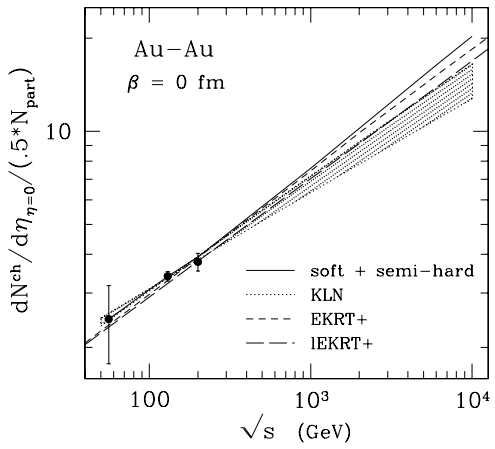

Figure 4.14: Comparison of the prediction of the saturation models on the energy dependence of charged particle multiplicity per participant pair. The shaded area shows the theoretical uncertainty in the EKRT model. In the EKRT model(s) the uncertainty is difficult to evaluate and is not shown. In the production saturation model at $b = 0$ we expect uncertainties to be small.

- Saturation in the minijet production predicts a slope which increases decidedly with energy, due to an increasing role of minijets in particle production in the initial stage of the collision.

Both the EKRT+ and the ℓEKRT+ models are sensitive to variations of the k and γ factors and to inclusion of additional dynamics like intrinsic k_T. On the other hand, the production saturation model is rather stable with respect to the above effects Initial or final state parton-parton fusion processes may come into play in the production saturation mechanism at $\sqrt{s} > 1$ TeV, and decrease the slope in semi-central collision.

The data at $\sqrt{s} = 130$ GeV are well described both in the KLN model and in the "production saturation" model. Also, the improved final state saturation model, both in the local and global version, accounts well for the data, while the original local saturation criterion (ℓEKRT) seems disfavoured. At $\sqrt{s} = 200$ GeV all the models, except ℓEKRT, predict basically the same slope. The situation changes drastically at $\sqrt{s} = 6$ TeV, where all models make distinct predictions. Initial state saturation predicts the smallest multiplicity for central and semicentral collisions, with the smallest slope. Local final state saturation still gives a flat curve with an intermediate normalization. Improved final state saturation predicts increasing curve, the ℓEKRT+ one less steep than the EKRT+ one. The global EKRT+ model presents also a very rapid rise in nearly central collisions which distinguish it from all the other models. The production saturation mechanism predicts the steeper dependence on the number of participants and the higher multiplicity in semi-central events. Therefore, at LHC energy we should be able to discriminate among the various models, while at lower energy the results are too similar to allow a clear distinction. The discriminating power of this observable might improve by studying the energy dependence at $b \neq 0$.

In Fig. 4.14 we show the energy dependence of the charged multiplicity per participant pair at impact parameter $b = 0$. The KLN initial state mechanism is very much dependent on the value of the parameter $\lambda = 0.25 - 0.3$, which describes the small-x rise of the gluon distribution in the proton. At LHC energies the results vary by nearly 50 percent, and with $\lambda = 0.3$ the KLN model even gives the a result very similar to the EKRT model. The "production saturation" mechanism gives a steeper increase in the charged multiplicity than the other two, however at energies larger than 1 TeV additional initial or final state interactions could set in and lower the slope in the TeV energy range. Therefore it is still too early to say if this observable will help in distinguishing between the three mechanisms.

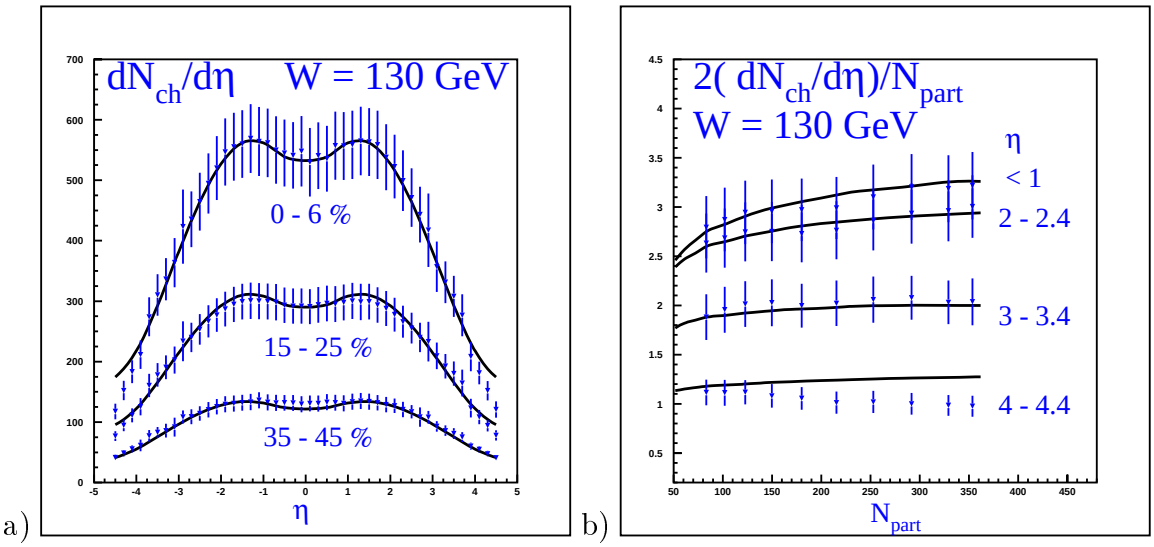

Figure 4.15: *a)* pseudorapidity dependence of charged multiplicity at different centrality cuts in the KLN model at $W \equiv \sqrt{s} = 130$ GeV. *b)* Centrality dependence at various rapidity cuts. Data taken are from [112]. Figures taken from [61].

When better measurement of the gluon distribution will be available may be that it will be possible at least to distinguish between production or final state saturation on one hand and initial state saturation on the other. In any case it would be very interesting to have a good scan of the energy range between RHIC energy of $\sqrt{s} = 200$ GeV and the maximum LHC energy of $\sqrt{s} = 6$ TeV.

Another observable which should be sensitive enough on the different dynamics encoded in the various models is the rapidity distribution of charged particles. The KLN model results are shown in Fig. 4.15a. Also the centrality dependence at different rapidity cuts is a promising observable that should allow to distinguish between the various models, Fig. 4.15b. Computations in the EKRT model [39] and in the production saturation model are in progress.

The three models differ slightly also in the predicted atomic number dependence. In both initial state and production saturation the produced gluon multiplicity is roughly proportional to the gluon distribution computed at the saturation scale: $dN^{ch}/d\eta \propto x_{sat}G(x_{sat}, Q^2_{sat}) \propto A^{\delta}$, where $x_{sat} = 2Q_s/\sqrt{s}$ and $\delta \lesssim 1$. Indeed, at fixed x and Q we have $xG \propto A$. However, as the atomic number increases, the high gluon density regime is reached at higher saturation scales Q_s, which translates in a smaller gluon multiplicity than with a fixed Q_s. The EKRT model predicts $dN^{ch}/d\eta \propto A^{\epsilon}$ with $\epsilon = 0.922$ (smaller than the value $\epsilon = 4/3$ expected from the Eikonal minijet production picture, due the saturation criterion adopted to fix the saturation scale). The differences in the A scaling may therefore be too small to lead to measurable differences. On the other hand, the A scaling of the multiplicity at $b = 0$ in the EKRT saturation model depends only on the exponent ξ [see Eq. (4.2.4)]. Since ξ is related to the behaviour of the running coupling constant, using an α_s-dependent coefficient in the saturation criterion (4.2.1) would therefore change the A dependence. In conclusion the A dependence of the charged multiplicity could be a direct probe of the saturation criterion itself [38].

4.5 Conclusions

The inclusion of semihard parton rescatterings in the interaction dynamics of heavy-ion collisions at very high energy allows a reliable computation of the initial conditions, like the minijet multiplicity, and the introduction of a nearly parameter-free saturation criterion to determine the infrared cutoff to be used in the perturbative computations. The proposed saturation mechanism is intermediate between the initial and final state ones in that it deals with the saturation in the production of minijets.

We tested our approach against RHIC data on the centrality dependence of charged multiplicities by using a two-component model in which the semihard part is assumed to be completely given by the proposed saturation criterion. At $\sqrt{s} = 130$ GeV we find a good agreement with the data, which allows us to extrapolate the results at the highest RHIC energy of $\sqrt{s} = 200$ GeV and at LHC energy, $\sqrt{s} = 6$ TeV, by putting upper and lower bounds on the charged multiplicities per participant pairs as a function of the number of participants and by predicting their slope. The proposed saturation mechanism is also applicable to study pseudorapidity distributions of charged particles.

The problem of the correct definition of the interaction area is a central one both for the final state and production saturation models. Indeed, the centrality dependence of observables like the minijet multiplicity per participant is very sensitive to the actual definition, which may lead to qualitative different behaviours. For this reason, we believe that we should avoid introducing arbitrary parameters in this definition and proposed a way to do that by use of the Glauber model of nuclear collisions.

Discriminating among the various saturation mechanism described in this chapter is possible by the combined study of the centrality, pseudorapidity and energy dependence of the charged particle multiplicity. Present RHIC data at $\sqrt{s} = 130$ GeV seem not to privilege one or another. The forthcoming data at $\sqrt{s} = 200$ GeV might give further indications but to really say a final word we have probably to wait for data from the LHC.

Chapter 5

Minijet transverse spectrum

The purpose of this chapter is to discuss the effects of the rescatterings on the minijet transverse spectrum in the case of hadron-nucleus interactions (hA, for brevity). Being intermediate between hadron-hadron (hh) and nucleus-nucleus (AA) interactions, in hA collisions the theoretical models can be tested against experimental data in a situation where further nuclear effects are absent, like, e.g., the formation of a hot and dense medium which can further modify the transverse spectrum via energy loss [9, 93]. Therefore a detailed understanding of hA collisions represents an important baseline for the generalization to AA collisions [70, 91] and for the discovery of novel physical effects [69, 101].
Besides its intrinsic interest, the inclusion of semihard rescatterings in the computation of the transverse spectrum was advocated by many authors [57, 68, 86, 89, 90] as the basic mechanism underlying the Cronin effect [119], namely the deformation of the hadron p_t spectra in nuclear collisions as compared with the expectations of a single large-p_t production mechanism. Multiple parton collisions have also been related to higher-twist parton distributions [44, 72, 81]. A nonperturbative study of the transverse spectrum in hA collisions in the framework of the McLerran-Venugopalan model for nuclear and hadronic collisions was presented in [65, 66].

After the introduction of semihard parton rescatterings, integrated quantities such as the semihard cross section and the minijet multiplicity show a weak dependence on the infrared cutoff needed to regularize the infrared divergences arising in perturbative computations [3, 17]. Conversely, it will be shown that differential quantities such as the minijet p_t spectrum are more sensitive to the detailed dynamics of the interaction and show a stronger dependence on the cutoff, if only logarithmic. To reduce this dependence on the cutoff one needs to improve the picture of the dynamics further by also including gluon radiation in the interaction process. Some steps along this line in the case of deep inelastic electron-nucleus scattering were presented in [44]. In this paper, however, we neglect the problem of the gluon radiation and concentrate on the effects of elastic rescatterings.

The deformation of the high-p_t hadron spectra which leads to the Cronin effect was studied in terms of semihard parton rescatterings in Refs. [57, 68, 86, 89], where partons that suffered up to two scatterings where included. This leads to a good description of the data for pA collisions up to $\sqrt{s} = 39$ GeV in the hadron-nucleon center of mass frame. However, the two-scattering approximation breaks down at higher energies, except

at very high p_t, and the whole wounded parton transverse spectrum is needed. More phenomenological approaches [90, 91] model the effects of multiple scattering as Gaussian p_t broadening for each rescattering suffered by a parton. A random-walk model of the multiple scatterings was proposed in [70].

In Sec. 5.1 we discuss the inclusive minijet transverse spectrum with particular emphasis on the mechanism of subtraction of infrared divergences, which is explicitly implemented in our approach. Results of numerical evaluations of the inclusive spectra of minijets in hadron-nucleus collisions are presented in Sec. 5.3. Finally, Sec. 5.4 is devoted to a concluding summary. Some technical issues are discussed in Appendix A.

5.1 Inclusive minijet transverse spectrum

We can expand the average number of projectile wounded partons [Eq. (3.1.7)] at a given x and b in a collision with impact parameter β, in the following way[1]:

$$W_h(x,b,\beta) = \Gamma_h(x,b-\beta)\sum_{\nu=1}^{\infty}\frac{\langle n_A(x,b)\rangle^\nu}{\nu!}\,e^{-\langle n_A(x,b)\rangle}\ ,$$

where $\langle n_A(x,b)\rangle \equiv \int dx'\Gamma_A(x',b)\sigma(xx')$ is the average number of scatterings of a projectile parton at a given x and b [19]. The average number of wounded partons is then given by the average number of incoming partons Γ_h multiplied by the probability of having at least one semihard scattering, which is given by a Poisson distribution in the number ν of scatterings, with an average number $\langle\nu\rangle = \langle n_A(x,b)\rangle$. Therefore, we can obtain the inclusive differential distribution in p_t by introducing a constraint in the transverse momentum integrals that give the integrated parton-parton cross sections in the expression above:

$$\begin{aligned}\frac{dW_h}{d^2p_t}(x,b,\beta) \ &= \Gamma_h(x,b-\beta)\sum_{\nu=1}^{\infty}\frac{1}{\nu!}\int\Gamma_A(x_1',b)\ldots\Gamma_A(x_\nu',b)\,e^{-\int dx'\Gamma_A(x',b)\sigma(xx')} \\ &\quad\times\frac{d\sigma}{d^2k_1}\ldots\frac{d\sigma}{d^2k_\nu}\,\delta^{(2)}(\mathbf{k}_1+\cdots+\mathbf{k}_\nu-\mathbf{p_t})\,d^2k_1\ldots d^2k_\nu\,dx_1'\ldots dx_\nu'\ .\end{aligned} \tag{5.1.1}$$

The limits of integration on x_i' and x' are respectively $xx_i's \geq 4k_i^2$ and $xx's \geq 4p_0^2$, respectively, and all the distribution functions are evaluated for simplicity at a fixed scale.

By using the above formula one can study the p_t broadening of a wounded parton, in particular the square root of the average transverse momentum squared acquired through its path across the nucleus. Consider a single projectile parton with fixed x and b. The probability that it acquires a certain p_t after the collision is given by Eq. (5.1.1) divided by the number, $\Gamma_h(x,b-\beta)$, of incoming partons:

$$\frac{d\mathcal{P}_A(x,b)}{d^2p_t} = \frac{dW_h}{d^2p_t}(x,b,\beta)\frac{1}{\Gamma_h(x,b-\beta)}\ .$$

[1] In this section we changed slightly the notation and used $W \equiv N^{mj}$.

Then, the average transverse momentum squared of a wounded parton is given by $\langle p_t^2(x,b)\rangle_A = \langle\langle p_t^2\rangle\rangle/\langle\langle 1\rangle\rangle$, where $\langle\langle f(p_t)\rangle\rangle = \int d^2p_t f(p_t) d\mathcal{P}_A/d^2p_t$. By exploiting the azimuthal symmetry of the differential parton-parton cross sections, and the symmetry of (5.1.1) under exchanges of k_i, it is easy to see that

$$\langle p_t^2(x,b)\rangle_A = \frac{1}{\mathcal{P}_A}\int d^2p_t dx' p_t^2 \frac{d\sigma}{d^2p_t}(xx')\Gamma_A(x',b) = \langle p_t^2(x,b)\rangle_1 \frac{\langle n_A(x,b)\rangle}{\mathcal{P}_A(x,b)} \ , \tag{5.1.2}$$

where $\langle p_t^2(x,b)\rangle_1 = \int d^2p_t dx' p_t^2 \frac{d\sigma(xx')}{d^2p_t}\Gamma_A(x',b)/\int dx'\sigma(xx')\Gamma_A(x',b)$ is the average transverse momentum squared in a single parton-parton collision. The p_t broadening of the wounded partons in a hA collision is then given by the p_t broadening in a single collision multiplied by the average number of rescatterings suffered by a wounded parton. A similar result for the p_t broadening of a fast parton traversing a nuclear medium was derived in Ref. [52]. Two interesting limits can be considered:

$$\langle p_t^2(x,b)\rangle_A \sim \begin{cases} \langle p_t^2(x,b)\rangle_1 & \text{as } p_0\to\infty \\ \langle p_t^2(x,b)\rangle_1\langle n_A(x,b)\rangle & \text{as } p_0\to 0 \ . \end{cases} \tag{5.1.3}$$

Since the minijet yield is dominated by transverse momenta of the order of the cutoff, these two limits say roughly that the minijets at high p_t [i.e., high p_0 in Eq. (5.1.3)] suffer mainly one scattering. Conversely, at low p_t [i.e., low p_0 in Eq. (5.1.3)] they undergo a random walk in the transverse momentum plane and the broadening is proportional to the average number of steps in the random walk, $\langle n_A\rangle$. This picture will be studied in more detail in Sec. 5.3.1.

An explicit formula for the transverse spectrum can be obtained by studying its Fourier transform, since all the convolutions in Eq. (5.1.1) turn into products and the sum over ν may be explicitly performed. To this end, we introduce the Fourier transform of the parton-parton scattering cross section

$$\tilde\sigma(v;xx') = \int d^2k\, e^{i\mathbf{k}\cdot\boldsymbol{v}}\frac{d\sigma}{d^2k}(xx') \ .$$

Note that $\tilde\sigma(0;xx') = \sigma(xx')$ and that due to the azimuthal symmetry of $d\sigma/d^2k$, its Fourier transform depends only on the modulus, v, of $\boldsymbol{v}$. Then the transverse spectrum [Eq. (5.1.1)] may be written as:

$$\frac{dW_h}{d^2p_t}(x,b,\beta) = \Gamma_h(x,b-\beta)\int\frac{d^2v}{(2\pi)^2}\, e^{-i\mathbf{p_t}\cdot\boldsymbol{v}}\,\widetilde{W}_h(v;x,b) \ , \tag{5.1.4}$$

where

$$\begin{aligned}\widetilde{W}_h(v;x,b) &= \sum_{\nu=1}^{\infty}\frac{1}{\nu!}\left[\int dx'\Gamma_A(x',b)\tilde\sigma(v;xx')\right]^{\nu} e^{-\int dx'\Gamma_A(x',b)\tilde\sigma(0;xx')} \\ &= e^{\int dx'\Gamma_A(x',b)\{\tilde\sigma(v;xx')-\tilde\sigma(0;xx')\}} - e^{-\int dx'\Gamma_A(x',b)\tilde\sigma(0;xx')} \ .\end{aligned} \tag{5.1.5}$$

An immediate consequence is that the transverse spectrum has a finite limit as $p_t\to 0$, even when a cutoff on the momentum exchange is used:

$$\left.\frac{dW_h}{d^2p_t}\right|_{\mathbf{p_t}=0}(x,b,\beta) = \Gamma_h(x,b-\beta)\int\frac{d^2v}{(2\pi)^2}\widetilde{W}_h(v;x,b) \ .$$

5.2 Expansion in the number of scatterings

We can obtain an expansion of $\widetilde{W}_h$ in the number of the rescatterings suffered by the incoming parton by expanding Eq. (5.1.5) in powers of $\tilde{\sigma}$:

$$\widetilde{W}_h(v;x,b) = \sum_{\nu=1}^{\infty} \widetilde{W}_h^{(\nu)}(v;x,b) \tag{5.2.1}$$
$$= \sum_{\nu=1}^{\infty} \frac{1}{\nu!}\Big[\Big(\int dx' \Gamma_A(x',b)\big[\tilde{\sigma}(v;xx') - \tilde{\sigma}(0;xx')\big]\Big)^{\nu} - \Big(-\int dx' \Gamma_A(x',b)\tilde{\sigma}(0;xx')\Big)^{\nu}\Big] \ .$$

Coming back to the p_t space, the expansion of the transverse spectrum in number of scatterings reads

$$\frac{dW_h}{d^2p_t}(x,b,\beta) = \sum_{\nu=1}^{\infty} \frac{dW_h^{(\nu)}}{d^2p_t}(x,b,\beta) = \sum_{\nu=1}^{\infty} \Gamma_h(x,b-\beta) \int \frac{d^2v}{(2\pi)^2}\, e^{-i\mathbf{p}_t\cdot\boldsymbol{v}} \widetilde{W}_h^{(\nu)}(v;x,b) \ . \tag{5.2.2}$$

The series (5.2.1) can be obtained also by expanding $\widetilde{W}(v)$ around $v=0$. Since the variable v is Fourier-conjugated to p_t, the expansion of the transverse spectrum [Eq. (5.2.2)] will be valid at high p_t and we expect a breakdown of any truncation at sufficiently low momentum. Note that we can obtain this high-p_t expansion of the spectrum directly in p_t space by expanding the exponential in Eq. (5.1.1) and collecting the terms of the same order in σ. As an example, the first three terms, Eqs. (A.4), (A.5) and (A.9), can be found in the appendices.

5.2.1 Cancellation of the divergences

All terms of expansion (5.2.2) are divergent in the infrared region, so that we need to cure them with the regulator p_0. Nevertheless, the infrared divergences are already regularized to a large extent by the subtraction terms originated by the expansion of $\exp[-\langle n_A(x,b)\rangle]$ appearing in Eq. (5.1.1); namely by the constraint of probability conservation. This cancellation mechanism was observed also in Ref.[57] for the two-scattering term and in Ref.[93] in a different context.

It is instructive to examine in detail how the subtraction works for the lower order terms of the expansion. We start by considering the case of a single rescattering ($\nu=2$). To simplify the notation we write the elementary differential cross section $d\sigma/d^2k$ as $\sigma(\mathbf{k})$, and note that it depends only on the modulus k of the momentum. By expressing the semihard cross section as $\sigma = \int d^2k\sigma(\mathbf{k})$ the term of order σ^2 may be written as

$$\frac{dW_h^{(2)}}{d^2p_t}(x,b,\beta) = \Gamma_h(x,b-\beta) \int dx_1' dx_2' d^2k_1 d^2k_2 \Gamma_A(x_1',b)\Gamma_A(x_2',b) \tag{5.2.3}$$
$$\times \frac{\sigma(\mathbf{k}_1)\sigma(\mathbf{k}_2)}{2}\Big[\delta^{(2)}(\mathbf{k}_1+\mathbf{k}_2-\mathbf{p}_t) - \delta^{(2)}(\mathbf{k}_1-\mathbf{p}_t) - \delta^{(2)}(\mathbf{k}_2-\mathbf{p}_t)\Big] \ ,$$

where the first term in the square brackets represents two successive scatterings with no absorption. The two negative terms are the corrections induced by the expansion of the

absorption factor $\exp[-\langle n_A(x,b)\rangle]$ of the single-scattering term, $\nu = 1$ in Eq. (5.1.1), and correspond to a single-scattering along with the effects of absorption in the initial or final state. The expression we obtained is symmetric in the integration variables $\mathbf{k}_1$ and $\mathbf{k}_2$. The cutoff dependence is originated by the singular behavior of the integrand for $\mathbf{k}_1 \approx 0$ or for $\mathbf{k}_2 \approx 0$, since the δ functions in the square brackets prevent the possibility of $\mathbf{k}_1$ and $\mathbf{k}_2$ being both zero at the same time. Because of the symmetry under the exchange $\mathbf{k}_1 \leftrightarrow \mathbf{k}_2$, to study the cutoff dependence of Eq. (5.2.3) it is enough to discuss the integration around $\mathbf{k}_1 = 0$. In the region $\mathbf{k}_1 \approx 0$ the term $\delta^{(2)}(\mathbf{k}_1 - \mathbf{p}_t)$ does not contribute, as long as $\mathbf{p}_t$ is finite. The integration in $\mathbf{k}_2$ is done with the help of the δ functions, and one obtains

$$\int d^2k_1 \sigma(\mathbf{k}_1)\Big[\sigma(\mathbf{p_t} - \mathbf{k}_1) - \sigma(\mathbf{p_t})\Big] \ .$$

On the other hand, for $\mathbf{k}_1 \approx 0$, one may use the expansion $\sigma(\mathbf{p_t} - \mathbf{k}_1) \simeq \sigma(\mathbf{p_t}) - \sigma'(\mathbf{p_t})\mathbf{p}_t \cdot \mathbf{k}_1/p_t$, where $\mathbf{p}_t \cdot \mathbf{k}_1$ represents the scalar product of the two vectors, and $\sigma'(\mathbf{p_t}) = \frac{d}{d|\mathbf{p_t}|}\sigma(\mathbf{p_t})$ depends only on the modulus of $\mathbf{p_t}$. One is left with

$$-\frac{\sigma'(\mathbf{p_t})}{p_t}\int \mathbf{p}_t \cdot \mathbf{k}_1 \sigma(\mathbf{k}_1) d^2k_1 = 0 \ ,$$

where the vanishing result is due to the azimuthal symmetry of $\sigma(\mathbf{k}_1)$. The dominant contribution to the integral comes therefore from the next term in the expansion of $\sigma(\mathbf{k}_1 - \mathbf{p}_t)$, which goes as k_1^2. Hence the resulting singularity is only logarithmic in p_0, since $\sigma(\mathbf{k}) \sim k^{-4}$ as $k \to 0$. The subtraction terms, originated by the absorption factor $\exp[-\langle n_A(x,b)\rangle]$ in Eq. (5.2.3), have canceled the singularity of the rescattering term almost completely. This feature is common to all the terms of expansion (5.2.3) as is discussed briefly at the end of Appendix A.1, where the three-scattering term is discussed in detail.

Before concluding this section we want to point out that for the numerical computation of the series it is necessary to symmetrize each of its terms *after* having exploited the delta functions. A general method to do this is explained at length in Appendix A.2.

5.3 Numerical results and discussion

In this section we discuss in detail, both qualitatively and quantitatively, the modifications induced by the rescatterings on the minijet inclusive transverse spectrum. We consider a proton-lead collision with center of mass energy $\sqrt{s} = 6$ TeV in the proton-nucleon center of mass frame and impact parameter $\beta = 0$. In the numerical computations we used the leading order perturbative parton-parton cross section with a mass regulator $m \equiv p_0$:

$$\frac{d\sigma}{d^2p}(xx') = k\frac{9\pi\alpha_s(Q)^2}{(p^2+m^2)^2}\theta\big(xx's - 4(p^2+m^2)\big)\theta\big(1-x\big)\theta\big(1-x'\big)$$

where k is the k factor that simulates next-to-leading order corrections (we chose $k = 2$). The single-parton nuclear distribution function has been taken to be factorized in x and b,

$$\Gamma_A(x,b) = \tau_A(b)G(x,Q) \ ,$$

where τ_A is the nuclear thickness function normalized to A and G is the proton distribution function. We evaluated the strong coupling constant and the nuclear distribution functions at a fixed scale $Q = m$. In the computations we used a hard-sphere geometry

$$\tau_A(b) = A\frac{3}{2\pi R^3}\sqrt{R^2 - b^2}\theta(R^2 - b^2) \ ,$$

where $R = 1.12A^{1/3}$ is the nuclear radius. For G we used the GRV98LO parameterization [135]. At low p_t the spectrum is obtained by computing numerically the Fourier transform in Eq. (5.1.4), but at high p_t the result begins to oscillate too much, and in that region the spectrum was computed by using the expansion in the number of scattering up to the three-scattering term [the formulae actually used, Eqs. (A.4), (A.7) and (A.11), are discussed in Appendix A.2]. We checked that the spectrum obtained by Fourier transformation matched the expansion smoothly.

5.3.1 Effects of rescatterings

In this section we discuss the projectile and the target transverse spectrum averaged over a given rapidity interval,

$$\frac{dW_h}{d^2p_t}(\beta, \eta_{min}, \eta_{max}) = \frac{1}{\eta_{max} - \eta_{min}} \int_{\eta\in[\eta_{min},\eta_{max}]} dx d^2b \ \frac{dW_h}{d^2p_t}(x, b, \beta) \ , \tag{5.3.1}$$

where we approximated the pseudorapidity by $\eta = \log(x\sqrt{s}/p_0)$. The target spectrum dW_A/d^2p_t is obtained by interchanging h and A in Eq. (5.3.1). Note that now we are taking into account all possible rescatterings of the target, as well.

In Fig. 5.1 we compare the full transverse spectrum (solid line) with its expansion in the number of scatterings up to three scatterings (dotted and dashed lines). We show both the projectile and target minijet spectrum in a pseudorapidity region $\eta \in [3, 4]$ for the projectile and $\eta \in [-4, -3]$ for the target. Note that the rapidity is defined with reference to the projectile hadron direction of motion. The choice of a forward region (backward for the target) is done to enhance the effect of the rescatterings and to better discuss the deformation induced in the spectrum. Indeed, in those regions the average fractional momentum of an incoming parton is large, so that the number of available target partons is large and the probability of rescattering becomes large.

First we look at the projectile spectrum. At high p_t the spectrum is enhanced with respect to the single scattering approximation because of the p_t broadening induced by the rescatterings. As p_t is further increased it approaches the single-scattering spectrum, as expected on general grounds when the p_t distribution of the elementary scattering follows a power law. This can be understood qualitatively by looking at the path in p_t space followed by the incoming parton. Given a final large p_t, due to the leading divergences in Eq. (5.2.3), the leading processes to obtain that p_t with two semihard scatterings are a first scattering with momentum transfer $q_1 \approx p_0$ followed by a second one with $q_2 \approx p_t$, and vice versa. For an analogous reason, the leading configuration to reach the final p_t with three scatterings is $q_1 \approx p_t$ plus $q_2 \approx q_3 \approx p_0$ and permutations. This sequence of three scatterings is less probable than the process with two scatterings as p_t increases because the fraction of phase space volume that this process occupies decreases much faster with p_t than in the two-scattering case. For an analogous reason

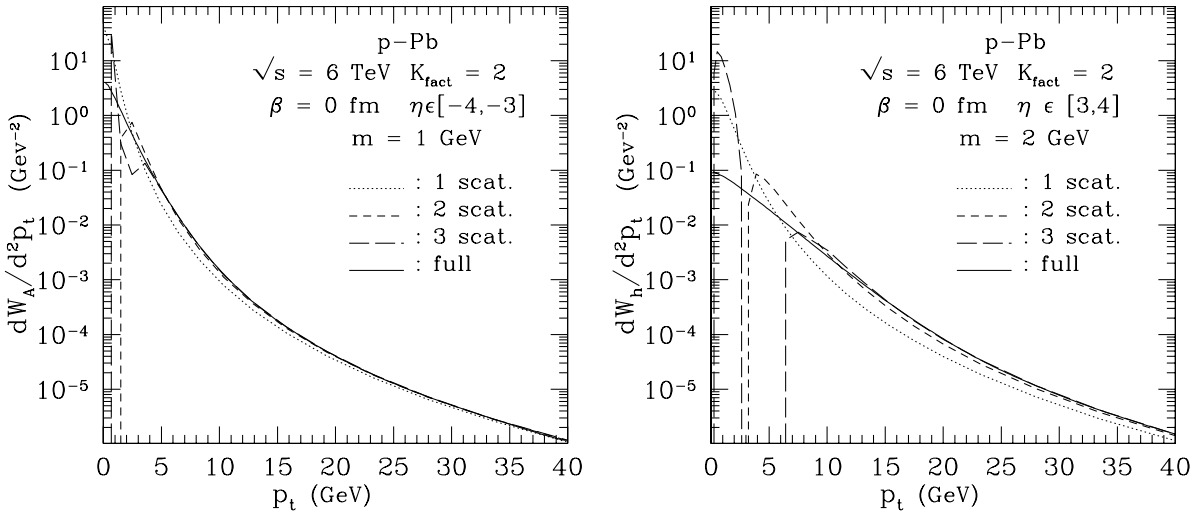

Figure 5.1: *Left:* Target p_t spectrum for $\eta \in [-4,-3]$. *Right:* Projectile p_t spectrum for $\eta \in [3,4]$. The full transverse spectrum (solid line) is compared with the one-, two- and three-scattering approximations (viz., dotted, short-dashed and long-dashed lines).

the relative importance of the two-scattering term with respect to the single-scattering term also decreases as p_t increases. In conclusion as p_t increases the average number of scatterings per parton decreases, and eventually the spectrum is well described by the single-scattering approximation.

At intermediate p_t the average number of scatterings per parton increases and the shape of the spectrum is more and more distorted with respect to the single-scattering case. In fact, the fraction of phase space available to the leading configuration of a multiple scattering process ($q_1 \approx p_t$, $q_2 \approx \cdots \approx q_n \approx p_0$ and permutations) increases as p_t decreases. However, this is not the only mechanism at work. Indeed, in our computation each wounded parton is counted as one minijet in the final state, independently of the number of rescatterings. On the other hand, in the single-scattering approximation one identifies the number of minijets in the final state with the number of parton-parton collision. This leads to an overestimate of the jet multiplicity and to a divergence of the spectrum at $p_t = 0$ as p_0 goes to zero. Therefore at low p_t the minijet yield is more and more suppressed with respect to the single scattering approximation.

At very low transverse momentum $p_t \lesssim p_0$ a parton undergoes a large number of rescatterings, all with $q_i \approx p_0$. Hence the parton performs a random walk in the transverse plane and the spectrum becomes flat as $p_t \to 0$ because the phase space becomes isotropically populated. This shows that at very low p_t multiple semihard scatterings are consistent with the random-walk model of Ref. [70], while at moderate and high-p_t the physical picture is rather different.

By comparing the results for the projectile and target transverse spectrum one "sees" that a projectile parton is traversing a very dense target and the effects of the rescatterings are large. On the contrary, a target parton sees a rather dilute system, and its minijet spectrum does not differ too much from the single-scattering result, except at very low

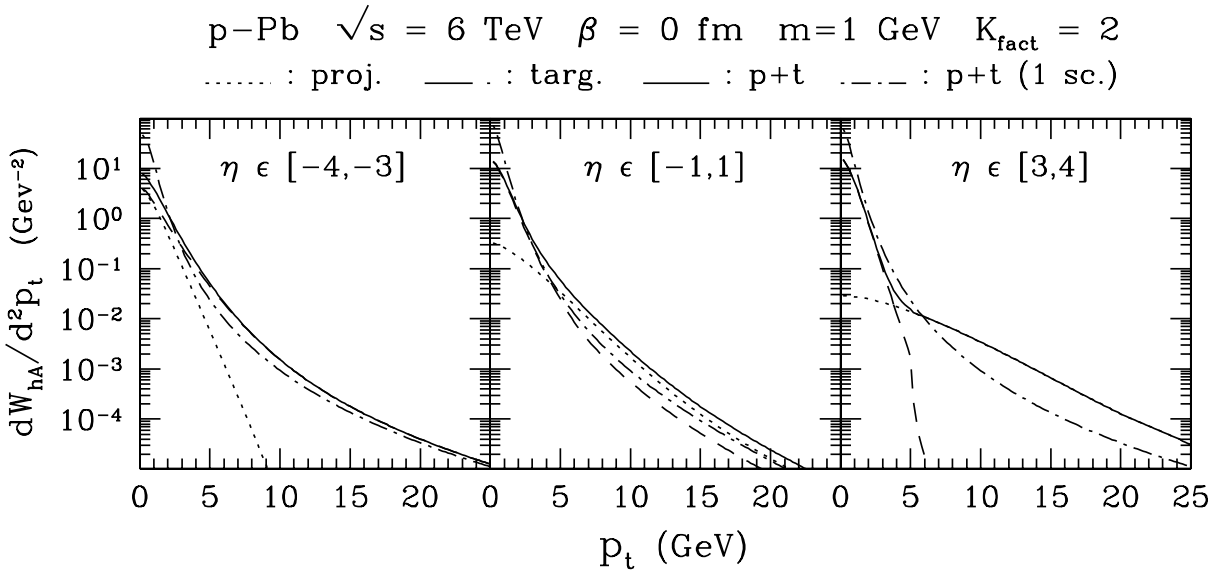

Figure 5.2: Projectile plus target p_t spectrum (solid line) at different rapidities compared to the result of the one-scattering approximation (dot-dashed line). Also shown are the contributions of the projectile minijets (dotted line) and the target minijets (dashed line).

p_t. Moreover the changes induced by the rescatterings on integrated quantities, like those entering in the expression for the hadron-nucleus cross section, are minimal. This is consistent with our approximation of not including rescatterings for the target partons to obtain analytical formulae for the hadron-nucleus cross section. One can also see that the three-scattering approximation well describes the projectile spectrum for $p_t \gtrsim 15$ GeV, while it breaks down completely at $p_t \lesssim 7$ GeV, where it becomes negative. For the target spectrum the three-scattering approximation is not accurate for $p_t \lesssim 4$ GeV.

5.3.2 Minijet inclusive transverse spectrum

In this section we study the minijet transverse spectrum resulting from the sum of the transverse spectra of the projectile and target wounded partons:

$$\frac{dW_{hA}}{d^2p_t}(\beta,\eta_{min},\eta_{max}) = \frac{1}{\eta_{max}-\eta_{min}}\int_{\eta\in[\eta_{min},\eta_{max}]} dx d^2b \left(\frac{dW_h}{d^2p_t}(x,b,\beta)+\frac{dW_A}{d^2p_t}(x,b,\beta)\right) . \quad (5.3.2)$$

We analyze the spectrum in three rapidity regions, namely $\eta \in [-4,-3]$, $\eta \in [-1,1]$ and $\eta \in [3,4]$ (respectively "backward", "central" and "forward" with reference to the projectile direction of motion). While the target partons basically do not suffer any rescattering in all three regions, the projectile partons undergo many rescatterings in the forward region, some in the central region and basically no one backwards.

In Fig. 5.2 we show the spectrum (5.3.2) (solid line) and the contributions of the projectile and of the target (dotted and dashed lines, respectively). For comparison also the total spectrum obtained in the one-scattering approximation is also plotted (dot-dashed line). The spectra are computed with a regulating mass $m = 1$ GeV.
In the backward region both the projectile and the target suffer mainly one scattering

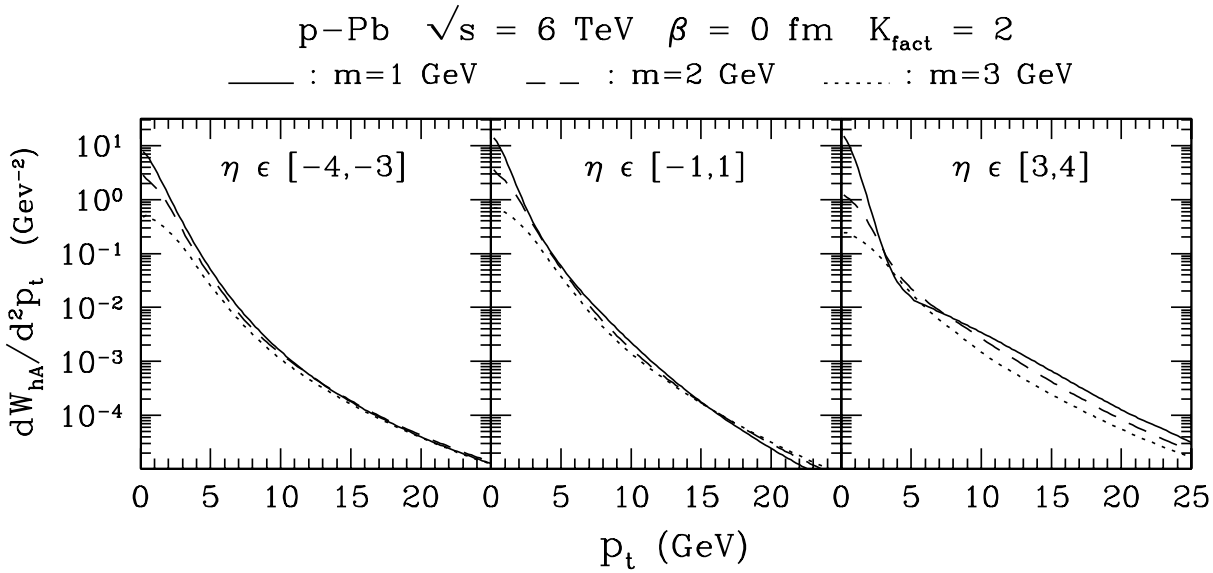

Figure 5.3: Regulator dependence of the projectile plus target p_t spectrum at different rapidities for $m = 1, 2$ and 3 GeV (viz., solid, dashed and dotted lines).

over all the p_t range except at $p_t \sim 0$, and the spectrum is dominated almost everywhere by target minijets.
In central and forward regions the target jets still suffer basically one scattering over all the p_t range. Conversely, the projectile crosses a denser and denser target and undergoes an average number of rescatterings that increases with pseudorapidity. This means that at low p_t the projectile spectrum is very reduced with respect to the one-scattering approximation, and the minijet yield may become negligible with respect to the minijet yield from the target. The overall effect is that at low p_t the spectrum is dominated by minijet production from the target, while at intermediate and high p_t it is dominated by minijet production from the projectile.
At very forward rapidities this effect becomes quite dramatic and the spectrum acquires a structured shape: it follows the inverse power behaviour of the single-scattering term at high p_t, it is concave at intermediate p_t because of the suppression of the projectile minijets, and becomes convex again at low p_t, where the target begins to dominate.

In Fig.5.3 we study the dependence of the spectrum on the choice of the cutoff, and plot the result for $m = 1, 2$ and 3 GeV. The deformation of the spectrum decreases as the regulator increases (indeed, the average number of rescattering decreases) and for $m \gtrsim 3$ GeV it begins to become negligible.

The effects of the rescatterings are better displayed by studying the ratio of the full transverse spectrum and the single-scattering approximation,

$$R_\beta(p_t) = \frac{dW_{hA}/d^2p_t}{dW^{(1)}_{hA}/d^2p_t} = \frac{dW_{hA}/d^2p_t}{A_\beta \; dW^{(1)}_{pp}/d^2p_t} \; , \tag{5.3.3}$$

where $A_\beta = \int d^2b \tau_h(b-\beta)\tau_A(b)$ is the number of target nucleons interacting with the projectile at a given impact parameter.

In Fig.5.4 we plotted the ratio $R_\beta(p_t)$, which measures the Cronin effect for minijet

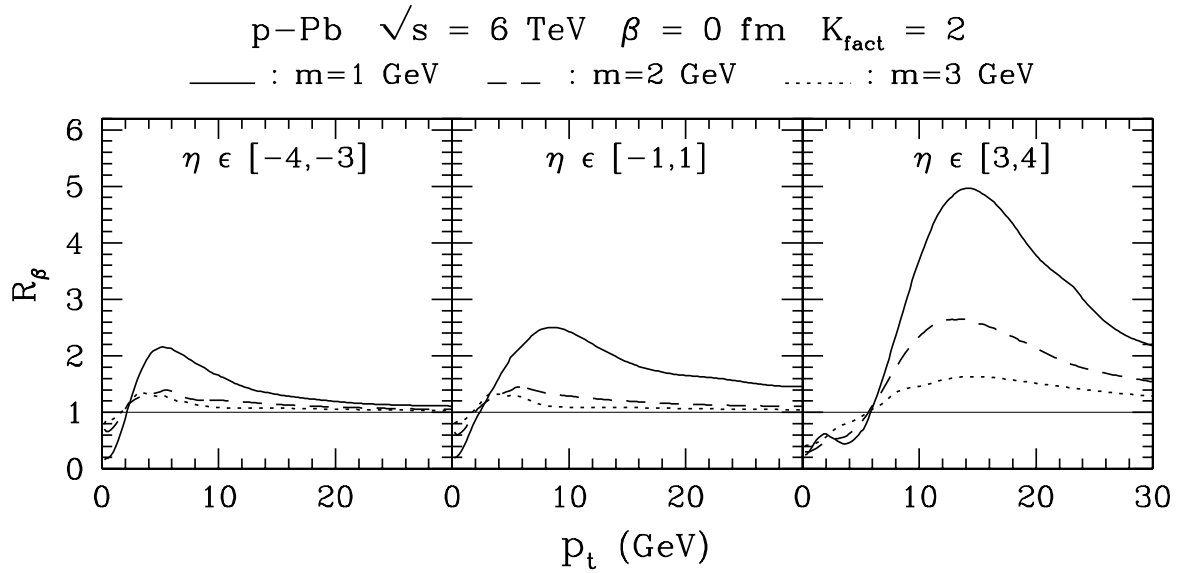

Figure 5.4: Ratio of the full projectile plus parton p_t spectrum to the one-scattering approximation at different rapidities and for $m = 1, 2, 3$ GeV (viz., solid, dashed and dotted line).

production, computed with three different regulators $m = 1, 2, 3$ GeV. At $m = 3$ GeV the effect of the rescatterings is rather small in all the three rapidity intervals, except at very low p_t, and does not affect the integrated quantities like the average number of minijets. As the regulating mass is decreased the rescatterings begin to show up, and lead to a large effect in the forward region.

The ratio $R_\beta(p_t)$ is characterized by three quantities: the momentum $p_\times$ where the R_β crosses 1, the momentum p_M where it reaches the maximum and the height R_M of the maximum. The sensitivity of $p_\times$ on the cutoff decreases as the pseudorapidity increases. Loosely speaking, when the average number of scatterings is high, as it is the case at $p_t \simeq p_\times$, the jets loose memory of p_0, which gives the order of magnitude of the typical momentum exchanged in each collision. p_M shows a slightly larger sensitivity on the regulator, since it lies in a region where the average number of scatterings is smaller. This behaviour is very different from the conclusions drawn by considering only the expansion up to two scatterings, where both $p_\times$ and p_M are proportional to p_0 [86]. In fact, at low center of mass energies the two-scattering is a good approximation in all rapidity ranges, except may be very forward. However, it breaks down in any case at transverse momenta comparable to the regulator p_0. Therefore, while most of the spectrum is well described by the two-scattering approximation, the behaviour of $p_\times$ and p_M is not.

On the other hand, the height of the peak is much more sensitive to the cutoff, since its leading term is roughly proportional to some power of the logarithm of the regulator:

$$\left[\frac{dW_{hA}}{d^2p_t} - \frac{dW^{(1)}_{hA}}{d^2p_t}\right]_{p_t=p_M} \underset{p_0\to 0}{\sim} \left[\log\left(\frac{p_M^2}{p_0^2}\right)\right]^{\langle n_{resc}(p_M)\rangle}$$

Since p_M is not very large, the average number of rescatterings at that value of the transverse momentum, $\langle n_{resc}(p_M)\rangle$, is much greater than 1 and the sensitivity of R_M on p_0 is high. At high p_t the average number of rescatterings tends to zero, so the sensitivity

of the R_β on p_0 decreases and disappears at very large transverse momenta.

Note that the peak is located in a p_t region, where soft interactions (which have been disregarded in our approach) are expected to be negligible, therefore in that region our perturbative computations should describe the spectrum almost completely. Following Ref. [86] we might interpret p_0 as the momentum scale at which the interaction deviates from the perturbative computations. With this interpretation p_0 would acquire a physical meaning: though Physics does not know about the artificial subdivision in hard and soft interactions, it is a well defined question to ask up to what scale the perturbative computations are good. If the collision dynamics would be determined by parton multiple elastic scatterings alone, then the measure of the height of the peak would be a way of measuring p_0.
On the other hand, the sensitivity of R_β on p_0 is rather signaling a weakness in our description of the dynamics underlying the hadron-nucleus collision. We expect that such a sensitivity will be considerably reduced when also including in the dynamics the gluon radiation emitted by the multiply scattering partons. Some of the effects of the radiation on the transverse spectrum might however be described by the parameter p_0 in our model, in which radiation is neglected. Since the inclusion of gluon radiation in the dynamics would introduce new physical scales, like the radiation formation time, related to the energy of the collision and the nuclear size, we would expect in any case that the value of p_0 will depend on $\sqrt{s}$ and A.

5.4 Conclusions

The purpose of this chapter is to draw attention to some of the advantages of studying hadron-nucleus semihard interactions at the LHC. As in the case of lower energies, hA interactions represent an important intermediate step to relate hh and AA reactions, being much simpler to understand as compared with the latter. Moreover, even at higher energies, like those obtainable at RHIC and LHC, in hA collisions we do not expect the formation of a dense and hot system, like the quark-gluon plasma, so that one can study directly the nuclear modification of the dynamics without the need of disentangling the effects of the structure of the target and those due to the formation and evolution of the dense system. Hadron-nucleus interactions represent therefore the baseline for the detection and the study of new phenomena peculiar to AA collisions.

We faced the problem of unitarity corrections to the semihard cross section by including explicitly semihard parton rescatterings in the collision dynamics, exploiting the self-shadowing property of the semihard interactions. In the interaction mechanism we took into account just elastic parton-parton collisions, while we neglected the production processes at the partonic level (e.g., all $2 \to 3$ etc. elementary partonic processes), whose inclusion represents a non-trivial step in our approach and deserves further study.
Contrary to the case of AA collisions, it is possible to obtain closed analytical expressions for the semihard hA cross section, [see Eq. (2.5.15)]. To that purpose a crucial assumption has been to consider the hadron as a dilute system, so that rescatterings of nuclear partons can be neglected, while rescatterings of the projectile are fully taken into account. In our expressions we have disregarded correlations in the nuclear multiparton distributions, whose effect may nevertheless be studied in a straightforward way within

the present functional approach.
We have then focused on the inclusive minijet transverse spectrum at fixed impact parameter [Eq. (5.1.4)] which is influenced in a more direct way by rescatterings. The modifications of the transverse spectrum induced by the semihard rescatterings of the projectile partons is emphasized in the ratio $R_\beta(p_t)$, [Eq. (5.3.3)], defined as our p_t spectrum divided by the impulse approximation. In particular, we have evaluated it at $\beta = 0$ for different values of the regulator p_0. The results are described by the values of $p_\times$ (defined by $R_\beta(p_\times) = 1$), p_M (which is the value of p_t that maximizes the ratio) and R_M (which is the maximum of R_β). We obtain that both $p_\times$ and p_M depend weakly on p_0, while R_M has, on the contrary, a strong dependence on p_0 also when the regulator is rather small. Therefore, the results for the spectrum also allows us to identify the limits of the picture of the dynamics considered in this paper. Analogously to the average transverse energy and the number of minijets in AA collisions [3], some of the features of R_β, like $p_\times$ and p_M, show a tendency toward a limiting value at small p_0. All these quantities depend therefore only marginally on details of the dynamics which have not been taken into account in the present approach. Conversely, the limits of the simplified picture of the interaction show up in R_M. Because of its strong dependence on p_0, in order to describe the spectrum one needs to fix the value of p_0 experimentally by measuring R_M. This feature might be not so unpleasant, because if one limits the analysis to the inclusive transverse spectrum of minijets in hA collisions, all the effects which are not taken into account in the interaction (like the gluon radiation in the elementary collision process) are summarized by the value of a single phenomenological parameter. However this feature will not hold any further if one had to evaluate more differential properties of the produced state, which can be properly discussed only after introducing explicitly further details into the description of the elementary interaction process.
The experimental measure of the Cronin effect in minijet production in hA collisions would therefore be of major importance: it would allow one to establish the correctness of the whole approach described here and it would represent the basis for a deeper insight in the semi hard interaction dynamics both for hA and AA collisions.

Appendix A

More on the transverse spectrum

A.1 Cancellation of the divergences in the three-scattering term

Hereafter we consider in detail the cancellation of the divergences in the term with three scatterings:

$$\begin{aligned}\frac{dW_h^{(3)}}{d^2p_t}(x,b,\beta) = \Gamma_h(x,b-\beta)\int \Gamma_A(x_1',b)\Gamma_A(x_2',b)\Gamma_A(x_3',b)dx_1'dx_2'dx_3'd^2k_1d^2k_2d^2k_3 \\ \times\frac{\sigma(\mathbf{k}_1)\sigma(\mathbf{k}_2)\sigma(\mathbf{k}_3)}{6}\Big[\delta^{(2)}(\mathbf{k}_1+\mathbf{k}_2+\mathbf{k}_3-\mathbf{p}_t) \\ -\delta^{(2)}(\mathbf{k}_1+\mathbf{k}_2-\mathbf{p}_t)-\delta^{(2)}(\mathbf{k}_2+\mathbf{k}_3-\mathbf{p}_t)-\delta^{(2)}(\mathbf{k}_3+\mathbf{k}_1-\mathbf{p}_t) \\ +\delta^{(2)}(\mathbf{k}_1-\mathbf{p}_t)+\delta^{(2)}(\mathbf{k}_2-\mathbf{p}_t)+\delta^{(2)}(\mathbf{k}_3-\mathbf{p}_t)\Big]\ . \qquad (A.1)\end{aligned}$$

The different δ functions in Eq. (A.1) correspond to all the terms of order σ^3 in Eq. (5.1.1) and represent the triple scattering term together with all subtraction terms induced by the expansion of the absorption factor $\exp[-\langle n_A(x,b)\rangle]$ of the double- and of the single-scattering terms. The expression has been symmetrized with respect to $\mathbf{k}_1$, $\mathbf{k}_2$ and $\mathbf{k}_3$ and is singular for $\mathbf{k}_1=0$, $\mathbf{k}_2=0$ and $\mathbf{k}_3=0$. The δ functions in (A.1) prevent the tree momenta to be close to zero at the same time, then we start by discussing the most singular configuration corresponding to two integration variables both close to zero. Given the symmetry of the integrand it is enough to study the integration region with $\mathbf{k}_1\approx 0$, $\mathbf{k}_2\approx 0$. In this region the terms $\delta^{(2)}(\mathbf{k}_1+\mathbf{k}_2-\mathbf{p}_t)$, $\delta^{(2)}(\mathbf{k}_1-\mathbf{p}_t)$ and $\delta^{(2)}(\mathbf{k}_2-\mathbf{p}_t)$ do not contribute. The integrals on the transverse momenta are therefore written as

$$\int d^2k_1d^2k_2\sigma(\mathbf{k}_1)\sigma(\mathbf{k}_2)\Big[\sigma(\mathbf{p}_t-\mathbf{k}_1-\mathbf{k}_2)-\sigma(\mathbf{p}_t-\mathbf{k}_1)-\sigma(\mathbf{p}_t-\mathbf{k}_2)+\sigma(\mathbf{p_t})\Big]\ . \qquad (A.2)$$

In the region $\mathbf{k}_1\approx 0$, $\mathbf{k}_2\approx 0$ one may use the expansion

$$\sigma(\mathbf{p_t}-\mathbf{k})\simeq\sigma(\mathbf{p_t})-\sigma'(\mathbf{p_t})\frac{\mathbf{p_t}\cdot\mathbf{k}}{p_t}+\frac{1}{2}\left[\sigma''(\mathbf{p_t})\frac{(\mathbf{p_t}\cdot\mathbf{k})^2}{p_t^2}-\sigma'(\mathbf{p_t})\ \frac{(\mathbf{p_t}\times\mathbf{k})^2}{p_t^3}\right]\ , \qquad (A.3)$$

where $\mathbf{p_t}\times\mathbf{k}$ represents the vector product of $\mathbf{p_t}$ and $\mathbf{k}$ and $\sigma''(\mathbf{p_t})=\frac{d^2}{d|\mathbf{p_t}|^2}\sigma(\mathbf{p_t})$ depends only on the modulus of $\mathbf{p_t}$. All terms proportional to $\sigma(\mathbf{p_t})$ cancel and all the terms linear in $\mathbf{k}$ integrate to zero thanks to the azimuthal symmetry of $\sigma(\mathbf{k})$. Then one is left with

$$\begin{aligned}\int d^2k_1d^2k_2\sigma(\mathbf{k}_1)\sigma(\mathbf{k}_2)\Bigg\{\frac{\sigma''(\mathbf{p_t})}{2p_t^2}\Big[\big(\mathbf{p}_t\cdot(\mathbf{k}_1+\mathbf{k}_2)\big)^2-\big(\mathbf{p}_t\cdot\mathbf{k}_1\big)^2-\big(\mathbf{p}_t\cdot\mathbf{k}_2\big)^2\Big] \\ -\frac{\sigma'(\mathbf{p_t})}{2p_t^3}\Big[\big(\mathbf{p}_t\times(\mathbf{k}_1+\mathbf{k}_2)\big)^2-\big(\mathbf{p}_t\times\mathbf{k}_1\big)^2-\big(\mathbf{p}_t\times\mathbf{k}_2\big)^2\Big]\Bigg\}\ ,\end{aligned}$$

which simplifies to

$$\int d^2k_1 d^2k_2 \sigma(\mathbf{k}_1)\sigma(\mathbf{k}_2)\left\{\frac{\sigma''(\mathbf{p_t})}{p_t^2}\big(\mathbf{p}_t\cdot\mathbf{k}_1\big)\big(\mathbf{p}_t\cdot\mathbf{k}_2\big) - \frac{\sigma'(\mathbf{p_t})}{p_t^3}\big(\mathbf{p}_t\times\mathbf{k}_1\big)\big(\mathbf{p}_t\times\mathbf{k}_2\big)\right\} = 0\ .$$

The result is again zero because of the azimuthal symmetry of $\sigma(\mathbf{k})$. Hence, all terms of the expansion (A.3) up to the second order in k do not contribute. All other terms linear in $\mathbf{k}_1$ or in $\mathbf{k}_2$, which are obtained from the first terms in the square brackets in Eq. (A.2), do not contribute for the same reason, so the first term different from zero is at least of order $k_1^2 k_2^2$, and originates a square-logarithm singularity as a function of the regulator p_0.

One may repeat the argument for the regions where only one of the integration variables is close to zero. We consider in detail the case $\mathbf{k}_1 \approx 0$ and $\mathbf{k}_2$, $\mathbf{k}_3$ both finite. In this region the term $\delta^{(2)}(\mathbf{p_t}-\mathbf{k})$ does not contribute to Eq. (A.1). The transverse momentum integrals are therefore

$$\int d^2k_1 d^2k_2 \sigma(\mathbf{k}_1)\sigma(\mathbf{k}_2)\Big\{\sigma(\mathbf{p}_t-\mathbf{k}_1-\mathbf{k}_2)-\sigma(\mathbf{p}_t-\mathbf{k}_1)-\sigma(\mathbf{p}_t-\mathbf{k}_2)+\sigma(\mathbf{p_t})\Big\}$$
$$+\int d^2k_1 d^2k_3 \sigma(\mathbf{k}_1)\sigma(\mathbf{k}_3)\Big\{-\sigma(\mathbf{p}_t-\mathbf{k}_1)+\sigma(\mathbf{p_t})\Big\}\ .$$

To study the singularity it is sufficient to keep the first two terms in the expansion of $\sigma(\mathbf{k})$ in Eq. (A.3), the remaining ones leading to a logarithmic divergence. One obtains

$$\int d^2k_1 d^2k_2 \sigma(\mathbf{k}_1)\sigma(\mathbf{k}_2)$$
$$\times\left\{\sigma(\mathbf{p}_t-\mathbf{k}_2)-\sigma'(\mathbf{p}_t-\mathbf{k}_2)\frac{(\mathbf{p}_t-\mathbf{k}_2)\cdot\mathbf{k}_1}{\mathbf{p}_t-\mathbf{k}_2}-\sigma(\mathbf{p_t})+\sigma'(\mathbf{p_t})\frac{\mathbf{p}_t\cdot\mathbf{k}_1}{p_t}-\sigma(\mathbf{p}_t-\mathbf{k}_2)+\sigma(\mathbf{p_t})\right\}$$
$$+\int d^2k_1 d^2k_3 \sigma(\mathbf{k}_1)\sigma(\mathbf{k}_3)\left\{-\sigma(\mathbf{p_t})+\sigma'(\mathbf{p_t})\frac{\mathbf{p}_t\cdot\mathbf{k}_1}{p_t}-\sigma(\mathbf{p_t})\right\}\ ,$$

which simplifies to

$$\int d^2k_1 d^2k_2 \sigma(\mathbf{k}_1)\sigma(\mathbf{k}_2)\left\{-\sigma'(\mathbf{p}_t-\mathbf{k}_2)\frac{(\mathbf{p}_t-\mathbf{k}_2)\cdot\mathbf{k}_1}{\mathbf{p}_t-\mathbf{k}_2}+2\sigma'(\mathbf{p_t})\frac{\mathbf{p}_t\cdot\mathbf{k}_1}{p_t}\right\}=0\ .$$

As in the previous case one obtains a vanishing result thanks to the azimuthal symmetry of $\sigma(\mathbf{k})$.

In summary, all integrations in the singular points of the three-scattering term, Eq. (A.1), induce at most a square-logarithm singularity, as a function of the cutoff.

The reduction of the divergences from power-like to logarithmic is a common feature of all the terms of the expansion of th etransverse spectrum in the number of scatterings as one may see by looking at its Fourier transform, Eq. (5.1.5). Indeed, to study the dependence of the inclusive spectrum on the regulator p_0 at a given p_t different from zero one needs to consider the first term in the square brackets only. The cutoff enters in the difference

$$\tilde\sigma(v)-\tilde\sigma(0)=\int\frac{d\sigma}{d^2k}\Big[e^{i\mathbf{k}\cdot\mathbf{v}}-1\Big]d^2k=-v^2\frac{\pi}{2}\int_{p_0}^{\infty}k^3\frac{d\sigma}{d^2k}dk+\ \text{finite terms}$$

so that, also in this case, the divergence for $p_0\to 0$ is only logarithmic.

A.2 Symmetrization of the expansion in the number of scatterings

For the numerical computation of the high-p_t expansion of the minijet spectrum in the number of scatterings suffered by a projectile parton it is convenient to implement the subtraction of the IR divergences directly in the integrand. In this way the Monte Carlo integrations, which we use because of the high dimensionality of the phase space (in particular for three or more scatterings), work at their best. In fact, Eqs. (5.2.3) and (A.1) are not suited for numerical implementation due to the delta functions. The basic property that allowed the cancellation of the divergence in the integrand was the symmetry under exchanges of the integration variables. Unfortunately after using the delta functions to perform on of the integrals, one obtains in general non-symmetric expressions.

The goal of this appendix is to study how to symmetrize each term of the expansion of the transverse spectrum. We will discuss them in detail up to the three-scattering term, but the techniques discussed can be applied also to the generic term in the expansion. For simplicity, we will use the following notation, already introduced in the main text:

$$\sigma(\mathbf{k}) = \frac{d\sigma}{d^2k}(xx') \ .$$

One-scattering term

The one-scattering term doesn't include any subtraction term, so that we don't need to symmetrize it. It is simply given by

$$\frac{dW_h}{d^2p_t}^{(1)}(x,b,\beta) = \Gamma_h(x,b-\beta)\int dx'\Gamma_A(x',b)\sigma(\mathbf{p_t}) \ , \tag{A.4}$$

and corresponds to the result one obtains by considering just disconnected parton collisions and neglecting parton rescatterings. It corresponds also to modeling the hadron-nucleus collision as a superposition of hadron-nucleus collisions.

Two-scattering term

The two-scattering term is given by Eq. (5.2.3), and we need to perform one integration over $\mathbf{k}_1$ or over $\mathbf{k}_2$ to dispose of the δ functions. By calling simply $\mathbf{q}$ the remaining integration variable we obtain

$$\begin{aligned}\frac{dW_h^{(2)}}{d^2p_t}(x,b,\beta) = \Gamma_h(x,b-\beta)\int \Gamma_A(x_1',b)\Gamma_A(x_2',b)dx_1'dx_2' \\ \times\int d^2q\Big[\sigma(\mathbf{q})\sigma(\mathbf{p_t}-\mathbf{q}) - 2\sigma(\mathbf{q})\sigma(\mathbf{p_t})\Big]\end{aligned} \tag{A.5}$$

As discussed in Section 5.2, the negative term in the expression above subtracts the leading inverse power divergence in the integrand leaving only a logarithmic divergence. However, the cancellation happens only after performing the integral over $\mathbf{q}$, which may be a difficult result to achieve numerically (actually this is not a problem for the two-scattering term, due to the low dimensionality of the integral, but becomes a big issue from three scatterings on).

There are two divergences to be subtracted: one in $\mathbf{q} \sim 0$ and the other in $\mathbf{q} \sim \mathbf{p_t}$, but the subtraction term is divergent just in $\mathbf{q} \sim 0$, and the cancellation of the inverse power singularities is obtained only after performing the integration over $\mathbf{q}$. To allow the numerical integration to do a better and faster job, we want that the divergences in the convolution term and in the subtraction term be cancelled directly in the integrand. This is obtained by symmetrizing the integrand with respect to an interchange of the two singularities in the convolution term. Let's introduce therefore an operator that performs the interchange of the two singularities:

$$\mathbb{T} \ : \ \mathbf{q} \to \mathbf{p_t} - \mathbf{q} \ ,$$

so that

$$\mathbb{T} \int \mathrm{d}^2 q \, f(\mathbf{q}) = \int \mathrm{d}^2 q \, f(\mathbf{p_t} - \mathbf{q}) \ .$$

Note that the change of variables operated by $\mathbb{T}$ has unit Jacobian and that $\mathbb{T}^2 = \mathbb{I}$. Then, we define the symmetrized two-scattering term as

$$\left. \frac{dW_A^{(2)}}{d^2 p_t} \right|_{sym} = \mathbb{S}^{(2)} \frac{dW_h^{(2)}}{d^2 p_t} \ ,$$

where we introduced the symmetrization operator

$$\mathbb{S}^{(2)} = \frac{1}{2}(\mathbb{I} + \mathbb{T}) \ . \tag{A.6}$$

The result is:

$$\begin{aligned} \left. \frac{dW_A^{(2)}}{d^2 p_t} \right|_{sym} (x, b, \beta) \ &= \Gamma_h(x, b - \beta) \int \Gamma_A(x_1', b) \Gamma_A(x_2', b) dx_1' dx_2' \\ &\times \int d^2 q \Big[\sigma(\mathbf{q}) \sigma(\mathbf{p_t} - \mathbf{q}) - \sigma(\mathbf{q}) \sigma(\mathbf{p_t}) - \sigma(\mathbf{p_t} - \mathbf{q}) \sigma(\mathbf{p_t}) \Big] \ . \end{aligned} \tag{A.7}$$

Note that the first term in (A.7) describes two subsequent scatterings with total transverse momentum p_t and is the naive pQCD result. The two negative terms are the absorption terms induced by probability conservation. The two IR divergences of the first term are canceled by these two subtraction terms: as $\mathbf{q} \to \mathbf{0}$ by the first one and as $\mathbf{q} \to \mathbf{p_t}$ by the second one. The remaining linear singularity gives a zero contribution because it is odd in a neighborhood of $\mathbf{q} = 0$ and $\mathbf{q} = \mathbf{p_t}$ so that only the logarithmic divergence remain. Note that now the two divergences are subtracted directly in the integrand, which was the goal of the symmetrization procedure.
Eq. (A.7) is the expression that we use in the numerical computations of the transverse spectrum at high p_t. It could have been guessed directly from Eq. (A.5), but the use of the symmetrization operator (A.6) will facilitate the discussion of the more complicated three scattering term.

Three-scattering term

To prepare the ground for the treatment of the three-scattering term, we note that $\mathbb{T}$ generates the group of the permutations of the two singularities $\mathbf{q} \sim 0$ and $\mathbf{q} \sim \mathbf{p_t}$; this is called the symmetric group of order 2 and indicated as $S_2 = \langle \mathbb{T} \rangle = \{\mathbb{I}, \mathbb{T}\}$, where $\langle \mathbb{T} \rangle$ means "generated by $\mathbb{T}$". It's then easy to see that we can construct the symmetrizing operator (A.6) by summing all the elements of S_2 and by dividing by its cardinality.

From Eq. (A.1), after exploiting the δ functions, the three-scattering term reads

$$\frac{dW_h^{(3)}}{d^2p_t}(x,b,\beta) = \Gamma_h(x, b-\beta) \int \Gamma_A(x_1', b)\Gamma_A(x_2', b)\Gamma_A(x_3', b) dx_1' dx_2' dx_3' \tag{A.8}$$

$$\times \frac{1}{3!} \int \mathrm{d}^2q \mathrm{d}^2r \left[\sigma(\mathbf{q})\sigma(\mathbf{r})\sigma(\mathbf{p_t}-\mathbf{q}-\mathbf{r}) - 3\sigma(\mathbf{q})\sigma(\mathbf{p_t}-\mathbf{q})\sigma(\mathbf{p_t}) + 3\sigma(\mathbf{q})\sigma(\mathbf{r})\sigma(\mathbf{p_t})\right]. \tag{A.9}$$

Following the general analysis previously done at the end of the last paragraph, we observe that in (A.9) in absence of the cutoff we would have four divergences, i.e:

$$\mathbf{q} \sim 0, \qquad \mathbf{r} \sim 0, \qquad \mathbf{p_t} - \mathbf{q} - \mathbf{r} \sim 0, \qquad \mathbf{p_t} - \mathbf{q} \sim 0 \tag{A.10}$$

Then, to write the symmetrized three-scattering term, we need to consider the group S_4 of the permutations of these four divergences, which has $4! = 24$ elements:

$$\mathcal{P}_{Bsym}^{(3)} = \mathbb{S}^{(3)} \mathcal{P}_B^{(2)}$$

where

$$\mathbb{S}^{(3)} = \frac{1}{24} \sum_{\mathbb{T} \in S_4} \mathbb{T}$$

When applying this operator to the three-scattering term the resulting expression has 49 terms and is too long to be discussed here. To have an idea of the result, we will consider only the subgroup S_3 given by the permutations of the first three divergences in (A.10), which are the divergences that appear in the first term of (A.9), i.e. the naive three-scattering term. After the symmetrization it will be immediate to check that all the "single" divergences cancel explicitly in the integrand, while "double" divergences cancel only after performing the integrations over the transverse momenta. We call "single" divergence a point $(\mathbf{q}, \mathbf{r})$ such that only one of the expressions in (A.10) is near zero, and "double" divergence a point such that two of these terms are nearly zero. For example $\{\mathbf{q} \sim 0;\ \mathbf{r} \not\sim 0, \mathbf{p_t}, \mathbf{p_t} - \mathbf{q}\}$ and $\{\mathbf{q} \sim 0;\ \mathbf{r} \sim \mathbf{p_t}\}$ are respectively a single and a double divergence.

The first step is the definition of the operators that exchange the three singularities:

$$\mathbb{T}_1 \ : \ \begin{cases} \mathbf{q} \to \mathbf{r} \\ \mathbf{r} \to \mathbf{q} \end{cases} \qquad \mathbb{T}_2 \ : \ \begin{cases} \mathbf{q} \to \mathbf{p_t} - \mathbf{q} - \mathbf{r} \\ \mathbf{r} \to \mathbf{r} \end{cases} \qquad \mathbb{T}_3 \ : \ \begin{cases} \mathbf{q} \to \mathbf{q} \\ \mathbf{r} \to \mathbf{p_t} - \mathbf{q} - \mathbf{r} \end{cases}$$

Note that they are idempotent: $\mathbb{T}_i = \mathbb{I}$. Next, we observe that the group S_3 of the permutations of the three singularities is made of $3! = 6$ objects, and that

$$S_3 = \langle \mathbb{T}_1, \mathbb{T}_2, \mathbb{T}_3 \rangle = \{\mathbb{T}_0, \mathbb{T}_1, \mathbb{T}_2, \mathbb{T}_3, \mathbb{T}_4, \mathbb{T}_5\} \ ,$$

where $\mathbb{T}_0 = \mathbb{I}$, $\mathbb{T}_4 = \mathbb{T}_1\mathbb{T}_2$ and $\mathbb{T}_5 = \mathbb{T}_1\mathbb{T}_3$, so that the reduced symmetrizing operator is

$$\mathbb{S}^{(3)}_{red} = \frac{1}{3!}\sum_{i=0}^{5}\mathbb{T}_i \ .$$

Finally one can write the partially symmetrized three-scattering probability:

$$\begin{aligned}
\left.\frac{dW_A^{(3)}}{d^2p_t}\right|_{sym}(x,b,\beta) &= \mathbb{S}^{(3)}_{red}\frac{dW_A^{(3)}}{d^2p_t}(x,b,\beta) = \\
&= \Gamma_h(x,b-\beta)\int \Gamma_A(x_1',b)\Gamma_A(x_2',b)\Gamma_A(x_3',b)dx_1'dx_2'dx_3'd^2k_1d^2k_2d^2k_3 \\
&\quad\times\frac{1}{3!}\int \mathrm{d}x'\mathrm{d}^2q\mathrm{d}^2r\Big[\sigma(\mathbf{q})\sigma(\mathbf{r})\sigma(\mathbf{p_t}-\mathbf{q}-\mathbf{r}) \\
&\qquad -\frac{1}{2}\sigma(\mathbf{q})\sigma(\mathbf{r})\sigma(\mathbf{p_t}-\mathbf{q}) + \frac{1}{2}\sigma(\mathbf{q})\sigma(\mathbf{p_t}-\mathbf{q})\sigma(\mathbf{p_t}) \\
&\qquad -\frac{1}{2}\sigma(\mathbf{q})\sigma(\mathbf{r})\sigma(\mathbf{p_t}-\mathbf{r}) + \frac{1}{2}\sigma(\mathbf{p_t}-\mathbf{r})\sigma(\mathbf{q})\sigma(\mathbf{p_t}) \\
&\qquad -\frac{1}{2}\sigma(\mathbf{p_t}-\mathbf{q}-\mathbf{r})\sigma(\mathbf{q})\sigma(\mathbf{p_t}-\mathbf{q}) + \frac{1}{2}\sigma(\mathbf{p_t}-\mathbf{r})\sigma(\mathbf{p_t}-\mathbf{q})\sigma(\mathbf{p_t}) \\
&\qquad -\frac{1}{2}\sigma(\mathbf{p_t}-\mathbf{q}-\mathbf{r})\sigma(\mathbf{r})\sigma(\mathbf{p_t}-\mathbf{r}) + \frac{1}{2}\sigma(\mathbf{p_t}-\mathbf{r})\sigma(\mathbf{p_t}-\mathbf{q}-\mathbf{r})\sigma(\mathbf{p_t}) \\
&\qquad -\frac{1}{2}\sigma(\mathbf{r})\sigma(\mathbf{p_t}-\mathbf{q}-\mathbf{r})\sigma(\mathbf{q}+\mathbf{r}) + \frac{1}{2}\sigma(\mathbf{r})\sigma(\mathbf{q}-\mathbf{r})\sigma(\mathbf{p_t}) \\
&\qquad -\frac{1}{2}\sigma(\mathbf{q})\sigma(\mathbf{p_t}-\mathbf{q}-\mathbf{r})\sigma(\mathbf{q}+\mathbf{r}) + \frac{1}{2}\sigma(\mathbf{q})\sigma(\mathbf{q}-\mathbf{r})\sigma(\mathbf{p_t})\Big] \ . \qquad \text{(A.11)}
\end{aligned}$$

Analogously to what has been done for the two-scattering term, one can see by inspection that the four single divergences (A.10) explicitly cancel in the integrand, while double divergences cancel only after performing the integrations over q and r. By considering all four singularities, and by using the whole S_4 group we would get explicit cancellation of both "single" and "double" divergences directly in the integrand, as is discussed in Appendix A.1. Nonetheless, the partial symmetrization is enough to get satisfactory numerical results.

In conclusion, to compute numerically the expansion of the transverse minijet spectrum in the number of scatterings one has to fully exploit the symmetry properties of each term, in such a way that all the divergences get cancelled directly in the integrand. This is crucial to obtain a good numerical precision and to speed up the computation of the terms with three or more scatterings. In this appendix we developed a general technique to perform such a symmetrization.

A.3 Generalization of the transverse spectrum

In this section we discuss how to generalize the rescattering formalism discussesd in Chapter 2 to include a rather generic choice of the scale in the parton distributions and in the strong coupling constant α_s. For brevity, we will illustrate this in the specific case in which parton correlations inside the nuclei are neglected. The following discussion may be nevertheless done using the more general formalism discussed in Chapter 2.

We start from the formula (5.1.1) for the transverse minijet spectrum. We can rewrite it in terms of the pseudorapidity $\eta = \log(x\sqrt{s}/p_t)$ of the wounded projectile parton (which, from now on, will be called minijet), and show explicitly the dependence of various quantities from the momentum scale:

$$\frac{dW_h}{d\eta\, d^2p_t}(x,b,\beta) \;=\; \left[x\Gamma_h(x,b-\beta;Q)\right]_{x=(p_t/\sqrt{s})\exp(\eta)} \tag{A.12}$$

$$\times \sum_{\nu=1}^{\infty} \frac{1}{\nu!} \int \Gamma_A(x_1',b;Q_1') \ldots \Gamma_A(x_\nu',b;Q_\nu')\, e^{-\int dx' \Gamma_A(x',b) \int d^2k\, d\sigma(xx';Q')/d^2k}$$

$$\times \frac{d\sigma(xx_1';Q_1')}{d^2k_1} \ldots \frac{d\sigma(xx_\nu';Q_\nu')}{d^2k_\nu}\, \delta^{(2)}(\mathbf{k}_1 + \cdots + \mathbf{k}_\nu - \mathbf{p_t})\, d^2k_1 \ldots d^2k_\nu\; dx_1' \ldots dx_\nu' \;. \tag{A.13}$$

The scale for the target parton distributions and the coupling constant for each scattering may be naturally chosen to be a function g of the transverse momentum exchanged in each interaction:

$$Q_i' = g(k_i) \quad \text{and} \quad Q' = g(k) \;,$$

and typically we may choose $g(k_i) = k_i$. The choice of the scale for the projectile parton is less evident. However, in the spirit of Sec. 2.3 we think to the projectile parton as interacting with the whole target, therefore the most natural choice is to take the scale to be a function of the overall exchanged momentum, i.e., p_t:

$$Q = f(p_t) \;,$$

typically $f(p_t) = p_t$. Let us define the Fourier transform of the product of the traget parton distribution and the differential parton-parton cross section:

$$\widetilde{\Omega}_A(v;x,b) = \int d^2k\, e^{-i\mathbf{k}\cdot\mathbf{v}} \int dx' \Gamma_A\big(x',b;g(k)\big)\, \frac{d\sigma(xx';g(k))}{d^2k} \;.$$

After Fourier transforming the sum in Eq. (A.13), and performing the sum over ν, the spectrum may be written as

$$\boxed{\frac{dW_h}{d\eta\, d^2p_t}(b,\beta) \;=\; \left[x\Gamma_h\big(x,b-\beta;f(p_t)\big) \int \frac{d^2v}{(2\pi)^2} e^{-i\mathbf{p_t}\cdot\mathbf{v}} \widetilde{W}_A(v;x,b)\right]_{x=(p_t/\sqrt{s})\exp(\eta)}} \;, \tag{A.14}$$

where

$$\boxed{\widetilde{W}_A(v;x,b) \;=\; \sum_{\nu=1}^{\infty} \frac{1}{\nu!} \Big[\widetilde{\Omega}_A(v;x,b)\Big]^\nu \; e^{-\widetilde{\Omega}_A(0;x,b)} = e^{\widetilde{\Omega}_A(v;x,b) - \widetilde{\Omega}_A(0;x,b)} - e^{-\int \widetilde{\Omega}_A(0;x,b)}}\;.$$

Equation (A.14) may be computed numerically and gives good results for not too large p_t, after which the result begins to oscillate too much. For higher p_t we may use a suitable generalization of the results of Appendix A.2. Then, the low-p_t and high-p_t part

of the spectrum must be glued together. The gluing point turns out to be a function of the infrared regulator p_0, such that we did not find a good way to glue the two parts automatically and we had to do it by hand.

To compute integrated quantities like the pseudorapidity distribution of minijets,

$$\frac{dW_h}{d\eta} = \int d^2p_t \, \frac{dW_h}{d\eta d^2p_t} \; , \tag{A.15}$$

it would be better to have an analytical formula. We start from a simpler problem, namely the computation of the x distribution of minijets,

$$\frac{dW_h}{dx} = \int d^2p_t \, \Gamma_h\big(x, b-\beta; f(p_t)\big) \int \frac{d^2v}{(2\pi)^2} e^{-i\mathbf{p_t}\cdot\mathbf{v}} \widetilde{W}_A(v; x, b) \; .$$

Next, let us introduce the Fourier transform of the projectile parton distribution:

$$\widetilde{\Gamma}_h(w; b-\beta) = \int d^2p_t \, e^{-i\mathbf{p_t}\cdot\mathbf{w}} \Gamma_h\big(x, b-\beta; f(p_t)\big) \; . \tag{A.16}$$

Note that $\widetilde{\Gamma}$ is a function of the modulus w of the Fourier variable $\mathbf{w}$ conjugated to $\mathbf{p_t}$, and that $\widetilde{\Gamma}(v) = \widetilde{\Gamma}(-v)$. Then, it is easy to prove that

$$\begin{aligned} \frac{dW_h}{dx d^2p_t}(b,\beta) &= \int d^2w \, \widetilde{\Gamma}_h(w; b-\beta) \widetilde{W}_A(w; x, b) & \text{(A.17)} \\ &= 2\pi \int dw \, w \, \widetilde{\Gamma}_h(w; b-\beta) \widetilde{W}_A(w; x, b) \; . & \text{(A.18)} \end{aligned}$$

The computation of the pseudorapidity distribution of minijets [Eq. (A.15)] is more complicated because the integrand in Eq. (A.16) has to be evaluated at $x = (p_t/\sqrt{s})\exp(\eta)$ and it is no more possible to obtain as a simple equation as Eq. (A.18). To simplify a little bit the problem we define

$$\widetilde{\Gamma}^*_h(w; b) = \int d^2p_t \, e^{-i\mathbf{p_t}\cdot\mathbf{w}} \left[x\Gamma_h\big(x, b-\beta; f(p_t)\big)\right]_{x=(p_t/\sqrt{s})\exp(\eta)} \; .$$

Note that $\widetilde{\Gamma}$ is a function of the modulus v of the Fourier variable $\mathbf{v}$ conjugated to $\mathbf{p_t}$, and that $\widetilde{\Gamma}(v) = \widetilde{\Gamma}(-v)$. Then the minijet pseudorapidity distribution may be written as

$$\frac{dW_h}{d\eta} = \int d^2v \, d^2w \, d^2p_t \, e^{-i\mathbf{p_t}\cdot\mathbf{v}} e^{-i\mathbf{p_t}\cdot\mathbf{w}} \widetilde{\Gamma}^*_h(w; b) \; \widetilde{W}_A(v; x, b)\Big|_{x=(p_t/\sqrt{s})\exp(\eta)} \; .$$

Since $\widetilde{\Gamma}$ and $\widetilde{W}_A$ depend only on the moduli of $\mathbf{u}$, $\mathbf{v}$, and $\mathbf{p_t}$, we obtain

$$\boxed{\frac{dW_h}{d\eta} = \int dv \, dw \, dp_t \, J_0(p_t v) J_0(p_t w) \; \Big[w \, \widetilde{\Gamma}^*_h(w; b)\Big] \; \Big[p_t v \, \widetilde{W}_A(v; x, b)\Big]_{x=(p_t/\sqrt{s})\exp(\eta)}} \; .$$

Whether this equation is of practical use or not is a question under investigation.

Acknowledgements

I would like to thank my advisor, D. Treleani, for introducing me in this fascinating subject, for his guidance and help and for giving me the possibility to participate in many conferences and schools, where I could meet people and learn a lot. Thank you very much also to my colleagues at the department of theoretical physics, in particular to A. Del Fabbro, E. Deotto, and R. Romano, who had the (bad) luck to share the office with me.
I am indebted also to many others for sharing with me their wisdom during the last three years. They helped me in learning various aspects of heavy-ion physics and encouraged me in many ways to endure the research whose results have been reported in this thesis. They are R. Arnaldi, K.J. Eskola, P. Huovinen, M. Gyulassy, D. Kharzeev, B. Kopeliovich, I. Lokhtin, L. McLerran, A.H. Mueller, H. J. Pirner, A. Polleri, C. Salgado, K. Tuominen, U. Wiedemann, and F. Yuan. In listing them I have for sure forgot someone, but I wish to express my deep gratitude to all of them.
Last but not least, thank you to my family for their never ending love and support.

Bibliography

Theory

[1] Proceedings of the "15th International Conference on Ultrarelativistic Nucleus-Nucleus Collisions" (QM2001), Stony Brook (NY), USA, 15-20 Jan 2001, to be published in Nucl. Phys. A.

[2] V. A. Abramovsky, V. N. Gribov and O. V. Kancheli, Yad. Fiz. **18**, 595 (1973); L. Bertocchi and D. Treleani, J. Phys. G **G3**, 147 (1977).

[3] A. Accardi and D. Treleani, Phys. Rev. D **63** (2001) 116002.

[4] A. Accardi, *Talk given at 36th Rencontres de Moriond on QCD and Hadronic Interactions, Les Arcs, France, 17-24 Mar 2001*, hep-ph/0104060.

[5] A. Accardi and D. Treleani, hep-ph/0106306, to be published in Phys. Rev. D.

[6] A. Accardi, hep-ph/0107301, to be published in Phys. Rev. C.

[7] L. Ametller and D. Treleani, Int. J. Mod. Phys. **A3**, 521 (1988);

[8] N. Armesto and C. Pajares, Int. J. Mod. Phys. A **15** (2000) 2019.

[9] R. Baier, Y. L. Dokshitzer, A. H. Mueller, S. Peigne and D. Schiff, Nucl. Phys. B **484** (1997) 265.

[10] R. Baier, A. H. Mueller, D. Schiff and D. T. Son, Phys. Lett. B **502** (2001) 51.

[11] A. Bialas, M. Bleszynski and W. Czyz, Nucl. Phys. **B111**, 461 (1976);

[12] J. D. Bjorken, Phys. Rev. D **27** (1983) 140.

[13] J. P. Blaizot and A. H. Mueller, Nucl. Phys. **B289** (1987) 847;

[14] J. P. Blaizot, *Talk given at QM2001* [1], nucl-th/0107025.

[15] R. Blankenbecler, A. Capella, C. Pajares, J. Tran Thanh Van and A. Ramallo, Phys. Lett. B **107** (1981) 106; C. Pajares and A. V. Ramallo, Phys. Rev. D **31** (1985) 2800;

[16] W. Busza and A. S. Goldhaber, Phys. Lett. B **139** (1984) 235.

[17] G. Calucci and D. Treleani, Phys. Rev. **D41**, 3367 (1990);

[18] G. Calucci and D. Treleani, Phys. Rev. **D44**, 2746 (1991);

[19] G. Calucci and D. Treleani, Int. J. Mod. Phys. A **6** (1991) 4375.

[20] G. Calucci and D. Treleani, Phys. Rev. D **49** (1994) 138; Phys. Rev. D **50** (1994) 4703.

[21] A. Capella, U. Sukhatme, C. Tan and J. Tran Thanh Van, Phys. Rept. **236** (1994) 225; A. B. Kaidalov and K. A. Ter-Martirosian, Sov. J. Nucl. Phys. **39** (1984) 979 [Yad. Fiz. **39** (1984) 1545]; S. Bondarenko, E. Gotsman, E. Levin and U. Maor, Nucl. Phys. A **683** (2001) 649.

[22] A. Capella, J. Tran Thanh Van and J. Kwiecinski, Phys. Rev. Lett. **58**, 2015 (1987);

[23] A. Del Fabbro and D. Treleani, Phys. Rev. D **63** (2001) 057901, and references therein.

[24] J. Dias de Deus and R. Ugoccioni, Phys. Lett. B **494** (2000) 53; A. Capella and D. Sousa, Phys. Lett. B **511** (2001) 185; N. Armesto and C. A. Salgado, hep-ph/0011352.

[25] Y. L. Dokshitzer, Sov. Phys. JETP **46** (1977) 641 [Zh. Eksp. Teor. Fiz. **73** (1977) 1216]; V. N. Gribov and L. N. Lipatov, Yad. Fiz. **15** (1972) 781 [Sov. J. Nucl. Phys. **15** (1972) 438]; G. Altarelli and G. Parisi, Nucl. Phys. B **126** (1977) 298.

[26] H. J. Drescher, M. Hladik, S. Ostapchenko, T. Pierog and K. Werner, Phys. Rept. **350** (2001) 93.

[27] L. Durand and H. Pi, Phys. Rev. Lett. **58** (1987) 303; A. Capella, J. Tran Thanh Van and J. Kwiecinski, Phys. Rev. Lett. **58** (1987) 2015; T. Sjostrand and M. van Zijl, Phys. Rev. D **36** (1987) 2019; B. Margolis, P. Valin, M. M. Block, F. Halzen and R. S. Fletcher, Phys. Lett. B **213** (1988) 221; W. R. Chen and R. C. Hwa, Phys. Rev. D **39** (1989) 179.

[28] V. Emel'yanov, A. Khodinov, S. R. Klein and R. Vogt, Phys. Rev. **C61**, 044904 (2000); N. Hammon, H. Stocker and W. Greiner, Phys. Rev. **C61**, 014901 (2000);

[29] K. J. Eskola, J. Qiu and X. Wang, Phys. Rev. Lett. **72**, 36 (1994); J. Jalilian-Marian and X. Wang, Phys. Rev. D **63** (2001) 096001.

[30] K. J. Eskola, B. Muller and X. Wang, Phys. Lett. **B374**, 20 (1996);

[31] K. J. Eskola, K. Kajantie and P. V. Ruuskanen, Eur. Phys. J. **C1**, 627 (1998);

[32] K. J. Eskola, hep-ph/9911350.

[33] K. J. Eskola, K. Kajantie, P. V. Ruuskanen and K. Tuominen, Nucl. Phys. B **570** (2000) 379;

[34] K. J. Eskola and K. Tuominen, Phys. Lett. B **489** (2000) 329.

[35] K. J. Eskola, K. Kajantie and K. Tuominen, Phys. Lett. B **497** (2001) 39;

[36] K. J. Eskola, P. V. Ruuskanen, S. S. Rasanen and K. Tuominen, hep-ph/0104010;

[37] K. J. Eskola, *Talk given at QM2001* [1], hep-ph/0104058;

[38] K. J. Eskola, K. Kajantie and K. Tuominen, hep-ph/0106330.

[39] K. J. Eskola and K. Tuominen, private communication

[40] T. K. Gaisser and F. Halzen, Phys. Rev. Lett. **54** (1985) 1754; G. Pancheri and Y. Srivastava, Phys. Lett. B **159** (1985) 69 and Phys. Lett. B **182** (1986) 199;

[41] G. Gatoff and C. Y. Wong, Phys. Rev. D **46** (1992) 997.

[42] K. Golec-Biernat and M. Wusthoff, Phys. Rev. D **59** (1999) 014017; Phys. Rev. D **60** (1999) 114023; A. M. Stasto, K. Golec-Biernat and J. Kwiecinski, Phys. Rev. Lett. **86** (2001) 596.

[43] L. V. Gribov, E. M. Levin and M. G. Ryskin, Phys. Rept. **100** (1983) 1.

[44] X. Guo and X. Wang, Phys. Rev. Lett. **85** (2000) 3591; X. Wang and X. Guo, hep-ph/0102230.

[45] M. Gyulassy, *Lectures given at "Dense Matter" (IUKT 40), Schladming, Austria, 3-10 Mar 2001*, nucl-th/0106072.

[46] U. W. Heinz and M. Jacob, nucl-th/0002042.

[47] U. W. Heinz, Nucl. Phys. A **685** (2001) 414.

[48] U. W. Heinz, hep-ph/0109006.

[49] A. Hosoya and K. Kajantie, Nucl. Phys. B **250** (1985) 666; P. Danielewicz and M. Gyulassy, Phys. Rev. D **31** (1985) 53; S. Gavin, Nucl. Phys. A **435** (1985) 826.

[50] J. Jalilian-Marian and X. Wang, Phys. Rev. D **60** (1999) 054016.

[51] S. Jeon and J. Kapusta, Phys. Rev. C **63** (2001) 011901; D. E. Kahana and S. H. Kahana, Phys. Rev. C **63** (2001) 031901; Z. Lin, S. Pal, C. M. Ko, B. Li and B. Zhang, Phys. Rev. C **64** (2001) 011902; N. Armesto, C. Pajares and D. Sousa, hep-ph/0104269; see also [92]

[52] M. B. Johnson, B. Z. Kopeliovich and A. V. Tarasov, Phys. Rev. C **63** (2001) 035203.

[53] D. E. Kahana and S. H. Kahana, Phys. Rev. C **63** (2001) 031901;

[54] K. Kajantie, Nucl. Phys. **A663**, 191 (2000); N. Armesto and C. Pajares, Int. J. Mod. Phys. **A15**, 2019 (2000);

[55] K. Kajantie, P. V. Landshoff and J. Lindfors, Phys. Rev. Lett. **59** (1987) 2527; K. J. Eskola, K. Kajantie and J. Lindfors, Nucl. Phys. B **323** (1989) 37; K. J. Eskola and K. Kajantie, Z. Phys. C **75** (1997) 515;

[56] F. Karsch, *Lectures given at "Dense Matter" (IUKT 40), Schladming, Austria, 3-10 Mar 2001*, hep-lat/0106019.

[57] K. Kastella, Phys. Rev. D **36** (1987) 2734. K. Kastella, G. Sterman and J. Milana, Phys. Rev. D **39** (1989) 2586; K. Kastella, J. Milana and G. Sterman, Phys. Rev. Lett. **62** (1989) 730.

[58] D. Kharzeev, nucl-th/0107033.

[59] D. Kharzeev, C. Lourenco, M. Nardi and H. Satz, Z. Phys. C **74** (1997) 307.

[60] D. Kharzeev and M. Nardi, Phys. Lett. B **507** (2001) 121.

[61] D. Kharzeev and E. Levin, nucl-th/0108006.

[62] P. F. Kolb, U. Heinz, P. Huovinen, K. J. Eskola and K. Tuominen, hep-ph/0103234, and references therein.

[63] P. F. Kolb, nucl-th/0104089.

[64] P. F. Kolb, P. Huovinen, U. W. Heinz and H. Heiselberg, Phys. Lett. B **500** (2001) 232; P. Huovinen, P. F. Kolb, U. W. Heinz, P. V. Ruuskanen and S. A. Voloshin, Phys. Lett. B **503** (2001) 58.

[65] Y. V. Kovchegov and A. H. Mueller, Nucl. Phys. B **529** (1998) 451; A. Dumitru and L. McLerran, hep-ph/0105268.

[66] Y. V. Kovchegov, hep-ph/0011252; Y. V. Kovchegov, *Talk given at QM2001* [1], hep-ph/0106313.

[67] A. Krasnitz and R. Venugopalan, *Talk given at QM2001* [1], hep-ph/0104168; A. Krasnitz, Y. Nara and R. Venugopalan, hep-ph/0108092.

[68] J. Kuhn, Phys. Rev. D **13** (1976) 2948; A. Krzywicki, J. Engels, B. Petersson and U. Sukhatme, Phys. Lett. B **85** (1979) 407. M. Lev and B. Petersson, Z. Phys. **C21** (1983) 155.

[69] P. Levai, G. Papp, G. Fai, M. Gyulassy, G. G. Barnafoldi, I. Vitev and Y. Zhang, *Talk given at QM2001* [1], nucl-th/0104035; X. Wang, *Talk given at QM2001* [1], nucl-th/0105053.

[70] A. Leonidov, M. Nardi and H. Satz, Z. Phys. C **74** (1997) 535.

[71] F. M. Liu, H. J. Drescher, S. Ostapchenko, T. Pierog and K. Werner, hep-ph/0109104.

[72] M. Luo, J. W. Qiu and G. Sterman, Phys. Rev. D **50** (1994) 1951; X. Guo, Phys. Rev. D **58** (1998) 036001, Phys. Rev. D **58** (1998) 114033;

[73] L. McLerran, *Lectures given at "Dense Matter" (IUKT 40), Schladming, Austria, 3-10 Mar 2001*, hep-ph/0104285 and references therein;

[74] L. D. McLerran and R. Venugopalan, Phys. Rev. D **49** (1994) 2233; Phys. Rev. D **49** (1994) 3352; Phys. Rev. D **50** (1994) 2225; Phys. Rev. D **59** (1999) 094002; A. Ayala, J. Jalilian-Marian, L. D. McLerran and R. Venugopalan, Phys. Rev. D **53** (1996) 458.

[75] A. H. Mueller, Nucl. Phys. A **654** (1999) 37C.

[76] A. H. Mueller, Nucl. Phys. B **558** (1999) 285; Nucl. Phys. B **572** (2000) 227.

[77] A. H. Mueller and J. Qiu, Nucl. Phys. **B268**, 427 (1986);

[78] J. L. Nagle, nucl-ex/0109016.

[79] G. C. Nayak, A. Dumitru, L. D. McLerran and W. Greiner, Nucl. Phys. A **687** (2001) 457; J. Ruppert, G. C. Nayak, D. D. Dietrich, H. Stocker and W. Greiner, hep-ph/0109043.

[80] H. J. Pirner and F. Yuan, Phys. Lett. B **512** (2001) 297, and private communication.

[81] J. Qiu, Phys. Rev. D **42** (1990) 30.

[82] R. Ragazzon and D. Treleani, Z. Phys. C **65** (1995) 305.

[83] K. Rajagopal, hep-ph/0109135.

[84] D. Treleani, Int. J. Mod. Phys. A **11** (1996) 613.

[85] L. Van Hove and A. Giovannini, Acta Phys. Polon. B **19** (1988) 917; Y. L. Dokshitzer, V. A. Khoze and S. I. Troian, Z. Phys. C **55** (1992) 107.

[86] E. Wang and X. N. Wang, Phys. Rev. C **64** (2001) 034901.

[87] X. N. Wang and M. Gyulassy, Phys. Rev. D **44** (1991) 3501; Phys. Rev. D **45** (1992) 844; Comput. Phys. Commun. **83** (1994) 307.

[88] X. N. Wang, Phys. Rev. D **46** (1992) 1900; Phys. Rev. D **47** (1993) 2754.

[89] X. N. Wang, Phys. Rept. **280** (1997) 287.

[90] X. N. Wang, Phys. Rev. C **61** (2000) 064910;

[91] X. Wang, Phys. Rev. Lett. **81** (1998) 2655; M. Gyulassy and P. Levai, Phys. Lett. B **442** (1998) 1; G. Papp, P. Levai and G. Fai, Phys. Rev. C **61** (2000) 021902; G. Papp, G. G. Barnafoldi, G. Fai, P. Levai and Y. Zhang, *Talk given at QM2001* [1], nucl-th/0104021.

[92] X. N. Wang and M. Gyulassy, Phys. Rev. Lett. **86** (2001) 3496

[93] U. A. Wiedemann, Nucl. Phys. B **588** (2000) 303; M. Gyulassy, P. Levai and I. Vitev, Nucl. Phys. B **594** (2001) 371.

[94] C. Y. Wong, "Introduction to high-energy heavy ion collisions," *World Scientific, Singapore, 1994.*

[95] B. Zhang,C. M. Ko, B. Li, Z. Lin Phys. Rev. C **61** (2000) 067901;

[96] Y. Zhang, G. Fai, G. Papp, G. G. Barnafoldi and P. Levai, hep-ph/0109233.

Experiments

[97] F. Abe *et al.* [CDF Collaboration],, Phys. Rev. D **41** (1990) 2330.

[98] M. C. Abreu *et al.* [NA50 Collaboration], Phys. Lett. B **477** (2000) 28.

[99] K. Adcox *et al.* [PHENIX Collaboration], Phys. Rev. Lett. **86** (2001) 3500.

[100] K. Adcox *et al.* [PHENIX Collaboration], Phys. Rev. Lett. **87** (2001) 052301.

[101] K. Adcox *et al.* [PHENIX Collaboration], nucl-ex/0109003.

[102] C. Adler *et al.* [STAR Collaboration], Phys. Rev. Lett. **87** (2001) 112303.

[103] T. Affolder *et al.* [CDF Collaboration], Phys. Rev. D **64** (2001) 032001, and references therein.

[104] G. Agakishiev *et al.* [CERES Collaboration], hep-ex/0003012.

[105] M. M. Aggarwal *et al.* [WA98 Collaboration], Phys. Rev. Lett. **81** (1998) 4087, Erratum-ibid. **84** (1998) 578.

[106] M. M. Aggarwal *et al.* [WA98 Collaboration], Eur. Phys. J. C **18** (2001) 651

[107] C. Albajar *et al.* [UA1 Collaboration], Jets," Nucl. Phys. B **309** (1988) 405.

[108] B. Alper *et al.* [British-Scandinavian Collaboration], Nucl. Phys. B **87** (1975) 19; K. Alpgard *et al.* [UA5 Collaboration], Phys. Lett. B **107** (1981) 310.

[109] H. Appelshauser *et al.* [NA49 Collaboration], Phys. Rev. Lett. **82** (1999) 2471.

[110] B. B. Back *et al.* [PHOBOS Collaboration], Phys. Rev. Lett. **85** (2000) 3100.

[111] B. B. Back *et al.* [PHOBOS Collaboration], nucl-ex/0105011

[112] B. B. Back *et al.* [PHOBOS Collaboration], Phys. Rev. Lett. **87** (2001) 102303.

[113] B. B. Back *et al.* [PHOBOS Collaboration], nucl-ex/0108009.

[114] M. Banner *et al.* [UA2 Collaboration], Phys. Lett. B **118** (1982) 203; G. Arnison *et al.* [UA1 Collaboration], Phys. Lett. B **123** (1983) 115; T. Akesson *et al.* [AFS Collaboration], Phys. Lett. B **123** (1983) 133.

[115] D. S. Barton *et al.*, Phys. Rev. D **27** (1983) 2580.

[116] I. G. Bearden *et al.* [BRAHMS Collaborations], nucl-ex/0108016.

[117] A. E. Brenner *et al.*, Phys. Rev. D **26** (1982) 1497.

[118] M. D. Corcoran *et al.* [E609 collaboration], Phys. Lett. B **259** (1991) 209.

[119] J. W. Cronin et al., Phys. Rev. D **11** (1975) 3105; D. Antreasyan et al., Phys. Rev. **D 19** (1979) 764; P. B. Straub *et al.*, Phys. Rev. Lett. **68** (1992) 452.

[120] J. E. Elias *et al.*, W. Busza, C. Halliwell, D. Luckey, P. Swartz, L. Votta and C. Young, Phys. Rev. D **22** (1980) 13.

[121] D.E.Groom *et al.*, Eur. Phys. Jou. C**15** (2000) 1, Fig. 37.19

[122] I. P. Lokhtin and L. I. Sarycheva [CMS Collaboration], Nucl. Phys. A **681** (2001) 229.

[123] G. Martinez [ALICE Collaboration], *Talk given at 36th Rencontres de Moriond on QCD and Hadronic Interactions, Les Arcs, France, 17-24 Mar 2001*, hep-ex/0106034.

[124] A. Milov [PHENIX Collaboration], *Talk given at QM2001* [1], nucl-ex/0107006.

[125] D. Naples *et al.* [E683 Collaboration], Phys. Rev. Lett. **72** (1994) 2341.

[126] J. Rak [CERES Collaboration], *Talk given at QM2001* [1].

[127] F. Rimondi [CDF Collaboration], Nucl. Phys. B (Proc. Suppl.) **92** (2001) 114.

[128] C. Roland *et al.* [PHOBOS Collaboration], *Talk given at 36th Rencontres de Moriond on QCD and Hadronic Interactions, Les Arcs, France, 17-24 Mar 2001*, hep-ex/0105043;

[129] R. J. Snellings [STAR Collaboration], nucl-ex/0104006.

[130] J. Stachel and G. R. Young, Ann. Rev. Nucl. Part. Sci. **42** (1992) 537.

[131] W. Thome *et al.* [Aachen-CERN-Heidelberg-Munich Collaboration], Nucl. Phys. B **129** (1977) 365.

[132] F. Videbaek [BRAHMS Collaboration], *Talk given at QM2001* [1], J. Phys. G **27** (2001) 671; W. A. Zajc *et al.* [PHENIX Collaboration], *Talk given at QM2001* [1], nucl-ex/0106001; J. Harris [STAR Collaboration], *Talk given at QM2001* [1].

Parton distribution functions

[133] K. J. Eskola, V. J. Kolhinen and C. A. Salgado, Eur. Phys. J. C **9** (1999) 61.

[134] M. Gluck, E. Reya and A. Vogt, Z. Phys. C **67** (1995) 433.

[135] M. Gluck, E. Reya and A. Vogt, Eur. Phys. J. **C5** (1998) 461;

[136] H. L. Lai *et al.* [CTEQ Collaboration], Eur. Phys. J. C **12** (2000) 375.